High Fidelity Modeling of Field-Reversed Configuration (FRC) Thrusters

Justin Koo   R. Martin
Eder M. Sousa (ERC)

Air Force Research Laboratory (AFMC)
In-Space Propulsion Branch
AFRL/RQRS
1 Ara Drive
Edwards AFB, CA 93524

April 2017

In-House Final Report

STINFO COPY

AIR FORCE RESEARCH LABORATORY
AEROSPACE SYSTEMS DIRECTORATE

■ **Air Force Materiel Command**   ■ **United States Air Force**   ■ **Edwards Air Force Base, CA 93524**

- STINFO COPY -
NOTICE AND SIGNATURE PAGE

Using Government drawings, specifications, or other data included in this document for any purpose other than Government procurement does not in any way obligate the U.S. Government. The fact that the Government formulated or supplied the drawings, specifications, or other data does not license the holder or any other person or corporation; or convey any rights or permission to manufacture, use, or sell any patented invention that may relate to them.

Qualified requestors may obtain copies of this report from the Defense Technical Information Center (DTIC) (http://www.dtic.mil).

AFRL-RQ-ED-TR-2017-0002 HAS BEEN REVIEWED AND IS APPROVED FOR PUBLICATION IN ACCORDANCE WITH ASSIGNED DISTRIBUTION STATEMENT.

FOR THE DIRECTOR:

//signed//   //signed//

_____   _____
ROBERT S. MARTIN   JUSTIN W. KOO, Ph.D.
Program Manager   Technical Advisor
                                                                     In-Space Propulsion Branch

//signed//

_____
Technical Advisor
Rocket Propulsion Division

This report is published in the interest of scientific and technical information exchange, and its publication does not constitute the Government's approval or disapproval of its ideas or findings.

REPORT DOCUMENTATION PAGE

Public reporting burden for this collection of information is estimated to average 1 hour per response, including the time for reviewing instructions, searching existing data sources, gathering and maintaining the data needed, and completing and reviewing this collection of information. Send comments regarding this burden estimate or any other aspect of this collection of information, including suggestions for reducing this burden to Department of Defense, Washington Headquarters Services, Directorate for Information Operations and Reports (0704-0188), 1215 Jefferson Davis Highway, Suite 1204, Arlington, VA 22202-4302. Respondents should be aware that notwithstanding any other provision of law, no person shall be subject to any penalty for failing to comply with a collection of information if it does not display a currently valid OMB control number. **PLEASE DO NOT RETURN YOUR FORM TO THE ABOVE ADDRESS.**

1. REPORT DATE *(MM-DD-YYYY)*	2. REPORT TYPE	3. DATES COVERED *(From - To)*
April 22, 2017	In-House Final Report	1/28/2014 - 1/18/2017

4. TITLE AND SUBTITLE

High Fidelity Modeling of Field-Reversed Configuration (FRC) Thrusters

5a. CONTRACT NUMBER
14RQ13COR

5b. GRANT NUMBER

5c. PROGRAM ELEMENT NUMBER

6. AUTHOR(S)
Justin Koo; R. Martin; Eder M. Sousa (ERC)

5d. PROJECT NUMBER

5e. TASK NUMBER

5f. WORK UNIT NUMBER
Q1AM

7. PERFORMING ORGANIZATION NAME(S) AND ADDRESS(ES)

Air Force Research Laboratory (AFMC)
AFRL/RQRS
1 Ara Drive
Edwards AFB CA 93524

8. PERFORMING ORGANIZATION REPORT NO.

9. SPONSORING / MONITORING AGENCY NAME(S) AND ADDRESS(ES)

Air Force Research Laboratory (AFMC)
AFRL/RQR
5 Pollux Drive
Edwards AFB CA 93524-7048

10. SPONSOR/MONITOR'S ACRONYM(S)

11. SPONSOR/MONITOR'S REPORT NUMBER(S)
AFRL-RQ-ED-TR-2017-0002

12. DISTRIBUTION / AVAILABILITY STATEMENT
Approved for public release; distribution unlimited.

13. SUPPLEMENTARY NOTES
PA Clearance No. 17398

14. ABSTRACT

This work develops an advanced multi-scale and multi-fidelity Modeling & Simulation (M&S) capability targeted at the fundamental studies of the physical characteristics of Field Reversed Configuration (FRC) plasma for advanced space propulsion. The work consists of numerical method development, physical model development, and systematic studies of the non-linear plasma dynamics and chemical processes governing FRC formation, acceleration, stability and interaction with the environment. FRC thrusters are a new class of advanced, mission-enabling spacecraft electric propulsion (EP) technology. They operate at high efficiency, relatively high thrust, and have the potential for hybrid chemical/electric operation. Further development and optimization of this technology requires a more complete and fundamental understanding of the dynamic physical properties of FRC plasma thruster at multiple scales and multiple levels of fidelity. This also requires the development and validation of the corresponding M&S tools for predictive capability of future designs and on-orbit operation. The specific challenges of the research can all be found in the complex non-linearities and dynamic multi-scale aspects of the plasma as it evolves during the various characteristic time scales of the typical thruster operation. By leveraging recent and current research efforts in fundamental mathematics and algorithms for multi-scale plasma simulations as well as the development of advanced models of collisional plasma physics, a unique, state-of-the-art M&S capability is produced. Utilizing these numerical tools, fundamental studies must be performed to elucidate various issues in the efficiency of plasma formation, capture of propellant mass, and coupling efficiency to the accelerating coils that have been encountered experimentally. In the course of this study, fundamental aspects of basic plasma turbulence for these non-equilibrium, magnetized plasma conditions as well as unique radiative spectral signatures which can be used for direct, non-invasive, comparison with experimental diagnostics can be produced. This research will be directly transferred into an in-house 6.2 R&D program through integration and demonstration within the Thermophysics Universal Research Framework (TURF) and will pave the way for future fundamental research in other applications of interest to the USAF.

15. SUBJECT TERMS

16. SECURITY CLASSIFICATION OF:			17. LIMITATION OF ABSTRACT	18. NUMBER OF PAGES	19a. NAME OF RESPONSIBLE PERSON
a. REPORT	**b. ABSTRACT**	**c. THIS PAGE**	SAR	167	Dr. Justin Koo
Unclassified	**Unclassified**	**Unclassified**			**19b. TELEPHONE NO** *(include area code)* N/A

This Page Intentionally Left Blank

Contents

List of Figures

List of Symbols and Acronyms

CEX	Charge Exchange
CFP	Closed-Field Plasmoid
C-R	Collisional-Radiative
DAE	Differential algebraic equation
DAG	Directed Acyclic Graph
DG	Discontinuous Galerkin
DSMC	Direct Simulation Monte Carlo
EEDF	Electron Energy Distribution Function
ELF	Electrodeless Lorentz Force
EMPT	Electromagnetic Plasmoid Thruster
EP	Electric Propulsion
FRC	Field-Reversed Configuration
HET	Hall Effect Thruster
ICP	Inductively Coupled Plasma
ISRU	In-Situ Resource Utilization
K-H	Kelvin-Helmholz
LPI	Laser Plasma Interaction
M&S	Modeling & Simulation
MCC	Monte Carlo Collision
MFP	Multi-Fluid Plasma
MHD	Magnetohydrodynamics
NLTE	Non-Local Thermodynamic Equilibrium
ODE	Ordinary Differential Equation
PDE	Partial Differential Equation
PETSc	Portable, Extensible Toolkit for Scientific Computation
PI	Preionization
PIC	Particle-In-Cell
QSS	Quasi-Steady-State
RF	Radio Frequency
RMF	Rotating Magnetic Field
SSP	Strong-Stability Preserving
TS	Time Stepping
TURF	Thermophysics Universal Research Framework
VTK	Visualization ToolKit
WARPX	Washington Approximate Riemann Plasma Solver

High Fidelity Modeling of Field-Reversed Configuration (FRC) Thrusters

Justin Koo[†], Éder M. Sousa[‡], R. Martin[§]

April 18, 2017

1 Introduction and Program Description

The project has focused on developing the required tools for accurately simulating Field-Reversed Configuration (FRC) thruster operation. This thruster concept was chosen as it is representative of many of the ubiquitous modeling challenges in the domain of dynamic low-temperature magnetized plasma. For the spacecraft power levels expected in the foreseeable future, a deep understanding of this plasma regime is critical to advance plasma propulsion technology beyond the current generation of electrostatic propulsion devices such as the Hall thrusters and ion thrusters in use today. In this report, FRC technology is first reviewed. Then an overview of the challenges the technology poses as well as the progress that has been made thus far on the project is provided. The subsequent sections describe in greater detail the efforts and successes for each of three critical phases of FRC operation. Finally, the appendices provide auxiliary reference material and work published in pursuit of these objectives.

1.1 Review of FRC Technology

The FRC, a type of Closed-Field Plasmoid (CFP), is a self-organized, magnetized plasma configuration in the shape of a highly compact toroid characterized by the presence of closed magnetic field lines and a high ratio of toroidal to poloidal current. The ratio of plasma pressure to magnetic pressure (β) is close to unity, i.e. the highest plasma density that can be attained for given external magnets. A small poloidal field also contributes to the particle confinement. Since FRCs are magnetically insulated from the external field - the plasma is not tied to an external field line - they can readily detach from the confining external field. Furthermore, most of the current in FRCs is in a layer near the surface of the plasmoid so they can be efficiently translated and accelerated by applied magnetic fields. Due to a number of ancillary benefits for this configuration such as having no external electrodes (the plasma being quasi-neutral, there is no need for beam neutralization), wide propellant compatibility, high power efficiency, and low specific weight, FRCs are attractive candidates for next-generation Air Force in-space propulsion needs.

The interest in using FRCs for space propulsion involves much lower power levels (in the tens-hundreds of kW) compared to fusion energy applications which have been the focus of prior interest in the configuration. This leads to the biggest challenge in designing FRC thrusters - the difficulty

---

[†]corresponding author: justin.koo@us.af.mil, AFRL, Edwards AFB
[‡]ERC Inc., Edwards AFB
[§]AFRL , Edwards AFB

in efficiently producing and accelerating plasmoids within the constraints of a limited on-orbit power budget.[1] A fundamental constraint on any fixed-power EP system is the tradeoff between propellant mass efficiency (known as specific impulse or Isp) and total thrust. Given the very disparate range of Air Force mission requirements - high Isp/low thrust for on-orbit operations and low Isp/high thrust for rapid orbit transfer - it is critical to optimize a FRC system over a very wide trade-space. Spanning this space requires an innovative approach to thruster design for which high-fidelity simulations play a very important role. Therefore, developing this fundamental capability to study the plasma physics, especially associated with FRC thrusters, is at the heart of this report.
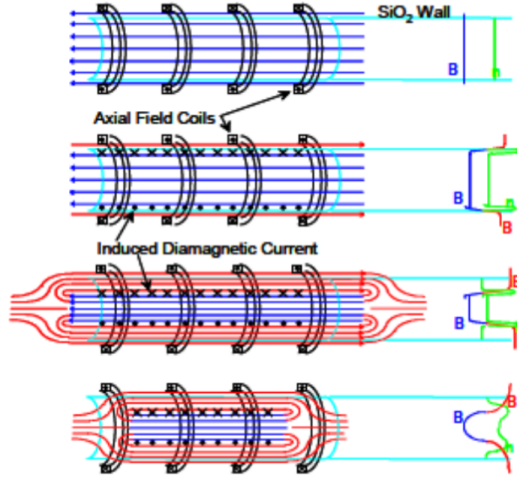
Figure 1: Schematic of θ-pinch FRC formation

To date, a limited number of laboratory thrusters have demonstrated the feasibility of using FRCs for propulsion application. Two of the most advanced designs are the Electromagnetic Plasmoid Thruster (EMPT), which uses a θ-pinch formation, and the Electrodeless Lorentz Force (ELF) thruster [1].In the θ-pinch formation, starting from a background uniform plasma at a constant axial (bias) field, the FRC is formed by pulsing external coils and reversing the applied field. This induces currents at the plasma boundary and "pinching" of the plasma at both ends (see Fig. 1). The initial bias field is trapped inside the plasma and forced to reconnect at the end points (X-points of the "separatrix") creating an elongated toroidal shape. In the second approach, a RMF, produced by two AC antennas typically phased at 90 degrees, creates an electron plasma current large enough to reverse the axially applied bias magnetic field (see Fig. 2).

Though recent efforts to assess the feasibility of neutral entrainment and peristaltic dynamic acceleration [2, 3] (capture of ambient gas) for higher thruster performance have greatly furthered the engineering design of FRC thrusters, significant gaps remain in the scientific understanding of the critical plasma processes involved in basic FRC formation, acceleration, and interaction with ambient gases. Computationally, the primary challenge lies in the multiscale (a typical FRC thruster spans over 5 orders of magnitude in space and 6 orders in time[2]) and multiphysics (approximate mod-

---

[1]In addition, design of any flight-like system must necessarily have a high power efficiency otherwise the challenges due to heat rejection become insurmountable.

[2]Temporal scales range from inertial effects of electron motion (i.e. plasma frequency, ω_{pe}) to the transit time of neutral flows - from O(1 ns) to O(100 ms) - and spatial length scales range from the electron Debye length (λ_{De}) to the device size - from O(1 μm) to O(10 cm).
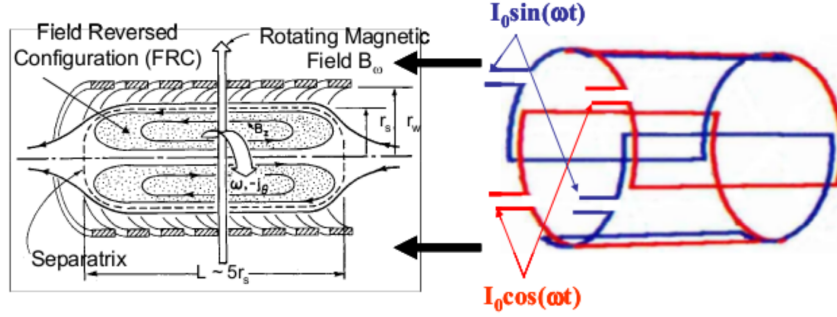
Figure 2: Schematic of RMF FRC thruster (left) and typical saddle coil geometry (right)

els are known to miss important physics while fully detailed kinetic simulations are computationally prohibitive) aspects of the problem. Furthermore, as progress has been made computationally, the need for highly resolved validation data have increased rapidly. To this end, AFRL/RQRS has led both 6.1 and 6.2 (on-going) experimental efforts to develop diagnostics and FRC testbeds specifically to support better understanding of critical FRC plasma processes. Although this experimental campaign is critical to developing general design philosophies for low-power plasmoid formation, the complexity of non-linear plasma processes rapidly reduces the utility of approximate design tools as the design space moves away from known regions. Ultimately, numerical simulations are an essential component for robust predictive design and optimization capability for FRC thrusters.

1.2 Technical Challenges

The overall goals of the project were aimed at developing and using high-fidelity modeling tools to study the most important physical processes in FRC operation with the aim of improving thruster design and developing a predictive design capability. It is important to describe briefly the operational phases of the FRC thruster in order to better identify the technical challenges associated with each of them. These phases are:

1. **Preionization** - An FRC pulse begins with neutral propellant flow into the thruster. In all but the highest power FRCs, it is necessary to create a low level ($\approx 1\%$) of background plasma through some sort of Preionization (PI) process. The energetic requirements for this PI stage are low; however, the spatial distribution defines critical ionization initial conditions [4] for the formation of the first plasmoid. Recent results by Kirtley indicate that for multi-pulse plasmoid operation, the second and subsequent FRC formation processes are inherently facilitated by the final conditions of the previous pulse. The implication of this is that the residual species distribution from the first pulse must be modeled correctly. Modeling preionization in general is extremely difficult since injected propellant could be preionized by a number of different mechanisms - indeed, besides various gas injection strategies, propellants as diverse as ionic liquids requiring separate vaporization stages are already being tested as potential FRC propellants. Since even the shortest of FRC firings consists of hundreds of individual plasmoid ejections, high-fidelity modeling effort focused on weakly ionized, rarefied, chemically reacting flow for the accurate evaluation of the residual state of the neutral gas for the 10s of milliseconds after FRC expulsion until the subsequent formation pulse.

2. **Formation** - The plasmoid formation sequence contains the most complex series of physical processes needed for accurately modeling the operation of FRC thrusters. During this phase, the critical details of ionization kinetics drive the flow from a weakly ionized rarefied state to a fully ionized continuum state. Given the very weak collisionality at the beginning of this

3

process, it is strongly suspected that non-equilibrium aspects of the Electron Energy Distribution Functions (EEDFs) play a critical role in the beginning of FRC formation. As the degree of ionization of the plasma increases, the EEDF should relax toward local thermodynamic equilibrium and the spatio-temporal interaction between the electron current and the applied magnetic field becomes more and more critical in defining the final envelope of the FRC.

3. **Translation** - After formation, the typical plasmoid residence time in the thruster is on the order of 10 μs. During this time, the plasma remains essentially fully ionized and the strong toroidal current interacts with the external field to produce the Lorentz force which accelerates the plasmoid. As the plasmoid translates downstream, it interacts with slow neutrals in its path through elastic and inelastic collisions. Predicting the degree to which these interactions remove/add[3] momentum from the plasmoid dictates the ultimate performance of the FRC. While the electrons may be sufficiently collisional to maintain a Maxwellian EEDF, the ions and neutrals, especially those external to the FRC, are unlikely to reach such an equilibrium and therefore may require additional kinetic treatment to accurately model their interactions with the FRC and trajectories in the near-spacecraft environment.

Each phase of FRC operation is associated with a set of technical challenges which, in turn translate into several areas of focus of our research program. The technical challenges are the following:

1. **Field/plasma model** - Plasmas are extremely rich in physics largely because of the coupling between the phase space configuration and self-induced electromagnetic forces; furthermore, in a sharp break from neutral flows, plasma responds to non-local effects (such as external magnetic fields) at the timescales of the speed-of-light. In FRCs, given the relatively slow frequency of the RMF driving field and the diffusion of neutral gases relative to the electron plasma frequency, there is an enormous range of timescales which the field/plasma model must resolve. Different plasma models attempt to circumvent this multi-scale problem through fundamental assumptions which restrict the limit to which the model is valid. For instance, MHD has been frequently used for FRC simulation but makes the very strict assumption that the plasma is a single quasi-neutral fluid. While this is most likely not the case (as the electron current moves almost orthogonal to the bulk ion motion), these models can provide good qualitative insight and are computationally inexpensive. Moving through the hierarchy of fluid models gradually relaxes these assumptions and permits more fundamental physics of the FRC device to emerge. Kinetic models, such as a Particle-In-Cell (PIC) approach, free the simulation to explore the full range of plasma even when non-local thermal equilibrium is required.

2. **Collisional physics** - The kinetics of ionization are critical to the efficiency (and ultimate success) of FRC formation at low power levels. This process can best be simulated through the use of a sufficiently detailed Collisional-Radiative (C-R) model. Furthermore, since the electrons are likely to be non-Maxwellian to some degree during the formation process (especially since the PI stage generates such a small number of electrons), the potential need for non-Maxwellian C-R must also be considered. Inelastic particle collisions, particularly dealing with momentum and energy exchange between charged and neutral species in the multi-fluid plasma model, must also be consistently derived from underlying excitation, recombination and ionization cross sections to ensure that comparison/hybridization between continuum (which use rate based terms) and kinetic (which use cross-sections) codes are consistent.

---

[3]The neutral entrainment concept actually relies on the elastic Charge Exchange (CEX) mechanism to recover momentum from the flow between pulses of additional downstream coils

3. **Multi-scale effects** - FRC simulation is particularly challenging because of the dramatic differences in plasma behavior inside and outside the separatrix. In the interior, continuum approaches can generally be used effectively to average the small scale features (such as the Debye length and Larmor radius); however, it is the kinetic effects which at the boundary of the separatrix, such as magnetic reconnection at the X-points, which drive critical physics of FRC formation. Developing numerical techniques to extend kinetic simulation to larger time and length-scales without losing numerical stability and accuracy, as well as developing hybridization techniques to couple with continuum models is critical to resolution of the full spectrum of scales necessary to correctly predict FRC physics.

4. **System complexity** - Any realistic FRC simulation toolkit requires at least a certain level of accuracy in the representation of geometric and materials complexities. For instance, the driving coil for the RMF requires an antenna with a complex shape ("saddle coil", see Fig. 2) which results in an applied field that is neither truly uniform nor conveniently symmetric. Although the experimental validation program at AFRL/RQRS is attempting to reduce the geometric complexity as much as possible, certain geometric complexities such as a conical discharge channel and finite size downstream acceleration coils may be unavoidable. In addition, while gaseous monatomic propellants are the first choice for study of FRC thrusters, new materials such as ionic liquids are rapidly gaining traction as potential propellants. The complex physics of propellant decomposition, vaporization, and potentially even combustion require the development and integration of complex numerical and physical models.

Though necessary for understanding FRC thrusters, the technical challenges listed above have application to a broad range of plasma conditions beyond FRCs. For instance, the same challenges we will address with the field/plasma model are immediately applicable to problems as theoretical as astrophysics and applied as plasma processing. Similarly, the same collisional physical models needed to study FRC plasma evolution are critical to developing spectral profiles for Space Situational Awareness. Similarly, the same multi-scale effects which characterize FRC thrusters also challenge our existing generation of Hall Effect Thruster (HET) simulation tools [5, 6]. Any advancements made in bridging the scale gap will contribute directly to further investigation of the plasma turbulence characterizing virtually all magnetized plasma environments, both for propulsion and power generation.

1.3   Progress and Objectives

The overall goal is to develop a coherent hierarchy of computational models from kinetic to continuum regimes capable of modeling complex multi-scale plasma encountered in Air Force propulsion applications like those specifically encountered in the FRC thruster. Though understanding the details of every phase of FRC operation is a lofty challenge, enormous progress can be made through the appropriate development and implementation of fundamental physics models.

In addition, gains in algorithmic acceleration, hardware acceleration, and the recent development of our modern, flexible object-oriented simulation framework, TURF[7], offer promising opportunities to apply and couple these disparate models. Computational developments coupled with our ongoing in-house 6.2 experimental validation campaign and preionization studies provide a comprehensive foundation which can dramatically improve our ability to engineer high-efficiency, low-power FRC thrusters.

In particular, considerable progress has been made during the course of this LRIR initiative in the following areas:

1. **Multi-scale/multi-physics capability** - Numerical simulation tools have been developed based on a hierarchy of models so that various physical assumptions may be explored in relevant regimes for FRC physics. For example, a multi-fluid plasma framework which includes electron momentum potentially crucial for understanding the validity and breakdown of standard magnetohydrodynamic physics in the FRC thruster has been developed. Though relying on fewer assumptions, the inclusion of the electron physics adds disparate time scales to the model and additional numerical efficiency must therefore be attained to complete simulations in a timely manner. This effort has been the primary focus of this LRIR initiative as described in Section 3 and Appendix B.2 to support the late-stage formation and translation phases of the FRC modeling effort. This development has focused on the groundwork for coupling a multi-physics framework that includes not only fluid macro-properties but coil-fields, elastic collision, and collisional-radiative solvers in a consistent manner. These multi-fluid methods are historically the least extensively developed of the plasma hierarchy, but they are expected to be the critical component required for coupling the extremely expensive kinetic models to the more computationally efficient fluid resistive MHD models of the type traditionally employed in FRC thruster design.

2. **FRC formation dynamics** - Initial formation simulations using the θ-pinch and RMF have been conducted in Section 3. Though field reversal was expected on the axis of symmetry, the simulations show that the reversal instead begins in isolated magnetic islands that eventually coalesce at the geometric axis of the experiment. Those simulations, however, assume an initially fully ionized gas which is dissimilar to the experimental reality. There therefore remains a need to implement inelastic collision effects such as ionization, recombination and charge exchange models into the multi-fluid models.

3. **Preionization** - The initial phase of this ionization process will occur with a high degree of non-equilibrium, both in velocity and atomic state, that is fundamentally inaccessible to the multifluid approach. To tackle this initial weakly ionized, rarefied, early stage, fully kinetic efforts in parallel to the multi-fluid work have also been explored. These efforts include both in-house work adapting the TURF tool for neutral flow in the preionization stage as described in Section 2 as well as the development of coherent inelastic complex collision models for the atomic state distribution in collaboration with university partners for ionization and neutral entrainment described in Section 4 along with Appendices A and C.

4. **FRC stability and turbulence onset** - The multifluid simulations of Section 3 eventually become unstable and crash due to the formation of finer scales than are representable in the model. Numerous such physical plasma instabilities are known to exist in the FRC regime including tilt, rotational (with the n=2 one being the most likely), and even possibly the lower-hybrid drift instability. This last instability could lead to an increase in the resistivity of the plasma. Anomalous resistivity effects can be measured and the first indications point to them being at least one order of magnitude larger than the Spitzer resistivity. Though additional studies are required in order to verify this observation, this represents an interesting path for further investigation into the effects of anomalous resistivity in electric propulsion devices.

5. **Collisional-radiative characteristics** - Leveraging work from an ongoing 6.2 program to couple a detailed argon collisional-radiative model into TURF, the Maxwellian C-R model has been adapted to a form compatible with multi-fluid codes to provide detailed spectra for validation with experimental measurements as described in Section C.3. The inelastic cross-sections underlying this detailed model have been leveraged through the Laser Plasma

Interaction (LPI) LRIR to generate mass, momentum and energy exchange terms for the MF closure model in the method suggested by Le [8, 9]. This ensures that the plasma hierarchy is consistent with respect to collisional transport. In the future, this work will be extended to the application of non-Maxwellian C-R models as in Section C.2 to the problem of non-equilibrium kinetic behavior of the plasma during the initial phases of ionization.

These components enable many of the most challenging physical problems critical to FRC modeling to be addressed within their own limited temporal and spatial scales. Integrating these disparate models into a unified framework capable of spanning the time, space, and complexity scales required for the full device operation, however, remains an outstanding challenge impeding understanding of the full end-to-end operation of these devices. Addressing this challenge is critical to accelerating the development cycle of such plasma propulsion systems. Coupling these models requires asymptotic consistency to be established through convergence to equivalent solutions in regimes where more than one of the models should be applicable. Establishing this level of consistency would enable computational efficiency to be dynamically balanced with required fidelity moving towards fully hybrid methods able to traverse this model hierarchy with a bounded level of error. This tighter model integration remains a key area of focus for the effort moving forward.

2 Preionization Model Development

Work on the preionization stage of FRC modeling currently has been split between two distinct physical regimes. In the first, basic neutral rarefied kinetic modeling of noble gas flow is applied to the complex injector geometry of the RP3X FRC experimental collaboration between MSNW Inc. and AFRL/RQRS. The second regime consists of the MHD fluid modeling of molecular fuels with non-equilibrium collisional-radiative (C-R) decomposition and ionization kinetics in a simplified glow geometry in collaboration with the efforts of Professor Panesi's group at the University of Illinois Urbana Champaign. Combining these capabilities consistently will be a major goal of the continued efforts in modeling these systems.

2.1 Rarefied Neutral Flow

In the context of a steady-state operation of a FRC pulse train, the preionization phase consists of the highly rarefied predominately neutral flow in the time between pulses as well as the evolution of the weak ionization and recombination processes occurring intermixed with the neutral flow. Current FRC designs tend to rely on a steady neutral flow to circumvent expected reliability issues with puff valves in the required cycling lifetimes. It also removes additional degrees of freedom in the complexity of the design to simply flow the propellant gas. Even with steady flow, the preionization and injection design has been primarily empirical. Figure 3 shows an example of rarefied neutral flow in the preionization stage of such an injection scheme designed for the RP3X FRC as generated by the TURF code developed at AFRL/RQRS.

The simulation is based on the experimentally defined 20sccm xenon choked inflow through a 1/16th inch diameter orifice using the gas injector CAD model design for a domain extending from the rear of the feed tube up to the conical section of the thruster 10.5cm downstream. The standard Direct Simulation Monte Carlo (DSMC) method[10] was used to model the collisions throughout the domain though the neutral collisionality is negligible outside the injector nozzle. The range of spatial scales, density scales, and geometric complexity highlight many of the key factors that make this problem challenging.

Strong statistical noise dominates in the crucial downstream region of the RP3X simulation while the vast majority of computational particles and expense is dominated by the high density feed
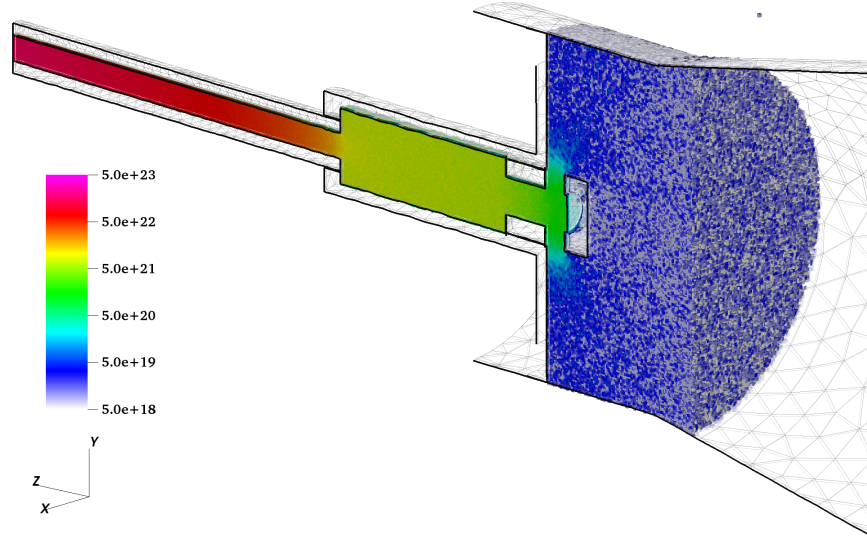
Figure 3: Rarefied neutral xenon density (m^{-3}) for typical mass flow rates in the RP3X FRC feed lines and preionizer 8μs after initiation of flow.

line as the cost of the DSMC method scales proportionally to the number density. This highlights the need for advanced fractional DSMC methods such as the one under development described in Appendix C.1 that enable dynamic control over the number of physical particles represented by each simulation macroparticle. Though this method was also developed within TURF, it has not yet been fully transitioned into the main codebase that is capable of modeling realistic triangulated surface physics. This upgrade is expected to provide a major enhancement of computational fidelity at a fraction of the cost. This speedup will be even more critical once transient rather than time average mean flows are required for the inter-pulse regime.

2.2   Non-equilibrium RF Ionization

Accurate modeling of the ionization process is a critical first step in understanding the evolution of the plasma conductivity needed for successful field-reversal. Experimentally, a seed ionization source is required to initiate the process even though the residual ionization from previous pulses may be sufficient for subsequent pulses in quasi-steady multi-pulse operation. Because the geometry is relatively simple and they operate in a continuous mode, the reduced complexity of the preionization sources compared to the full system is particularly advantageous. Despite this apparent simplicity, the high frequency operation (on the order of MHz) facilitates direct probing of rich, Non-Local Thermodynamic Equilibrium (NLTE), physical effects which are likely critical to the 100ns-1μs FRC formation process timescales through a much more experimentally accessible quasi-steady operating condition than that of the full pulsed FRC system. This makes preionization a particularly useful testbed for model validation critical to understanding these NLTE processes. Figure 4 depicts an example of one such RF preionization stage under development at AFRL.

For the typical noble gas propellant commonly used in electric propulsion such as argon and xenon gas, these C-R processes were investigated in great detail as part of an associated Laser Plasma Interaction lab task (14RQ05COR, PM: Dr. J. Marshall). Future 6.2 and 6.3 model development

8

Figure 4: AFRL 15MHz RF preionizer for FRC applications.

for FRC thruster design using these gases will rely heavily on the developments therein.

However, one of the major advantages of the FRC technology compared to Hall and ion thrusters currently in use is the potential for greatly enhanced fuel flexibility resulting from the electrode-less design. MSNW has explored several such potential fuels for an In-Situ Resource Utilization (ISRU) study as shown in Figure 5 during the course of a related NASA SBIR program (Contract NoNNX11CB24C) they presented in Reference [11].
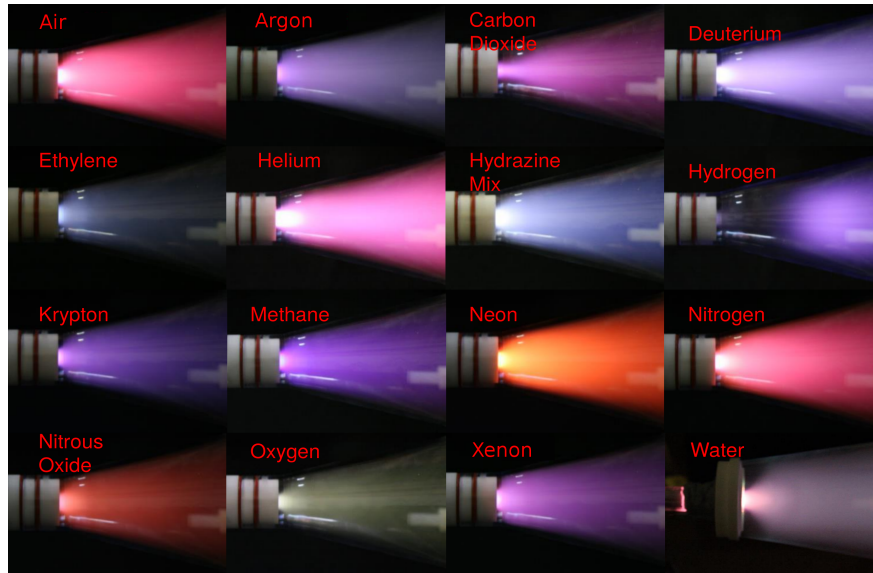
Figure 5: MSNW Preionizer Experiments using a variety of potential FRC fuels.

As application of greater interest than ISRU for Air Force applications would be the use of chemical thruster propellant as electric propulsion reaction mass. This "multi-mode" operation would enable an unprecedented degree of mission flexibility through the use of a combination of high thrust and high ISP maneuvers selected as needed throughout the spacecraft lifetime.

In particular, the AF-M315E energetic green ionic liquid mono-propellant (a blend of primarily

hydroxyethylhydrazinium nitrate, hydroxylammonium nitrate, and water) as a proposed multi-mode hybrid thruster fuel is on the long term roadmap for FRC technology. However, due to the limited availability of chemical kinetic and ionization cross section data for AF-M315E specific molecules, validation on component surrogate and decomposition product gasses where more data is available such as the case for water and nitrogen gas represents a particularly fruitful direction of investigation for the near term. This surrogate gas approach provides a key route in limiting the number of interacting unknowns for the critical physical and numerical parameters required to validate the technique prior to addressing the full complexity system. Once the methods have been validated with the well understood gasses, the codes then become a tool for investigating the related processes and missing data for the complex fuels.

To that end, efforts were coordinated with and leveraged Professor Panesi's AFOSR Summer Faculty Fellowship program to extend the NLTE hybrid State-to-State C-R models for nitrogen gas to develop models for an Inductively Coupled Plasma (ICP) RF plasma torch similar to the preionizers under development at AFRL and MSNW. Appendix A shows the results of these efforts contrasting the full NLTE results to simplified multi-temperature models. The most dramatic differences were observed in the near wall regions. Further efforts to validate the models against experimental data are left to future efforts however.

3   FRC Formation Physics

The FRC formation studies constitute the core of the in-house efforts directed towards this lab task. The following sections describe the multi-fluid plasma model efforts as well as an investigation into the applicability of the quasi-steady state collisional model in place of a full collisional-radiative modeling for propulsion relevant conditions.

3.1   The Multi-Fluid Plasma Model

The multi-fluid plasma model is obtained by taking velocity moments of the Boltzmann equation for each of the species present in the plasma. The model is a reduction from the kinetic representation of the plasma by assuming a Maxwellian distribution function. Each species is modeled as a separate fluid with its mass, momentum and total energy are described as,

$$\frac{\partial \rho_s}{\partial t} + \nabla \cdot (\rho_s \mathbf{u}_s) = 0, \tag{1}$$

$$\frac{\partial \rho_s \mathbf{u}_s}{\partial t} + \nabla \cdot \left(\rho_s \mathbf{u}_s \mathbf{u}_s + p_s \overleftrightarrow{\mathbf{I}} \right) = \frac{\rho_s q_s}{m_s} \left(\mathbf{E} + \mathbf{u}_s \times \mathbf{B} \right) + \sum_{r \neq s} \mathbf{R}_{rs}, \tag{2}$$

$$\frac{\partial \varepsilon_s}{\partial t} + \nabla \cdot ((\varepsilon_s + p_s)\mathbf{u}_s) = \left(\frac{\rho_s q_s}{m_s} \mathbf{E} + \sum_{r \neq s} \mathbf{R}_{rs} \right) \cdot \mathbf{u}_s + \sum_{r \neq s} Q_{rs}, \tag{3}$$

where the subscript s denotes the species, ρ_s is the density, $\mathbf{u}_s$ is the velocity, $\mathbf{E}$ and $\mathbf{B}$ are the electric and magnetic fields, m is the mass, q_s is the charge, $p_s = n_s T_s$ is the pressure, and ε_s is the total energy given as

$$\varepsilon_s = \frac{p_s}{\gamma - 1} + \frac{1}{2} \rho_s |\mathbf{u}_s|^2. \tag{4}$$

The momentum transfer between species s and r is accounted for by the term $\mathbf{R}_{rs}$, and $\mathbf{R}_{rs} \cdot \mathbf{u}_s$ is Ohmic heating. The momentum transfer term is described as

$$\mathbf{R}_{ei} = -n_e^2 e^2 (\eta_\parallel \mathbf{v}_\parallel + \eta_\perp \mathbf{v}_\perp) \tag{5}$$

where η is the resistivity and $\mathbf{v} = \mathbf{u}_e - \mathbf{u}_i$. The subscripts $\parallel$ and $\perp$ denote the directions parallel and perpendicular to the magnetic field.

The Spitzer resistivity is used to calculate the parallel component,

$$\eta_\parallel = \frac{\pi e^2 m_e^{1/2} \ln \Lambda}{(4\pi\varepsilon_o)^2 T_e^{3/2}}, \tag{6}$$

where $\ln \Lambda$ is the Coulomb logarithm and the electron temperature, T_e, is in units of energy. The perpendicular component of the resistivity is $\eta_\perp = 1.96\eta_\parallel$.

In Eq. (3), Q_{rs} is the thermal equilibration term between species, which drives the plasma to reach an equilibrium temperature for all species in the absence of other transport terms. The thermal equilibration is evaluated differently for ions and electrons, respectively

$$Q_{ie} = Q_\Delta = \frac{3\eta_\parallel n_e^2 e^2}{m_i}(T_e - T_i), \tag{7}$$

$$Q_{ei} = -\mathbf{R}_{ie} \cdot (\mathbf{u}_e - \mathbf{u}_i) - Q_\Delta. \tag{8}$$

To close the system, the electromagnetic fields are evolved using the Maxwell's equations in purely hyperbolic form[12],

$$\frac{\partial \mathbf{B}}{\partial t} + \nabla \times \mathbf{E} + \gamma \nabla \Psi = 0, \tag{9}$$

$$\frac{1}{c^2}\frac{\partial \mathbf{E}}{\partial t} - \nabla \times \mathbf{B} + \chi \nabla \Phi = -\mu_o \sum_s \frac{q_s}{m_s}\rho_s \mathbf{u}_s, \tag{10}$$

$$\frac{1}{\chi}\frac{\partial \Phi}{\partial t} + \nabla \cdot \mathbf{E} = \sum_s \frac{q_s}{m_s}\rho_s, \tag{11}$$

$$\frac{1}{\gamma c^2}\frac{\partial \Psi}{\partial t} + \nabla \cdot \mathbf{B} = 0. \tag{12}$$

The equations are presented in this form to account for the divergence constraint of the magnetic field and Gauss' law. The divergence errors that arise due to numerical discretizations are propagated out of the computational domain at speeds γc and χc, therefore, larger values will result in faster "cleaning" of the computational domain. However, larger values of γ and χ impose smaller time-steps, and, choosing a value of one is usually sufficient.

3.1.1 Initial FRC formation Studies in WARPX

FRC formation studies were initially conducted for the RMF and a theta-pinch configurations using the Washington Approximate Riemann Plasma Solver (WARPX)[13] code. WARPX is a structured, second order finite volume two-fluid plasma code developed at the university of Washington. The r-θ simulations try to reproduce the RMF results produced by Milroy[14] in an attempt to verify our simulations.

For a better understanding of the formation physics, different aspects are investigated separately by turning certain terms of the equations on and off. The first simulations are conducted assuming a collisionless fully-ionized hydrogen plasma, $\mathbf{R}_{rs} = \overleftrightarrow{\boldsymbol{\Pi}}_s = \mathbf{q}_s = \mathbf{0}$ and $Q_{rs} = 0$. According to Ref. [1], the appropriate generalized Ohm's law is given as

$$\mathbf{E} = \eta\mathbf{J} + \frac{\mathbf{J} \times \mathbf{B}}{ne}, \tag{13}$$

11
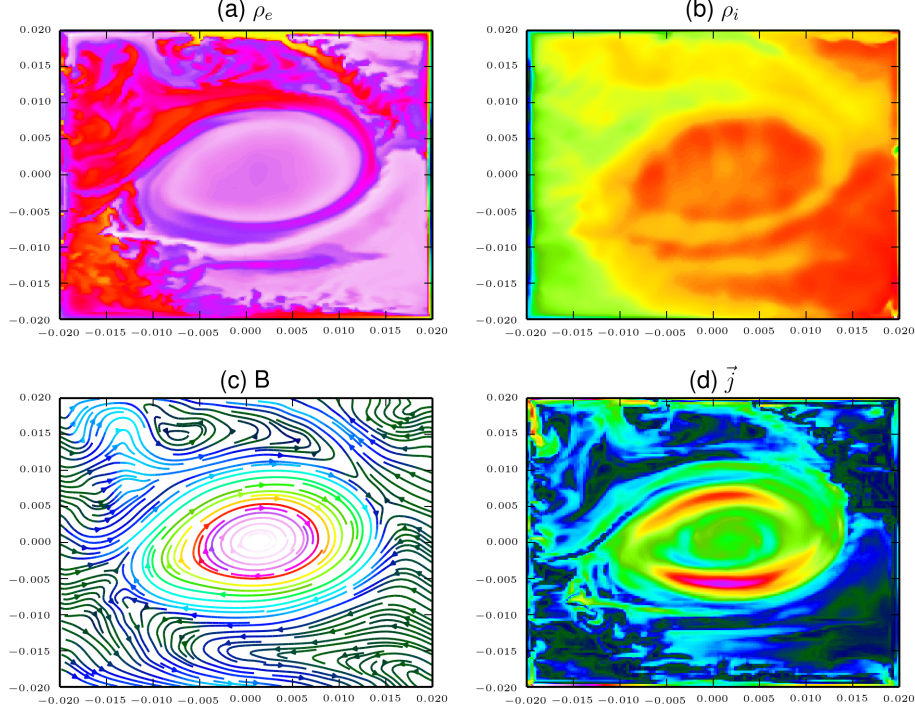
Figure 6: Electron mass density (a), ion mass density (b), magnetic field (c), and current profiles for a collisionless multi-fluid plasma simulation using a RMF boundary condition. The formation of the closed field lines and the current in the theta direction point to the formation of a FRC.

and the dominance of the second term, $\mathbf{J} \times \mathbf{B} > \eta \mathbf{J}$, leads to the FRC formation. In a collisionless plasma the $\eta \mathbf{J}$ term is zero since the resistivity is zero. In this limit FRC formation is governed by the RMF magnitude and frequency. Because the electron inertial is not neglected (as is the case in MHD) the electrons rotate synchronously with the rotating field and form a current in the θ-direction as can be seen in Figure 6. Starting from a uniform plasma with RMF boundary conditions, a FRC forms in the center of the domain with closed magnetic field lines.

Modeling Instabilities:

Unbalanced forces in a plasma can cause instability, and different plasma configuration are susceptible to certain known instabilities. For FRCs, the three principal global instabilities are:

1. Rotational instability, which is driven by the centrifugal effect of rotational flow, causes friction between the plasma and the wall and consequently loss of energy;
2. Tearing instability, where friction in the plasma causes the topological changes in the magnetic field configuration;
3. Tilt instability, which can distort the X-point, can cause magnetic reconnection and the opening closed magnetic surfaces.

In addition to these global instabilities, during the formation of a FRC, other local instabilities can grow. For a RMF there are two competing torques on the electrons. The first torque is produced by the RMF that penetrates the plasma and drive the electrons into a synchronous rotation with the RMF (θ-direction current). The second is a resistive torque that results from the electron-ion collisions. At the interface of these competing torques, the plasma develops a shear layer that

is prone to instabilities resembling Kelvin-Helmholz (K-H). For FRCs formed using a θ-pinch, Rayleigh-Taylor instabilities, shown in Figure 7, dominate caused by the acceleration resulting from the increasing magnetic pressure external to the FRC.

Our model, with a separate electron fluid, is ideal for the understanding of plasma early instability onset in FRCs. The model couples the RMF with the electron fluid through the Maxwell equations, producing the RMF torque, and quantifies the electron-ion momentum transfer, which produces the resistive torque. Instabilities are inherently a multi-scale problems where small disturbances in the flow grow to large disruptions in the flow ultimately leading to generation of turbulence.

To overcome the high cost of resolving all these electron time scales to extend this methodology into the longer time scales of the turbulent regime suggests implicit-time integration for the stiff terms. Initial studies in one dimension have been successfully implemented in Reference [15] and are also described in the publication of Appendix B.3, where the stiff portion of the multi-fluid model - electron fluid and electromagnetic field - are integrated implicitly. This work is to be extended to space-time formulation described in Reference [16], to adapt locally in both the spatial and temporal directions for higher resolution only where it is needed. This will not only speed up the calculations, but with the higher resolution will lead to a better understanding of the underlying physics.

Ultimately the simulations on structured rectangular domain produced some artifacts at corners that seem to be unphysical which has led to the development of an unstructured solver to properly compute these flows.

(a) Charge separation, $n_e - n_i$. (b) Magnetic field lines.
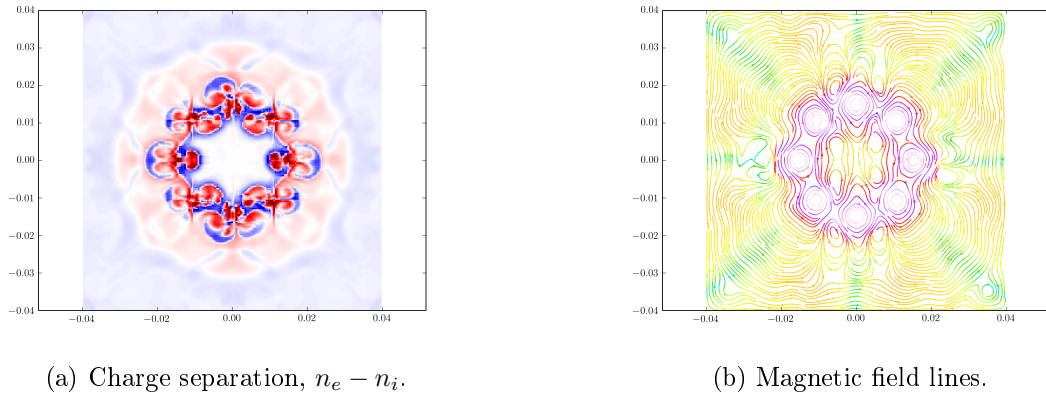
Figure 7: Initial simulations of the FRC formation using a theta pinch show the development of Rayleigh-Taylor instabilities. In figure (a) regions in red depict where the electron number density is higher while blue is where the ion density is higher.

3.1.2 Investigation of FRC formation physics using Apollo

The RMF FRC formation problem is a primary area of interest. The RMF can be implemented through boundary conditions, but successful solution of this problem also requires good coupling between the fluid variables and the fields. The problem is inherently multi-scale (disparate time scales between the electrons and the ions fluids) and multi-physics.

For these simulations, a new unstructured DG tool, Apollo, was created to better handle the complex geometry and boundary conditions as described in Appendix B. The nodal DG method used is described in greater detail in Appendix B.1.2 and validation of the resulting tool is covered in Appendix B.2.
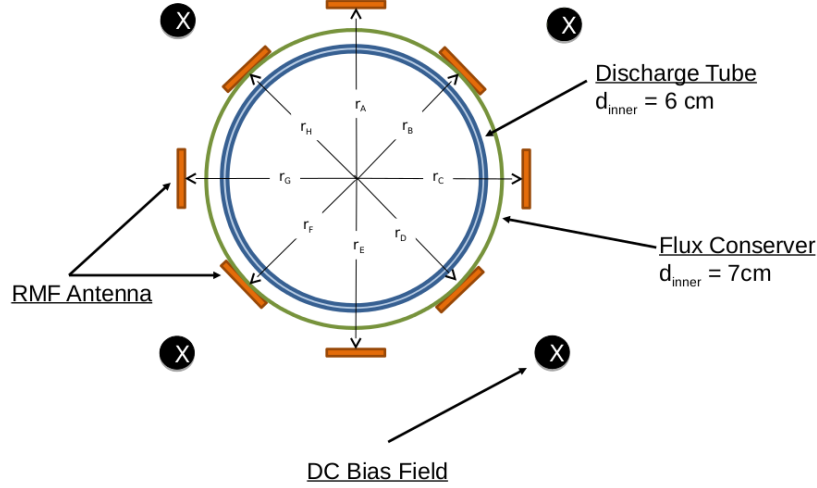
Figure 8: Schematic of the experimental setup. The RMF field is produced by the antennas, the flux conserver maintains the total magnetic flux through the plasma cross-section constant, and the bias field generates the initial B_z field perpendicular to the shown cross-section.

A significant benefit of using the DG method is that it provides good coupling between the fluxes and the source terms, which in turn allows for multi-physics models to couple the fluid through the source terms without the need for source splitting schemes. This makes DG an excellent method for the RMF FRC formation problem.

FRC simulations schematic:

The simulations are based on an experimental device at AFRL Edwards. It is modeled in 2D as an infinite length quartz cylinder of radius 3 cm. A successful simulation couples the electromagnetic fields with the plasma, described here as an electron fluid and an ion fluid (two-fluid plasma model).

The experimental setup schematic is shown in Figure 8. The RMF antennas produce an in-plane rotating field, while the flux conserver maintains a constant integrated flux through the discharge tube, $\int_A B_z dA =$constant.

The eight coils carry a time dependent current in such way as to produce a RMF. Each coil is designed to produce a desired peak magnetic field of magnitude B_ω uniformly around the plasma chamber. The time-dependent magnitude of the magnetic field is given as $B_t = B_\omega \left[1 - exp(-t/\tau)\right]$, where τ is the amplitude of the rise time.

Boundary Conditions:

Separate boundary conditions need to be applied for the magnetic fields produced by the RMF antenna and the flux conserver. It is worth pointing out that the antenna field is in the plane (B_x and B_y), while the flux conserver boundary conditions is the plane perpendicular to the plane, B_z.

The RMF consists of a fundamental component ($j = 1$) that rotates at an angular frequency of ω, and odd spacial harmonics ($j = 2, 3, 4, ...$). The $(2j - 1)$th harmonic rotates at a angular frequency of $(-1)^{j-1}\omega/(2j - 1)$, indicating that every other harmonic rotates in the direction opposite to the

14

fundamental [17].

The magnetic vector potential for a polyphase winding of a two-phase system with two coils per phase is given in [17] as

$$A_z = \frac{2\mu_o I_o}{\pi} \sum_{j=1}^{\infty} \frac{\cos((2j-1)\alpha/2)}{2j-1} \left(\frac{r}{R}\right)^{2j-1} \sin\left[\omega t + (-1)^j (2j-1)\theta\right] \tag{14}$$

where α is the angular spacing between two coils pertaining to each phase, R is the radius of the location of the coils, ω is the RMF frequency, and (r,θ) is the polar coordinates along the boundary.

In the case of the two-fluid plasma model, the boundary conditions are actually applied to the electric ($\mathbf{E}$) and magnetic ($\mathbf{B}$) fields, which can be obtained from the magnetic vector potential by taking the time derivative and curl respectively,

$$\mathbf{E} = -\frac{\partial \mathbf{A}}{\partial t}, \qquad \mathbf{B} = \nabla \times \mathbf{A}.$$

The flux conserving ring produces a current in the θ-direction that keeps the B_z flux constant, using a boundary condition is described in [18], given as

$$B_z(a,t) = \frac{b^2 B_a(0)}{b^2 - a^2} - \frac{1}{\pi(b^2 - a^2)} \int_0^a r dr \int_0^{2\pi} d\theta B_z(r,\theta,t) d\theta, \tag{15}$$

where $r = a$ is the plasma radius, $r = b$ is the radius of the flux conserver, $B_a(0)$ is the initial value of B_z at $r = a$. The second term on the right-hand-side represents the calculation of the axial flux throughout the plasma. Solid wall boundary conditions are applied for the electron and ion fluids.

FRC Simulation Results:

The formation of the FRC using a RMF follows certain steps which should culminate in the reversal of the B_z field. What is expected to be seen in the simulations is the generation of a current in the θ-direction caused by the fact that electrons, which are frozen-in the magnetic field lines, get spun by the RMF. The current causes inhomogeneities in the magnetic field which results in a change in the magnetic flux through the computational domain. The flux conserving ring will react to the changing B_z in an attempt to keep the total flux constant and reversing the field.

For the simulation, we assume that the plasma is initially a charge neutral ($n_i = n_e$), uniform, hydrogen plasma. The initialization is $T_i = T_e = 5$ eV, $B_\omega = 10$ G, $B_z = 30$ G, $n = 10^{19}$ m^{-3}, $\omega = 2.2$ MHz and all other variables of the two-fluid plasma model are set to zero.

There are two competing torques exerted on the electrons; the RMF torque and the retarding torque caused by collisions of electrons with ions (resistivity). The RMF torque manifests itself by producing a current in the θ-direction because the electron fluid is frozen to the B-field and moves as the field rotates. In Figure 9 we can see that the penetration of the field into the plasma occurs early in the simulation at about $t=12ns$. The momentum transfer term of Eq. 2 is responsible for generating the retarding torque by modeling ion-electron collisions needed to break the frozen-in flux condition of the electrons. However, in this case the temperature is relatively high which decreases the resistivity and the RMF is capable of penetrating the plasma with relative ease.

In Figure 10a the current density generated by the RMF is plotted at $100ns$. It can be seen that the current is dominant at the plasma edge where the magnetic field has had the opportunity to penetrated the plasma. In Figure 10b the number density for both species shows that there are high frequency oscillations in the electron fluid and large gradients towards the edge where the current density is larger. Broad and thick current sheets are associated with "anomalous" resistivity[19].

15

(a) $t=5ns$ (b) $t=12ns$
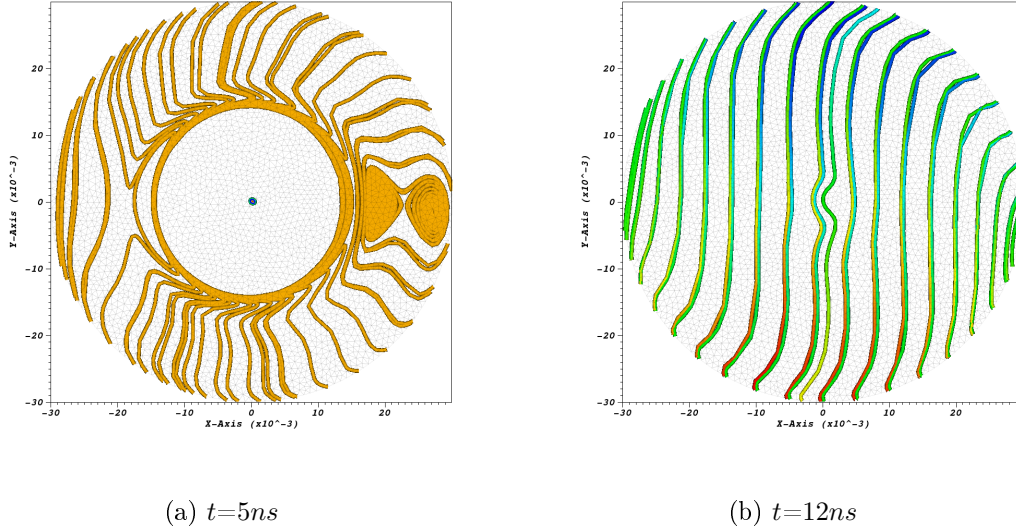
Figure 9: Magnetic field lines showing that the penetration of the field in the plasma occurs early.

Anomalous resistivity is a process by which electrons are slowed down by collisions with random electric field fluctuations instead of ion collisions. This process is usually associated with plasma turbulence, but in our case the field fluctuations are due to the RMF.

The B_z-field reverses direction at the edge of the plasma, as can be seen in Figure 11a. However as time progresses the field goes from a strong reversal at $t=100ns$ to a weak reversal at $t=300ns$. This is due to the fact that the J_θ current is being disrupted and does not form a uniform current sheet, as can be seen in Figure 11b. From Figures 10a and 11b we can see that the cross-sectional shape of the current density and B_z field, respectively, becomes elliptical, which points to the development of an n=2 (where n is the azimuthal mode number) rotational instability[20]. The development of this instability occurs when the ion get spun-up (rotate) in the same direction as electrons causing currents in opposing directions. The effect of having ion and electron current in opposing directions also reduces the B_z flux through the plasma cross-sectional, which reduces the current in the flux conserver and the strength of the field reversal. At $t=520ns$ the field reversal is completely eliminated and the simulation behaves more like a θ-pinch.

For the simulations shown in fig. 12 we can see the magnitude of the z-component of the magnetic field. The plots show that the field reversal initially occurs in small islands and eventually coalesce at the center of the computational domain. The simulations are spatially fourth-order accurate, and start from a uniform fully ionized hydrogen plasma. This is a boundary value problem as the dynamics of the simulation is driven by the RMF through the boundary conditions.

Previous simulations of FRC formation have used the MHD model, which neglects the electron inertia and remove plasma frequency oscillations. In this particular problem, however, the electron dynamics are quite relevant and high frequency field oscillations (through the RMF) play an important role. This demonstrates the need for the Multi-Fluid Plasma (MFP) model for problems of this type.

With the MFP model, multiple instabilities that arise during the FRC formation can be studied. Micro-instabilities are of particular interest because they increase transport rates[21] and can disrupt the plasma current. Figure 13 plots the in-plane magnetic field lines and the electric current. In

(a)

(b)
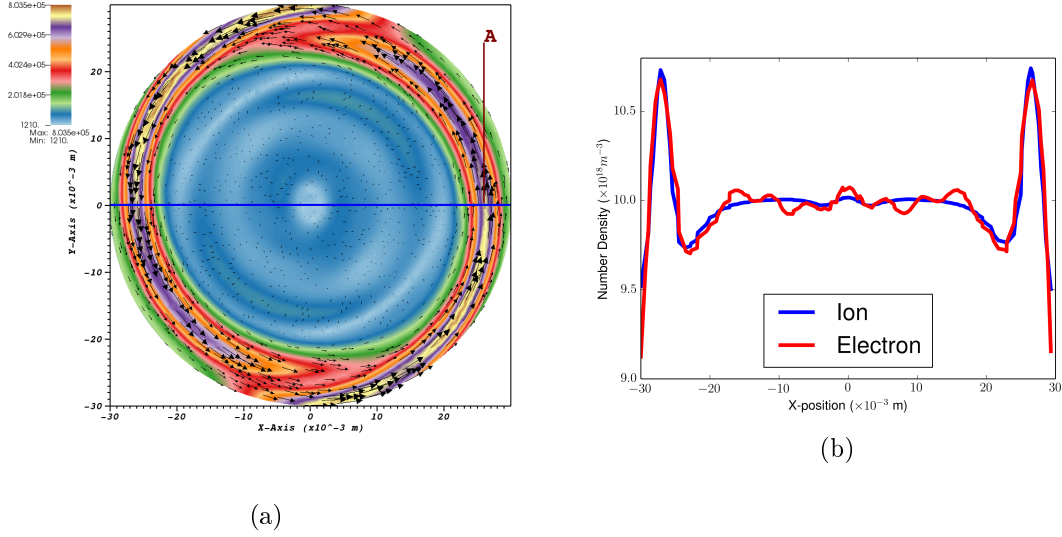
Figure 10: (a) In plane current density magnitude and direction at t=100ns. The RMF has caused the electrons at the plasma edge to rotate, but collisions with the ions at the center have slowed the electrons down. (b) Ion and Electron number density across the mid-plane at t=100ns. There is an inhomogeneous density distribution of both species, which could trigger instabilities.

(a)

(b)
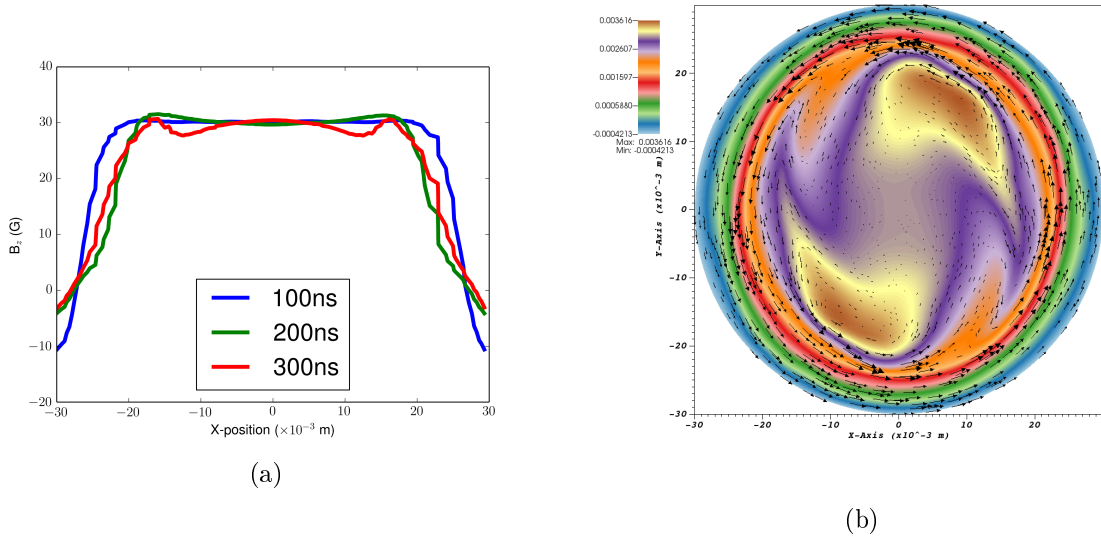
Figure 11: (a) B_z-field profile at t=100, 200, 300ns. The field reversal at the plasma edge is decreasing over time. (b) B_z and current density vector plot at t=300ns. The current density can no longer be characterized as a uniform current sheet.

(a) t=250ns (b) t=500ns (c) t=1500ns
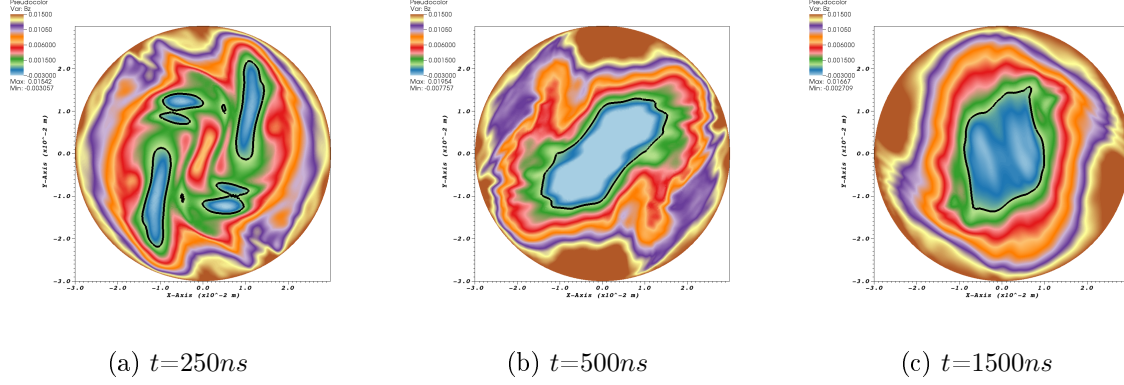
Figure 12: Z-component of the magnetic field is plotted over time showing the field reversal is achieved at the center as a result of small magnetic islands coalescence.
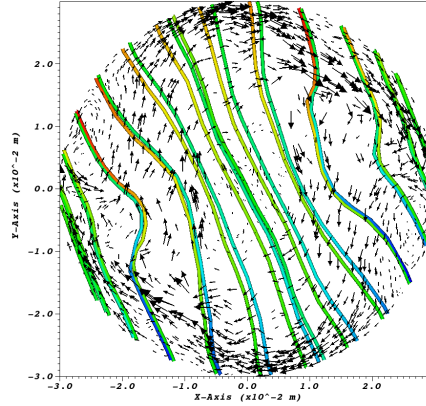
Figure 13: Electric current (black vectors) and in-plane magnetic field lines at t=4000ns. We can see that there is full RMF penetration in the plasma and that current in the θ-direction has formed as expected.

this particular case, the field line show a full penetration into the plasma. In addition, simulations show that the field reversal is dependent on the chosen value of the resistivity. At high resistivity ($\sim 10\mu\Omega$) the field does not reverse. This result is consistent with previous simulations[22].

3.2 Collisional-Radiative Model and the QSS Approximation

Through other prior and existing LRIR efforts (PM: John Luginsland / Jason Marshall), we have an extremely detailed C-R model for argon ($\sim 52,0000$ lines) and an innovative level grouping scheme by Le [23] to more efficiently implement this dataset. However, potentially even more relevant is the possibility of reducing the computational complexity further through the use of a QSS C-R model.

The QSS solutions of the C-R rate equations offer a convenient approach to take into account excited states in the effective exchange rates between charge states. The two key assumptions are (a) the time scales of the excited states are much faster compared to the transport time scales and (b) the number density of the excited states is much smaller than the ground state ions. This greatly

simplifies the implementation cost as only ground states for the neutrals and ions need to be tracked directly. For a more thorough discussion, the reader is referred to [24, 25, 26] and the references therein.

Previous work in justifying the QSS approximation have focused on fusion-like plasma conditions [27, 28]. Our goal in this work was to establish whether a QSS assumption could be used for relevant propulsion conditions. For the purposes of this study, the atomic data for all the charge states of argon (Ar^{+0}-Ar^{+18}) was compiled by Los Alamos National Laboratory as extracted from Cowan's CATS code (https://www.amdis.iaea.org/LANL/argon/)[29]. Similar to Sawada and Fujimoto [27], unsteady simulations were performed to validate the QSS rates. In the first test, shown in Figure 14a, an ionizing plasma was simulated, i.e., the excited states are populated only through excitation from the ground state, with $n_e = 10^{20}$ m^{-3} and $T_e = 5$ eV, by solving the C-R rate equations in a time accurate fashion. This result indicates that the time it takes for the excited states to reach QSS, denoted as τ_{QSS}, is about 0.1 μs, and the ionization rates converge to the QSS values as expected. In the second test, we simulate a recombining plasma, i.e., the excited states are populated only through recombination, with same n_e and T_e. The results in Figure 14b indicate the same value of τ_{QSS} and convergence to QSS recombination rates. The same results for $n_e = 10^{19}$ m^{-3} are shown in Figure 15.

(a) Ionization rates

(b) Recombination rates
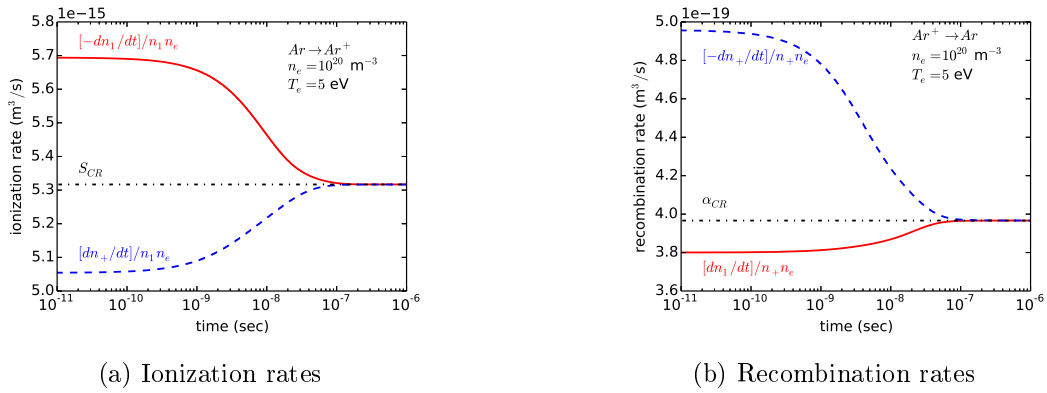
Figure 14: Various rates for an unsteady simulation of an ionizing Ar plasma with density of 1E20 particles per cubic meter. The dashed-dotted line corresponds to the QSS rate.

(a) Ionization rates

(b) Recombination rates
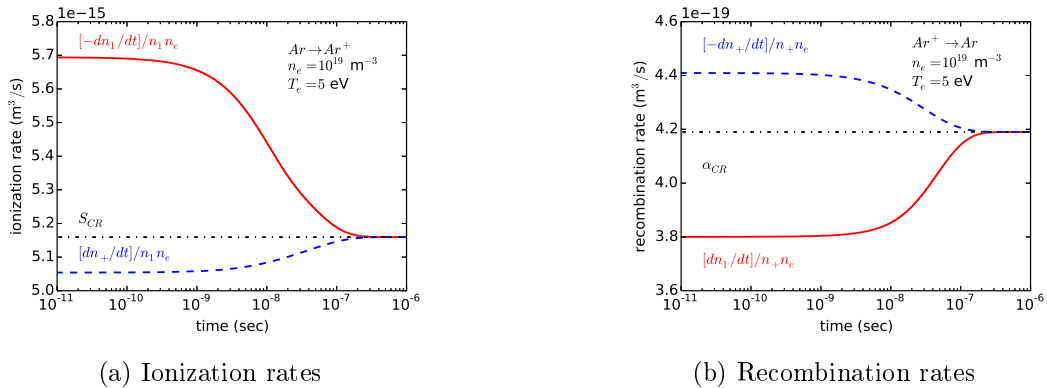
Figure 15: Various rates for an unsteady simulation of an ionizing Ar plasma with density of 1E19 particles per cubic meter. The dashed-dotted line corresponds to the QSS rate.
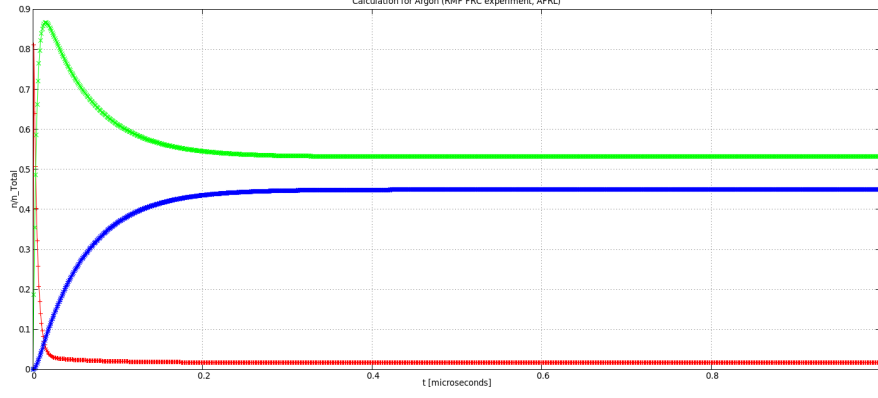
Figure 16: Results of a calculation for argon using the QSS model for plasma conditions similar to the AFRL FRC experiment ($n_e = 10^{19} \ [m^{-3}]$, $T_e = 3 \ [ev]$). Red color is neutral argon, green is singly ionized argon and blue is doubly ionized argon.
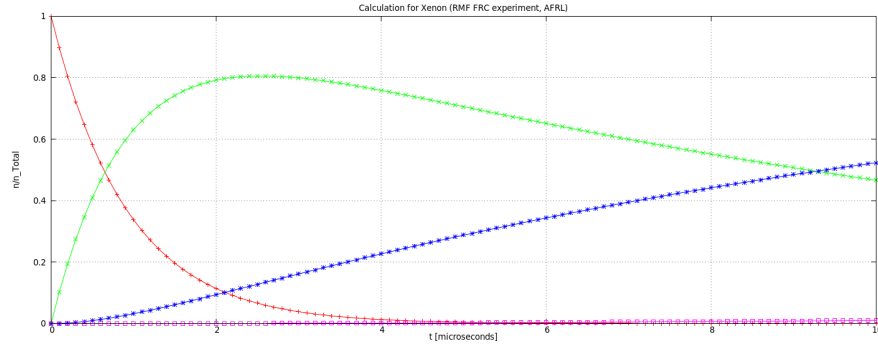
Figure 17: Results of a calculation for xenon using the QSS model for plasma conditions similar to the AFRL FRC experiment ($n_e = 10^{19} \ [m^{-3}]$, $T_e = 5 \ [ev]$). Red color is neutral xenon, green is singly ionized xenon and blue is doubly ionized xenon.

Based on these results, it appears possible to leverage the QSS-mode for propulsion plasma with timesteps of >1 ns at the cost of, at maximum, approximately 10% from detailed ionization rates. (In reality, this is an overly pessimistic estimate as typical plasma conditions, such as ionization processes shown in Figure 16 and Figure 17 do not change significantly on such a short timescale.) Leveraging the QSS-based OpenADAS [30] database for plasma spectroscopy through a well-engineered interface with TURF will allow us to readily evaluate the spectrum and energy balance from C-R processes for most of the elements of the periodic table. This would represent a significant computational cost savings for fluid and multi-fluid simulations over the $\mathcal{O}(10ms)$ timescales important to late stage formation and translation and where detailed rate information is unavailable. The dramatic reduction in the number of independent plasma species required to be independently tracked also represents a major benefit for kinetic modeling. This consistent kinetic cross-section data underlying both kinetic and fluid treatments is a critical step towards future consistent model hybridization efforts as well.

4 Translation and Neutral Entrainment

Attempts at modeling of the transition phase of FRC propulsion concepts have typically relied on single fluid MHD codes such as NIMROD[31] and Mach2[32] adapted from the fusion community. Work of this type was extended by Meier[33, 34] to two fluids to include plasma-neutral interactions, but the plasma model remained inherently a single fluid dissipative MHD representation. At propulsion relevant energies and densities, the inherent assumptions of fully ionized single plasma fluid MHD are not expected to remain valid.

The efforts of Brackbill et. al. in conjunction with the initiation of this project on neutral entrainment for FRC thrusters in Reference [35] is a notable extension to include kinetic effects. Neutral entrainment is a concept to enable FRC thrusters to attain a wider range of potential specific impulses by modifying the accelerated mass for a given energy through charge exchange collisions as the plasmoid translates through a region of background neutral density. In this work, the fully kinetic Celeste3D implicit particle in cell code was adapted to include critical elastic and inelastic collision processes for elastic, charge exchange, electron impact ionization, Coulomb, and C-R collisions needed to accurately model the complex plasma chemistry and dynamics. Figure 18 depicts a parametric study of the impact of various background neutral density profiles on the initial Schmid-Burgk kinetic equilibrium distribution. For these simulations, neon gas was used as it was identified as a good candidate for balancing radiation energy losses with effective charge exchange cross section. The simulation was performed in the translating plasmoid reference frame relative to background neutrals. Background density cases were performed at 0, 1E18, and 3E18 m^{-3} densities and at either 20 or 30 km/s relative velocity. The difference between the 1E18 and 3E18 density results demonstrate a strong sensitivity to background neutral density in this density range.
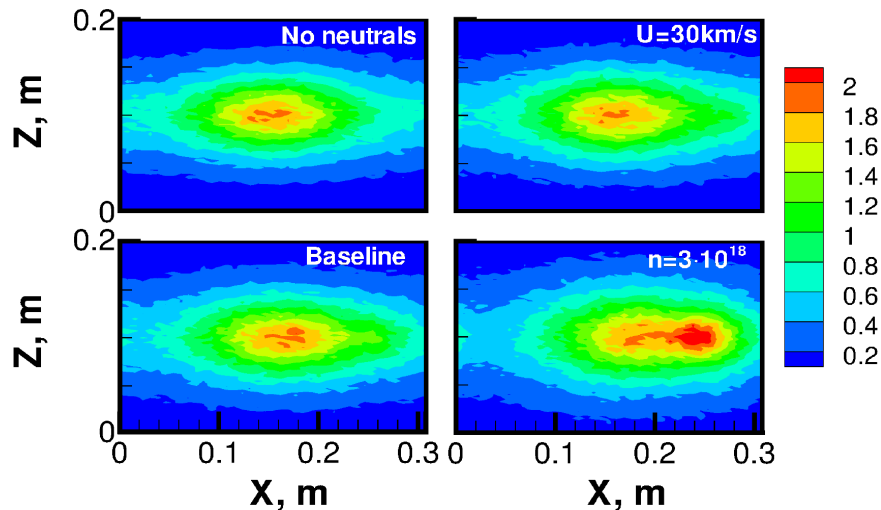
Figure 18: Free molecular neon ion density (10^{18}m^{-3}) of parametric FRC neutral entrainment simulations from Reference [35].

The simulations were performed in 2D on a coarse mesh due to the significant computational cost of performing the fully kinetic simulation. Even with these constraints, the electron mass had to be greatly increased to allow for tractable computation time. This directly modifies the plasma frequency and the potential impact of this change on effective anomalous resistivity remains an open question. This demonstrates how far the computational tools must still evolve before kinetic simulations might be used to estimate the interaction of FRC plasmoids with realistic three-dimensional residual neutral distributions from prior FRC pulses.

To extend the neutral entrainment activities described above, Appendix C shows some progress made during the course of this lab task in conjunction with 14RQ05COR (PM:Marshall) as well as AFOSR Grant FA9550-14-1-0283 (PM:Marshall) to develop the necessary elastic and inelastic collision models for kinetic and multi-fluid FRC simulations. The models will be used to augment or accelerate the kinetic (Section 2) and multi-fluid (Section 3.1) models currently in use for these types of plasma and described in the prior sections.

Consistent coupled in-elastic collision models are necessary not only for neutral entrainment but also the initial ionization in the formation process. Appendix C.2 demonstrates efficient Monte Carlo Collision (MCC) kinetic techniques that enable stochastic sampling of these inelastic collisions. This technique is consistent with the C-R rate equations needed for the source terms to the multi-fluid models which were also developed in Appendix C.3. This model consistency is critical to the future hybridization of the kinetic and multi-fluid models.

Though Appendix C.1 deals only with standard elastic DSMC kinetic collisions, it demonstrates a first step toward fully three-dimensional kinetic collision kernels that could potentially hybridize stochastic particle methods with multifluid collision models. Though this approach may already improve the efficiency for kinetic models with extremely disparate density scales, extending the approach to split the first five moments of the distribution from positive and negative weight deviational particles in the manner pioneered by Caflisch and Yan in References [36, 37] with the distinction of variable positive and negative particle weights offers an exciting path towards hybridization of the kinetic and fluid models.

Unifying all of these disparate tools into one consistent framework is a critical next step along this path towards the development of computational tools capable of tackling these types of plasma which fall on the boundary between kinetic and continuum fluid regimes. This unification effort is a primary focus to the follow-on work.

References

[1] John T Slough, David E Kirtley, and Thomas Weber. "Pulsed Plasmoid Propulsion: The ELF Thruster". In: *31 th Int. Electr. Propuls. Conf.* Ann Arbor, Michigan, 2009, pp. 1–24. URL: http://erps.spacegrant.org/uploads/images/images/iepc_articledownload_1988-2007/2009index/IEPC-2009-265.pdf.

[2] David Kirtley et al. *Neutral Entrainment Demonstation in a Xenon FRC Thruster Experiment.* Tech. rep. ADA596806. PA#13192. DTIC, Mar. 2013.

[3] Jeremiah Brackbill et al. "Ionization and Charge Exchange Reactions in a Neutral Entrainment of a Field Reversed Configuration Thruster". In: *AIAA-2012-4102.* 48th AIAA Joint Propulsion Conference. Atlanta, GA, 2012.

[4] M. Tuszewski. "Field reversed configurations". In: *Nuclear Fusion* 28 (1988), pp. 2033–2092.

[5] M. Gibbons and et. al. "Flexible Three-Dimensional Modeling of Electric Thrusters in Vaccum Chambers". In: *AIAA/ASME/SAE/ASEE Joint Propulsion Conference and Exhibit.* 2003.

[6] John Michael Fife. "Hybrid-PIC Modeling and Electrostatic Probe Survey of Hall Thrusters". Ph.D Thesis. Department of Aeronautics and Astronautics: Massachusetts Institute of Technology, 1998.

[7] Robert Martin and Justin Koo. THERMOPHYSICS UNIVERSAL RESEARCH FRAMEWORK - INFRASTRUCTURE RELEASE. Version 1.0.0. Air Force Research Laboratory (AFRL/RQRS). 2015.

[8] H. Le and J.-L. Cambier. "Modeling of Inelastic Collisions in a Multifluid Plasma: Excitation and Deexcitation". In: *Physics of Plasmas* 22 (2015), p. 093512.

[9] H. Le and J.-L. Cambier. "Modeling of Inelastic Collisions in a Multifluid Plasma: Ionization and Recombination". Submitted to Physics of Plasmas (2016).

[10] G.A. Bird. *Molecular Gas Dynamics and the Direct Simulation of Gas Flows.* Oxford University Press, 1994.

[11] Anthony Pancotti et al. "Adaptive Electric Propulsion for ISRU Missions". In: *20th Advanced Space Propulsion Workshop.* NASA Glenn Research Center, 2014.

[12] R Schneider C. D. Munz P. Omnes, E Sonnendruer, and U Voss. "Divergence Correction Techniques for Maxwell Solvers Based on a Hyperbolic Model". In: *J. Comput. Phys.* 161 (2000), pp. 484–511.

[13] Ammar Hakim. "High-resolution Wave Propagation Schemes for Two-Fluid Plasma Simulations". PhD thesis. University of Washington, 2006.

[14] Richard D. Milroy. "Effects of open field line plasma on rotating magnetic field current drive in a field-reversed configuration". In: *Phys. Plasmas* 8.6 (2001), pp. 2804–2807. ISSN: 1070664X. DOI: 10.1063/1.1368140.

[15] E M Sousa. "A Blended Finite Element Method for Multi-Fluid Plasma Modeling". PhD thesis. University of Washington, 2014.

[16] L T Diosady and S M Murman. "Design of a Variational Multiscale Method for Turbulent Compressible Flows". In: *21st AIAA Computational Fluid Dynamics Conference* 2870 (2013).

[17] W. N. Hugrass. "The Influence of the Spacial Harmonics on the Rotating Magnetic Field Current Drive". In: *Aust. J. Physi.* 39 (1986), pp. 513–527.

[18] W. N. Hugrass and R. C. Grimm. "A Numerical Study of the Generation of an Azimuthal Current in a Plasma Cylinder using a Transverse Rotating Magnetic Field". In: *J. Plasma Phys.* 26.3 (1981), pp. 455–464.

[19] A Hakim and U Shumlak. "Two-fluid Physics and Field-Reversed Configuration". In: *Phys. Plasmas* 14.055911 (2007).

[20] D. S. Harned. "Rotational instabilities in the field-reversed configuration: Results of hybrid simulations". In: *Phys. Fluids* 26.1320 (1983).

[21] Loren C. Steinhauer. "Review of field-reversed configurations". In: *Phys. Plasmas* 18.070501 (2011). ISSN: 1070664X. DOI: 10.1063/1.3613680. URL: http://dx.doi.org/10.1063/1.3613680.

[22] R. Milroy. "A numerical study of rotating magnetic fields as a current drive for field reversed configurations". In: *Phys. Plasmas* 6.7 (1999), pp. 2771–2780.

[23] Hai Le, Ann Kargozian, and Jean-Luc Cambier. "'Complexity reduction of collisional-radiative kinetics for atomic plasma". In: *Physics of Plasmas* 20 (12 2013), p. 123304.

[24] D. R. Bates, A. E. Kingston, and R. W. P. McWhirter. "Recombination Between Electrons and Atomic Ions. I. Optically Thin Plasmas". en. In: *Proceedings of the Royal Society A: Mathematical, Physical and Engineering Sciences* 267.1330 (May 1962), pp. 297–312. ISSN: 1364-5021, 1471-2946. DOI: 10.1098/rspa.1962.0101. URL: http://rspa.royalsocietypublishing.org/cgi/doi/10.1098/rspa.1962.0101 (visited on 04/11/2015).

[25] J.A.M. van der Mullen. "Excitation equilibria in plasmas; a classification". In: *Physics Reports* 191.2-3 (1990), pp. 109–220. ISSN: 03701573. DOI: 10.1016/0370-1573(90)90152-R. URL: http://linkinghub.elsevier.com/retrieve/pii/037015739090152R (visited on 12/27/2013).

[26] T. Fujimoto. *Plasma spectroscopy*. The international series of monographs on physics 123. Oxford : New York: Clarendon Press ; Oxford University Press, 2004. ISBN: 978-0-19-853028-2.

[27] K. Sawada and T. Fujimoto. "Temporal relaxation of excited-level populations of atoms and ions in a plasma: Validity range of the quasi-steady-state solution of coupled rate equations". en. In: *Physical Review E* 49.6 (1994), pp. 5565–5573. ISSN: 1063-651X, 1095-3787. DOI: 10.1103/PhysRevE.49.5565. URL: http://link.aps.org/doi/10.1103/PhysRevE.49.5565 (visited on 04/10/2016).

[28] S. D. Loch et al. "Collisional-radiative study of lithium plasmas". en. In: *Physical Review E* 69.6 (June 2004). ISSN: 1539-3755, 1550-2376. DOI: 10.1103/PhysRevE.69.066405. URL: http://link.aps.org/doi/10.1103/PhysRevE.69.066405 (visited on 04/10/2016).

[29] R.D. Cowan. *The Theory of Atomic Structure and Spectra*. Los Alamos series in basic and applied sciences 3. Berkeley: University of California Press, 1981. ISBN: 978-0-520-03821-9.

[30] *OPEN-ADAS Atomic Data and Analysis Structure*. 2015. URL: http://www.adas.ac.uk.

[31] John Slough et al. "Recent Computational Code Development for Compact Toroids and Suitability for Space Propulsion Applications". In: *43rd AIAA/ASME/SAE/ASEE Joint Propulsion Conference and Exhibit*. 2007.

[32] Shawn W. Miller and Joshua L. Rovey. "Progress in Modeling of Pre-ionization and Geometric Effects on a Field-Reversed Configuration Plasma Thruster". In: *AIAA-2009-3733*. 40th AIAA Plasma-dynamics and Lasers Conference. San Antonio, TX, 2009.

[33]   Eric T. Meier. "Modeling Plasmas with Strong Anisotropy, Neutral Fluid Effects, and Open Boundaries". Ph.D Thesis. Department of Aeronautics and Astronautics: University of Washington, 2011.

[34]   D. Kirtley et al. "Pulsed Plasmoid Propulsion: Air-Breathing Electromagnetic Propulsion". In: 32nd Int. Electric Propulsion Conf. (IEPC). Wiesbaden, Germany, Sept. 2011, IEPC–2011–015.

[35]   Jeremiah Brackbill et al. "Numerical Analysis of Neutral Entrainment Effect on Field-Reversed Configuration Thruster Efficiency". In: Journal of Propulsion and Power 30.6 (2014), pp. 1450–1458. DOI: DOI:10.2514/1.B35260.

[36]   Bokai Yan and Russel E. Caflisch. "A Monte Carlo method with negative particles for Coulomb collisions". In: Journal of Computational Physics 298 (2015), pp. 711 –740. ISSN: 0021-9991. DOI: http://dx.doi.org/10.1016/j.jcp.2015.06.021. URL: http://www.sciencedirect.com/science/article/pii/S0021999115004180.

[37]   Bokai Yan. "A hybrid method with deviational particles for spatial inhomogeneous plasma". In: Journal of Computational Physics 309 (2016), pp. 18 –36. ISSN: 0021-9991. DOI: http://dx.doi.org/10.1016/j.jcp.2015.12.050. URL: http://www.sciencedirect.com/science/article/pii/S0021999115008694.

This Page Intentionally Left Blank

NON-EQUILIBRIUM MODELING OF INDUCTIVELY COUPLED RF PLASMAS

Alessandro Munafò[1], Jean-Luc Cambier[2], and Marco Panesi[3]

[1]*University of Illinois at Urbana-Champaign, Talbot Laboratory, 104 S. Wright St., Urbana, IL 61801, USA*
[2]*Edwards Air Force Base Research Laboratory, 10 E. Saturn Blvd., CA 93524, USA*
[3]*University of Illinois at Urbana-Champaign, Talbot Laboratory, 104 S. Wright St., Urbana, IL 61801, USA*

ABSTRACT

This paper discusses the modeling of non-equilibrium effects in inductively coupled plasma facilities. The model relies on the solution of the Navier-Stokes and Maxwell equations in a one-dimensional geometry. Steady-state solutions are obtained by means of an implicit Finite Volume method. Non-equilibrium effects are treated by means of a hybrid State-to-State formulation. The electronic states of atoms are treated as separate species, allowing for non-Boltzmann distributions of their populations. Thermal non-equilibrium between the translation and vibrational of heavy-particles is accounted for by means of a multi-temperature approach. The results show that non-equilibrium plays an important role close to the walls, due to the combined effects of Ohming heating, and chemical composition and temperature gradients.

Key words: NLTE plasmas, State-to-State modeling, Inductively Coupled Plasma torch.

1. INTRODUCTION

Inductively coupled plasma (ICP) torches have wide range of possible applications which include deposition of metal coatings, synthesis of ultra-fine powders, generation of high purity silicon and testing of thermal protection materials for atmospheric entry vehicles [1, 2].

In its simplest configuration, an ICP torch consists of a quartz tube surrounded by an inductor coil made of a series of parallel current-carrying rings. The radio-frequency (RF) currents running through the inductor induce toroidal currents in the gas which is heated thanks to Ohmic dissipation [2, 3]. If the energy supplied is large enough, the gas flowing through the torch can undergo ionization, leading to the formation of a plasma.

The accurate modeling of the flow-field and electromagnetic phenomena inside an ICP torch requires the coupled solution of the Navier-Stokes and Maxwell equations [2]. In literature, the Local Thermodynamic Equilibrium (LTE) assumption is often used to describe the state of the gas in the discharge region [4–17]. However,

Non Local Thermodynamic Equilibrium (NLTE) simulations of Argon [18, 19] and air plasmas [20], have shown that the LTE assumption may not always hold.

An accurate modeling of NLTE effects in ICP RF plasmas can be achieved by means of State-to-State models [21–33]. These treat each internal energy state as a separate *pseudo species*, thus allowing for non-Boltzmann distributions. Rate coefficients are usually obtained through quantum chemistry calculations [34–39] or through phenomenological models [40, 41]. State-to-State models provide a superior description compared to conventional multi-temperature models, which are based on Maxwell-Boltzmann distributions [42–45]. However, due to the large number of governing equations to be solved, their application to multi-dimensional problems can become computationally demanding [46–50].

The purpose of the present work is the development of a magneto-hydrodynamic NLTE model for an ICP torch. The flow model has to be simple enough to allow for the implementation of sophisticated NLTE models describing the kinetics of atoms and molecules in the inductor region. The final goal is the assessment of the extent of non-equilibrium phenomena occurring in ICP generators used for Thermal Protection System (TPS) testing.

The paper is structured as follows. Section 2 describes the physical model. The numerical method is presented in Sect. 3. Computational results are discussed in Sect. 4. Conclusions are outlined in Sect. 5.

2. PHYSICAL MODELING

The NLTE model for the ICP torch is built based on the torch geometry displayed in Figure 1. To make the problem tractable, the following assumptions are introduced:

(i) Constant pressure and no *macroscopic streaming*,

(ii) Charge neutrality and no displacement current,

(iii) Steady-state conditions for gas quantities (i.e., $\partial()/\partial t = 0$),

(iv) No gradients along the axial and circumferential directions (i.e., $\partial()/\partial z = 0$, $\partial()/\partial \phi = 0$).
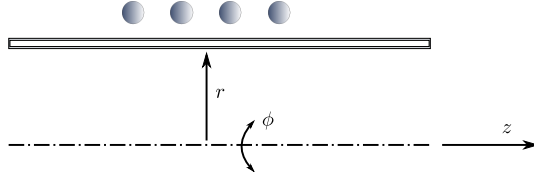
Figure 1: Torch geometry and adopted reference frame.

2.1. Electromagnetic field

The electromagnetic field inside the ICP torch is described by the Maxwell equations:

$$\nabla \cdot \mathbf{E} = \frac{\rho^c}{\epsilon_0} \tag{1}$$

$$\nabla \cdot \mathbf{B} = 0 \tag{2}$$

$$\nabla \times \mathbf{E} = -\frac{\partial \mathbf{B}}{\partial t} \tag{3}$$

$$\nabla \times \mathbf{B} = \mu_0 \mathbf{J} + \mu_0 \epsilon_0 \frac{\partial \mathbf{E}}{\partial t} \tag{4}$$

where quantities $\mathbf{E}$ and $\mathbf{B}$ are the electric and magnetic fields, respectively. Quantity ρ^c stands for the charge density. The current density $\mathbf{J}$ is assumed to obey Ohm's law $\mathbf{J} = \sigma_e \mathbf{E}$ [51], with σ_e being the electrical conductivity. Quantities ϵ_0 and μ_0 are the vacuum permittivity and magnetic permeability, respectively. The application of the simplifying assumptions just introduced to the Maxwell equations (1)-(4) leads to the following induction equation for the induced toroidal electric field:

$$\frac{\partial}{\partial r}\left(\frac{1}{r}\frac{\partial r E_\phi}{\partial r}\right) = -\mu_0 \sigma_e \frac{\partial E_\phi}{\partial t} \tag{5}$$

Since the induced eddy currents which are responsible for the heating of the gas are induced by a primary current whose intensity varies sinusoidally in time, it seems natural to seek for a mono-chromatic wave solution, $E_\phi = E \exp(\imath 2\pi f t)$, where f is the frequency of the primary current. To account for the possible phase difference between the induced electric and magnetic fields, the amplitude E is taken complex, $E = E_{re} + \imath E_{im}$. The substitution of $E \exp(\imath 2\pi f t)$ in Eq. (5) leads to:

$$0 \times \frac{\partial r \mathbf{U}_{em}}{\partial t} + \frac{\partial r \mathbf{F}_{em}}{\partial r} = r \mathbf{S}_{em} \tag{6}$$

The electromagnetic (em) conservative variable, flux and source term vectors are:

$$\mathbf{U}_{em} = \begin{bmatrix} E_{re} & E_{im} \end{bmatrix}^T \tag{7}$$

$$\mathbf{F}_{em} = \begin{bmatrix} \dfrac{\partial E_{re}}{\partial r} & \dfrac{\partial E_{im}}{\partial r} \end{bmatrix}^T \tag{8}$$

$$\mathbf{S}_{em} = \begin{bmatrix} \dfrac{E_{re}}{r^2} + \omega\mu_0\sigma_e E_{im} & \dfrac{E_{im}}{r^2} - \omega\mu_0\sigma_e E_{re} \end{bmatrix}^T \tag{9}$$

where the angular frequency is $\omega = 2\pi f$. The symbol T denotes the transpose operator.

Equation (6) must be supplemented with boundary conditions at the axis ($r = 0$) and at the torch wall ($r = R$, with R being the torch radius). On the axis, due to symmetry, both the real and imaginary components of the induced electric field must vanish:

$$E_{re} = 0, \quad E_{im} = 0, \quad \text{at } r = 0 \tag{10}$$

The boundary condition at the torch wall is obtained as follows. The amplitudes of the toroidal electric field and the axial magnetic field are linked via [17]:

$$\frac{1}{r}\frac{\partial r E}{\partial r} = -\imath\omega B \tag{11}$$

where the amplitude B is taken complex. Immediately outside the wall the magnetic field must be real and, since there is no plasma outside the tube, its value can only depend on the ICP operating conditions and characteristics. If the torch is long enough, the magnetic field at the torch wall can be approximated with the expression for an infinite solenoid, $B(r = R) = \mu_0 N I_c$, where quantities N and I_c are the number of turns per unit-length and the amplitude of the primary current. The evaluation of Eq. (11) at the torch wall and the use of the relation $B(r = R) = \mu_0 N I_c$ gives the wall boundary condition for the induced electric field:

$$\frac{1}{r}\frac{\partial r E_{re}}{\partial r} = 0, \quad \frac{1}{r}\frac{\partial r E_{im}}{\partial r} = -\omega\mu_0 N I_c, \quad \text{at } r = R \tag{12}$$

2.2. Gas field

The gas contained in the torch is made of electrons, atoms and (diatomic) molecules. Charged particles comprise electrons and positively singly charged ions. The set $\mathcal{S}$ stores the chemical components, and the heavy-particles are stored in the set $\mathcal{S}_h$. The atomic and molecular components are stored in the sets $\mathcal{S}_a$ and $\mathcal{S}_m$, respectively. The previously introduced sets satisfy the relations $\mathcal{S}_h = \mathcal{S}_a \cup \mathcal{S}_m$ and $\mathcal{S} = \{e^-\} \cup \mathcal{S}_m$, where the symbol e^- indicates the free-electrons. The electronic levels of the heavy components are stored in sets $\mathcal{I}_s^{el}$ (with $s \in \mathcal{S}_h$) and are treated as separate *pseudo-species* based on a State-to-State approach [52]. The notation s_i is then introduced to denote the i-th electronic level of the heavy component $s \in \mathcal{S}_h$, with the related degeneracy and energy being $g_{s_i}^{el}$ and $E_{s_i}^{el}$, respectively. A multi-temperature model is instead used for vibration of molecules and translation of free-electrons (with the related temperatures being T_v and T_e, respectively) [53]. Rotational non-equilibrium effects are disregarded.

Thermodynamics

The gas pressure is computed based on Dalton's law of partial pressures by summing the contributions of free-electrons and heavy-particles, $p = p_e + p_h$, where the

symbol k_B stands for Boltzmann's constant. The partial pressures of free-electrons and heavy-particles are, respectively, $p_e = n_e k_B T^e$ and $p_h = n_h k_B T$, where quantities n_e and n_h denote, respectively, the related the number densities. The number density of heavy-particles is obtained via $n_h = \sum_{s \in S_h} n_s$, with $n_s = \sum_{i \in \mathcal{I}_s^{el}} n_{s_i}$.

The gas total, vibrational and free-electron energy densities read:

$$\rho e = \frac{3}{2}p + \sum_{s \in \mathcal{S}_m} n_s[\tilde{E}_s^r(T) + \tilde{E}_s^v(T_v)] + \sum_{s \in \mathcal{S}_h} n_s \Delta E_s^f +$$
$$\sum_{\substack{s \in \mathcal{S}_h \\ i \in \mathcal{I}_s^{el}}} n_{s_i} E_{s_i}^{el} \qquad (13)$$

$$\rho e_v = \sum_{s \in \mathcal{S}_m} n_s \tilde{E}_s^v(T_v), \quad \rho e_e = \frac{3}{2}p_e \qquad (14)$$

Quantity ΔE_s^f stands for the formation energy (per particle) of the heavy component $s \in \mathcal{S}_h$. The average particle rotational and vibrational energies ($\tilde{E}_s^r$ and $\tilde{E}_s^v$, $s \in \mathcal{S}_m$, respectively) are computed, respectively, according to the rigid-rotor and harmonic-oscillator models [54].

Thermodynamic data used in this work are taken from Gurvich tables [55] (with the exception of the spectroscopic data for the electronic levels taken from [26]).

Kinetics

Collisional processes The NLTE model for ICP RF plasmas developed in this work accounts for the following kinetic processes:

(i)   Excitation by electron impact (EX_e),

(ii) Ionization by electron impact (I_e),

(iii) Dissociation by electron impact (D_e),

(iv) Dissociation by heavy-particle impact (D_h),

(v)   Associative ionization (AI).

Rate coefficients and production terms The endothermic rate coefficients for electron induced processes and associative ionization reactions are taken from the ABBA model [26–29]. Those for dissociation by heavy-particle impact are taken from the work of Park [43]. Reverse rate coefficients are obtained based on microreversibility [56, 57].

The mass production terms for free-electrons and heavy-particles due to the kinetic processes considered in this work are computed based on the zeroth-order reaction rate theory [56, 57]. In what follows, the latter quantities are indicated with the notation ω_e and ω_{s_i}.

The energy transfer terms for the gas vibrational energy account for (i) vibrational-translational (vt) energy exchange in molecule heavy-particle collisions, (ii) vibrational-electron (ve) energy exchange in molecule electron collisions, and (iii) the creation/destruction of vibrational energy in chemical reactions (cv). The first two energy transfer terms (indicated in what follows with Ω_{vt} and Ω_{ve}, respectively) are evaluated based on a Landau-Teller model [58], while the chemistry-vibration coupling term (Ω_{cv}) is computed by using the non-preferential dissociation model of Candler [59]. The relaxation times for vt energy transfer are computed by means of the modified formula of Millikan and White proposed by Park [43]. The energy transfer in molecule-electron inelastic collisions is considered only for N_2. The corresponding relaxation time is taken from the work of Bourdon [60].

The energy transfer terms for the free-electron gas account for energy exchange undergone by free-electrons in (i) elastic collisions with heavy-particles (Ω_{el}), (ii) inelastic electron induced excitation, ionization and dissociation processes (Ω_{in}) and (iii) Joule heating (Ω_j). The expressions for the first two can be found in [27–29]. The (time-averaged) Joule heating source term is obtained by averaging over a period the instantaneous Joule heating power and reads [15, 17]:

$$\Omega_j = \frac{1}{2}\sigma_e(E_{re}^2 + E_{im}^2) \qquad (15)$$

Transport

Transport phenomena are treated based on the results obtained from the application of the Chapman-Enskog method to the Boltzmann equation [61]. In the present work, transport phenomena are modeled by assuming that (i) inelastic and reactive collisions have a no effect on the transport properties and fluxes and (ii) the collision cross-sections for elastic scattering do not depend on the internal quantum states. In view of the last assumption, the dimension of the transport matrices shrinks from the number of species to the number of chemical components.

Heavy-particle gas The translational component of thermal conductivity (λ_t) is:

$$\lambda_t = \sum_{s \in \mathcal{S}_h} \alpha_s^\lambda X_s \qquad (16)$$

where the mole fractions of the heavy components are $X_s = n_s k_B T/p$ ($s \in \mathcal{S}_h$). The coefficients α_s^λ are solution of the linear (symmetric) transport system:

$$\sum_{p \in \mathcal{S}_h} G_{sp}^\lambda \alpha_s^\lambda = X_s \qquad (17)$$

$s \in \mathcal{S}_h$. Quantities G_{sp}^λ are the entries of the thermal conductivity (symmetric) transport matrix [56]. The contributions of the gas rotational and vibrational degrees of

freedom to the thermal conductivity (λ_r and λ_v, respectively) are taken into account by means of the generalized Eucken's correction [56].

Electron gas The thermal and electrical conductivity of the electron gas are (in the second and third-order Laguerre-Sonine approximations, respectively) [62, 63]:

$$\lambda_e = \frac{75}{8}k_B\sqrt{\frac{2\pi k_B T_e}{m_e}}\frac{X_e\Lambda_{ee}^{22}}{\Lambda_{ee}^{11}\Lambda_{ee}^{22}-(\Lambda_{ee}^{12})^2} \quad (18)$$

$$\sigma_e = \frac{3}{2}\frac{e^2}{k_B}\sqrt{\frac{2\pi k_B}{m_e T_e}}\frac{X_e\Lambda_{ee}^{11}}{\Lambda_{ee}^{00}\Lambda_{ee}^{11}-(\Lambda_{ee}^{10})^2} \quad (19)$$

where the mole fraction of free-electrons is $X_e = n_e k_B T_e/p$ and $e = 1.602 \times 10^{-19}$ C is the electron charge. Quantities $\Lambda_{ee}^{i,j}$ are the Devoto collision integrals [62].

Mass diffusion and heat fluxes The mass diffusion fluxes are found by solving the Stefan-Maxwell equations under the constraints of global mass conservation and ambipolar diffusion [62–65]. The diffusion driving forces include only mole fraction gradients (thermal and baro diffusion are both neglected). In view of the assumed independence of the elastic collision cross-section on the internal quantum states, the Stefan-Maxwell equations are solved for the free-electron and heavy component diffusion fluxes (J_e and J_s, $s \in \mathcal{S}_h$, respectively). The mass diffusion fluxes for the internal (electronic) levels are then found as shown in [17]. The total, vibrational and free-electron heat fluxes are:

$$q = \sum_{s\in\mathcal{S}_h}\left(\frac{5}{2}k_B T + \Delta E_s^f\right)\frac{J_s}{m_s} + \sum_{s\in\mathcal{S}_m}\tilde{E}_s^r(T)\frac{J_s}{m_s} +$$
$$\sum_{\substack{s\in\mathcal{S}_h\\i\in\mathcal{I}_s^{el}}}E_{s_i}^{el}\frac{J_{s_i}}{m_s} - \lambda_{tr}\frac{\partial T}{\partial r} + q_v + q_e \quad (20)$$

$$q_v = \sum_{s\in\mathcal{S}_m}\tilde{E}_s^v(T_v)\frac{J_s}{m_s} - \lambda_v\frac{\partial T_v}{\partial r} \quad (21)$$

$$q_e = \left(\frac{5}{2}k_B T_e\right)\frac{J_e}{m_e} - \lambda_e\frac{\partial T_e}{\partial r} \quad (22)$$

where the translational-rotational thermal conductivity of the heavy-particle gas is $\lambda_{tr} = \lambda_t + \lambda_r$.

Governing equations

The governing equations for the gas chemical composition and temperature distribution in the ICP torch are:

$$\frac{\partial r\mathbf{U}_g}{\partial t} + \frac{\partial r\mathbf{F}_g}{\partial r} = r\mathbf{S}_g \quad (23)$$

where the gas (g) conservative variable, flux and source term vectors are:

$$\mathbf{U}_g = \begin{bmatrix} \rho_e & \rho_{s_i} & \rho e & \rho e_v & \rho e_e \end{bmatrix}^T \quad (24)$$

$$\mathbf{F}_g = \begin{bmatrix} J_e & J_{s_i} & q & q_v & q_e \end{bmatrix}^T \quad (25)$$

$$\mathbf{S}_g = \begin{bmatrix} \omega_e & \omega_{s_i} & \Omega_j & \Omega_v & \Omega_e \end{bmatrix}^T \quad (26)$$

$i \in \mathcal{I}_s^{el}$, $s \in \mathcal{S}_h$, with $\Omega_v = \Omega_{vt} + \Omega_{ve} + \Omega_{cv}$ and $\Omega_e = \Omega_{el} + \Omega_{in} + \Omega_j$.

The boundary conditions used for solving Eq. (23) are a symmetry boundary condition at the axis and an isothermal non-catalytic boundary condition at the torch wall (with the related imposed wall temperature indicated with T_w). In analogy with the work of Mostaghimi *et al.* [18, 19], an adiabatic boundary condition is used for the vibrational and free-electron temperatures at the torch wall.

3. NUMERICAL METHOD

3.1. Coupled formulation

The governing equations for the gas and the electromagnetic fields are strongly coupled due to the presence of the Joule heating term in Eq. (26) and the electrical conductivity in Eq. (9). This suggests to adopt a fully coupled approach by casting Eqs. (6) and (23):

$$\frac{\partial r\mathbf{\Gamma}\mathbf{U}}{\partial t} + \frac{\partial r\mathbf{F}}{\partial r} = \mathbf{S} \quad (27)$$

where conservative variable, flux and source term vectors are now $\mathbf{U} = (\mathbf{U}_g, \mathbf{U}_{em})$, $\mathbf{F} = (\mathbf{F}_g, \mathbf{F}_{em})$ and $\mathbf{S} = (\mathbf{S}_g, \mathbf{S}_{em})$. The matrix $\mathbf{\Gamma}$ in Eq. (27) reads:

$$\mathbf{\Gamma} = \begin{pmatrix} 1 & 0 & 0 & 0 & 0 & 0 & 0 \\ 0 & \delta_{s_i p_j} & 0 & 0 & 0 & 0 & 0 \\ 0 & 0 & 1 & 0 & 0 & 0 & 0 \\ 0 & 0 & 0 & 1 & 0 & 0 & 0 \\ 0 & 0 & 0 & 0 & 1 & 0 & 0 \\ 0 & 0 & 0 & 0 & 0 & 0 & 0 \\ 0 & 0 & 0 & 0 & 0 & 0 & 0 \end{pmatrix} \quad (28)$$

$i \in \mathcal{I}_s^{el}$, $j \in \mathcal{I}_p^{el}$, $s, p \in \mathcal{S}_h$, where $\delta_{s_i p_j} = \delta_{sp}\,\delta_{ij}$, with δ being Kronecker's delta.

3.2. Spatial discretization

The application of the Finite Volume method to Eq. (27) leads to the following ODE describing the time-evolution of the conservative variables of cell c:

$$\mathbf{\Gamma}\frac{\partial\mathbf{U}_c}{\partial t}r_c\Delta r_c + r_{c+\frac{1}{2}}\mathbf{F}_{c+\frac{1}{2}} - r_{c-\frac{1}{2}}\mathbf{F}_{c-\frac{1}{2}} = \mathbf{S}_c r_c\Delta r_c \quad (29)$$

with the cell volume (length) and centroid location being $\Delta r_c = r_{c+1/2} - r_{c-1/2}$ and $r_c = 1/2(r_{c+1/2} +$

$r_{c-1/2}$), respectively. The evaluation of the diffusive flux $\mathbf{F}_{c+1/2}$ is performed by approximating the values and the gradients of a given quantity p (e.g., temperatures and electric field components) by means of an arithmetic average and a second order central finite difference, respectively. To facilitate the implementation of the constant pressure constraint, the solution update is performed on primitive variables consisting of mass fractions, temperatures and electric field components, $\mathbf{P} = (y_e, y_{s_i}, T, T_v, T_e, E_{re}, E_{im})$:

$$\mathbf{\Gamma T}_c \frac{\partial \mathbf{P}_c}{\partial t} r_c \Delta r_c + r_{c+\frac{1}{2}} \mathbf{F}_{c+\frac{1}{2}} - r_{c-\frac{1}{2}} \mathbf{F}_{c-\frac{1}{2}} = \mathbf{S}_c r_c \Delta r_c \tag{30}$$

The transformation matrix $\mathbf{T}$ can be easily obtained from the time-derivative of the conservative variables ($\partial \mathbf{U}/\partial t$) by exploiting the global continuity equation (i.e., $\partial \rho / \partial t = 0$).

3.3. Temporal discretization

Equation (30) is integrated in time by means of the backward Euler method [66]:

$$\mathbf{\Gamma T}_c^n \frac{\delta \mathbf{P}_c^n}{\Delta t_c} r_c \Delta r_c + r_{c+\frac{1}{2}} \mathbf{F}_{c+\frac{1}{2}}^{n+1} - r_{c-\frac{1}{2}} \mathbf{F}_{c-\frac{1}{2}}^{n+1} = \mathbf{S}_c^{n+1} r_c \Delta r_c \tag{31}$$

where $\delta \mathbf{P}_c^n = \mathbf{P}_c^{n+1} - \mathbf{P}_c^n$. The local time-step Δt is computed based on the von Neumann number (ξ) as $\Delta t = \xi/(2\rho^d)$ [67], where quantity ρ^d stands for the spectral radius of the diffusive flux Jacobian $\partial \mathbf{F}/\partial \mathbf{U}$.

In order to advance the solution from the time-level n to the time-level $n + 1$, Eq. (31) is linearized around the time-level n. To facilitate the linearization procedure, the flux $\mathbf{F}$ is written as $\mathbf{F} = \mathbf{A}\partial \mathbf{P}/\partial r$ and the matrix $\mathbf{A}$ is kept frozen during the linearization. The source term is linearized by evaluating the related Jacobian analytically to enhance stability. The outcome of the linearization procedure is a block-tridiagonal algebraic system to be solved at each time-step:

$$\mathbf{M_L}_c^n \delta \mathbf{P}_{c-1}^n + \mathbf{M_C}_c^n \delta \mathbf{P}_c^n + \mathbf{M_R}_c^n \delta \mathbf{P}_{c+1}^n = -\mathbf{R}_c^n \tag{32}$$

where the right-hand-side residual is:

$$\mathbf{R}_i = -\left(r_{c+\frac{1}{2}} \mathbf{F}_{c+\frac{1}{2}} - r_{c-\frac{1}{2}} \mathbf{F}_{c-\frac{1}{2}} \right) + \mathbf{S}_c r_c \Delta r_c \tag{33}$$

The left (L), central (C) and right (R) block matrices can be found from the linearization procedure (see, for instance, [68] for more details). The block-tridiagonal system (32) is solved by means of Thomas' algorithm [67] and the solution updated at the time-level $n + 1$, $\mathbf{P}_c^{n+1} = \mathbf{P}_c^n + \delta \mathbf{P}_c^n$. This process is continued until steady-state is reached.

Boundary conditions are implemented through ghost cells [67] and the related folding in the central block matrices $\mathbf{M_C}$ is performed as suggested by Candler [59].

4. COMPUTATIONAL RESULTS

The gas contained in torch consists of nitrogen molecules and the related dissociation and ionization products (i.e., $\mathcal{S} = \{e, N, N_2, N_2^+, N^+\}$). Simulations are performed by means of the ABBA State-to-State (StS) model [26–29] and the multi-temperature (MT) model proposed by Park [43].

The torch radius, the number of coils per unit-length, the frequency of the primary current and the wall temperature are set to 0.08 m, 50, 0.5 MHz and 350 K, respectively. The current intensity of the primary circuit is not prescribed. Instead the former is found from the solution by imposing that the dissipated power (per unit-length) in the plasma:

$$P = 2\pi \int_0^R \Omega_j \, r \, dr, \tag{34}$$

is equal to $P_0 = 350\,000$ W/m. In order to match the condition $P = P_0$ at steady-state, the current intensity is multiplied by the scaling factor $\gamma = \sqrt{P_0/P}$ after updating the solution at each time-step [12, 16]. Three different values are adopted for the pressure in the torch: 3000 Pa, 5000 Pa and $10\,000$ Pa.

In all the cases, the solution is initialized with a uniform equilibrium distribution at 7500 K (with both electric field components equal to 0.1 V/m). The starting of the simulation is quite violent. Severe temperature and chemical composition gradients occur at the wall, due to the cold temperature imposed. During this initial phase (in particular when using the StS model), the time-step must be limited to avoid numerical instabilities. For this reason, during the first few iterations, the von Neumann number is kept within the range 1000-$10\,000$. Once the initial transient passed, its value is increased interactively (up to $500\,000\,000$) to accelerate convergence to steady-state. Such large values are possible due to the adoption of a fully coupled implicit time-integration method.

For the conditions adopted in the present work, the vibrational and free-electron temperature profiles are essentially on top of each other. This is due to the efficient energy exchange in N_2-e^- interactions [53]. For this reason, in what follows, the vibrational and free-electron temperatures are indicated as a unique temperature by means of the notation T_{ve}.

4.1. Assessment of NLTE effects

Before investigating in detail NLTE effects, an LTE simulation is performed and compared with the NLTE results to assess the extent of the departure from equilibrium. The pressure is set to 10000 Pa as, for this relatively high value, LTE conditions are often assumed [17].

Figure 2 compares the LTE and NLTE translational-rotational temperature, Joule heating and electric field distributions. Close to the wall, the curvature of the LTE
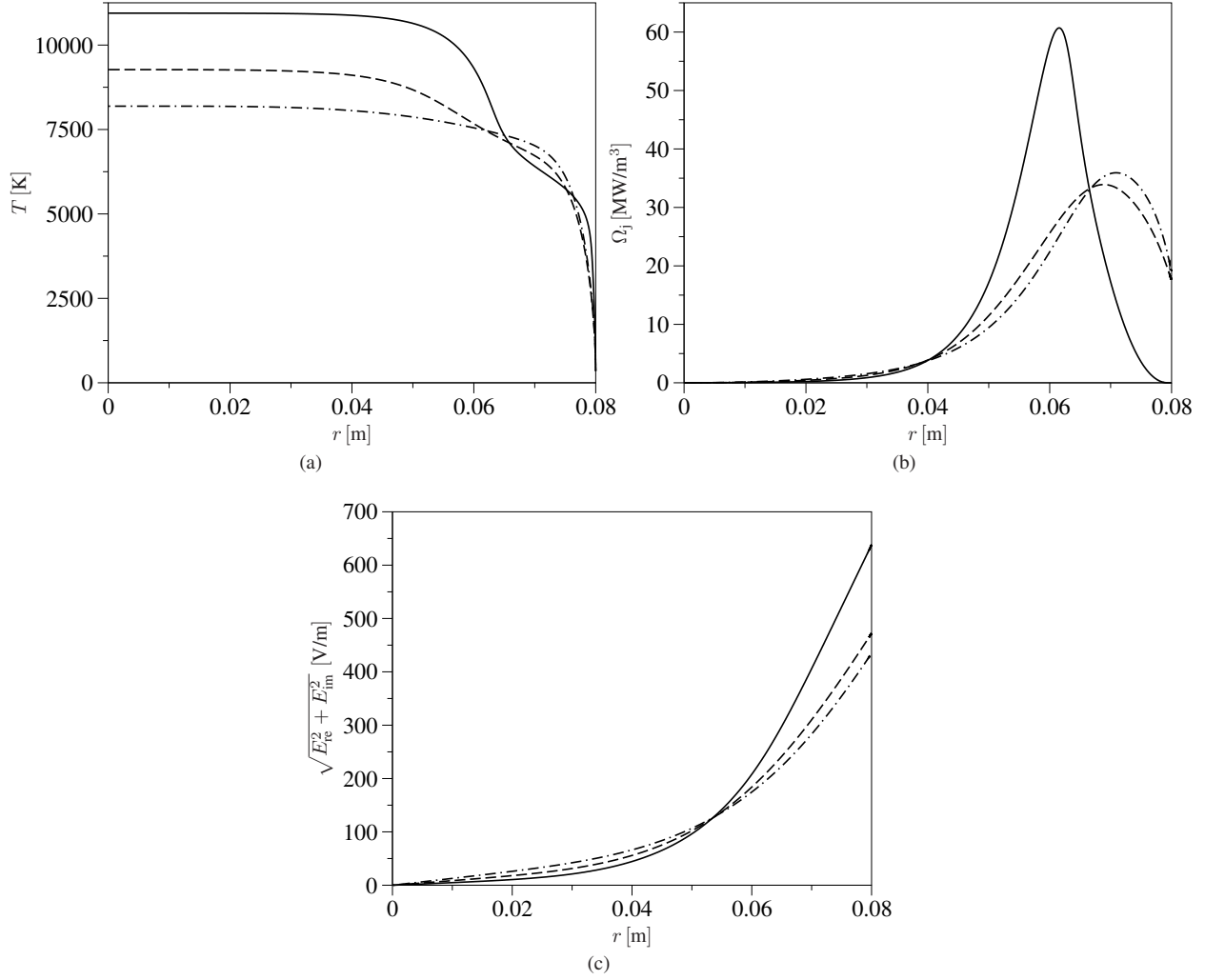
Figure 2: LTE and NLTE translational-rotational temperature (a), Joule heating (b) and induced electric field magnitude (c) distributions at $10\,000\,\mathrm{Pa}$ (unbroken line LTE, dashed line MT, dotted-dashed line StS).

temperature distribution changes sign. This is a consequence of the non-monotone behavior of the equilibrium total thermal conductivity of the working gas (nitrogen). The same trend is also found in the MT solution (though less enhanced), while the one predicted by the StS model does not exhibit any sign change in its curvature. Both NLTE models predict that the gas is in thermal equilibrium close to the axis (the free-electron temperature is not shown in Figure 2a), though the equilibrium is different between the MT and StS solutions. In both the LTE and NLTE simulations, the temperature is maximum on the axis, due to the absence of radiative losses in the plasma [7, 8]. Overall, the LTE solution predicts higher temperature values, with the difference being maximum on the axis. This is a general trend observed in all the simulations performed in this work (and also in the multi-dimensional results obtained by other investigators in [17, 20]). In NLTE conditions, the temperature is lower because the plasma is heated over a wider region compared to LTE conditions. This is confirmed by the Joule heating distribution shown in Figure 2b. The results in

Figure 2 show that, even when adopting relatively high pressure values, the LTE assumption can lead to a severe overestimation of the gas temperature and, as a related consequence, to a prediction of the chemical composition. It is worth to recall that in the present work, the effects of a macroscopic gas flow (which enhance non-equilibrium) are neglected.

4.2. StS vs MT

After assessing the importance of NLTE effects, the predictions obtained by the StS and MT models are compared in Figure 3 in terms of temperature and N mole fraction. For both the StS and MT solutions, decreasing the pressure has the effect of enhancing thermal non-equilibrium. In the case of the MT model, the translational-rotational temperature is maximum on the axis and decreases monotonically when approaching the wall.
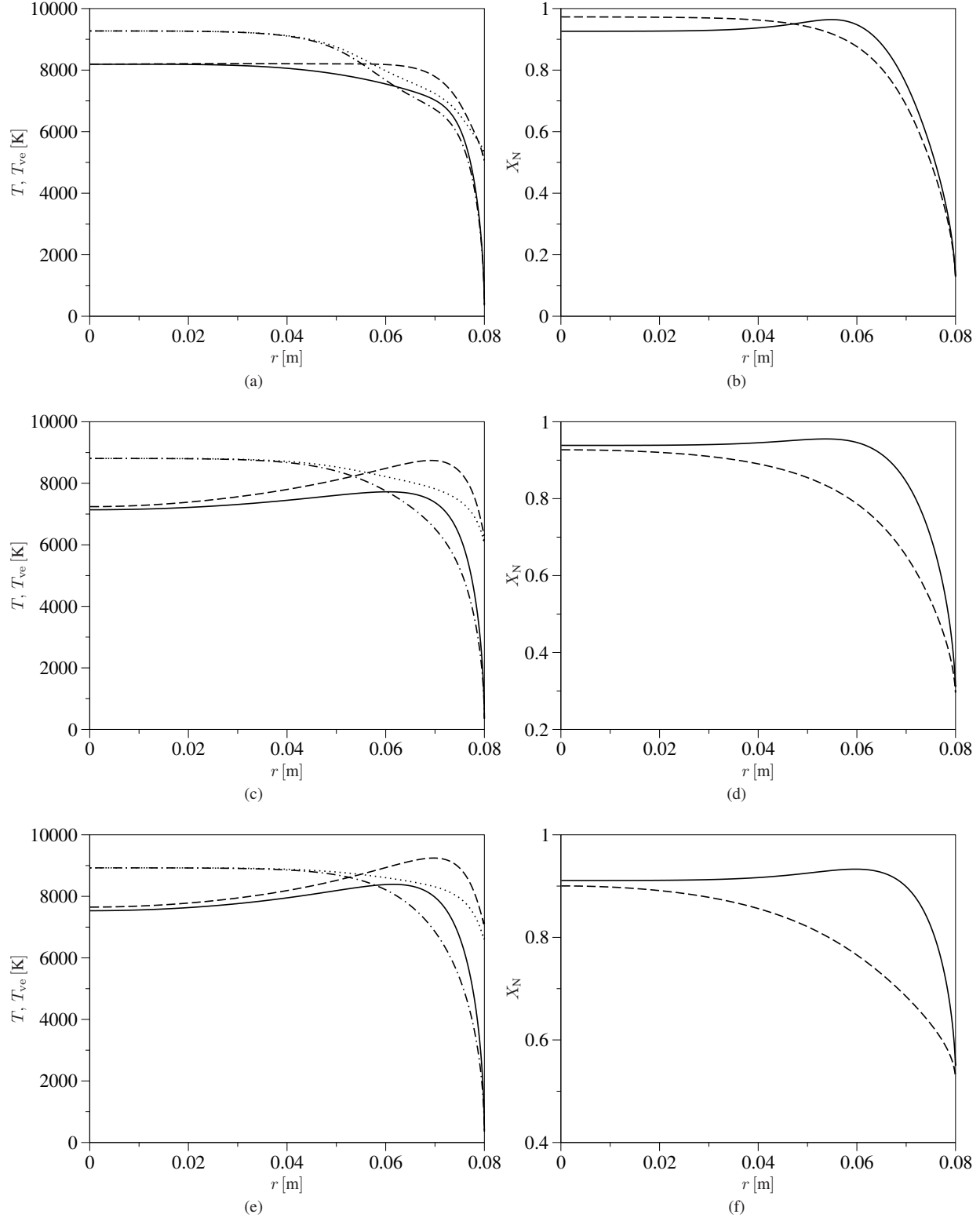
Figure 3: Comparison between the StS and MT solutions in terms of temperature (left) and N mole fraction (right) at different pressures: (a)-(b) $p = 10\,000\,\text{Pa}$, (c)-(d) $p = 5000\,\text{Pa}$, (e)-(f) $p = 3000\,\text{Pa}$ (in (a), (c) and (e) unbroken line T StS, dashed line T_{ve} StS, dotted-dashed line T MT, dotted line T_{ve} MT; in (b), (d) and (f) unbroken line StS, dashed line MT).

A-8
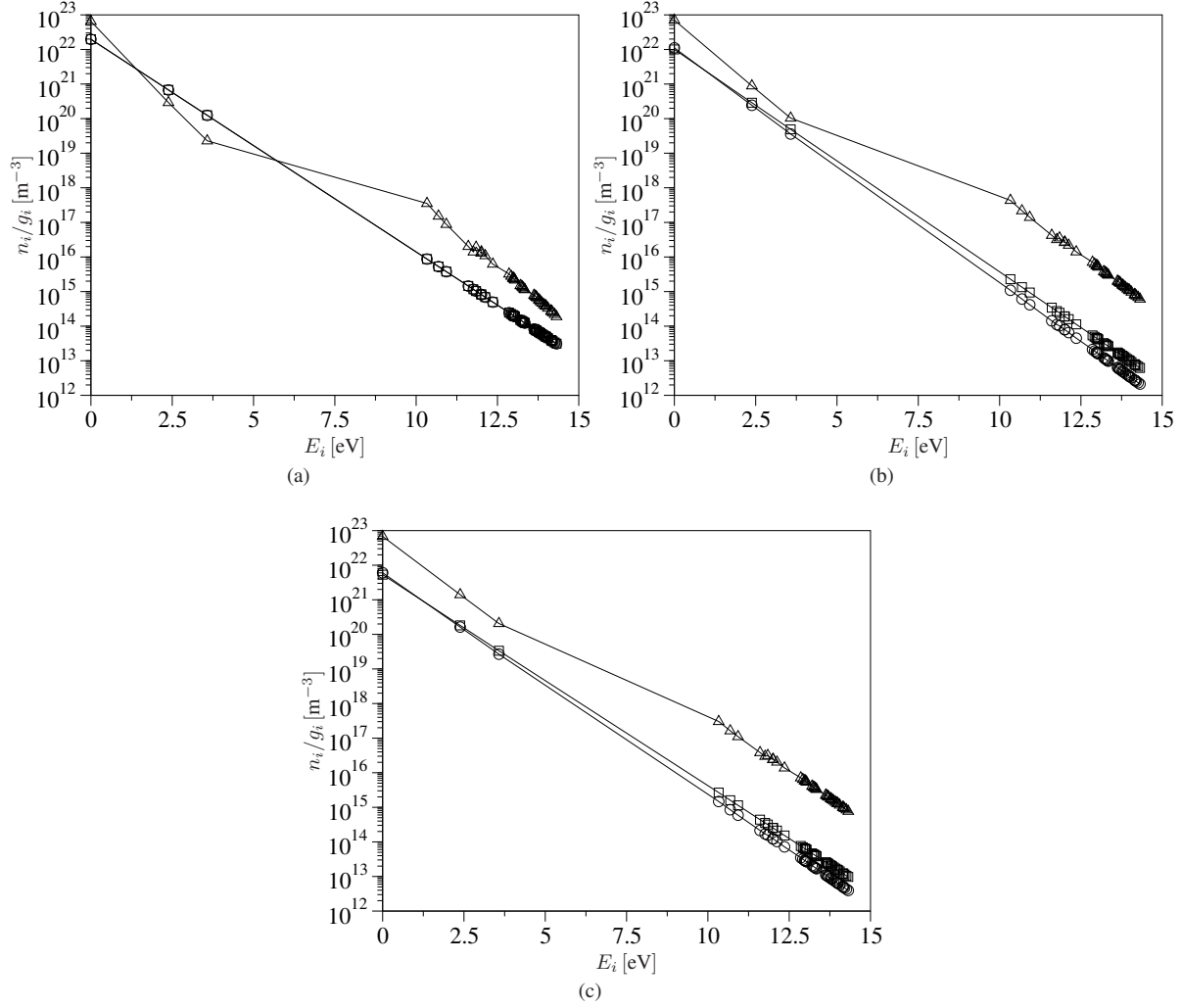
Figure 4: Normalized population of the electronic levels of N at different pressures: (a) $p = 10\,000\,\text{Pa}$, (b) $p = 5000\,\text{Pa}$, (c) $p = 3000\,\text{Pa}$ (line with circles $r = 0\,\text{m}$ [axis], line with squares $r = 0.04\,\text{m}$, line with triangles $r = 0.08\,\text{m}$ [wall]).

On the other hand the free-electron temperature increases, reaches a maximum and then decreases till reaching the value determined from the adiabatic boundary condition. The observed behavior is due to the balance between the Joule heating (which heats up the electron gas) and the energy loss in elastic and inelastic collisions, and chemical reactions. The peak location of the free-electron temperature moves towards the wall when decreasing the pressure. This is a consequence of the Joule heating distribution (not shown in Figure 3) which becomes sharper and clustered to the wall at lower pressures.

It is worth to notice that, in the StS simulation, (i) the translational-rotational temperature no longer exhibits a monotone behavior and (ii) the axis values of both temperatures are systematically lower than those predicted by the MT model. The differences observed between the StS and MT distribution have an effect, as it should be expected, on the chemical composition of the gas (see Figures 3b, 3d and 3f).

Figure 4 shows the normalized population of the electronic levels of N on the torch axis (circles), in the midpoint of the torch (squares) and at the wall (triangles) at different pressures. The population distributions exhibit significant distortions from a Boltzmann shape only close to the wall (where recombination occurs and the Joule heating is close to its maximum value). Deviations from a Boltzmann distributions are more significant when increasing the pressure due to higher recombination (see Figures 3b, 3d and 3f).

5. CONCLUSIONS

A tightly coupled magneto-hydrodynamic solver for the study of the weakly ionized plasmas found in RF discharges has been developed. A hierarchy of thermophysical models have been added to the solver to model the non-equilibrium effects in atomic and molecular plasmas. These include LTE, multi-temperature and the more so-

phisticated State-to-State models. The governing equations for the flow and electromagnetic fields have been written as a system of time-dependent conservation-laws. Steady-state solutions have been obtained by means of an implicit Finite Volume Method.

Results obtained by using a multi-temperature and State-to-State models have shown that the LTE assumption does not hold and that its use can lead to a wrong prediction of the thermo-chemical state of the gas. The analysis of the translational-rotational and free-electron temperature distributions indicated that non-equilibrium plays an important role close to the walls, due to the combined effects of Ohming heating, and chemical composition and temperature gradients. The accurate investigation of the population of excited electronic states has shown that, in view of the absence of a macroscopic gas flow, non-Boltzmann distributions are limited to a narrow region close to the torch wall.

Future work will focus on (i) including the effects of radiation and macroscopic gas flow and (ii) using more sophisticated State-to-State models to better characterize NLTE effects.

ACKNOWLEDGMENTS

REFERENCES

[1] M. I. Boulos. The inductively coupled R.F. (radio frequency) plasma. *Pure & Appl. Chem.*, 9(57): 1321–1352, 1985.

[2] J. Mostaghimi and M. I. Boulos. In *Inductively Coupled Plasma in Analytical Spectrometry*, pages 949–984, 1992.

[3] T. B. Reed. Induction coupled plasma torch. *J. Appl. Phys.*, 32(5):821–824, 1961.

[4] M. P. Freeman and J. C. Chase. Energy transfer mechanism and typical operating characteristics of the thermal rf plasma generator. *J. Appl. Phys.*, 39 (1):180–190, 1968.

[5] R. C. Miller and R. J. Ayen. Temperature profiles and energy balances for an inductively coupled plasma torch. *J. Appl. Phys.*, 40(13):5260–5273, 1969.

[6] D. C. Pridmore-Brown. Numerical study of the inductive electrodeless discharge. *J. Appl. Phys.*, 41 (4):3621–3625, 1970.

[7] H. U. Eckert. Analysis of thermal induction plasmas dominated by radial conduction losses. *J. Appl. Phys.*, 41(4):1520–1528, 1970.

[8] H. U. Eckert. Analytical treatment of radiation and conduction losses in thermal induction plasmas. *J. Appl. Phys.*, 41(4):1529–1537, 1970.

[9] H. U. Eckert. Analysis of thermal induction plasmas between coaxial cylinders. *J. Appl. Phys.*, 43(1):46–52, 1972.

[10] D. R. Keefer, J. A. Sprouse, and F. C. Loper. The electrodeless arc with radial inflow. *IEEE Trans. Plasma Sci.*, 1(4):71–75, 1973.

[11] H. U. Eckert. Two-dimensional analysis of thermal induction plasmas in finite cylinders. *J. Appl. Phys.*, 48(4):1467–1472, 1977.

[12] M. I. Boulos. Flow and temperature fields in the fire-ball of an inductively coupled plasma. *IEEE Trans. Plasma Sci.*, 1(4):28–39, 1976.

[13] R. M. Barnes and S. Nikdel. Temperature and velocity profiles and energy balances for an inductively coupled plasma discharge in nitrogen. *J. Appl. Phys.*, 47(9):3929–3934, 1977.

[14] J. Mostaghimi, P. Proulx, and M. I. Boulos. Parametric study of the flow and temperature fields in an inductively coupled r.f. plasma torch. *Plasma Chem. Plasma Process.*, 3(4):199–217, 1984.

[15] X. Chen and E. Pfender. Modeling of RF plasma torch with a metallic tube inserted for reactant injection. *Plasma Chem. Plasma Process.*, 1(11):103–128, 1991.

[16] D. Vanden Abeele and G. Degrez. Efficient computational model for inductive plasma flows. *AIAA Journal*, 38(2):234–242, 2000.

[17] D. Vanden Abeele. *An Efficient Computational Model for Inductively Coupled Air Plasma Flows Under Thermal and Chemical Non-Equilibrium*. PhD thesis, Univesité Libre de Bruxelles, Bruxelles, Belgium, 2000.

[18] J. Mostaghimi, P. Proulx, and M. I. Boulos. A two-temperature model of the inductively coupled rf plasma. *J. Appl. Phys.*, 61(5):1753–1759, 1987.

[19] J. Mostaghimi and M. I. Boulos. Effect of frequency on local thermodynamic equilibrium conditions in an inductively coupled argon plasma at atmospheric pressure. *J. Appl. Phys.*, 68(6):2643–2648, 1990.

[20] W. Zhang, A. Lani, H. B. Chew, and M. Panesi. Modeling of non-equilibrium plasmas in an inductively coupled plasma facility. AIAA Paper 2014–2235, 2014. 45th AIAA Plasmadynamics and Lasers Conference, Atlanta, GA.

[21] J.-L. Cambier and S. Moreau. Simulation of a molecular plasma in collisional-radiative nonequilibrium. AIAA Paper 1993–3196, 1993. 24th Plasmadynamics and Laser Conference, Orlando, FL.

[22] M. Capitelli, I. Armenise, D. Bruno, M. Cacciatore, R. Celiberto, G. Colonna, O. De Pascale, P. Diomede, F. Esposito, C. Gorse, K. Hassouni,

A. Laricchiuta, S. Longo, D. Pagano, D. Pietanza, and M. Rutigliano. Non-equilibrium plasma kinetics: a state-to-state approach. Plasma sources, science and technology, 2006. 8th European Sectional Conference on Atomic and Molecular Physics of Ionized Gases.

[23] A. Bultel, B. van Ootegem, A. Bourdon, and P. Vervisch. Influence of Ar_2^+ in an argon collisional-radiative model. *Phys. Rev. E*, 65(4): 046406, 2002.

[24] Y. Liu, M. Vinokur, M. Panesi, and T. E. Magin. A multi-group maximum entropy model for thermochemical nonequilibrium. AIAA Paper 2010–4332, 2010. 10th AIAA/ASME Joint Thermophysics and Heat Transfer Conference, Chicago, IL.

[25] Y. Liu, M. Panesi, M. Vinokur, and P. Clarke. Microscopic simulation and macroscopic modeling of thermal and chemical non-equilibrium gases. AIAA Paper 2013–3146, 2013. 44th AIAA Thermophysics Conference, San Diego, CA.

[26] A. Bultel, B. G. Chéron, A. Bourdon, O. Motapon, and I. F. Schneider. Collisional-radiative model in air for earth re-entry problems. *Phys. Plasmas*, 13 (4):043502, 2006.

[27] M. Panesi, T. E. Magin, A. Bourdon, A. Bultel, and O. Chazot. Fire II flight experiment analysis by means of a collisional-radiative model. *J. Thermophys. Heat Transfer*, 23(2):236–248, 2009.

[28] M. Panesi, T. E. Magin, A. Bourdon, A. Bultel, and O. Chazot. Electronic excitation of atoms and molecules for the FIRE II flight experiment. *J. Thermophys. Heat Transfer*, 25(3):361–374, 2011.

[29] A. Munafò, A. Lani, A. Bultel, and M. Panesi. Modeling of non-equilibrium phenomena in expanding flows by means of a collisional-radiative model. *Phys. Plasmas*, 20(7):073501, 2013.

[30] M. Panesi, R. L. Jaffe, D. W. Schwenke, and T. E. Magin. Rovibrational internal energy transfer and dissociation of $N(^4S_u) + N_2(^1\Sigma_g^+)$ sytem in hypersonic flows. *J. Chem. Phys*, 138(4):044312, 2013.

[31] A. Munafò, M. Panesi, and T. E. Magin. Boltzmann rovibrational collisional coarse-grained model for internal energy excitation and dissociation in hypersonic flows. *Phys. Rev. E*, 89(2):023001, 2014.

[32] M. Panesi, A. Munafò, T. E. Magin, and R. L. Jaffe. Study of the non-equilibrium shock heated nitrogen flows using a rovibrational state-to-state method. *Phys. Rev. E*, 90:013009, 2014.

[33] H. P. Le, A. P. Karagozian, and J.-L. Cambier. Complexity reduction of collisional-radiative kinetics for atomic plasma. *Phys. Plasmas*, 20(12):123304, 2013.

[34] F. Esposito and M. Capitelli. Quasi-classical molecular dynamic calculations of vibrationally and rotationally state selected dissociation cross sections: $N + N_2(v, j) \rightarrow 3N$. *Chem. Phys. Lett.*, 302(1): 49–54, 1999.

[35] F. Esposito, I. Armenise, and M. Capitelli. $N - N_2$ state-to-state vibrational relaxation and dissociation rate ceffients based on quasi-classical calculations. *Chem. Phys.*, 331(1):1–8, 2006.

[36] D. W. Schwenke. Dissociation cross-sections and rates for nitrogen. In *Non-Equilibrium Gas Dynamics - From Physical Models to Hypersonic Flights*, Lecture Series. von Karman Institute for Fluid Dynamics, 2008.

[37] R. L. Jaffe, D. W. Schwenke, G. Chaban, and W. Huo. Vibrational and rotational excitation and relaxation of nitrogen from accurate theoretical calculations. AIAA Paper 2008–1208, 2008. 46th AIAA Aerospace Sciences Meeting and Exhibit, Reno, NV.

[38] G. Chaban, R. L. Jaffe, D. W. Schwenke, and W. Huo. Dissociation cross-sections and rate coefficients for nitrogen from accurate theoretical calculations. AIAA Paper 2008–1209, 2008. 46th AIAA Aerospace Sciences Meeting and Exhibit, Reno, NV.

[39] R. L. Jaffe, D. W. Schwenke, and G. Chaban. Theoretical analysis of N_2 collisional dissociation and rotation-vibration energy transfer. AIAA Paper 2009–1569, 2009. 47th AIAA Aerospace Sciences Meeting and Exhibit, Orlando, FL.

[40] I. V. Adamovich, S. O. Macheret, J. W. Rich, and C. E. Treanor. Vibrational relaxation and dissociation behind shock waves. Part 1: kinetic rate models. *AIAA J.*, 33(6):1064–1069, 1995.

[41] I. V. Adamovich, S. O. Macheret, J. W. Rich, and C. E. Treanor. Vibrational relaxation and dissociation behind shock waves. Part 2: master equation modeling. *AIAA J.*, 33(6):1070–1075, 1995.

[42] C. Park. Assessment of two-temperature kinetic model for ionizing air. *J. Thermophys. Heat Transfer*, 3(3):233–244, 1989.

[43] C. Park. Review of chemical-kinetic problems of future NASA missions, I: Earth entries. *J. Thermophys. Heat Transfer*, 7(3):385–398, 1993.

[44] C. Park, J. T. Howe, R. L. Jaffe, and G. V. Candler. Review of chemical-kinetic problems of future NASA missions, II: Mars entries. *J. Thermophys. Heat Transfer*, 8(1):9–23, 1994.

[45] C. Park, R. L. Jaffe, and H. Partridge. Chemical-kinetic parameters of hyperbolic earth entry. *J. Thermophys. Heat Transfer*, 15(1):76–90, 2001.

[46] E. Josyula, W. F. Bailey, and S. M. Ruffin. Reactive and nonreactive vibrational energy exchanges in nonequilibrium hypersonic flows. *Phys. Fluids*, 15(10):3223, 2003.

[47] M. Panesi and A. Lani. Collisional radiative coarse-grain model for ionization in air. *Phys. Fluids*, 25 (5):057101, 2013.

[48] M. G. Kapper and J.-L. Cambier. Ionizing shocks in argon. Part I: collisional-radiative model and steady-state structure. *J. Appl. Phys.*, 109(11): 113308, 2011.

[49] M. G. Kapper and J.-L. Cambier. Ionizing shocks in argon. Part II: transient and multi-dimensional effects. *J. Appl. Phys.*, 109(11):113309, 2011.

[50] A. Munafò, M. G. Kapper, J.-L. Cambier, and T. E. Magin. Investigation of nonequilibrium effects in axisymmetric nozzle and blunt body nitrogen flows by means of a reduced rovibrational collisional model. AIAA Paper 2012–0647, 2012. 50h AIAA Aerospace Sciences Meeting including the New Horizons Forum and Aerospace Exposition, Nashville, TN.

[51] M. Mitchner and C. H. Kruger. *Partially Ionized Gases*. John Wiley & Sons, 1973.

[52] M. Capitelli, C. M. Ferreira, B. F. Gordiets, and A. I. Osipov. *Plasma Kinetics in Atmospheric Gases*. Springer, 2000.

[53] C. Park. *Nonequilibrium Hypersonic Aerothermodynamics*. Wiley, New York, NY, 1990.

[54] L. Pauling and E. B. Wilson Jr. *Introduction to Quantum Mechanics with Applications to Chemistry*. Dover Books on Physics. Dover Publications, Mineola, NY, 1985.

[55] L. V. Gurvich. *Thermodynamic Properties of Individual Substances*. CRC press, 1994.

[56] V. Giovangigli. *Multicomponent Flow Modeling*. Birkhäuser, Berlin, 1999.

[57] E. Nagnibeda and E. Kustova. *Non-Equilibrium Reacting Gas Flows*. Springer, Berlin, 2009.

[58] L. Landau and E. Teller. Theory of sound dispersion. *Phys. Z Sowjetunion*, 10(1):34–43, 1936. in German.

[59] G. V. Candler and R. W. MacCormack. Computation of weakly ionized hypersonic flows in thermochemical nonequilibrium. *J. Thermophys. Heat Transfer*, 5(3):266–273, 1991.

[60] A. Bourdon and P. Vervisch. Three-body recombination rate of atomic nitrogen in low-pressure plasma flows. *Phys. Rev. E*, 52(2):1888–1898, 1996.

[61] J. H. Ferziger and H. G. Kaper. *Mathematical Theory of Transport Processes in Gases*. North-Holland Pub. Co., 1972.

[62] R. S. Devoto. Transport properties of ionized monatomic gases. *Phys. Fluids*, 9(6):1230–1240, 1966.

[63] T. E. Magin and G. Degrez. Transport properties of partially ionized and unmagnetized plasmas. *Phys. Rev. E*, 70(4):046412, 2004.

[64] T. E. Magin and G. Degrez. Transport algorithms for partially ionized and unmagnetized plasmas. *J. Comput. Phys.*, 198(2):424–449, 2004.

[65] V. Giovangigli. Mass conservation and singular multicomponent diffusion algorithms. *IMPACT Comput. Sci. Eng.*, 2(1):73–97, 1990.

[66] C. W. Gear. *Numerical Initial-Value Problems in Ordinary Differential Equations*. Prentice-Hall, Englewood Cliffs, NJ, 1971.

[67] C. Hirsch. *Numerical Computation of Internal and External Flows*. John Wiley & Sons, New York, NY, 1990.

[68] A. Munafò and T. E. Magin. Modeling of stagnation-line nonequilibrium flows by means of quantum based collisional models. *Phys. Fluids*, 26 (9):097102, 2014.

A tightly coupled non-equilibrium magneto-hydrodynamic model for Inductively Coupled RF Plasmas

A. Munafò,[1, a)] S. A. Alfuhaid,[1, b)] J.-L. Cambier,[2, c)] and M. Panesi[1, d)]

[1)]*Department of Aerospace Engineering, University of Illinois at Urbana-Champaign, Talbot Lab., 104 S. Wright St., Urbana, 61801 IL*

[2)]*Edwards Air Force Base Research Lab., 10 E. Saturn Blvd., CA 93524*

(Dated: 7 May 2015)

The objective of the present work is the development a tightly coupled magneto-hydrodynamic model for Inductively Coupled Radio-Frequency (RF) Plasmas. Non Local Thermodynamic Equilibrium (NLTE) effects are described based on a hybrid State-to-State (StS) approach. A multi-temperature formulation is used to account for thermal non-equilibrium between translation of heavy-particles and vibration of molecules. Excited electronic states of atoms are instead treated as separate *pseudo-species*, allowing for non-Boltzmann distributions of their populations. Free-electrons are assumed Maxwellian at their own temperature. The governing equations for the electro-magnetic field and the gas properties (*e.g.* chemical composition and temperatures) are written as a coupled system of time-dependent conservation laws. Steady-state solutions are obtained by means of an implicit Finite Volume method. The results obtained in both LTE and NLTE conditions over a broad spectrum of operating conditions demonstrate the robustness of the proposed coupled numerical method. The analysis of chemical composition and temperature distributions along the torch radius shows that: (i) the use of the LTE assumption may lead to an inaccurate prediction of the thermo-chemical state of the gas, and (ii) non-equilibrium phenomena play a significant role close the walls, due to the combined effects of Ohmic heating and macroscopic gradients.

I. INTRODUCTION

Inductively Coupled Plasma (ICP) torches have wide range of possible applications which include deposition of metal coatings, synthesis of ultra-fine powders, generation of high purity silicon and testing of thermal protection materials for atmospheric entry vehicles.[1,2] In its simplest configuration, an ICP torch consists of a quartz tube surrounded by an inductor coil made of a series of parallel current-carrying rings (see Fig. 1).
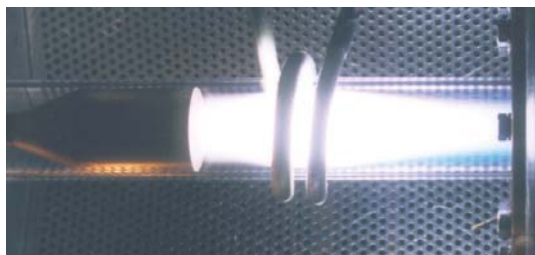
FIG. 1. Example of ICP torch in operating conditions (mini-torch facility; credits von Karman Institute for Fluid Dynamics).

The radio-frequency (RF) currents running through the inductor induce toroidal currents in the gas which

---

[a)]Electronic mail: munafo@illinois.edu
[b)]Electronic mail: alfuhai2@illinois.edu
[c)]Electronic mail: jean_luc.cambier@us.af.mil
[d)]Electronic mail: mpanesi@illinois.edu

is heated thanks to Ohmic dissipation.[2,3] If the energy supplied is large enough, the gas flowing through the torch can undergo ionization, leading to the formation of a plasma.

The physico-chemical modeling of the flow-field and electromagnetic phenomena inside an ICP torch requires, in theory, the coupled solution of the Navier-Stokes and the Maxwell equations. The numerical solution of this coupled system of partial differential equations represents a challenging task, due to the disparity between the flow and the electro-magnetic field time-scales.[4] Since in the modeling of ICP facilities one is not normally interested in resolving electro-magnetic field oscillations,[5] displacement currents can be safely neglected without introducing an appreciable error.[2,6] This leads to a more tractable formulation, as it eliminates the speed of light from the eigenvalues of the governing equations.[4]

The first attempts to model the temperature and electro-magnetic field distributions inside ICP torches were published in the 1960-1970's. Examples are the works of Freeman and Chase,[7] Keefer *et. al.*,[8] and the series of papers by Eckert.[9–12] In most of these references, the torch was approximated as an infinite solenoid and the plasma generated was considered in Local Thermodynamic Equilibrium (LTE) conditions. This reduces the problem to the coupled solution of the energy equation for the gas (known as the *Elenbaas-Heller* equation[7,13]) and an induction equation for the electric field. The induction equation is formally identical to the one describing induction heating of metals.[14,15] The authors use the heat conduction potential (*i.e.* $s = \int \kappa \, dT$), in place of the temperature T, as thermodynamic variable. This choice allows one to hide the non-linearity of the gas (total) thermal conductivity κ and can partially alle-

viate numerical instabilities that may arise when solving the discretized set of equations by means of an iterative procedure. As recognized by Pridmore and Brown,[16] the use of the heat conduction potential becomes less effective for molecular gases (*e.g.* air and nitrogen mixtures). The major developments achieved in the field of Computational Fluid Dynamics (CFD) during the 1970-1980's, led to the possibility of solving the ICP magneto-hydrodynamic equations in multi-dimensional configurations. Examples are given in the papers by Boulos,[17] Mostaghimi, Proulx Bouos and co-workers,[18–23] Kolesnikov and co-workers,[24–30] Chen and Pfender,[31] van den Abeele and Degrez[32], and more recently Panesi *et. al.*[33] and Morsli and Proulx.[34] In these works, numerical solutions are obtained using an *explicit coupling* approach, by solving independently the flow and the electric field governing equations, and updating coupling terms after each iteration. As observed by van den Abeele and Degrez,[32] the *explicit coupling* approach prevents the use of Newton's method during the first iterations and requires to resort to more conservative iterative techniques (*e.g* Picard's method[32]) at the beginning of the simulation. Convergence issues with Newton's method may also arise when solving the flow governing equations in time-dependent form. This is especially true when the current intensity in the inductor is updated to match the imposed value of the power dissipated in the plasma. The cause of the instability is most probably due to the *lagged update* of the Joule heating term in the energy equation, which is quadratic in the electric field amplitude.[17,31,32]

Most of the simulations available in the literature assume that the plasma in the torch is in LTE conditions.[17–19,31–33,35] This assumption is often justified by saying that, for the pressure values at which ICP facilities are operated (*e.g.* $\approx 10^4$ Pa and above), the collisional rate among the gas particles are sufficiently large to maintain local equilibrium. A second, and more practical reason, is the significant stiffness and CPU time reduction compared to Non-LTE (NLTE) situations. Moreover, in LTE conditions, the gas thermodynamic and transport properties are only function of two independent state variables[36] (*e.g.* pressure and temperature). Hence, they can be easily tabulated to further reduce the computational time. Simulations performed by Mostaghimi *et al.*[20,22] and by Zhang *et al.*[37] (in Argon and air plasmas, respectively) have shown, however, that the use of the LTE assumption may not always hold.

An accurate modeling of NLTE effects in ICP plasmas can be achieved by means of State-to-State (StS) models.[38–50] These treat each internal energy state as a separate *pseudo species*, thus allowing for non-Boltzmann distributions. Rate coefficients are usually obtained through quantum chemistry calculations[51–56] or through phenomenological models providing a simplified description of the kinetic process under investigation.[57,58] State-to-State models provide a superior description compared to conventional multi-temperature models, which are based on Maxwell-Boltzmann distributions.[59–62] However, due to the large number of governing equations to be solved, their application to multi-dimensional problems can become computationally demanding.[63–67]

The purpose of the present paper is development of a tightly coupled non-equilibrium model for ICP RF plasmas. To alleviate the possible occurrence of numerical instabilities, typical of an *explicit coupling* approach, the following steps are taken: (i) the flow and the induced electric field governing equations are solved in a fully coupled fashion, and (ii) steady-state solutions are obtained by means of a time-marching approach (as often done in CFD applications[68]). The governing equations are discretized in space by using the Finite Volume method. Time-integration is then performed by means of a fully implicit method. As it is shown in the paper, the time-dependent formulation introduces a *local relaxation* in the set of space-discretized equations, which enhances convergence significantly. The computational ICP framework developed in this work allows for the use of both LTE and NLTE physico-chemical models. Non-LTE effects are described based on a hybrid StS model. A multi-temperature (MT) formulation is used to account for thermal non-equilibrium between translation of heavy-particles and vibration of molecules. Excited electronic states of atoms are instead treated as separate *pseudo-species*. Free-electrons are assumed Maxwellian at their own temperature.

The paper is organized as follows. Section II describes the physical model. The numerical method for solving the governing equations is given in Sec. III. Computational results are presented in Sec. IV. Conclusions are discussed in Sec. V.

II. PHYSICAL MODELING

This section describes the physical model developed for the investigation of non-equilibrium effects in ICP RF plasmas. The non-equilibrium model for the ICP torch is built based on the torch geometry displayed in Fig. 2. To make the problem tractable, the following assumptions are introduced:

(i) Constant pressure and no *macroscopic streaming*,

(ii) Charge neutrality and no displacement current,

(iii) Steady-state conditions for gas quantities (*i.e.* $\partial()/\partial t = 0$),

(iv) No gradients along the axial and circumferential directions (*i.e.* $\partial()/\partial z = 0$, $\partial()/\partial \phi = 0$).
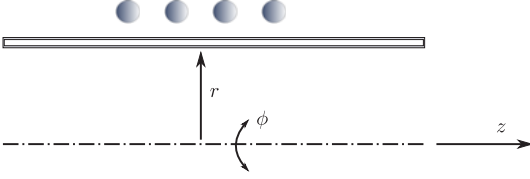
FIG. 2. Torch geometry and adopted reference frame.

A. Electro-magnetic field

The electromagnetic field inside the ICP torch is described by the Maxwell equations:

$$\nabla \cdot \mathbf{E} = \frac{\rho^{\mathrm{c}}}{\epsilon_0}, \quad \nabla \cdot \mathbf{B} = 0, \tag{1}$$

$$\nabla \times \mathbf{E} = -\frac{\partial \mathbf{B}}{\partial t}, \quad \nabla \times \mathbf{B} = \mu_0 \mathbf{J} + \mu_0 \epsilon_0 \frac{\partial \mathbf{E}}{\partial t}, \tag{2}$$

where quantities $\mathbf{E}$ and $\mathbf{B}$ are the electric and magnetic fields, respectively. Quantity ρ^{c} stands for the charge density. The current density $\mathbf{J}$ is assumed to obey Ohm's law $\mathbf{J} = \sigma_{\mathrm{e}}\mathbf{E}$, with σ_{e} being the electrical conductivity. Quantities ϵ_0 and μ_0 are the vacuum permittivity and magnetic permeability, respectively. The application of the simplifying assumptions just introduced to the Maxwell equations (1)-(2) leads to the induction equation for the induced toroidal electric field:

$$\frac{\partial}{\partial r}\left(\frac{1}{r}\frac{\partial r E_\phi}{\partial r}\right) = -\mu_0 \sigma_{\mathrm{e}} \frac{\partial E_\phi}{\partial t}. \tag{3}$$

Since the induced eddy currents which are responsible for the heating of the gas are induced by a primary current whose intensity varies sinusoidally in time, it seems natural to seek for a monochromatic wave solution, $E_\phi = E \exp(\imath \omega t)$, where $\omega = 2\pi f$ (with f being the frequency of the primary current). To account for the possible phase difference between the electric and magnetic fields, the amplitude E is taken complex, $E = E_{\mathrm{re}} + \imath E_{\mathrm{im}}$. The substitution of $E \exp(\imath \omega t)$ in Eq. (3) leads to:

$$0 \times \frac{\partial r \mathbf{U}_{\mathrm{em}}}{\partial t} + \frac{\partial r \mathbf{F}_{\mathrm{em}}}{\partial r} = r \mathbf{S}_{\mathrm{em}}. \tag{4}$$

The electromagnetic (em) conservative variable, flux and source term vectors are:

$$\mathbf{U}_{\mathrm{em}} = \begin{bmatrix} E_{\mathrm{re}} & E_{\mathrm{im}} \end{bmatrix}^{\mathrm{T}}, \tag{5}$$

$$\mathbf{F}_{\mathrm{em}} = \begin{bmatrix} \dfrac{\partial E_{\mathrm{re}}}{\partial r} & \dfrac{\partial E_{\mathrm{im}}}{\partial r} \end{bmatrix}^{\mathrm{T}}, \tag{6}$$

$$\mathbf{S}_{\mathrm{em}} = \begin{bmatrix} \dfrac{E_{\mathrm{re}}}{r^2} + \omega\mu_0\sigma_{\mathrm{e}}E_{\mathrm{im}} & \dfrac{E_{\mathrm{im}}}{r^2} - \omega\mu_0\sigma_{\mathrm{e}}E_{\mathrm{re}} \end{bmatrix}^{\mathrm{T}}. \tag{7}$$

Equation (4) must be supplemented with boundary conditions at the axis ($r = 0$) and at the torch wall ($r = R$, with R being the torch radius). On the axis, due to symmetry, both components of the electric field must vanish:

$$E_{\mathrm{re}} = 0, \quad E_{\mathrm{im}} = 0, \quad \text{at } r = 0. \tag{8}$$

The boundary condition at the torch wall is obtained as follows. The amplitudes of the toroidal electric field and the axial magnetic field are linked via:[6]

$$\frac{1}{r}\frac{\partial r E}{\partial r} = -\imath \omega B, \tag{9}$$

where the amplitude B is taken complex. Immediately outside the wall the magnetic field must be real and, since there is no plasma outside the tube, its value can only depend on the ICP operating conditions and characteristics. If the torch is long enough, the magnetic field at the torch wall can be approximated with the expression for an infinite solenoid, $B = \mu_0 N I_{\mathrm{c}}$, where quantities N and I_{c} are the number of turns per unit-length and the amplitude of the primary current. The evaluation of Eq. (9) at the torch wall and the use of the relation $B = \mu_0 N I_{\mathrm{c}}$ gives the wall boundary condition for the induced electric field:

$$\frac{1}{r}\frac{\partial r E_{\mathrm{re}}}{\partial r} = 0, \quad \frac{1}{r}\frac{\partial r E_{\mathrm{im}}}{\partial r} = -\omega\mu_0 N I_{\mathrm{c}}, \text{ at } r = R. \tag{10}$$

B. Hydro-dynamics

The gas contained in the torch is made of electrons, atoms and molecules. Charged particles comprise electrons and positively singly charged ions. The set $\mathcal{S}$ stores the chemical components, and the heavy-particles are stored in the set $\mathcal{S}_{\mathrm{h}}$. The atomic and molecular components are stored in the sets $\mathcal{S}_{\mathrm{a}}$ and $\mathcal{S}_{\mathrm{m}}$, respectively. The previously introduced sets satisfy the relations $\mathcal{S}_{\mathrm{h}} = \mathcal{S}_{\mathrm{a}} \cup \mathcal{S}_{\mathrm{m}}$ and $\mathcal{S} = \{\mathrm{e}^-\} \cup \mathcal{S}_{\mathrm{h}}$, where the symbol e^- indicates the free-electrons. The electronic levels of the heavy components are stored in sets $\mathcal{I}_s^{\mathrm{el}}$ (with $s \in \mathcal{S}_{\mathrm{h}}$) and are treated as separate *pseudo species* based on a StS approach.[69] The notation s_i is used to denote the i-th electronic level of the heavy component $s \in \mathcal{S}_{\mathrm{h}}$, with the related degeneracy and energy being $g_{s_i}^{\mathrm{el}}$ and $E_{s_i}^{\mathrm{el}}$, respectively. A multi-temperature model is instead used for vibration of molecules and translation of free-electrons (with the related temperatures being T_{v} and T_{e}, respectively).[60] Rotational non-equilibrium effects are disregarded.

Thermodynamic properties

The gas pressure is computed as $p = p_{\mathrm{e}} + p_{\mathrm{h}}$, where the symbol k_{B} stands for Boltzmann's constant. The partial pressures of free-electrons and heavy-particles are, respectively, $p_{\mathrm{e}} = n_{\mathrm{e}}k_{\mathrm{B}}T_{\mathrm{e}}$ and $p_{\mathrm{h}} = n_{\mathrm{h}}k_{\mathrm{B}}T$, where quantities n_{e} and n_{h} denote, respectively, the related the number densities (with $n_{\mathrm{h}} = \sum_{s \in \mathcal{S}_h} n_s$ and $n_s = \sum_{i \in \mathcal{I}_s^{\mathrm{el}}} n_{s_i}$). The gas total, rotational, vibrational and free-electron energy densities are:

$$\rho e = \frac{3}{2}p + \rho e_{\mathrm{r}} + \rho e_{\mathrm{v}} + \sum_{s \in \mathcal{S}_{\mathrm{h}}} \sum_{i \in \mathcal{I}_s^{\mathrm{el}}} n_{s_i}(E_{s_i}^{\mathrm{el}} + \Delta E_s^{\mathrm{f}}) \tag{11}$$

$$\rho e_{\mathrm{r}} = \sum_{s \in \mathcal{S}_{\mathrm{m}}} n_s \tilde{E}_s^{\mathrm{r}}(T), \quad \rho e_{\mathrm{v}} = \sum_{s \in \mathcal{S}_{\mathrm{m}}} n_s \tilde{E}_s^{\mathrm{v}}(T_{\mathrm{v}}), \quad \rho e_{\mathrm{e}} = \frac{3}{2} p_{\mathrm{e}}. \tag{12}$$

Quantity ΔE_s^{f} stands for the formation energy (per particle) of the heavy component $s \in \mathcal{S}_{\mathrm{h}}$. The average particle rotational and vibrational energies ($\tilde{E}_s^{\mathrm{r}}$ and $\tilde{E}_s^{\mathrm{v}}$, $s \in \mathcal{S}_{\mathrm{m}}$,respectively) are computed, respectively, according to the rigid-rotor and harmonic-oscillator models[70]. Thermodynamic data used in this work are taken from Gurvich tables[71] (with the exception of the spectroscopic data for the electronic levels taken from Ref. 43).

Chemical-kinetics

The NLTE kinetic mechanism for ICP RF plasmas developed in this work accounts for:

(i) Excitation by electron impact,

(ii) Ionization by electron impact,

(iii) Dissociation by electron impact,

(iv) Dissociation by heavy-particle impact,

(v) Associative ionization.

The endothermic rate coefficients for electron induced processes and associative ionization reactions are taken from the ABBA StS model.[43–46] Those for dissociation by heavy-particle impact are taken from the work of Park.[60] Reverse rate coefficients are obtained based on micro-reversibility.[72,73]

The mass production terms for free-electrons and heavy-particles are computed based on the zeroth-order reaction rate theory.[72,73] In what follows, the latter quantities are indicated with the notation ω_{e} and ω_{s_i}, respectively

The energy transfer terms for the gas vibrational energy account for (i) vibrational-translational (vt) energy exchange in molecule heavy-particle collisions, (ii) vibrational-electron (ve) energy exchange in molecule electron collisions, and (iii) the creation/destruction of vibrational energy in chemical reactions (cv). The first two energy transfer terms (indicated in what follows with Ω_{vt} and Ω_{ve}, respectively) are evaluated based on a Landau-Teller model,[74] while the chemistry-vibration coupling term (Ω_{cv}) is computed by using the non-preferential dissociation model of Candler.[75] The relaxation times for vt energy transfer are computed by means of the modified formula of Millikan and White proposed by Park.[60] The energy transfer in molecule-electron inelastic collisions is considered only for N_2. The corresponding relaxation time is taken from the work of Bourdon.[76] The energy transfer terms for the free-electron gas account for energy exchange undergone by free-electrons in (i) elastic collisions with heavy-particles (Ω_{el}), (ii) inelastic electron induced excitation, ionization and dissociation processes (Ω_{in}) and (iii) Joule heating (Ω_{j}). The expressions for the first two can be

found in Refs. 44–46. The (time-averaged) Joule heating source term is obtained by averaging over a period the instantaneous Joule heating power and reads $\Omega_{\mathrm{j}} = \sigma_{\mathrm{e}}(E_{\mathrm{re}}^2 + E_{\mathrm{im}}^2)/2$.[31,32]

Transport properties and fluxes

Transport phenomena are treated based on the results of the Chapman-Enskog method for the Boltzmann equation[77] under the assumption that: (i) inelastic and reactive collisions have a no effect on the transport properties and fluxes and (ii) the collision cross-sections for elastic scattering do not depend on the internal quantum states.

The translational component of thermal conductivity is $\lambda_{\mathrm{t}} = \sum_{s \in \mathcal{S}_{\mathrm{h}}} \alpha_s^{\lambda} X_s$, where the mole fractions of the heavy components are $X_s = n_s k_{\mathrm{B}} T / p$ ($s \in \mathcal{S}_{\mathrm{h}}$). The coefficients α_s^{λ} are solution of the linear (symmetric) transport system for the translational thermal conductivity (see, for instance, Ref. 72 for the details). The contributions of the gas rotational and vibrational degrees of freedom to the thermal conductivity (λ_{r} and λ_{v}, respectively) are taken into account by means of the generalized Eucken's correction.[72] The thermal and electrical conductivity of the electron gas are:[78,79]

$$\lambda_{\mathrm{e}} = \frac{75}{8} k_{\mathrm{B}} \sqrt{\frac{2\pi k_{\mathrm{B}} T_{\mathrm{e}}}{m_{\mathrm{e}}}} \frac{X_{\mathrm{e}} \Lambda_{\mathrm{ee}}^{22}}{\Lambda_{\mathrm{ee}}^{11} \Lambda_{\mathrm{ee}}^{22} - (\Lambda_{\mathrm{ee}}^{12})^2}, \tag{13}$$

$$\sigma_{\mathrm{e}} = \frac{3}{2} \frac{e^2}{k_{\mathrm{B}}} \sqrt{\frac{2\pi k_{\mathrm{B}}}{m_{\mathrm{e}} T_{\mathrm{e}}}} \frac{X_{\mathrm{e}} \Lambda_{\mathrm{ee}}^{11}}{\Lambda_{\mathrm{ee}}^{00} \Lambda_{\mathrm{ee}}^{11} - (\Lambda_{\mathrm{ee}}^{10})^2}, \tag{14}$$

where the mole fraction of free-electrons is $X_{\mathrm{e}} = n_{\mathrm{e}} k_{\mathrm{B}} T_{\mathrm{e}}/p$ and e $= 1.602 \times 10^{-19}$ C is the electron charge. Quantities $\Lambda_{\mathrm{ee}}^{ij}$ denote the Devoto collision integrals.[78]

The mass diffusion fluxes are found by solving the Stefan-Maxwell equations under the constraints of global mass conservation and ambipolar diffusion.[78–81] The diffusion driving forces include only mole fraction gradients. In view of the assumed independence of the elastic collision cross-section on the internal quantum states, the Stefan-Maxwell equations are solved for the diffusion fluxes of chemical components (J_{e} and J_s, $s \in \mathcal{S}_{\mathrm{h}}$, respectively). The mass diffusion fluxes for the internal levels (J_{s_i}), are then found as shown in Ref. 6. The gas total, rotational, vibrational and free-electron heat flux are:

$$q = \sum_{s \in \mathcal{S}_{\mathrm{h}}} \sum_{i \in \mathcal{I}_s^{\mathrm{el}}} \left(\frac{5}{2} k_{\mathrm{B}} T + E_{s_i}^{\mathrm{el}} + \Delta E_s^{\mathrm{f}} \right) \frac{J_{s_i}}{m_s} - \lambda_{\mathrm{t}} \frac{\partial T}{\partial r} + q_{\mathrm{r}} + q_{\mathrm{v}} + q_{\mathrm{e}}, \tag{15}$$

$$q_{\mathrm{r}} = \sum_{s \in \mathcal{S}_{\mathrm{m}}} \tilde{E}_s^{\mathrm{r}}(T) \frac{J_s}{m_s} - \lambda_{\mathrm{r}} \frac{\partial T}{\partial r}, \tag{16}$$

$$q_{\mathrm{v}} = \sum_{s \in \mathcal{S}_{\mathrm{m}}} \tilde{E}_s^{\mathrm{v}}(T_{\mathrm{v}}) \frac{J_s}{m_s} - \lambda_{\mathrm{v}} \frac{\partial T_{\mathrm{v}}}{\partial r}, \tag{17}$$

$$q_{\mathrm{e}} = \left(\frac{5}{2} k_{\mathrm{B}} T_{\mathrm{e}} \right) \frac{J_{\mathrm{e}}}{m_{\mathrm{e}}} - \lambda_{\mathrm{e}} \frac{\partial T_{\mathrm{e}}}{\partial r}. \tag{18}$$

Governing equations

The governing equations for the gas chemical composition and temperature distribution in the ICP torch are:

$$\frac{\partial r\mathbf{U}_{\mathrm{g}}}{\partial t} + \frac{\partial r\mathbf{F}_{\mathrm{g}}}{\partial r} = r\mathbf{S}_{\mathrm{g}}. \qquad (19)$$

The gas (g) conservative variable, flux and source term vectors are:

$$\mathbf{U}_{\mathrm{g}} = \begin{bmatrix} \rho_{\mathrm{e}} & \rho_{s_i} & \rho e & \rho e_{\mathrm{v}} & \rho e_{\mathrm{e}} \end{bmatrix}^{\mathrm{T}}, \qquad (20)$$

$$\mathbf{F}_{\mathrm{g}} = \begin{bmatrix} J_{\mathrm{e}} & J_{s_i} & q & q_{\mathrm{v}} & q_{\mathrm{e}} \end{bmatrix}^{\mathrm{T}}, \qquad (21)$$

$$\mathbf{S}_{\mathrm{g}} = \begin{bmatrix} \omega_{\mathrm{e}} & \omega_{s_i} & \Omega_{\mathrm{j}} & \Omega_{\mathrm{v}} & \Omega_{\mathrm{e}} \end{bmatrix}^{\mathrm{T}}, \qquad (22)$$

$i \in \mathcal{I}_s^{\mathrm{el}}$, $s \in \mathcal{S}_{\mathrm{h}}$, with $\Omega_{\mathrm{v}} = \Omega_{\mathrm{vt}} + \Omega_{\mathrm{ve}} + \Omega_{\mathrm{cv}}$ and $\Omega_{\mathrm{e}} = \Omega_{\mathrm{el}} + \Omega_{\mathrm{in}} + \Omega_{\mathrm{j}}$.

The boundary conditions used for solving Eq. (19) are a symmetry boundary condition at the axis and an isothermal non-catalytic boundary condition at the torch wall. Following the work of Mostaghimi *et al.*,[20,22] an adiabatic wall boundary condition is used for the vibrational and free-electron temperatures.

III. NUMERICAL METHOD

The governing equations for the gas and the electromagnetic fields are strongly coupled due to the presence of the Joule heating term in Eq. (22) and the electrical conductivity in Eq. (7). This suggests to adopt a fully coupled approach by casting Eqs. (4) and (19):

$$\frac{\partial r\mathbf{\Gamma U}}{\partial t} + \frac{\partial r\mathbf{F}}{\partial r} = r\mathbf{S}, \qquad (23)$$

where the conservative variable, flux and source term vectors are now $\mathbf{U} = (\mathbf{U}_{\mathrm{g}}, \mathbf{U}_{\mathrm{em}})$, $\mathbf{F} = (\mathbf{F}_{\mathrm{g}}, \mathbf{F}_{\mathrm{em}})$ and $\mathbf{S} = (\mathbf{S}_{\mathrm{g}}, \mathbf{S}_{\mathrm{em}})$, respectively. The matrix $\mathbf{\Gamma}$ in Eq. (23) reads:

$$\mathbf{\Gamma} = \begin{pmatrix} \mathbf{I}_{(\mathrm{ns+nt})\times(\mathrm{ns+nt})} & \mathbf{0}_{(\mathrm{ns+nt})\times 2} \\ \mathbf{0}_{2\times(\mathrm{ns+nt})} & \mathbf{0}_{2\times 2} \end{pmatrix}, \qquad (24)$$

where quantities $\mathbf{I}$ and $\mathbf{0}$ are, respectively, the identity and null matrices. Their number of rows and columns are indicated by the first and second lower-scripts, respectively. The symbols ns and nt denote, respectively, the number of species and temperatures.

Spatial discretization

The application of the Finite Volume method to Eq. (23) leads to the following ODE governing the time-evolution of the conservative variables of cell j:[68]

$$\mathbf{\Gamma}\frac{\partial \mathbf{U}_j}{\partial t}r_j\Delta r_j = -\mathbf{Res}_j. \qquad (25)$$

The right-hand-side residual reads:

$$\mathbf{Res}_j = r_{j+\frac{1}{2}}\mathbf{F}_{j+\frac{1}{2}} - r_{j-\frac{1}{2}}\mathbf{F}_{j-\frac{1}{2}} - \mathbf{S}_j\, r_j\,\Delta r_j, \qquad (26)$$

where the cell volume (length) and its centroid location are computed as $\Delta r_j = r_{j+1/2} - r_{j-1/2}$ and $r_j = (r_{j+1/2} + r_{j-1/2})/2$, respectively. The evaluation of the diffusive flux $\mathbf{F}_{j+1/2}$ is performed by approximating the values and the gradients of a given quantity p (*e.g.* temperatures and electric field components) by means of an arithmetic average and a second order central finite difference, respectively. To facilitate the implementation of the constant pressure constraint, the solution update is performed on primitive variables ($\mathbf{P}$) consisting of mass fractions, temperatures and electric field components, $\mathbf{P} = (y_{\mathrm{e}}, y_{s_i}, T, T_{\mathrm{v}}, T_{\mathrm{e}}, E_{\mathrm{re}}, E_{\mathrm{im}})$:

$$\mathbf{\Gamma T}_j\frac{\partial \mathbf{P}_j}{\partial t}r_j\Delta r_c = -\mathbf{Res}_j. \qquad (27)$$

The transformation matrix $\mathbf{T}$ can be obtained from the time-derivative of the conservative variables ($\partial \mathbf{U}/\partial t$) by exploiting the global continuity equation, $\partial \rho/\partial t = 0$.

A. Temporal discretization

Equation (27) is integrated in time by means of the backward Euler method:[68]

$$\mathbf{\Gamma T}_j^n\frac{\delta \mathbf{P}_j^n}{\Delta t_j}r_j\Delta r_j = -\mathbf{Res}_j^{n+1}, \qquad (28)$$

where $\delta \mathbf{P}_j^n = \mathbf{P}_j^{n+1} - \mathbf{P}_j^n$. The local time-step Δt is computed based on the von Neumann number (ξ) as $\Delta t = \xi/(2\rho^{\mathrm{d}})$, where quantity ρ^{d} stands for the spectral radius of the diffusive flux Jacobian matrix $\partial \mathbf{F}/\partial \mathbf{U}$.[68] To advance the solution from the time-level n to the time-level $n + 1$, Eq. (28) is linearized around the time-level n. The outcome of the linearization is a block-tridiagonal algebraic system to be solved at each time-step:[68,82]

$$\mathbf{L}_j^n\,\delta \mathbf{P}_{j-1}^n + \mathbf{C}_j^n\,\delta \mathbf{P}_j^n + \mathbf{R}_j^n\,\delta \mathbf{P}_{j+1}^n = -\mathbf{Res}_j^n, \qquad (29)$$

where the left, right and central block matrices are:

$$\mathbf{L}_j = \frac{2\,r_{j-1/2}}{\Delta r_j + \Delta r_{j-1}}\mathbf{A}_{j-\frac{1}{2}}, \qquad (30)$$

$$\mathbf{R}_j = \frac{2\,r_{j+1/2}}{\Delta r_j + \Delta r_{j+1}}\mathbf{A}_{j+\frac{1}{2}}, \qquad (31)$$

$$\mathbf{C}_j = \left[\frac{\mathbf{\Gamma T}_j}{\Delta t_j} - \left(\frac{\partial \mathbf{S}}{\partial \mathbf{P}}\right)_j\right]r_j\Delta r_j - (\mathbf{L}_j + \mathbf{R}_j), \quad (32)$$

where quantity $\mathbf{A}$ stands for the (primitive) diffusive flux Jacobian matrix, $\mathbf{A} = \partial \mathbf{F}/\partial \mathbf{P}$. The block-tridiagonal system (29) is solved by means of Thomas' algorithm[68] and the solution updated at the next time-level, $\mathbf{P}_j^{n+1} = \mathbf{P}_j^n + \delta \mathbf{P}_j^n$. This process is continued until steady-state is reached.

Notice that the discretized time derivative in Eq. (32) plays the role of a *relaxation term.* Setting this term to zero (*i.e.* infinite time-step) is equivalent to solve the steady-state form of the governing equations (23) by means of Newton's method. Preliminary calculations performed in LTE conditions indicated that this strategy can easily lead to numerical instability problems in the initial transient of the simulation.

IV. APPLICATIONS

The gas contained in torch consists of molecular nitrogen and the related dissociation and ionization products, $\mathcal{S} = \{e^-, N, N_2, N_2^+, N^+\}$. Simulations have been performed by means of the ABBA StS model[43–46] and the MT model developed by Park.[60]

The torch radius, the number of coils per unit-length and the wall temperature are set to 0.08 m, 50, and 350 K, respectively. The current intensity of the primary circuit is found from the solution by imposing that the dissipated power (per unit-length) in the plasma:

$$P = 2\pi \int_0^R \Omega_j \, r \, dr, \qquad (33)$$

is equal to a fixed value P_0. To match the condition $P = P_0$ at steady-state, the current intensity is multiplied by the scaling factor $\gamma = \sqrt{P_0/P}$ after updating the solution at the new time-step. This approach was originally introduced by Boulos[17] in the 1970's, and it has been used since then by other investigators.[18,31–33,37] In the present work, no scaling is applied to the electric field (as opposed to *explicit coupling* methods[32]), due to the use of a fully coupled formulation.

In order to assess the influence of the ICP operating conditions on non-equilibrium effects, different values of pressure, frequency of the primary circuit and dissipated power have been adopted (see Table I).

TABLE I. Adopted values for the pressure, frequency of the primary circuit and dissipated power (per unit-length) in the plasma.

Quantity	Units	Values
Pressure (p)	Pa	3000, 5000 and 10 000
Frequency (f)	MHz	0.1, 0.5, 1 and 2.5
Dissipated power (P_0)	MW/m	0.2, 0.3, 0.35 and 0.4

A. Performance of the coupled numerical formulation

The coupled numerical method developed in Sect. III has been applied over a wide spectrum of operating conditions (given in Table I) in both LTE and NLTE conditions. In all cases treated in this work, no need arose for the use of techniques to cope with numerical instabilities such as under-relaxation factors, conservative iterative strategies (*e.g.* Picard's method) or choice of a *smart* initial guess for the solution.

To demonstrate in practice the robustness and the effectiveness of the proposed computational method, a MT NLTE simulation has been chosen as working example. The operating conditions are: $p = 10\,000$ Pa, $f = 0.5$ MHz and $P_0 = 0.35$ MW/m. For the sake of simplicity, an isothermal wall boundary conditions has been used for all temperatures. The solution has been initialized with a uniform equilibrium distribution at 7500 K, with both the real and imaginary electric field components set to 0.1 V/m. The initial value of the current intensity was 250 A.

(a)

(b)
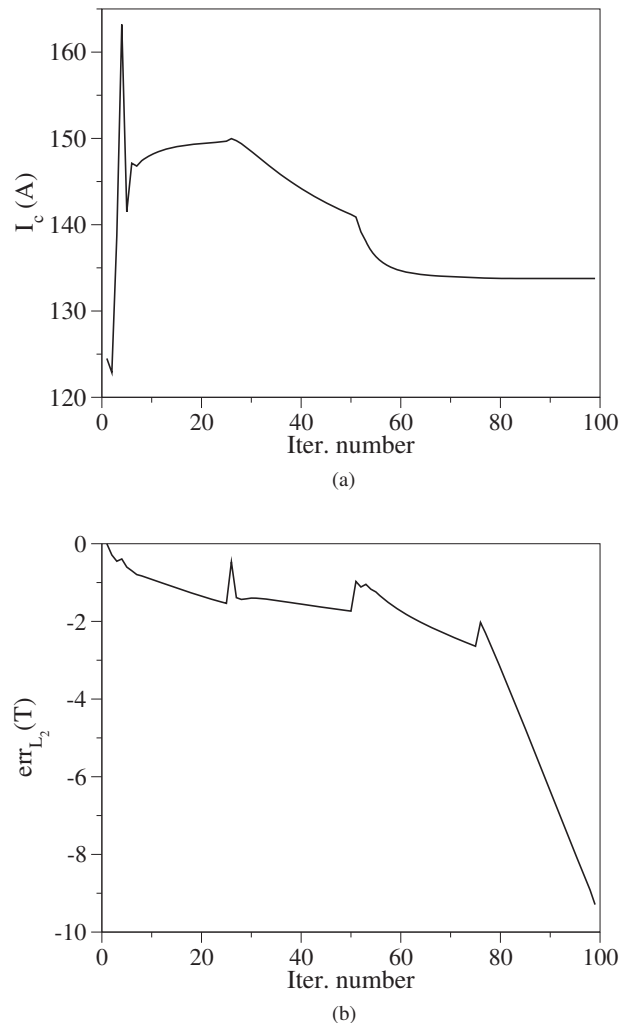
FIG. 3. Time-history of (a) current intensity and (b) normalized L_2 norm of the relative error on the translational-rotational temperature for the MT NLTE model ($p = 10\,000$ Pa, $f = 0.5$ MHz, $P_0 = 0.35$ MW/m; isothermal boundary condition for all temperatures).

In the early stages of the numerical simulation, strong gradients in temperature and chemical composition form in correspondence of the wall, due to the isothermal

boundary condition imposed. Despite the challenges imposed by the problem, the initial value of the von Neuman number was set to to 1×10^5, and increased interactively (every 25 iterations) up to 5×10^8. Such large values were possible due to the adoption of a fully implicit time-integration method. Figure 3 shows the time-history of the current intensity and the L_2 norm of the relative error on the translational-rotational temperature:

$$\mathrm{err}_{L_2}^n(T) = \sqrt{\frac{1}{\mathrm{nc}} \sum_{j=1}^{\mathrm{nc}} (\delta T_j^n)^2}, \qquad (34)$$

where quantity nc denotes the number of cells, and $\delta T_j^n = T_j^{n+1} - T_j^n$. A converged solution is achieved in less than 100 iterations (see Fig. 3(b)), with a reduction of more than nine orders of magnitude in the relative error for the temperature. In practice, the solution is already converged after 80 iterations, as can be observed from the current intensity time-history (see Fig. 3(a)).

Figure 4 shows the temperature distribution along the torch radius. Due to the efficient energy exchange in N_2-e^- interactions,[60,76,83] the vibrational and free-electron temperature profiles are essentially indistinguishable. This feature has been observed in all NLTE simulations performed. This is the reason for the use of the notation T_{ve} in Fig. 4 (and also in what follows).
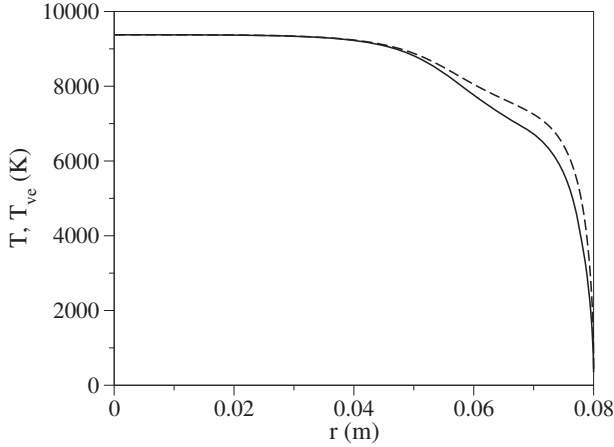
FIG. 4. MT NLTE temperature distribution ($p = 10\,000\,\mathrm{Pa}$, $f = 0.5\,\mathrm{MHz}$, $P_0 = 0.35\,\mathrm{MW/m}$; unbroken line T, dashed-line T_{ve}; isothermal boundary condition for all temperatures).

B. Assessment of non-equilibrium effects

Before discussing in detail NLTE effects, LTE simulations have been performed and compared with the MT NLTE results to assess the extent of the departure from equilibrium. The pressure is set to 10000Pa as, for this relatively high value, LTE conditions are often assumed.[6] The frequency and the dissipated power are 0.5 MHz and 0.35 MW/m, respectively.
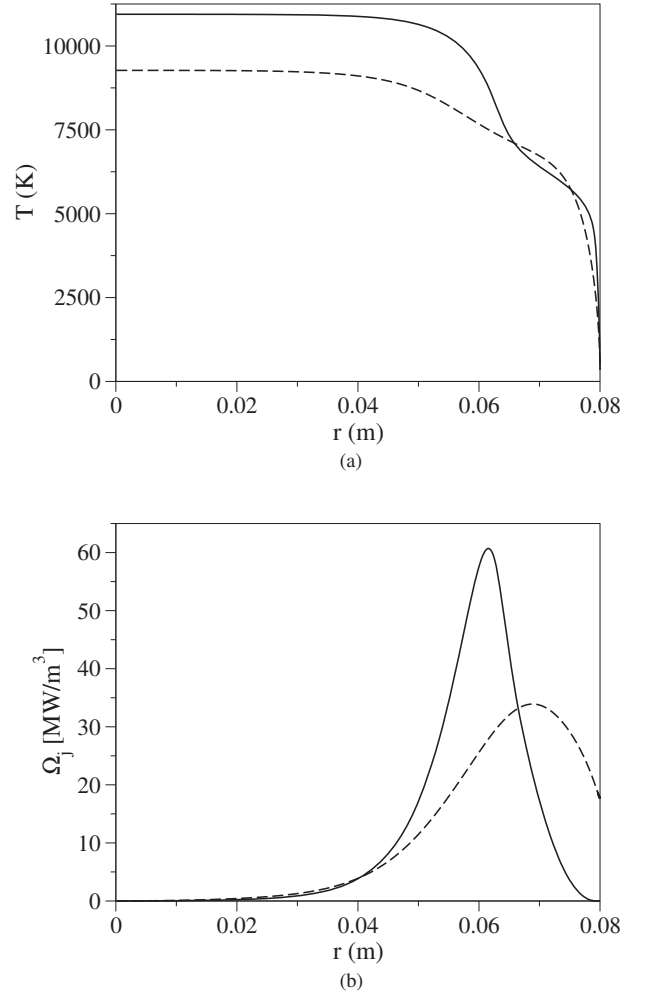
FIG. 5. Comparison between the LTE and the MT NLTE temperature (a) and Joule heating (b) distributions ($p = 10\,000\,\mathrm{Pa}$, $f = 0.5\,\mathrm{MHz}$, $P_0 = 0.35\,\mathrm{MW/m}$; unbroken line LTE, dashed line NLTE).

Figure 5 compares the LTE and NLTE translational-rotational temperature and Joule heating distributions. Close to the wall, the curvature of the LTE temperature distribution changes sign. This is a consequence of the non-monotone behavior of the equilibrium total thermal conductivity of the working gas (nitrogen). The same trend is also found for the MT solution, though less pronounced. The MT model predicts that the gas is in thermal equilibrium close to the axis (see Fig. 4). In both the LTE and NLTE simulations, the temperature is maximum on the axis, due to the absence of radiative losses in the plasma.[9,10] Overall, the LTE solution predicts higher temperature values, with the difference being maximum on the axis. This is a general trend observed in all the simulations performed in this work (and also in the multi-dimensional results obtained by other investigators in Refs. 6 and 37). In NLTE conditions, the temperature is lower because the plasma is heated over a wider region compared to LTE conditions. This is confirmed by the

Joule heating distribution shown in Fig. 5(c). Analogous conclusions can be drawn when comparing with the StS NLTE model adopted in this work.

The results in Fig. 5 demonstrate that, even at relatively high pressures, the LTE assumption can lead to a severe overestimation of the gas temperature and, in general, to an inaccurate prediction of the thermo-chemical state of the gas. This is further confirmed by the comparison for the mole fractions given in Fig. 6. It is worth recalling that in the present work, the effects of macroscopic flows (which enhance non-equilibrium) are neglected.
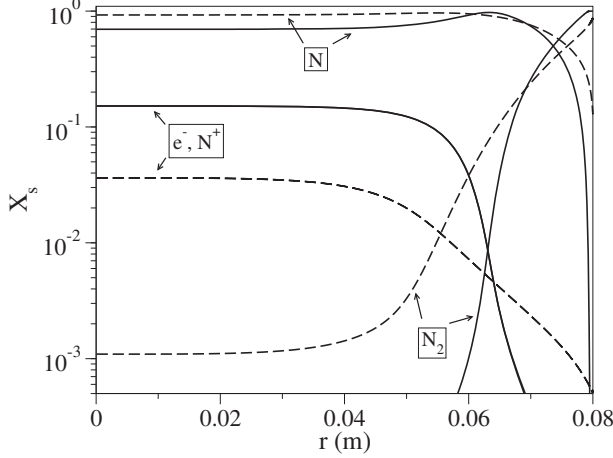

FIG. 6. Comparison between the LTE and the MT NLTE mole fraction distributions ($p = 10\,000\,\text{Pa}$, $f = 0.5\,\text{MHz}$, $P_0 = 0.35\,\text{MW/m}$; unbroken line LTE, dashed line NLTE). Due to the low concentration of N_2^+ (not shown), the mole fractions of e^- and N^+ are essentially indistinguishable in both LTE and NLTE conditions.

C. Influence of frequency and power on non-equilibrium

In order to assess the influence of operating conditions on non-equilibrium phenomena, it was decided to perform a parametric study on the frequency of the primary circuit and the power dissipated in the plasma. Figures 7-8 show the results of this investigation for the MT NLTE model at $p = 5000\,\text{Pa}$. Increasing the frequency (Fig. 7) has the effect of narrowing the extent of the *skin-depth*, which is the zone over which most of the power is dissipated by Ohmic heating. This can be seen from the relation for the *skin-depth*[14,15], $\delta = (\sigma_e \pi \mu_0 f)^{-1/2}$. The reduction of the *skin-depth* induces sharper gradients close to the wall, thereby enhancing non-equilibrium. These findings are in accordance with the observations reported by Mostaghimi *et al.*[22] for NLTE Argon plasmas. The increase of the dissipated power (Fig. 8) has an opposite effect. As can be observed from the results, higher power levels favor the establishment of thermal equilibrium conditions.
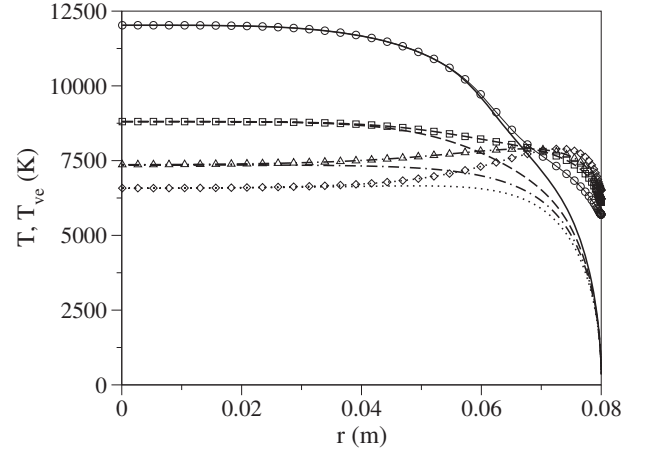
FIG. 7. MT NLTE temperature distributions for different values of the frequency of the primary circuit: unbroken line $f = 0.1\,\text{MHz}$, dashed line $f = 0.5\,\text{MHz}$, dotted-dashed line $f = 1\,\text{MHz}$, dotted line $f = 2.5\,\text{MHz}$ ($p = 5000\,\text{Pa}$, $P_0 = 0.35\,\text{MW/m}$; unbroken line T, line with symbols T_{ve}).
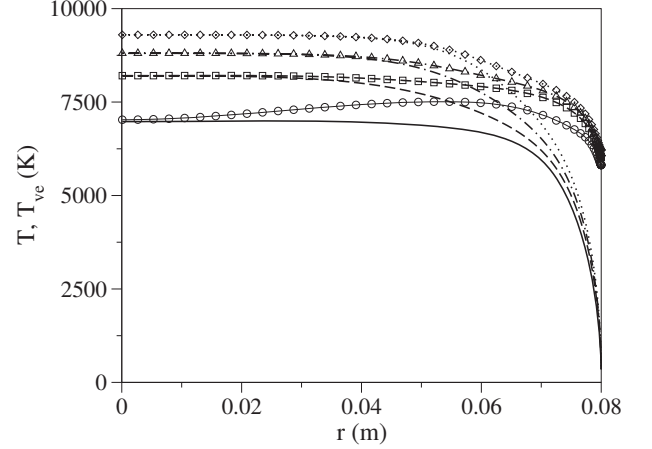
FIG. 8. MT NLTE temperature distributions for different values of the dissipated power (per unit-length) in the plasma: unbroken line $P_0 = 0.2\,\text{MW/m}$, dashed line $P_0 = 0.3\,\text{MW/m}$, dotted-dashed line $P_0 = 0.35\,\text{MW/m}$, dotted line $P_0 = 0.4\,\text{MW/m}$ ($p = 5000\,\text{Pa}$, $f = 0.5\,\text{MHz}$; unbroken line T, line with symbols T_{ve}).

D. Comparison between the StS and the MT predictions

This section compares the predictions obtained by the StS and MT NLTE models. Figure 9 shows the comparison in terms of temperatures and N mole fraction. For both the StS and MT solutions, decreasing the pressure has the effect of enhancing thermal non-equilibrium. In the case of the MT model, the translational-rotational temperature is maximum on the axis and decreases monotonically when approaching the wall.

On the other hand the free-electron temperature increases, reaches a maximum and then decreases until it reaches the value determined from the adiabatic bound-
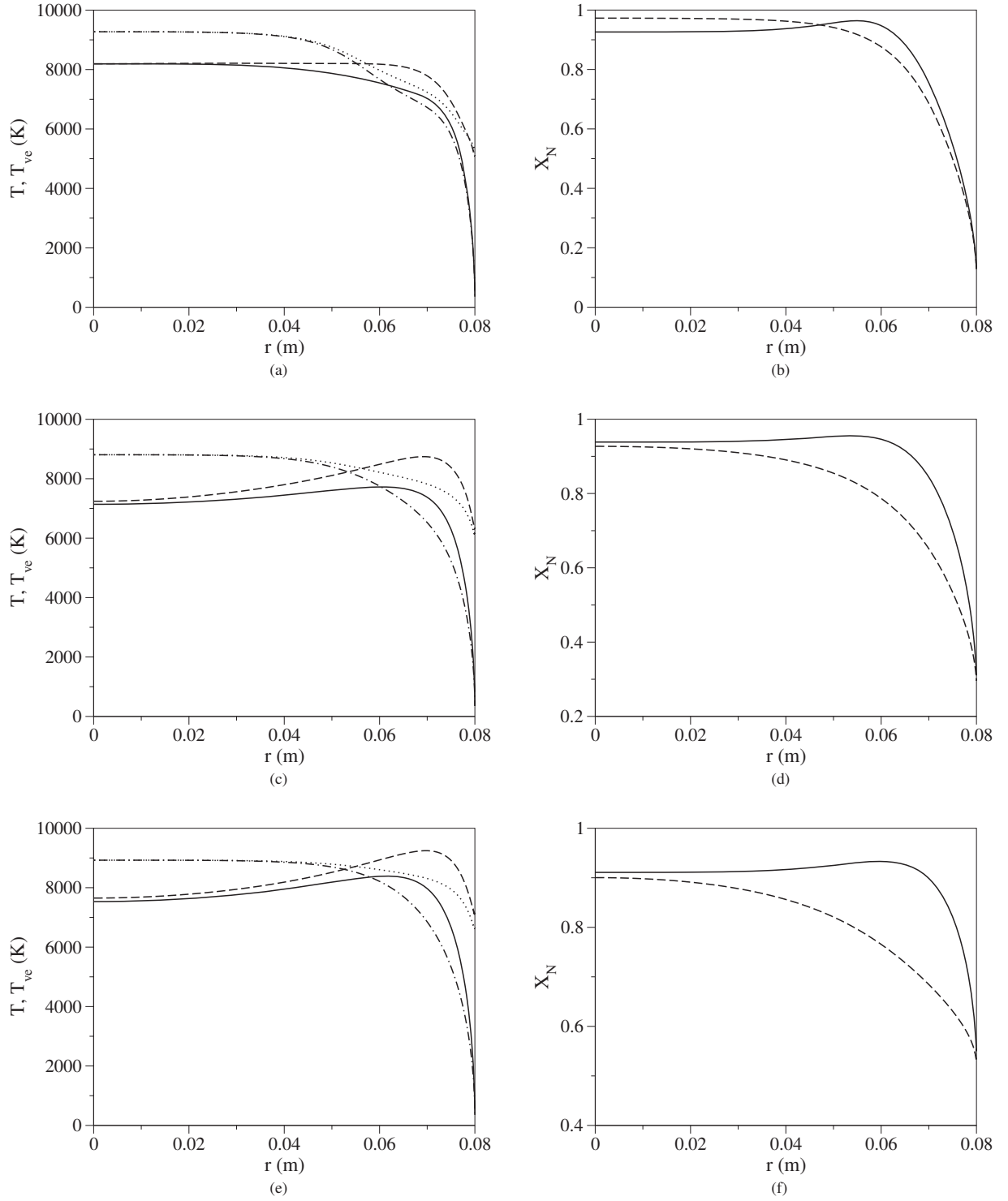
FIG. 9. Comparison between the translational-rotational temperature (left) and the N mole fraction (right) distributions predicted by the StS and the MT NLTE models at different pressures: (a)-(b) $p = 10\,000\,\text{Pa}$, (c)-(d) $p = 5000\,\text{Pa}$, (e)-(f) $p = 3000\,\text{Pa}$ ($f = 0.5\,\text{MHz}$, $P_0 = 0.35\,\text{MW/m}$; in (a), (c) and (e) unbroken line T StS, dashed line T_{ve} StS, dotted-dashed line T MT, dotted line T_{ve} MT; in (b), (d) and (f) unbroken line StS, dashed line MT).

ary condition. This behavior is due to the balance between the Joule heating (which heats up the electron gas) and the energy loss in elastic and inelastic collisions, and

chemical reactions. The peak location of the free-electron temperature moves towards the wall when decreasing the pressure. This is a consequence of the Joule heating dis-

tribution (not shown in Fig. 9) which becomes sharper and clustered to the wall at lower pressures. It is worth noticing that, in the StS simulation, (i) the translational-rotational temperature no longer exhibits a monotone behavior and (ii) the axis values of both temperatures are systematically lower than those predicted by the MT model. The differences observed between the StS and MT temperature distribution have an effect, as it should be expected, on the chemical composition (see Figs. 9(b), 9(d) and 9(f)).

Figure 10 shows the normalized population of the electronic levels of N on the torch axis (circles), in the mid-point of the torch (squares) and at the wall (triangles) at different pressures. The population exhibit significant distortions from a Boltzmann shape only close to the wall (where recombination occurs). Deviations from a Boltzmann distributions are more significant when increasing the pressure due to higher recombination.

V. CONCLUSIONS

A tightly coupled magneto-hydrodynamic solver for the study of the weakly ionized plasmas found in RF discharges has been developed. A hierarchy of thermophysical models have been added to the solver to model the non-equilibrium effects in atomic and molecular plasmas. These include LTE, multi-temperature and the more sophisticated State-to-State models. The governing equations for the flow and electromagnetic fields have been written as a system of coupled time-dependent conservation-laws. Steady-state solutions have been obtained by means of an implicit Finite Volume Method.

Results obtained by using a multi-temperature and State-to-State models have shown that the LTE assumption does not hold and that its use can lead to a wrong prediction of the thermo-chemical state of the gas. The analysis of the temperature distribution in the torch indicated that non-equilibrium plays an important role close to the walls, due to the combined effects of Ohmic heating, and chemical composition and temperature gradients. The accurate study of the population of excited electronic states has shown that, in view of the absence of a macroscopic gas flow, non-Boltzmann distributions are limited to a narrow region close to the torch wall.

ACKNOWLEDGMENTS

[1] M. I. Boulos, Pure & Appl. Chem. **9**, 1321 (1985).
[2] J. Mostaghimi and M. I. Boulos, in *Inductively Coupled Plasma in Analytical Spectrometry* (1992) pp. 949–984.
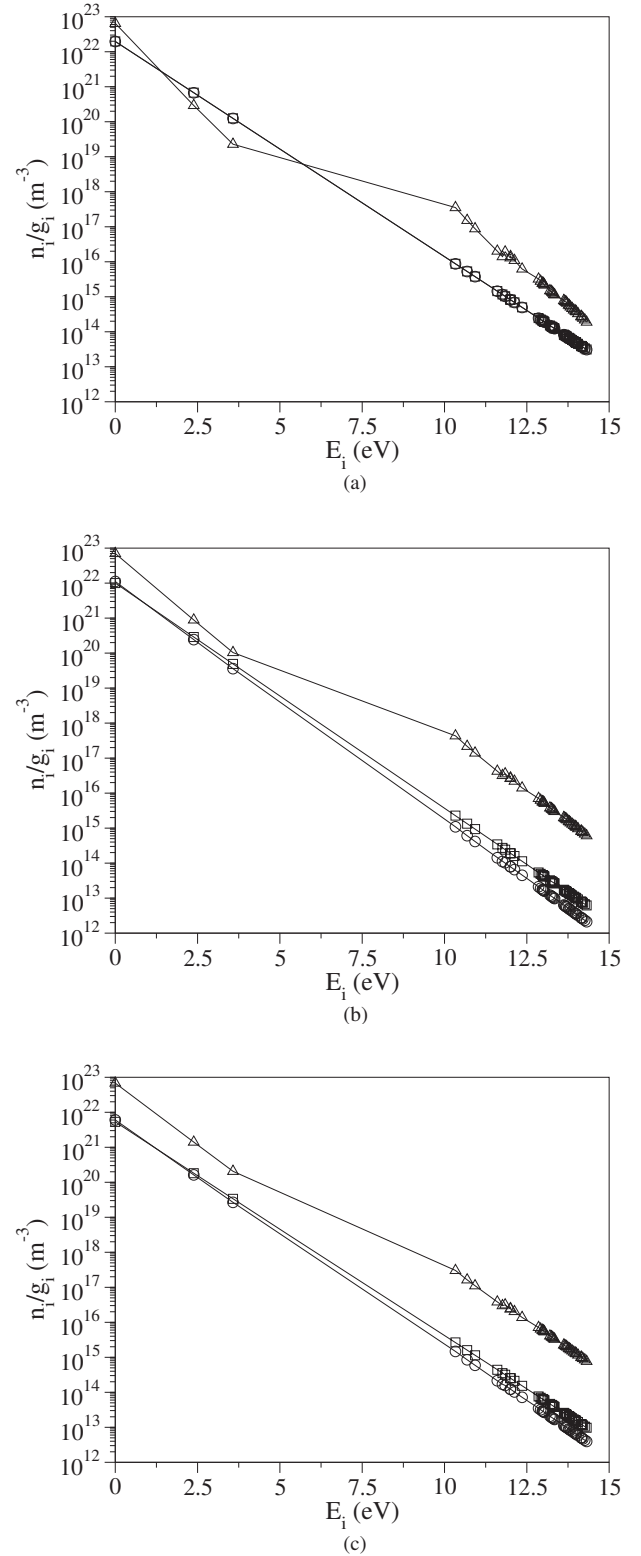

FIG. 10. Normalized population of the electronic levels of N at different pressures: (a) $p = 10\,000$ Pa, (b) $p = 5000$ Pa, (c) $p = 3000$ Pa ($f = 0.5$ MHz, $P_0 = 0.35$ MW/m; line with circles $r = 0$ m [axis], line with squares $r = 0.04$ m, line with triangles $r = 0.08$ m [wall]).

[3] T. B. Reed, J. Appl. Phys. **32**, 821 (1961).

[4] D. Giordano, "Hypersonic-flow governing equations with electromagnetic fields," AIAA Paper 2002–2165 (2002) 33rd Plasmadynamics and Lasers Conference, Maui, HW.

[5] T. G. Cowling, *Magnetohydrodynamics*, Monographs on Astronomical Subjects (Hilger, London, 1976).

[6] D. V. Abeele, *An Efficient Computational Model for Inductively Coupled Air Plasma Flows Under Thermal and Chemical Non-Equilibrium*, Ph.D. thesis, Univesité Libre de Bruxelles, Bruxelles, Belgium (2000).

[7] M. P. Freeman and J. C. Chase, J. Appl. Phys. **39**, 180 (1968).

[8] D. R. Keefer, J. A. Sprouse, and F. C. Loper, IEEE Trans. Plasma Sci. **1**, 71 (1973).

[9] H. U. Eckert, J. Appl. Phys. **41**, 1520 (1970).

[10] H. U. Eckert, J. Appl. Phys. **41**, 1529 (1970).

[11] H. U. Eckert, J. Appl. Phys. **43**, 46 (1972).

[12] H. U. Eckert, J. Appl. Phys. **48**, 1467 (1977).

[13] B. Shaw., J. Appl. Phys. **99**, 034906 (2006).

[14] J. J. Thompson, Phil. Mag. **4**, 1128 (1927).

[15] A. N. Tikhonov and A. A. Samarskii, *Equations of Mathematical Physics*, Dover Books on Physics (Dover Publications, Mineola, NY, 1990).

[16] D. C. Pridmore-Brown, J. Appl. Phys. **41**, 3621 (1970).

[17] M. I. Boulos, IEEE Trans. Plasma Sci. **1**, 28 (1976).

[18] J. Mostaghimi, P. Proulx, and M. I. Boulos, Plasma Chem. Plasma Process. **3**, 199 (1984).

[19] J. Mostaghimi and P. P. M. I. Boulos, Num. Heat Transfer **2**, 187 (1985).

[20] J. Mostaghimi, P. Proulx, and M. I. Boulos, J. Appl. Phys. **61**, 1753 (1987).

[21] P. Proulx, J. Mostaghimi, and M. I. Boulos, Plasma Chem. Plasma Process. **1**, 29 (1987).

[22] J. Mostaghimi and M. I. Boulos, J. Appl. Phys. **68**, 2643 (1990).

[23] R. Ye, P. Proulx, and M. I. Boulos, Int. J. Heat Mass Transfer **42**, 1585 (1999).

[24] A. F. Kolesnikov, in *Proc. of the 2nd ESA Symposium on Aerothermodynamics for Space Vehicles* (ESA Publication Div., The Netherlands, 1994) pp. 583–588.

[25] A. F. Kolensikov, in *Physico-Chemical Models for High Enthalpy and Plasma Flows*, Lecture Series (von Karman Institute for Fluid Dynamics, 1999).

[26] S. A. Vasil'evskii and A. F. Kolesnikov, Fluid Dyn. **35**, 769 (2000).

[27] N. G. Bykova, S. A. Vasilevskii, and A. F. Kolesnikov, High Temp. **42**, 12 (2004).

[28] A. N. Gordeev, A. F. Kolesnikov, and Y. K. Rulev, in *Proc. of the 5th ESA Symposium on Aerothermodynamics for Space Vehicles* (ESA Publication Div., The Netherlands, 2005) pp. 164–170.

[29] P. Rini, A. F. Kolesnikov, S. A. Vasil'evskii, O. Chazot, and G. Degrez, "CO$_2$ stagnation line flow simulation for mars entry applications," AIAA Paper 2005–5206 (2007) 38th AIAA Thermophysics Conference, Toronto, Canada.

[30] A. N. Gordeev and A. F. Kolesnikov, High Temp. **45**, 506 (2010).

[31] X. Chen and E. Pfender, Plasma Chem. Plasma Process. **1**, 103 (1991).

[32] D. V. Abeele and G. Degrez, AIAA Journal **38**, 234 (2000).

[33] M. Panesi, P. Rini, G. Degrez, and O. Chazot, J. Thermophys. Heat Transfer **21**, 57 (2007).

[34] M. E. Morsli and P. Proulx, J. Phys. D: Appl. Phys **40**, 4810 (2007).

[35] R. C. Miller and R. J. Ayen, J. Appl. Phys. **40**, 5260 (1969).

[36] For fixed values of the elemental fractions.

[37] W. Zhang, A. Lani, H. B. Chew, and M. Panesi, "Modeling of non-equilibrium plasmas in an inductively coupled plasma facility," AIAA Paper 2014–2235 (2014) 45th AIAA Plasmadynamics and Lasers Conference, Atlanta, GA.

[38] J.-L. Cambier and S. Moreau, "Simulation of a molecular plasma in collisional-radiative nonequilibrium," AIAA Paper 1993–3196 (1993) 24th Plasmadynamics and Laser Conference, Orlando, FL.

[39] M. Capitelli, I. Armenise, D. Bruno, M. Cacciatore, R. Celiberto, G. Colonna, O. D. Pascale, P. Diomede, F. Esposito, C. Gorse, K. Hassouni, A. Laricchiuta, S. Longo, D. Pagano, D. Pietanza, and M. Rutigliano., "Non-equilibrium plasma kinetics: a state-to-state approach," Plasma sources, science and technology (2006) 8th European Sectional Conference on Atomic and Molecular Physics of Ionized Gases.

[40] A. Bultel, B. van Ootegem, A. Bourdon, and P. Vervisch, Phys. Rev. E **65**, 046406 (2002).

[41] Y. Liu, M. Vinokur, M. Panesi, and T. E. Magin, "A multi-group maximum entropy model for thermo-chemical nonequilibrium," AIAA Paper 2010–4332 (2010) 10th AIAA/ASME Joint Thermophysics and Heat Transfer Conference, Chicago, IL.

[42] Y. Liu, M. Panesi, M. Vinokur, and P. Clarke, "Microscopic simulation and macroscopic modeling of thermal and chemical nonequilibrium gases," AIAA Paper 2013–3146 (2013) 44th AIAA Thermophysics Conference, San Diego, CA.

[43] A. Bultel, B. G. Chéron, A. Bourdon, O. Motapon, and I. F. Schneider, Phys. Plasmas **13**, 043502 (2006).

[44] M. Panesi, T. E. Magin, A. Bourdon, A. Bultel, and O. Chazot, J. Thermophys. Heat Transfer **23**, 236 (2009).

[45] M. Panesi, T. E. Magin, A. Bourdon, A. Bultel, and O. Chazot, J. Thermophys. Heat Transfer **25**, 361 (2011).

[46] A. Munafò, A. Lani, A. Bultel, and M. Panesi, Phys. Plasmas **20**, 073501 (2013).

[47] M. Panesi, R. L. Jaffe, D. W. Schwenke, and T. E. Magin, J. Chem. Phys **138**, 044312 (2013).

[48] A. Munafò, M. Panesi, and T. E. Magin, Phys. Rev. E **89**, 023001 (2014).

[49] M. Panesi, A. Munafò, T. E. Magin, and R. L. Jaffe, Phys. Rev. E **90**, 013009 (2014).

[50] H. P. Le, A. P. Karagozian, and J.-L. Cambier, Phys. Plasmas **20**, 123304 (2013).

[51] F. Esposito and M. Capitelli, Chem. Phys. Lett. **302**, 49 (1999).

[52] F. Esposito, I. Armenise, and M. Capitelli, Chem. Phys. **331**, 1 (2006).

[53] D. W. Schwenke, in *Non-Equilibrium Gas Dynamics - From Physical Models to Hypersonic Flights*, Lecture Series (von Karman Institute for Fluid Dynamics, 2008).

[54] R. L. Jaffe, D. W. Schwenke, G. Chaban, and W. Huo, "Vibrational and rotational excitation and relaxation of nitrogen from accurate theoretical calculations," AIAA Paper 2008–1208 (2008) 46th AIAA Aerospace Sciences Meeting and Exhibit, Reno, NV.

[55] G. Chaban, R. L. Jaffe, D. W. Schwenke, and W. Huo, "Dissociation cross-sections and rate coefficients for nitrogen from accurate theoretical calculations," AIAA Paper 2008–1209 (2008) 46th AIAA Aerospace Sciences Meeting and Exhibit, Reno, NV.

[56] R. L. Jaffe, D. W. Schwenke, and G. Chaban, "Theoretical analysis of N$_2$ collisional dissociation and rotation-vibration energy transfer," AIAA Paper 2009–1569 (2009) 47th AIAA Aerospace Sciences Meeting and Exhibit, Orlando, FL.

[57] I. V. Adamovich, S. O. Macheret, J. W. Rich, and C. E. Treanor, AIAA J. **33**, 1064 (1995).

[58] I. V. Adamovich, S. O. Macheret, J. W. Rich, and C. E. Treanor, AIAA J. **33**, 1070 (1995).

[59] C. Park, J. Thermophys. Heat Transfer **3**, 233 (1989).

[60] C. Park, J. Thermophys. Heat Transfer **7**, 385 (1993).

[61] C. Park, J. T. Howe, R. L. Jaffe, and G. V. Candler, J. Thermophys. Heat Transfer **8**, 9 (1994).

[62] C. Park, R. L. Jaffe, and H. Partridge, J. Thermophys. Heat Transfer **15**, 76 (2001).

[63] E. Josyula, W. F. Bailey, and S. M. Ruffin, Phys. Fluids **15**, 3223 (2003).

[64] M. Panesi and A. Lani, Phys. Fluids **25**, 057101 (2013).

[65] M. G. Kapper and J.-L. Cambier, J. Appl. Phys. **109**, 113308 (2011).

[66] M. G. Kapper and J.-L. Cambier, J. Appl. Phys. **109**, 113309 (2011).

[67] A. Munafò, M. G. Kapper, J.-L. Cambier, and T. E. Magin, "Investigation of nonequilibrium effects in axisymmetric nozzle and

blunt body nitrogen flows by means of a reduced rovibrational collisional model," AIAA Paper 2012–0647 (2012) 50h AIAA Aerospace Sciences Meeting including the New Horizons Forum and Aerospace Exposition, Nashville, TN.

[68]C. Hirsch, *Numerical Computation of Internal and External Flows* (John Wiley & Sons, New York, NY, 1990).

[69]M. Capitelli, C. M. Ferreira, B. F. Gordiets, and A. I. Osipov, *Plasma Kinetics in Atmospheric Gases* (Springer, 2000).

[70]L. Pauling and E. B. Wilson Jr., *Introduction to Quantum Mechanics with Applications to Chemistry*, Dover Books on Physics (Dover Publications, Mineola, NY, 1985).

[71]L. V. Gurvich, *Thermodynamic Properties of Individual Substances* (CRC press, 1994).

[72]V. Giovangigli, *Multicomponent Flow Modeling* (Birkhäuser, Berlin, 1999).

[73]E. Nagnibeda and E. Kustova, *Non-Equilibrium Reacting Gas Flows* (Springer, Berlin, 2009).

[74]L. Landau and E. Teller, Phys. Z Sowjetunion **10**, 34 (1936), in German.

[75]G. V. Candler and R. W. MacCormack, J. Thermophys. Heat Transfer **5**, 266 (1991).

[76]A. Bourdon and P. Vervisch, Phys. Rev. E **52**, 1888 (1996).

[77]J. H. Ferziger and H. G. Kaper, *Mathematical Theory of Transport Processes in Gases* (North-Holland Pub. Co., 1972).

[78]R. S. Devoto, Phys. Fluids **9**, 1230 (1966).

[79]T. E. Magin and G. Degrez, Phys. Rev. E **70**, 046412 (2004).

[80]V. Giovangigli, IMPACT Comput. Sci. Eng. **2**, 73 (1990).

[81]T. E. Magin and G. Degrez, J. Comput. Phys. **198**, 424 (2004).

[82]A. Munafò and T. E. Magin, Phys. Fluids **26**, 097102 (2014).

[83]K. L. Heritier, R. L. Jaffe, V. Laporta, and M. Panesi, J. Chem. Phys. **141**, 184302 (2014).

Appendix B Multifluid Plasma Simulation B-1

B.1 Apollo: An Unstructured Framework for Multi-Fluid Plasma Modeling

A great amount of time has been dedicated to the development of a code that is able to address some of the bigger challenges associated with plasma and FRC modeling. The multi-scale and multi-physics nature of the problem requires that special attention be payed to the numerical methods that are used, so that a seamless and accurate integration of the different physics is attained. With that in mind a framework, Apollo, has been developed that incorporates some of the best practices in scientific computing as it is shown schematically in Figure B1. The observations resulting from this investigation will make a major impact on the trajectory of the Thermophysics Universal Research Framework as it is adapted to encompass these types of models in the future.

B.1.1 Code Implementation

A hyperbolic solver framework for the multi-fluid plasma model has been developed. The objective was to create an unstructured solver that would be able to accommodate the complex geometry that is associated with experimental setup, as well as include the state-of-the-art scientific computing principles.

The framework is implemented using the PETSc[B1] developed at the Argonne National Laboratory to ease in the development of large-scale scientific application codes. It consists of a variety of libraries which manipulate a particular objects (like vectors and/or matrices) and the operations one would like to perform on the objects. In essence, PETSc addresses the various phases of solving Partial Differential Equations (PDEs), while separating the issues of parallelism from the choice of numerical methods.

A PETSc subclass that is particularly useful is the DMPlex[B2] for unstructured data management. DMPlex stores the connectivity information associated with the mesh as a layered Directed Acyclic Graph (DAG), which allows for dimension free programming, and optimization of not only file I/O but also parallel data distribution using graph partitioning libraries. The framework accepts meshes generated in gmsh[B3]. Gmsh is a fast, light and user-friendly finite element meshing tool with a built-in CAD engine and post-processor.

Output files are written using the VTK[B4] file format which can be easily read by Visit or Paraview. VTK is an open-source, object-oriented software system for computer graphics, visualization, and image processing.

PETSc Time Stepping (TS) library is used to advance the algorithm in time; this supports both the solution of PDE's and Differential algebraic equations (DAEs). Currently only explicit PDE's time integrators are implemented, with the default being the Strong-Stability Preserving (SSP) second order Runge-Kutta method[B5]. The DAE functionality will prove very useful when the code is extended to include implicit time integration to address the multi-scale nature of the plasma of interest for FRC applications.

The packages described above are the "backbone" of the framework meant to speedup file I/O, as well as making the domain partitioning and parallel communication more efficient. In addition the framework is not "married" to any specific numerical method, allowing any or many different spatial discretizations to be implemented.

B.1.2 Numerical Method: Discontinuous Galerkin Finite Element

Currently only the discontinuous Galerkin finite element method has been implemented, but the continuous Galerkin finite element method should follow soon as well. The nodal DG method[B6] belongs to the set of finite element methods that does not enforce C^0 continuity at element bound-
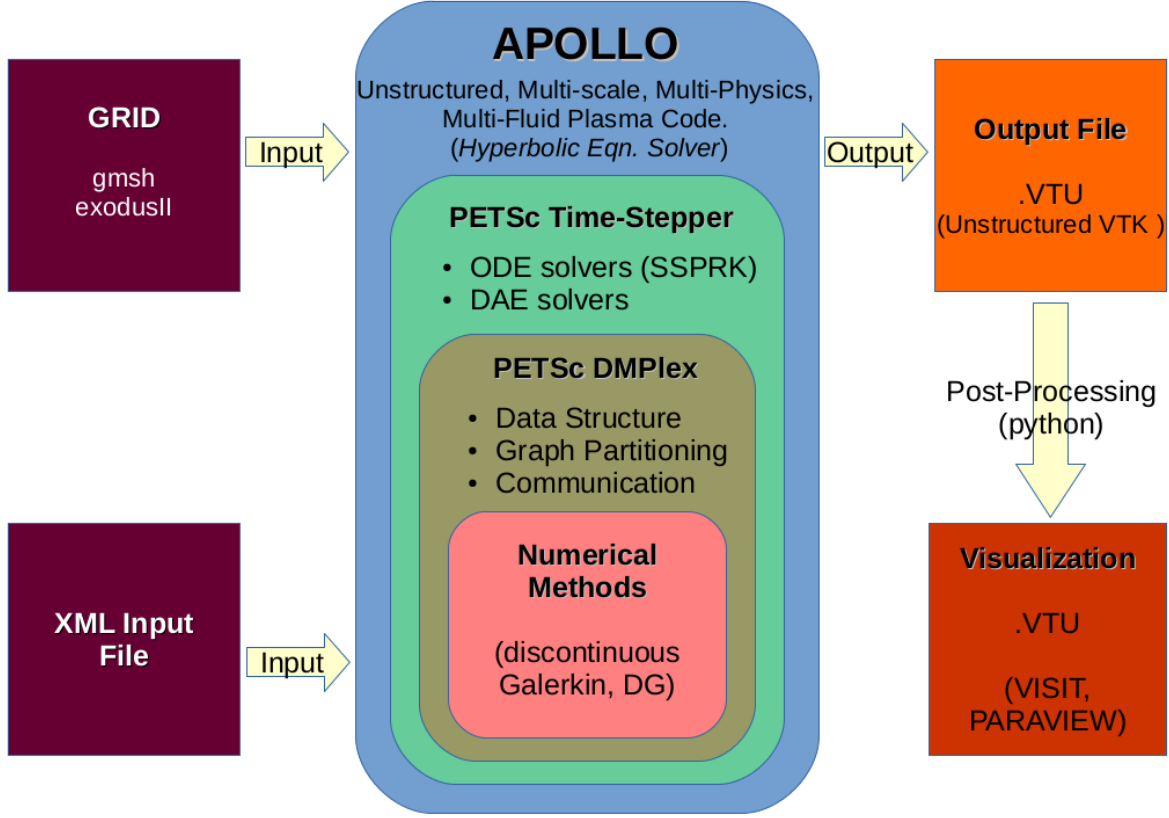
Figure B1: Schematic of the Apollo code. On the left is the input files, a grid file generated in gmsh or an exodusII file. The PETSc time-stepper evolves the framework in time, allowing for multiple strong-stability-preserving Runge-Kutta methods. The PETCs DMPlex handles the data structure and domain partitioning the communication between processors. On the right is the unstructured VTK file output (extension .vtu). The output .vtu files need to be post processed in order for it to be visualized in Visit or Paraview.

aries, i.e. at the boundary of two elements the variables are allowed to be discontinuous. In the DG method the conserved variables are represented as a summation of polynomial basis functions that describe how these variables change inside each element as

$$\mathbf{Q}^s(t,x) = \sum_{j=1}^{m} \mathbf{q}_j(t)\phi_j(x), \tag{16}$$

where ϕ_j are the spatial basis functions and $\mathbf{q}_j$ are the temporal coefficients.

The governing hyperbolic equations that evolve the conserved variables $\mathbf{Q}^s$ are multiplied by the test functions (in a Galerkin representation the test and the basis functions are the same), and integrated over each element volume,

$$\int_\Omega d\mathbf{x}\phi_i \frac{\partial \mathbf{Q}^s}{\partial t} + \int_\Omega d\mathbf{x}\phi_i \nabla \cdot \mathcal{F} = \int_\Omega d\mathbf{x}\phi_i \mathbf{S}^s. \tag{17}$$

Integration by parts is applied to the second term and the above equation becomes

$$\int_\Omega d\mathbf{x}\phi_i \frac{\partial \mathbf{Q}^s}{\partial t} + \oint_{\partial\Omega} d\mathbf{A} \cdot \mathcal{F}\phi_i - \int_\Omega d\mathbf{x}\nabla\phi_i \cdot \mathcal{F} = \int_\Omega d\mathbf{x}\phi_i \mathbf{S}^s. \tag{18}$$

The surface integral in Eq. (18) accounts for the fluxes across element boundaries, which are computed using a numerical flux, Lax-Friedrichs fluxes[B7] in this case, and given as

$$\mathcal{F} = \frac{1}{2}\left[\mathcal{F}(\mathbf{Q}_e^+) - \mathcal{F}(\mathbf{Q}_{e+1}^-)\right] - \frac{1}{2}|\lambda|(\mathbf{Q}_e^+ - \mathbf{Q}_{e+1}^-), \tag{19}$$

where $|\lambda|$ is the largest eigenvalue of the flux Jacobian using surface values averaged from elements e and $e + 1$, and where the superscripts $+$ and $-$ represent the values at the upper and lower boundaries of the elements. The surface and volume integrals are evaluated using quadrature rules.

Separating the temporally and spatially dependent terms, Eq. (18) can be written as

$$\frac{\partial \mathbf{q}_i}{\partial t} = \int_\Omega d\mathbf{x}\phi_i \mathbf{S}^s - \oint_{\partial\Omega} d\mathbf{A} \cdot \mathcal{F}\phi_i + \int_\Omega d\mathbf{x}\nabla\phi_i \cdot \mathcal{F} \equiv \mathbf{L}_i(\mathbf{Q}^s), \tag{20}$$

where $\mathbf{L}_i(\mathbf{Q}^s)$ is an operator containing all the spatially dependent term. One of the major benefits of the DG method is the data locality of the spatial operator, which is limited to nearest neighbor elements. The equation $\partial \mathbf{q}_i/\partial t = \mathbf{L}_i(\mathbf{Q}^s)$ becomes a simple or Ordinary Differential Equation (ODE) that can be integrated in time using simple Runge-Kutta time integrators. In this application second-order strong-stability-preserving method[B5] is used.

Prior to using the code for FRC simulations, the code was extensively verified for the solution of Maxwell's equations for the field solver and Euler equations for the fluid solver independently. This verification is discussed in more detail in Appendix B.2

B.2 Apollo Verification Cases

Before the code was used to study FRC formation simulations it was verified against standard problems. The verification consisted of two phases, the first one being for the Maxwell equations for the field solver, and the second one for the Euler equations for the fluids.
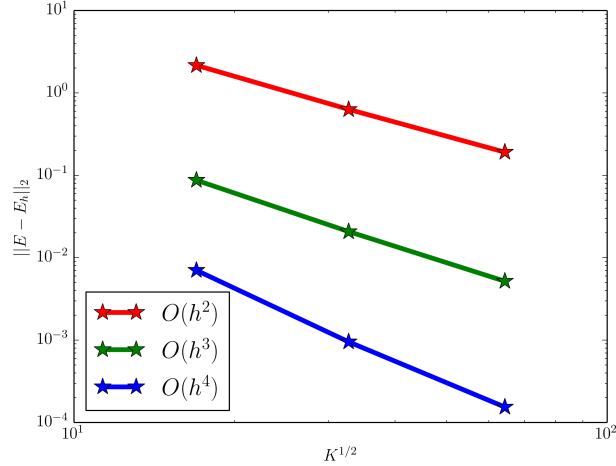
Figure B2: Convergence plot for 2nd, 3rd, and 4th order accurate for the nodal DG implementation. The slope of each line should be the order of accuracy of the numerical method.

The first problem that we use to test the code is the two-dimensional Maxwell equation in the transverse magnetic form[B7]. The problem models a metallic cavity, $\Omega = [-1, 1]^2$, where $\mu = \mu_o$ and $\varepsilon = \varepsilon_o$, the vacuum values. For boundary conditions the walls of the cavity are assumed to be perfectly electrically conducting such that the tangential component of the electric field vanishes at the wall. The magnetic field boundary conditions are implemented by setting the values on the outside of the boundary equal to the ones on the inside, $H^* = H^-$.

The benefits of using the cavity problem is that the exact solution over time is known, and given by,

$$H^x(x, y, t) = -\frac{\pi n}{\omega} \sin(m\pi x) \cos(n\pi y) \sin(\omega t), \tag{21}$$

$$H^y(x, y, t) = \frac{\pi m}{\omega} \cos(m\pi x) \sin(n\pi y) \sin(\omega t), \tag{22}$$

$$E^z(x, y, t) = \sin(m\pi x) \sin(n\pi y) \cos(\omega t), \tag{23}$$

where the resonance frequency is defined as $\omega = \pi\sqrt{m^2 + n^2}$. For all simulations presented here $m = n = 1$.

This problem is used to verify the spatial convergence of the discontinuous Galerkin finite element method numerical method. To do so multiple simulations were conducted, where the time-step was held constant, while the spatial resolution was increased. The resolution is increased either by increasing the number of elements, K, or the polynomial order of the DG representation.

Figure B2 plots the convergence of the electric field, under element and order refinement. The slope of each of the lines is 2, 3, and 4 corresponding to 2nd, 3rd, and 4th order spatial accuracy for the DG method.

Another problem used to benchmark the unstructured DG implementation is the forward facing step, and Fig. B3 shows agreement with the results given in Ref. [B8]. This test case shows the ability of the method to capture complex physics and represent non-trivial geometries that may be present.
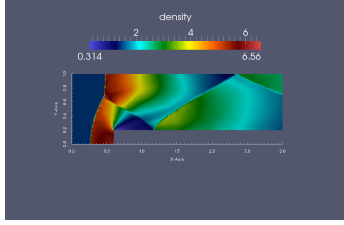
(a) Forward facing step.
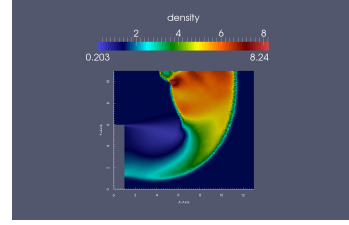
(b) Backward facing step.

Figure B3: Solution of the density for the forward and backward facing step problems[B8].

The forward facing step problem simulates a right-going Mach 3 uniform flow as it propagates through a wind tunnel of 1 unit wide and 3 units long. The step is 0.2 units high and is located 0.6 units from the left-hand end of the tunnel. Reflective boundary conditions are applied on the top and bottom walls of the tunnel, the right end has an in-flow and left end an out-flow boundary conditions. The corner of the step is a singularity; it is common to modify the numerical method around that point in order to proper entropy. In our cases no modification is applied to the scheme near the corner. No analytical solution is available for this problem so this is a qualitative comparison of Apollo with published results and there is visual agreement among the computational and published solutions.

The backward facing step simulation has a 1 unit×5 unit inflow forming a step attached to a 12 unit×11 unit downstream region. It is initialized with a right-moving Mach 5.09 shock which is initially located at 1/2 unit upstream from the step edge. The shock moves into undisturbed air at a density of 1.4 and pressure of 1. The boundary conditions are inflow upstream and outflow downstream. The other boundaries are either reflective on the top and back side of the step or Neumann at top and bottom of the domain. No special treatment is applied at the corner which is a singularity of the solution. Just like the forward facing step, the visual comparison of the Apollo solution and the published results show agreement. For both problems it is easy to get negative pressure errors and positivity is enforced by Tu and Aliabadi[B9] limiter.

References

[B1]   Satish Balay et al. *PETSc Users Manual*. Tech. rep. ANL-95/11 - Revision 3.5. Argonne National Laboratory, 2014. URL: http://www.mcs.anl.gov/petsc.

[B2]   Michael Lange, Matthew G. Knepley, and Gerard J. Gorman. "Flexible, Scalable Mesh and Data Management using PETSc DMPlex". In: (2015). arXiv:1505.04633. URL: http://arxiv.org/abs/1505.04633.

[B3]   C. Geuzaine and J. F. Remacle. "Gmsh: A 3-D finite element mesh generator with built-in pre- and post-processing facilities". In: *Int. J. Numer. Methods Eng.* 79.11 (2009), pp. 1309–1331.

[B4]   Lisa S. Avila et al. *The VTK User's Guide*. Tech. rep. 11th edition. Kitware Inc, 2010. URL: http://www.kitware.com/products/books/VTKUsersGuide.pdf.

[B5]   S Gottlieb, D Ketcheson, and C W Shu. *Strong Stability Preserving Runge-Kutta and Multistep Time Discretizations*. World Scientific, 2011.

[B6]   J.S Hesthaven and T Warburton. "Nodal High-Order Methods on Unstructured Grids: I. Time-Domain Solution of Maxwell's Equations". In: *J. Comput. Phys.* 181.1 (2002), pp. 186–221. ISSN: 00219991. DOI: 10.1006/jcph.2002.7118. URL: http://www.sciencedirect.com/science/article/pii/S0021999102971184.

[B7]   J S Hesthaven and T Warburton. *Nodal Discontinuous Galerkin Methods: Algorithms, Analysis, and Applications*. Springer, 2008.

[B8]   B Cockburn and C W Shu. "The Runge-Kutta Discontinuous Galerkin Method for Conservation Laws V: Multidimensional Systems". In: *J. Comput. Phys.* 141 (1998), pp. 199–244.

[B9]   Shuangzhang Tu and Shahrouz Aliabadi. "A Slope Limiting Procedure in Discontinuous Galerkin Finite Element Method for Gasdynamic Applications". In: *Int. J. Numer. Anal. Model.* 2.2 (2005), pp. 163–178. ISSN: 1705-5105. URL: http://www.math.ualberta.ca/ijnam/Volume-2-2005/No-2-05/2005-02-03.pdf.

CrossMark
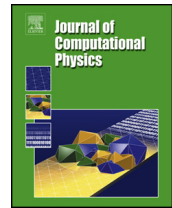
A blended continuous–discontinuous finite element method for solving the multi-fluid plasma model

E.M. Sousa *, U. Shumlak

Aerospace and Energetics Research Program, University of Washington, Seattle, WA, United States

A B S T R A C T

The multi-fluid plasma model represents electrons, multiple ion species, and multiple neutral species as separate fluids that interact through short-range collisions and long-range electromagnetic fields. The model spans a large range of temporal and spatial scales, which renders the model stiff and presents numerical challenges. To address the large range of timescales, a blended continuous and discontinuous Galerkin method is proposed, where the massive ion and neutral species are modeled using an explicit discontinuous Galerkin method while the electrons and electromagnetic fields are modeled using an implicit continuous Galerkin method. This approach is able to capture large-gradient ion and neutral physics like shock formation, while resolving high-frequency electron dynamics in a computationally efficient manner. The details of the Blended Finite Element Method (BFEM) are presented. The numerical method is benchmarked for accuracy and tested using two-fluid one-dimensional soliton problem and electromagnetic shock problem. The results are compared to conventional finite volume and finite element methods, and demonstrate that the BFEM is particularly effective in resolving physics in stiff problems involving realistic physical parameters, including realistic electron mass and speed of light. The benefit is illustrated by computing a three-fluid plasma application that demonstrates species separation in multi-component plasmas.

© 2016 Elsevier Inc. All rights reserved.

1. Introduction

Plasmas can be represented by a hierarchy of models; the more general the model, the higher the computational cost. In plasma simulations it is therefore important to devise methods that maximize computational efficiency, while capturing the desired physics.

In kinetic theory, each constituent plasma species is represented by a probability distribution function $f(\mathbf{x}, \mathbf{v}, t)$ that depends on position, velocity, and time. The evolution of the distribution function is governed by the Boltzmann–Maxwell equation system. Solving the Boltzmann equation is computationally expensive due to the fact that the distribution functions occupy a six-dimensional phase space.

The two-fluid plasma model can be derived from the kinetic model by taking velocity moments [1], which reduces the six-dimensional space to three dimensions. Inherent in the derivation of the two-fluid model is the assumption of local thermodynamic equilibrium within each species, but not between different species. The governing equations for the two-fluid model are derived by taking the first three velocity moments of the Boltzmann equation for the electrons and for

---

the ions. The zeroth moment describes the conservation of mass, the first moment describes the conservation of momentum, and the third moment describes the conservation of energy. The moments of the Boltzmann equation describe the evolution of the bulk properties of the plasma: density, momentum, and energy. In the simplest two-fluid description, the pressure is assumed to be isotropic and the heat flux is assumed to be negligible [1].

The magnetohydrodynamics (MHD) model, the most widely used plasma model, is derived from the two-fluid plasma model by neglecting the electron inertia (zero electron mass) and assuming the speed of light is much larger than any other speed in the system (infinite speed of light) [2]. As a consequence of neglecting the electron inertia, the electron momentum equation reduces to the generalized Ohm's law and the kinetic energy of the electrons is zero. By making these asymptotic assumptions, the physics of high frequency electromagnetic waves is ignored and the vacuum permittivity is effectively set to zero. This means that the displacement current term of Ampere's law is zero, and from Poisson's equation a zero permittivity implies that the electron and ion number density must always be equal, thereby enforcing charge neutrality. The MHD model is often further simplified to an ideal MHD model, which limits its applicability to high collisionality, small Larmor radius, and low resistivity regimes [3].

The two-fluid plasma model can be generalized to a multi-fluid plasma model that includes multiple ions and neutral species, where the mass, momentum, and energy of each species is evolved separately, and the species interact with each other through collisions and electromagnetic fields [4,5]. By separately evolving the constituent species, the multi-fluid plasma model is able to capture more generalized physics than MHD, but at a higher computational cost. The mass of the constituent species and their plasma parameters set the range of spatial and temporal scales. Since the multi-fluid plasma model does not make asymptotic assumptions about the speed of light, it captures more waves than MHD, including waves that propagate faster than the magnetosonic speed. This has been demonstrated for the two-fluid plasma model [1].

The characteristic speeds of the multi-fluid plasma model are the species' acoustic speeds and the speed of light, both of which can severely limit the time step size for the numerical time integration. In addition, the characteristic frequencies (plasma and cyclotron) need to be resolved to capture the full physics of the multi-fluid model.

For a given model, the partial differential equation (PDE) type informs the choice of numerical methods used to solve it. The multi-fluid plasma model is an inhomogeneous hyperbolic equation system and can be described by balance laws. Such equation systems can be solved using a variety of methods, including finite volume methods [6–8], continuous Galerkin finite element methods [9,10], and discontinuous Galerkin finite element methods [11–14].

Finite volume methods have been used extensively and differ depending on the technique used to evaluate fluxes. One type of finite volume method is the wave propagation method, which is second-order accurate and provides good resolution of shocks and discontinuities even when the initial conditions are smooth [6]. Other types of finite volume methods have been successfully applied to the MHD plasma model [15–17] and to the two-fluid plasma model [1,18]. Since the source terms in the PDEs cannot be directly incorporated into the calculation of the fluxes in the wave propagation method, the approach requires source splitting. As a result phase errors can be produced when the characteristic frequency is high compared to the frequency of information propagation [14].

Continuous Galerkin (CG) finite element methods have also been used for solving MHD [9] and extended MHD equations [10]. The CG method represents the solution variables within each element using polynomial basis functions. The order of the polynomial determines the spatial order of accuracy. The CG method enforces continuity of the solution across element boundaries, i.e. C^0 continuity. Some CG methods enforce C^1 continuity of the solution across element boundaries [9]. The CG method is particularly well suited for smooth solutions and offers the ability to compute solutions at high-order spatial accuracy on regular and unstructured grids [19–22]. With no dissipation, CG methods can be prone to dispersive errors and often require adding an artificial dissipation to damp high frequency oscillations [23]. The ideal multi-fluid plasma model has no physical source of dissipation, and thus using a CG method necessitates the introduction of artificial dissipation.

CG methods require the simultaneous solution of the global system of equations, which involves a matrix inversion. This feature allows CG to be coupled with an implicit time integration method with only minor modification. Plasma dynamics encompass a large range of timescales, which makes implicit time integration desirable. With implicit time integration, the solver is not subject to CFL (Courant–Friedrichs–Lewy) restrictions that limit time step size based on the fastest speed in the system. As two relevant plasma examples, in Ref. [24] an implicit method is applied together with a CG spatial discretization, and in Ref. [25] the hyperbolic MHD model is converted into parabolic equations in order to make them more amenable to multigrid and physics-based preconditioning that allow for fast Jacobian-free implicit time integration.

A numerical method that combines the shock capturing and conservation properties of finite volume methods with high-order accuracy and flux/source coupling of CG methods is the discontinuous Galerkin (DG) finite element method. The DG method was introduced in Ref. [26] for the study of two-dimensional neutron transport. Like the CG methods, DG methods represent the solution by a set of polynomial basis functions in each element; however, continuity of the solution is not enforced across the element boundaries. The DG method was expanded to solve non-linear equations in Ref. [11] who used it with total variation diminishing (TVD) Runge–Kutta time integration. Likewise the DG method has been applied to solve Navier–Stokes equations [27] on unstructured grids with linear, quadratic, and cubic elements [28–30].

In plasma simulations the DG method has been applied to the ideal MHD model [12,13,31], and to the Vlasov–Poisson equation system [32]. In Ref. [14] an extensive study of the DG method is applied to the two-fluid plasma model and explores the challenges associated with capturing the physical dispersion of the model. It is shown that the DG method is able to accurately capture physically expected high frequency oscillations using higher order discretizations without producing phase errors. A major benefit of the DG method is that it is remarkably robust in the presence of rapid oscillations while

simultaneously capturing discontinuity fronts. A drawback of the DG method is that with a polynomial basis function of degree p, the explicit time step size is limited by the CFL condition for the fastest wave to be less than $1/(2p-1)$ [33]. This can be extremely restrictive for problems that require high spatial accuracy. Using DG with implicit time integration can be challenging [34], this is because defining the Jacobian for a limited flux leads to a stiff matrix since small variations in the conserved variables can produce large changes in the flux. Reference [35] presents a complete two-fluid plasma model discretized using the DG method with an implicit time integrator; however, the non-linear Newton solver required for time advance does not always converge. This is due to the fact that regions that exhibit sharp gradients require limiters, which make the Jacobian for the non-linear solver ill-conditioned.

An ideal numerical method for the multi-fluid plasma model would have high-order accuracy, would be capable of capturing shocks, would provide good resolution of fast oscillations, and would not impose restrictive time step limitations. To that end, this paper presents a one-dimensional blended finite element method (BFEM) in which the electron fluid and the electromagnetic fields are represented using an implicit CG method, while all ions and neutral fluids are represented using an explicit DG method. This choice of blended discretization is informed by the physical properties of electrons, ions, neutrals, and fields.

Implicit–explicit (IMEX) methods have been used in the past for advection–diffusion problems where the implicit discretization is applied to parabolic diffusive source term and the explicit discretization is applied to the hyperbolic convective term [36]. IMEX methods have also been applied to geometry-induced stiffness [37], when a problem has complex geometry and consequently a broad range on mesh sizes. In our cases the stiffness comes from the electrons and electromagnetic fields that need to be solved everywhere in the domain and though the convective term. In the implicit–explicit scheme presented here is as if two separate problems exist, one advanced implicitly and the other explicitly and them both are coupled through the source term.

In many plasma configurations of interest, e.g. Z-pinches [38], tokamaks [39], stellarators [40], inertial confinement fusion capsules [41], the electron fluid and the electromagnetic fields may not have sharp gradients or discontinuities, which makes them suitable to being modeled with the CG method. Smooth solutions in the electron fluid and electromagnetic fields alleviate the need for limiters and enable the use of implicit time integration. Using the BFEM for the multi-fluid plasma model thus removes the strictest time step limitations associated with the speed of light, the electron acoustic speed, and the electron plasma and cyclotron frequencies. Shocks, which require limiters, only occur in ion and neutral fluids, and are efficiently captured with the DG method.

By coupling CG for the electrons and fields with DG for the ions and neutrals, the BFEM maintains high-order spatial accuracy, is able to resolve fast oscillations, efficiently captures shocks, and the implicit electron evolution relaxes the time step restrictions considerably by removing the most stringent limitations. This makes the BFEM for the multi-fluid plasma model more computationally efficient and robust than using a single type of finite element discretization.

This paper presents the development of a blended continuous–discontinuous finite element method, investigates its application to the multi-fluid plasma model. This method is particularly helpful in multiscale problems with disparate time-scales and where the fast dynamics does not play a vital role, nor is of much interest. Therefore, the fast dynamics is integrated using an implicit time integration to avoid very restrictive time-steps while the slow physics is integrated explicitly to capture the relevant aspects of the problem. The fast physics, which is unlikely to shock, is discretized using a continuous Galerkin finite element method and requires no limiters or flux calculations reducing the complexity of the numerical method. The slow dynamics is spatially discretized using a discontinuous Galerkin finite element method to capture shocks that may form in the solution. In summary the BFEM is designed to capture shocks for slow fluids while time-stepping over the fast dynamics fluids in problems where these two fluids are coupled throughout the computational domain. The paper is organized as follows: Section 2 describes the multi-fluid plasma model and the associated partial differential equation system. Section 3 introduces the BFEM implementation details and presents the continuous and discontinuous Galerkin portions of the method and their coupling. Section 4 presents numerical results for the two-fluid soliton problem and the electromagnetic shock tube problem. It also includes the application of the BFEM to a three-fluid plasma simulation of species separation [42] during the implosion of inertial confinement fusion capsules. Section 5 presents concluding remarks and opportunities for future work.

2. Multi-fluid plasma model

The multi-fluid plasma model [4] represents each species, e.g. electrons, ions, neutrals, as a separate fluid. The model allows for multiple ion and neutral species. Each fluid is described by its local mass density, momentum density, and total energy density. The evolution of these properties obeys underlying conservation laws. The motion of the electrically charged fluids generates and responds to electromagnetic fields, which are described by Maxwell's equations.

The equations that govern the evolution of the fluid properties of species α are derived by taking velocity moments of the Vlasov equation, where the nth moment is given by

$$m_\alpha \int \mathbf{v}^n \frac{\partial f_\alpha}{\partial t} d\mathbf{v} + m_\alpha \int \mathbf{v}^{n+1} \cdot \frac{\partial f_\alpha}{\partial \mathbf{x}} d\mathbf{v} + q_\alpha \int \mathbf{v}^n (\mathbf{E} + \mathbf{v} \times \mathbf{B}) \cdot \frac{\partial f_\alpha}{\partial \mathbf{v}} d\mathbf{v} = 0, \tag{1}$$

where $f_\alpha(\mathbf{x}, \mathbf{v})$ denotes the distribution function, m_α is the particle mass, and q_α is the charge. The electric and magnetic fields are $\mathbf{E}$ and $\mathbf{B}$.

Expressions for the conservation of mass, momentum, and total energy for each species are obtained from the first three moments, $n = \{0, 1, 2\}$, where a tensor contraction is performed for the second moment to give a scalar energy. The resulting equation system is the multi-fluid plasma model. Each fluid species α has a set of five moment equations,

$$\frac{\partial \rho_\alpha}{\partial t} + \nabla \cdot (\rho_\alpha \mathbf{u}_\alpha) = 0 \tag{2}$$

$$\frac{\partial \rho_\alpha \mathbf{u}_\alpha}{\partial t} + \nabla \cdot (\rho_\alpha \mathbf{u}_\alpha \mathbf{u}_\alpha + p_\alpha \mathcal{I}) = \frac{\rho_\alpha q_\alpha}{m_\alpha}(\mathbf{E} + \mathbf{u}_\alpha \times \mathbf{B}) \tag{3}$$

$$\frac{\partial \varepsilon_\alpha}{\partial t} + \nabla \cdot ((\varepsilon_\alpha + p_\alpha)\mathbf{u}_\alpha) = \frac{\rho_\alpha q_\alpha}{m_\alpha}\mathbf{u}_\alpha \cdot \mathbf{E}, \tag{4}$$

where ρ_α is the mass density, which is the product of the particle number density and particle mass, $\rho_\alpha = n_\alpha m_\alpha$, $\mathbf{u}_\alpha$ is the fluid velocity vector, p_α is the pressure, which is the product of the particle number density and temperature, $p_\alpha = n_\alpha T_\alpha$, $\mathcal{I}$ is the identity matrix, and ε_α is the total energy given by

$$\varepsilon_\alpha = \frac{p_\alpha}{\Gamma - 1} + \frac{1}{2}\rho_\alpha u_\alpha^2, \tag{5}$$

where Γ is the ratio of specific heats. Maxwell's equations govern the evolution of the electric and magnetic fields.

$$\frac{1}{c^2}\frac{\partial \mathbf{E}}{\partial t} - \nabla \times \mathbf{B} = -\mu_0 \sum_\alpha \frac{q_\alpha}{m_\alpha}\rho_\alpha \mathbf{u}_\alpha \tag{6}$$

$$\frac{\partial \mathbf{B}}{\partial t} + \nabla \times \mathbf{E} = 0 \tag{7}$$

$$\epsilon_0 \nabla \cdot \mathbf{E} = \sum_\alpha \frac{q_\alpha}{m_\alpha}\rho_\alpha \tag{8}$$

$$\nabla \cdot \mathbf{B} = 0 \tag{9}$$

where μ_0 and ϵ_0 are the vacuum permeability and permittivity, respectively, and $c = (\mu_0 \epsilon_0)^{-1/2}$ is the speed of light. Maxwell's equations are overdetermined with six scalar unknowns and eight equations. The two divergence expressions are analytically satisfied over time if they are initially satisfied, but computational round-off errors can produce fields that violate the divergence expressions. To clean the divergence errors, Maxwell's equations are cast in a purely hyperbolic form as described in Ref. [43].

$$\frac{\partial \mathbf{B}}{\partial t} + \nabla \times \mathbf{E} + \gamma \nabla \Psi = 0 \tag{10}$$

$$\frac{1}{c^2}\frac{\partial \mathbf{E}}{\partial t} - \nabla \times \mathbf{B} + \chi \nabla \Phi = -\mu_0 \sum_\alpha \frac{q_\alpha}{m_\alpha}\rho_\alpha \mathbf{u}_\alpha \tag{11}$$

$$\frac{1}{\chi}\frac{\partial \Phi}{\partial t} + \nabla \cdot \mathbf{E} = \sum_\alpha \frac{q_\alpha}{m_\alpha}\rho_\alpha \tag{12}$$

$$\frac{1}{\gamma c^2}\frac{\partial \Psi}{\partial t} + \nabla \cdot \mathbf{B} = 0 \tag{13}$$

Error correction potentials Φ and Ψ are introduced to propagate the divergence errors out of the computational domain. The divergence error propagation speeds are set by the dimensionless positive parameters χ and γ, which are set to values greater than one. Larger values better preserve the divergence constraints on the fields, and zero effectively eliminates any divergence corrections. The characteristic wave speeds for the purely hyperbolic Maxwell's equations are $\{\pm c, \pm \chi c, \pm \gamma c\}$.

The governing equations of the multi-fluid plasma model can be cast in balance law form as

$$\frac{\partial \mathbf{Q}}{\partial t} + \nabla \cdot \mathcal{F}(\mathbf{Q}) = \mathbf{S}(\mathbf{Q}), \tag{14}$$

where $\mathbf{Q}$ is the solution vector, $\mathcal{F}$ is the flux tensor and $\mathbf{S}$ is the source vector. The solution vector in Eq. (14) represents the union of the solution vector for electromagnetic field equations and the vector of the conserved variables for each fluid, e.g. electron fluid, ion fluid,..., such that $\mathbf{Q} = [\mathbf{Q}_{EM}, \mathbf{Q}_e, \mathbf{Q}_i, \ldots]$. The homogeneous version of Eq. (14) with $\mathbf{S} = 0$ is hyperbolic, meaning that the flux Jacobian, $\partial \mathcal{F}/\partial \mathbf{Q}$, is diagonalizable with real eigenvalues and has a complete set of eigenvectors. The source term in Eq. (14) depends only on $\mathbf{Q}$ and not on derivatives of $\mathbf{Q}$, such that $\mathbf{S}$ can be evaluated locally.

The eigenvalues of the flux Jacobian ($\partial \mathcal{F}/\partial \mathbf{Q}$) are the characteristic speeds of the multi-fluid equation system, and are combinations of the species' flow speeds, acoustic speeds, light speed, and divergence error propagation speeds. The eigen-

B-11

values of the source Jacobian ($\partial\mathbf{S}/\partial\mathbf{Q}$) are all purely imaginary [18,14] and the first three are $0, \pm i\omega_p$, where $\omega_p^2 = \sum_\alpha \omega_{p\alpha}^2$ and

$$\omega_{p\alpha} = \sqrt{\frac{\rho_\alpha q_\alpha^2}{\epsilon_0 m_\alpha^2}}, \tag{15}$$

which is the plasma frequency of the species α.

The imaginary eigenvalues of the source Jacobian indicate that dispersive behavior is physically expected and not necessarily a numerical artifact. This dispersion is due to the presence of a wide variety of plasma waves that result from the interaction of the charged fluids with the electromagnetic fields.

The characteristic timescales for the multi-fluid plasma model span a large range from extremely fast electromagnetic waves and electron response to much slower ion and neutral responses. The multi-fluid plasma model is mathematically stiff, which presents a challenge for numerical methods; explicit methods must resolve the shortest timescale, and implicit methods must invert a poorly conditioned matrix.

3. Blended finite element method

The stiffness introduced by the disparate timescales can be addressed by decomposing the multi-fluid plasma model according to physically expected temporal and spatial characteristics. The BFEM accomplishes this physics-based decomposition by modeling the ion and neutral fluids using a DG method with explicit Runge–Kutta time integration and modeling the electron fluid and the electromagnetic fields using a CG method with implicit time integration [44]. Since the fast moving electrons and the fields do not form spatial discontinuities, such as shocks, limiters are not needed and the Jacobian for a Newton solver is well-conditioned. This allows for larger time steps compared to an explicit method. The CFL constraint for explicit treatment of only the massive fluid species is less restrictive in this BFEM than in the case where all variables are evolved explicitly. Furthermore, the evolution of the ions and neutrals is often the goal of the simulation, so the temporal resolution provided by the explicit time steps is appropriate for these species. Source terms in the governing equations of the multi-fluid plasma model couple the fluids and fields, as described in Sec. 2. The BFEM computes the source terms in a manner that is consistent with both the CG and DG methods.

3.1. Continuous Galerkin finite element method

The finite element method discretizes the computational domain into elements and the solution is expanded within each element, Ω, in a series of polynomial basis functions. The order of the polynomials defines the spatial order of accuracy of the numerical method. The CG method enforces the solution to be continuous across element boundaries providing C^0 continuity. Continuity of derivatives across the element boundaries is not enforced [45].

The governing equations for the electron fluid and the electromagnetic fields of the multi-fluid plasma model are expressed by Eq. (14) where the solution vector is limited to $\mathbf{Q}^f = [\mathbf{Q}_{EM}, \mathbf{Q}_e]$. This subset of the governing equations accounts for the fast dynamics, denoted by the f superscript on the solution vector. The equation is then written as

$$\frac{\partial \mathbf{Q}^f}{\partial t} + \frac{\partial \mathcal{F}}{\partial \mathbf{Q}^f} \cdot \frac{\partial \mathbf{Q}^f}{\partial \mathbf{x}} = \mathbf{S}^f, \tag{16}$$

where $\partial\mathcal{F}/\partial\mathbf{Q}^f$ is the flux Jacobian. Since the flux $\mathcal{F}$ is a tensor of rank-2, $\mathcal{F}_{ij}$ in index notation, the flux Jacobian is a tensor of rank-3, $\mathcal{A}_{ijk} = \partial\mathcal{F}_{ki}/\partial Q_j^f$. Equation (16) can be expressed as

$$\frac{\partial Q_i^f}{\partial t} + \mathcal{A}_{ijk} \frac{\partial Q_j^f}{\partial x_k} = S_i, \tag{17}$$

where repeated indices in a term are summed, as usual in Einstein notation. The solution vector is expanded within each element using polynomial functions

$$\mathbf{Q}^f(t, x) = \sum_{j=1}^m \mathbf{q}_j(t)\psi_j(x), \tag{18}$$

where ψ_j are the spatial basis functions and $\mathbf{q}_j$ are the time-dependent coefficients. The f superscript is omitted from the temporal coefficients to simplify the notation. If Lagrange interpolation polynomials are used as the basis functions, $\mathbf{q}_j$ represent the values of the solution vector $\mathbf{Q}^f$ at each nodal location x^j. The Lagrange polynomials are defined as

$$\psi_j(x) = \prod_{k=1, k\neq j}^m \frac{x - x^k}{x^j - x^k}, \tag{19}$$

B-12

where x^j and x^k are nodal coordinates. The polynomials have the property that $\psi_j(x^i) = \delta_{ij}$, where δ_{ij} is the Kronecker delta and x^i is the nodal location. An $m-1$ order polynomial basis function is represented by m nodes.

The finite element method proceeds by multiplying the governing equation, Eq. (16), by test functions and integrating over each element volume

$$\int_\Omega d\mathbf{x} v_i \frac{\partial \mathbf{Q}^f}{\partial t} + \int_\Omega d\mathbf{x} v_i \frac{\partial \mathcal{F}}{\partial \mathbf{Q}^f} \cdot \frac{\partial \mathbf{Q}^f}{\partial \mathbf{x}} = \int_\Omega d\mathbf{x} v_i \mathbf{S}^f. \tag{20}$$

This integral equation is the weak form of the governing equation. The Galerkin method chooses the test functions to be the same as the basis functions, $v_i = \psi_i$, so the weak form of the governing equation with the solution expansion becomes

$$\int_\Omega d\mathbf{x} \psi_i \frac{\partial}{\partial t} \left(\sum_{j=1}^m \mathbf{q}_j \psi_j \right) + \int_\Omega d\mathbf{x} \psi_i \frac{\partial \mathcal{F}}{\partial \mathbf{Q}^f} \cdot \frac{\partial}{\partial \mathbf{x}} \left(\sum_{j=0}^m \mathbf{q}_j \psi_j \right) = \int_\Omega d\mathbf{x} \psi_i \mathbf{S}^f, \tag{21}$$

which is the element equation. Since the nodal values $\mathbf{q}_j$ are independent of x, the element equation can be rewritten as

$$\sum_{j=1}^m \left[\int_\Omega d\mathbf{x} \psi_i \psi_j \right] \frac{\partial \mathbf{q}_j}{\partial t} + \sum_{j=1}^m \left[\int_\Omega d\mathbf{x} \psi_i \frac{\partial \mathcal{F}}{\partial \mathbf{Q}^f} \cdot \frac{\partial \psi_j}{\partial \mathbf{x}} \right] \mathbf{q}_j = \int_\Omega d\mathbf{x} \psi_i \mathbf{S}^f. \tag{22}$$

The first integral is the element mass matrix for element e,

$$\mathcal{M}_{ij}^e = \int_\Omega d\mathbf{x} \psi_i \psi_j. \tag{23}$$

The element equation is integrated from time t to $t + \Delta t$, i.e. time level n to $n+1$, to give

$$\sum_{j=1}^m \mathcal{M}_{ij}^e \int_t^{t+\Delta t} dt \frac{\partial \mathbf{q}_j}{\partial t} = \sum_{j=1}^m \mathcal{M}_{ij}^e \left(\mathbf{q}_j^{n+1} - \mathbf{q}_j^n \right). \tag{24}$$

Moving the spatially dependent terms of Eq. (22) to the right-hand side of the equation, integrating over Δt, and combining with the previous result yields

$$\sum_{j=1}^m \mathcal{M}_{ij}^e \frac{\mathbf{q}_j^{n+1} - \mathbf{q}_j^n}{\Delta t} = -\sum_{j=1}^m \left[\int_\Omega d\mathbf{x} \psi_i \frac{\partial \mathcal{F}}{\partial \mathbf{Q}^f} \cdot \frac{\partial \psi_j}{\partial \mathbf{x}} \right] \mathbf{q}_j + \int_\Omega d\mathbf{x} \psi_i \mathbf{S}^f, \tag{25}$$

where the right-hand side is computed using values appropriately averaged over the time interval $[t, t + \Delta t]$.

The CG method as described by Eq. (25) introduces no dissipation, and in regions of sharp gradients high frequency oscillations (Gibbs phenomenon) can develop. These oscillations indicate numerical dispersion and can be dampened by adding an artificial dissipation. This is achieved by introducing a term to Eq. (14) that consists of a second derivative of the conserved variables,

$$\frac{\partial \mathbf{Q}^f}{\partial t} + \nabla \cdot \mathcal{F} = \mathbf{S}^f + \nabla \cdot \left(\kappa \nabla \mathbf{Q}^* \right), \tag{26}$$

where κ is the artificial diffusivity coefficient and is chosen to minimize the impact on the physical solution while minimizing numerical dispersion. The vector $\mathbf{Q}^*$ indicates that the variables being dissipated may be a subset of $\mathbf{Q}^f$.

Multiplying the dissipation term by the test functions, integrating over the element volume, and expanding $\mathbf{Q}^*$ with basis functions yields

$$\int_\Omega d\mathbf{x} \psi_i \frac{\partial}{\partial \mathbf{x}} \cdot \kappa \frac{\partial \mathbf{Q}^*}{\partial \mathbf{x}} = -\sum_{j=1}^m \left[\int_\Omega d\mathbf{x} \kappa \frac{\partial \psi_i}{\partial \mathbf{x}} \cdot \frac{\partial \psi_j}{\partial \mathbf{x}} \right] \mathbf{q}_j^* + \sum_{j=1}^m \left[\oint_{\partial\Omega} \mathbf{A} \cdot \frac{\partial \psi_j}{\partial \mathbf{x}} \kappa \psi_i \right] \mathbf{q}_j^*, \tag{27}$$

where the last term accounts for boundary conditions and is assumed to be equal across element boundaries since the solution for the electron species and the electromagnetic fields has C^0 continuity. Enforcing C^0 continuity is simplified by using the nodal representation given by Eq. (18) and placing nodes at the element boundaries. Nodes from neighboring elements overlap and the values at the overlapping nodes are set equal.

B-13

The CG method applied to the electron fluid and the electromagnetic fields of the two-fluid plasma model can be expressed in a simpler form by defining the element dissipation matrix

$$\mathcal{D}_{ij}^e = -\int_\Omega d\mathbf{x} \kappa \frac{\partial \psi_i}{\partial \mathbf{x}} \cdot \frac{\partial \psi_j}{\partial \mathbf{x}}, \tag{28}$$

and the element source vector

$$\mathbf{f}_i^e = \int_\Omega d\mathbf{x} \psi_i \mathbf{S}^f. \tag{29}$$

The element evolution equation can be written as

$$\mathcal{M}_{ij}^e \frac{\mathbf{q}_j^{n+1} - \mathbf{q}_j^n}{\Delta t} = -\left[\int_\Omega d\mathbf{x} \psi_i \frac{\partial \mathcal{F}}{\partial \mathbf{Q}^f} \cdot \frac{\partial \psi_j}{\partial \mathbf{x}}\right] \mathbf{q}_j + \mathbf{f}_i^e + \mathcal{D}_{ij}^e \mathbf{q}_j^* + \left[\oint_{\partial\Omega} \mathbf{A} \cdot \frac{\partial \psi_j}{\partial \mathbf{x}} \kappa \psi_i\right] \mathbf{q}_j^*, \tag{30}$$

where the summation over index j is assumed. Let $\mathbf{R}^e(\overline{\mathbf{q}_j})$ be the right-hand side of Eq. (30). $\mathbf{R}^e(\overline{\mathbf{q}_j})$ is computed using solution values that approximate the appropriately averaged values over the time interval $[t, t + \Delta t]$. Nodal values $\mathbf{q}_j^{n+1}$ are solved simultaneously for all elements. The element equations are assembled into a global system with global mass $\mathcal{M}$ and dissipation $\mathcal{D}$ matrices. The integral terms and the source vector $\mathbf{f}_i$ in Eq. (30) are evaluated by Gauss–Legendre quadrature rules and are also assembled into a global vectors. The correspondence between the element and global matrices is expressed through a connectivity matrix whose coefficient b_{ij} is the global node number corresponding to node j of element i. The element matrix coefficients $\mathcal{M}_{kl}^e$ are combined to give the global matrix according to

$$\mathcal{M}_{mn} = \sum_{e=1}^{E} \sum_{k=1}^{N} \sum_{l=1}^{N} \mathcal{M}_{kl}^e, \tag{31}$$

where global node numbers are defined using the connectivity matrix, $m = b_{ek}$, $n = b_{el}$. The mass matrix and dissipation matrices are assembled independently of each other. The total number of elements is E and the number of nodes per element is N. The resulting global matrix equation

$$\mathcal{M} \frac{\mathbf{q}^{n+1} - \mathbf{q}^n}{\Delta t} = \mathbf{R}(\overline{\mathbf{q}}) \tag{32}$$

can be solved to yield the solution for the electron fluid and electromagnetic field at the time level $n + 1$.

Time integration for the CG method requires a matrix inversion to solve the global matrix equation even if the RHS is explicitly defined as $\mathbf{R}(\mathbf{q}_j^n)$, while an implicit formulation only slightly complicates the solution method. However, an implicit solution method permits time steps larger than the short timescales dictated by the fast response of the electron fluid and electromagnetic field. Avoiding this limitation is a primary motivation for the BFEM and the physics-based decomposition.

The implicit formulation of the BFEM uses the θ-method [46] to solve the global evolution equation, which is written as

$$\mathcal{M} \frac{\mathbf{q}^{n+1} - \mathbf{q}^n}{\Delta t} = (1-\theta)\mathbf{R}(\mathbf{q}^n) + \theta \mathbf{R}(\mathbf{q}^{n+1}). \tag{33}$$

Choosing $\theta = 1$ gives the implicit backward Euler method, and $\theta = 0$ gives the explicit forward Euler method. Setting $\theta = 1/2$ gives the Crank–Nicolson method [47]. Because of its higher temporal accuracy, $\theta = 1/2$ is chosen for the BFEM implementation.

A Newton–Raphson method [48] is used to solve for $\mathbf{q}^{n+1}$. The Newton method yields an iterative process to find successively better approximations to the roots of a real-valued residual function, which for Eq. (33) is given by

$$\mathbf{G}(\mathbf{q}^{n+1}) = \frac{\mathcal{M}}{\Delta t}(\mathbf{q}^{n+1} - \mathbf{q}^n) - (1-\theta)\mathbf{R}(\mathbf{q}^n) - \theta \mathbf{R}(\mathbf{q}^{n+1}). \tag{34}$$

The Jacobian is

$$\mathcal{J}(\mathbf{q}^{n+1}) = \frac{\partial \mathbf{G}(\mathbf{q}^{n+1})}{\partial \mathbf{q}^{n+1}} = \frac{\mathcal{M}}{\Delta t} - \theta \frac{\partial \mathbf{R}(\mathbf{q}^{n+1})}{\partial \mathbf{q}^{n+1}}. \tag{35}$$

The Newton method is formulated as

$$\mathcal{J}(\mathbf{q}^m)\Delta \mathbf{q} = -\mathbf{G}(\mathbf{q}^m), \tag{36}$$

B-14

where $\Delta\mathbf{q} = \mathbf{q}^m - \mathbf{q}^n$ and m is an iteration index. When the iteration equation, Eq. (36), converges, the solution at the next time level is given by

$$\mathbf{q}^{n+1} = \mathbf{q}^n + \Delta\mathbf{q}, \tag{37}$$

using the value from the previous time level and the solution for $\Delta\mathbf{q}$ from the Newton method.

3.2. Discontinuous Galerkin finite element method

Similar to the CG method, the DG method discretizes the computational domain into elements and expands the solution in a series of polynomial basis functions. However, the DG method does not enforce continuity of the solution across element boundaries. Unique solutions to the weak form of the governing equations are determined within each element by specifying element boundary fluxes that are defined in a consistent manner – the flux leaving an element equals the flux entering the adjacent element, e.g. Ref. [11]. The DG method that is incorporated into the BFEM is similar to the implementations of Refs. [49,35,50].

The DG method evolves the ion and neutral fluids of the multi-fluid plasma model. The governing equations are expressed by Eq. (14) where the vector of conserved variables excludes the electron fluid and electromagnetic fields. Namely,

$$\mathbf{Q}^s = [\mathbf{Q}_{i1}, \mathbf{Q}_{i2}, \ldots, \mathbf{Q}_{n1}, \mathbf{Q}_{n2}, \ldots],$$

where multiple ion and neutral species are possible. This subset of the governing equations accounts for the slower dynamics. The vector of conserved variables is expanded within each element using polynomial functions as

$$\mathbf{Q}^s(t, x) = \sum_{j=1}^{m} \mathbf{q}_j(t)\phi_j(x), \tag{38}$$

where ϕ_j are the spatial basis functions and $\mathbf{q}_j$ are the temporal coefficients. The s superscript, denoting slow dynamics, is omitted from the temporal coefficients to simplify the notation. The DG method uses a modal representation of the solution within an element, unlike the nodal representation of the CG method; therefore, the temporal coefficients in Eq. (38) do not directly represent values of the solution vector $\mathbf{Q}^s$. A modal representation simplifies the application of flux limiters [49,50]. Legendre polynomials of order $m-1$ are used as basis functions because they form an orthogonal basis,

$$\int_0^1 dx\phi_i\phi_j = \frac{1}{2j+1}\delta_{ij}, \tag{39}$$

which can be normalized to the element volume.

The governing equations of Eq. (14) that evolve $\mathbf{Q}^s$ are multiplied by the test functions, which are the same as the basis functions, and integrated over each element volume,

$$\int_\Omega d\mathbf{x}\phi_i\frac{\partial\mathbf{Q}^s}{\partial t} + \int_\Omega d\mathbf{x}\phi_i\nabla\cdot\mathcal{F} = \int_\Omega d\mathbf{x}\phi_i\mathbf{S}^s. \tag{40}$$

Integration by parts is applied to the second term and the above equation becomes

$$\int_\Omega d\mathbf{x}\phi_i\frac{\partial\mathbf{Q}^s}{\partial t} + \oint_{\partial\Omega} d\mathbf{A}\cdot\mathcal{F}\phi_i - \int_\Omega d\mathbf{x}\nabla\phi_i\cdot\mathcal{F} = \int_\Omega d\mathbf{x}\phi_i\mathbf{S}^s. \tag{41}$$

When the solution vector is expanded using Eq. (38) and the orthogonality of the basis functions are taken into account the first term of Eq. (41) simplifies to

$$\int_\Omega d\mathbf{x}\phi_i\frac{\partial\mathbf{Q}^s}{\partial t} = \sum_{j=1}^{m}\frac{\partial\mathbf{q}_j}{\partial t}\int_\Omega d\mathbf{x}\phi_i\phi_j = \frac{\partial\mathbf{q}_i}{\partial t}\frac{V^\Omega}{2i+1}, \tag{42}$$

where V^Ω is the volume of the finite element. The surface integral in Eq. (41) accounts for the fluxes across element boundaries, which are computed using a numerical flux, such as an approximate Riemann flux [1,51] or a Lax–Friedrichs flux [52]. The surface integral is evaluated using Gauss–Legendre quadrature over the element's surface. Simpler Lax–Friedrichs fluxes are typically adequate and are given at any point along the surface by

$$\mathcal{F} = \frac{1}{2}\left[\mathcal{F}(\mathbf{Q}_e^+) - \mathcal{F}(\mathbf{Q}_{e+1}^-)\right] - \frac{1}{2}|\lambda|(\mathbf{Q}_e^+ - \mathbf{Q}_{e+1}^-), \tag{43}$$

where $|\lambda|$ is the maximum characteristic speed (eigenvalue of the flux Jacobian) using surface values averaged from elements e and $e+1$, and superscripts $+$ and $-$ represent the values at the upper and lower boundaries of the elements. The volume integrals in Eq. (41) are also evaluated using Gauss–Legendre quadrature rules.

Using the relation given by Eq. (42) and rearranging the temporally and spatially dependent terms, Eq. (41) can be written as

$$\frac{\partial \mathbf{q}_i}{\partial t} = \frac{2i+1}{V^\Omega} \left(\int_\Omega d\mathbf{x} \phi_i \mathbf{S}^s - \oint_{\partial\Omega} d\mathbf{A} \cdot \mathcal{F}\phi_i + \int_\Omega d\mathbf{x} \nabla\phi_i \cdot \mathcal{F} \right) \equiv \mathbf{L}_i(\mathbf{Q}^s), \tag{44}$$

where $\mathbf{L}_i(\mathbf{Q}^s)$ is an operator containing all the spatially dependent term. An attractive feature of the DG method is the data locality of the spatial operator, which has a spatial dependency that is limited to nearest neighbor elements. The equation $\partial \mathbf{q}_i/\partial t = \mathbf{L}_i(\mathbf{Q}^s)$ can be integrated in time to advance the solution from time level n to $n+1$.

The time integration for the DG method uses the second order total variation bounded (TVB) Runge–Kutta time integration scheme [11], which is given as

$$\mathbf{q}_i^* = \mathbf{q}_i^n + \Delta t \mathbf{L}_i(\mathbf{Q}^{sn}) \tag{45}$$

$$\mathbf{q}_i^{n+1} = \frac{1}{2}\mathbf{q}_i^* + \frac{1}{2}\mathbf{q}_i^n + \frac{1}{2}\Delta t \mathbf{L}_i(\mathbf{Q}^{s*}), \tag{46}$$

where $\mathbf{Q}^{s*}$ is evaluated by Eq. (38) using the temporal coefficients $\mathbf{q}_i^*$.

The CFL stability condition of the DG method limits the CFL number as

$$\frac{\lambda_{max}^s \Delta t}{\Delta x} \leq \frac{1}{2p-1}, \tag{47}$$

where Δx is the size of the element, p is the order of the basis function, and λ_{max}^s is the largest characteristic speed. The system of equations being solved by the explicit RKDG method only includes the slower responding ion and neutral species and excludes the fast dynamics of the electron fluid and electromagnetic field. Therefore, the fastest characteristic speed for this subset of the governing equations is an ion or neutral acoustic speed and is typically much slower than the fastest characteristic speed for the complete system discussed in Sec. 2. With the explicit treatment of the ions and neutrals, the maximum time step size that satisfies Eq. (47) can be significantly larger than the time step size for an explicit treatment of the full multi-fluid plasma model.

3.3. Source treatment for the continuous and discontinuous Galerkin methods

The fluids and fields couple through the source terms of the governing equations. Source terms couple the solution variables $\mathbf{Q}^f$ that represent the fast dynamics of the system to the solution variables $\mathbf{Q}^s$ that represent the slow dynamics of the system. Therefore, the CG and DG methods must provide an accurate source treatment that is consistent between the two methods. Although the CG method uses a nodal representation and the DG uses a modal representation, converting the variables between the representations to compute the source terms is unnecessary.

Both the CG and DG methods solve weak formulations of the governing equations, so the source terms appear as integrals over the element volume in Eqs. (29) and (41). The source term integrals are computed numerically using quadrature rules, which require evaluating the integrand and hence the solution vector at specified spatial locations. The solution expansions given by Eqs. (18) and (38) allow the evaluation of $\mathbf{Q}^f$ and $\mathbf{Q}^s$ at any spatial position within an element. The source term integrands are thereby evaluated at the quadrature locations using the nodal and modal representations directly to compute the integrals.

4. Benchmarks and performance of the BFEM

The BFEM is applied to a set of problems with known analytic solutions. Spatial and temporal convergence tests are first performed to verify that the order of accuracy of the solution is in agreement with analytical results. The BFEM is benchmarked against the one-dimensional two-fluid plasma soliton problem [53] and the two-fluid electromagnetic shock tube problem [1,50]. These tests compare the computational time and accuracy of the BFEM with that of conventional finite volume and pure DG methods. The tests also evaluate the effects of the artificial dissipation in the CG portion of the method, and investigate the consequences of the implicit time integration on the solution. In addition, a three-fluid species separation problem is solved, which demonstrates the computational savings potential of the BFEM in a realistic application.

4.1. Linear advection: convergence study

The linear advection equation is a simple homogeneous hyperbolic equation that provides a test case to study the spatial and temporal convergence of the solution as the polynomial order for the solution is increased [35]. The DG and
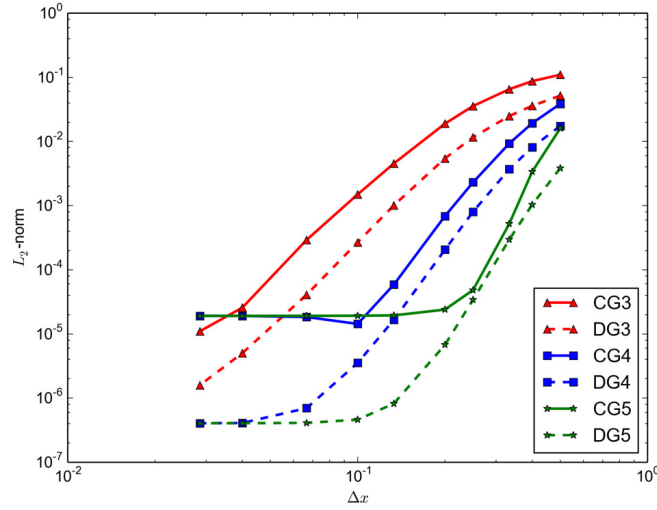
Fig. 1. Log–log plot of the L_2-norm of the error as a function of element size, Δx, for the linear advection problem using a fixed time step of $\Delta t = 1/800$ and spatial orders 3, 4, and 5 for the CG and the DG methods. The artificial dissipation coefficient used with the CG method is $\kappa = 10^{-7}$. The linear portion of each line has a slope that corresponds to the order of accuracy of the numerical method. Both methods converge as expected. Higher order CG methods saturate at larger values of Δx because the dissipation is applied at each node, and higher order methods have more nodes and therefore more dissipation.

CG components of the BFEM are separately used to solve the linear advection equation. The accuracy of the solution is determined by the order of accuracy of the numerical method. The one-dimensional linear advection equation is given by

$$\frac{\partial Q}{\partial t} + \frac{\partial Q}{\partial x} = 0, \tag{48}$$

where Q is a scalar variable and the advection speed is set to one. A Gaussian pulse is initialized with $Q(x) = e^{-10(x-2)^2}$ on a domain $[0, 10]$. The pulse's peak starts at $x = 2$ and propagates $x = 8$ over a total time interval of $t \in [0, 6]$ and is compared to the analytical solution given as $\hat{Q}(x) = e^{-10(x-8)^2}$. The error in the numerical solution is calculated by evaluating the L_2-norm as

$$||\Delta Q||_2 = \sqrt{\frac{1}{n} \sum_{i=1}^{n} \left(\hat{Q}(x_i) - Q(x_i) \right)^2}. \tag{49}$$

where $\hat{Q}$ is the analytical solution and Q is the numerical solution. The positions x_i represents the quadrature locations for both the DG and CG methods, and n is the total number of quadrature points [35].

Fig. 1 shows the L_2-norm of the error for the advected pulse using a fixed $\Delta t = 1/800$ with different order polynomial spatial basis functions for the DG and the CG methods. Using a fixed time step size isolates the spatial convergence. The plot shows that for basis functions of the same order the CG and DG methods converge at the same rate as the grid is refined. The slope of the curves for similar order DG and CG should be the same even though the DG method is slightly more accurate than then CG one. The L_2-norm of the CG method plateaus around 10^{-5} due to the artificial numerical dissipation, which damps the solution and decreases the peak of the original Gaussian shape. The required value of κ for stability decreases as the polynomial order is increased. The fixed value of $\kappa = 10^{-7}$ is the minimum value required for the coarsest grid for spatial order three and used for all simulations for consistency, allowing only on variable to change.

To test the temporal convergence rate, a fixed time step size is chosen. The time step size is set as $\Delta t = \Delta x$ for all polynomial orders of the spatial basis functions, which isolates the temporal convergence. For the CG method, a value of $\theta = 0.5$ is selected to give the second-order accurate Crank–Nicolson method. The DG method uses a second-order TVB Runge–Kutta time integration. Fig. 2 shows the calculated L_2-norm for the advection problem using a fixed CFL number. The slope of the lines for both methods is two for all polynomial orders of the spatial basis functions. The convergence rates of the error for a fixed CFL verify that the temporal integration is second-order accurate for the implicit CG method as well as the explicit DG method.

4.2. Plasma soliton: accuracy and computational cost

The propagation of a one-dimensional plasma soliton [53] is modeled using the multi-fluid plasma model. This problem is used to study the accuracy and computational cost of the BFEM as compared with an explicit DG method. The soli-
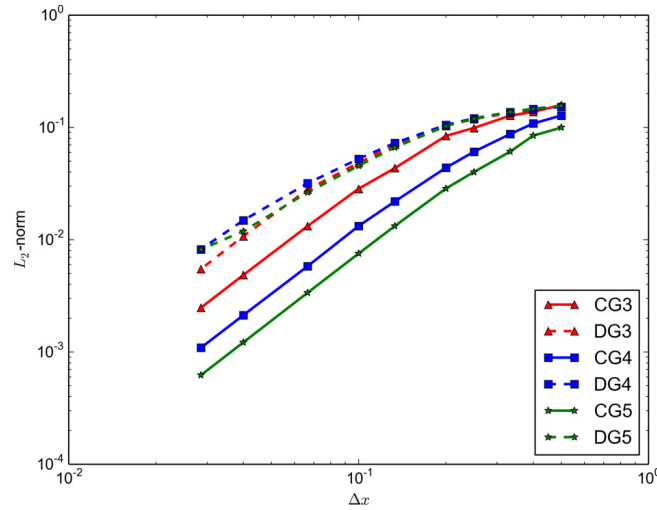
Fig. 2. Log–log plot of the L_2-norm of the error as a function of element size, Δx, for the linear advection problem using a fixed CFL of one and spatial orders 3, 4, and 5 for the CG and the DG methods. The artificial diffusivity coefficient used with the CG method is $\kappa = 10^{-7}$. The linear portions of all lines have a slope of two corresponding to the temporal order of accuracy of both the implicit CG and explicit DG portions of the BFEM method.

Table 1
Total computational time and time savings for plasma soliton simulations using the BFEM as compared to an explicit DG method for different values of electron to ion mass ratio and of the ratio of the speed of light to the ion sound speed.

Case	m_i/m_e	c/c_{si}	DG time (s)	BFEM time (s)	BFEM cost over DG
1	25	$10/\sqrt{2}$	0.32	37.7	+11681%
2	100	$10/\sqrt{2}$	1.28	37.7	+2845%
3	500	$10/\sqrt{2}$	6.82	37.7	+452.8%
4	1000	$10/\sqrt{2}$	12.4	38.2	+208.1%
5	1836	$10/\sqrt{2}$	23.5	40.4	+71.91%
6	3672	$10/\sqrt{2}$	47.2	39.2	−16.95%
7	3672	$100/\sqrt{2}$	520	265	−49.04%
8	3672	$1000/\sqrt{2}$	5274	2735	−48.14%

ton consists of a two-fluid plasma composed of an electron fluid and an ion fluid, and offers a simple test case for the BFEM. The expected solution is smooth, which requires minimal artificial dissipation for achieving stable solutions with the BFEM, eliminating the detrimental effect on convergence that is described in the previous section. The artificial diffusivity coefficient κ, used in Eq. (26), is set to a value of 10^{-10}.

The normalized variables of the two-fluid plasma model are initialized with a uniform transverse magnetic field $B_z = 1.0$, uniform ion and electron temperatures $T_i = T_e = 0.01$, no fluid velocity $\mathbf{u}_i = \mathbf{u}_e = \mathbf{0}$, and unitary charges $q_i = -q_e = 1$. The initial particle number densities produce a Gaussian pulse on top of a background value $n_i = n_e = 1 + e^{-10(x-6)^2}$ on a domain $x \in [0, 12]$. The ratio of specific heats as used in Eq. (5) is set to $\Gamma = 2$. The simulation uses 512 second-order elements both for the BFEM and for the comparison case using the DG method. Periodic boundary conditions are used.

It is common practice in plasma simulations to artificially decrease the ion to electron mass ratio as well as the ratio of speed of light to ion sound speed [54]. This is done to relax the numerical time step restriction imposed by electron plasma frequency and the speed of light. Using an artificial mass ratio and/or an artificial speed of light can, however, affect the physics of the problem. To evaluate the effect of using physical and unphysical parameters, the computational cost of the BFEM versus the DG method is compared for artificial and realistic mass and speed ratios.

Since the implicit CG component of the BFEM allows time steps that are unconstrained by the electromagnetic fields or electron fluid, computational savings of the BFEM over the explicit DG method are achieved when using physical values for the ion to electron mass ratio and the speed of light to ion sound speed ratio. Table 1 shows the computational time needed to advance the solution from normalized time $t = 0$ to $t = \sqrt{2}/120 L/c_{si}$ for different mass ratios and normalized speeds of light. The ion sound speed is defined as $c_{si} = \sqrt{\Gamma p_i/\rho_i}$. For a mass ratio of 25, the DG method is considerably faster than the BFEM; however, as the mass ratio is increased by decreasing the electron mass, the computational time of the DG method increases while that of the BFEM remains about the same. This is due to the fact that the decreasing electron mass increases the electron plasma frequency, which needs to be resolved when explicit time integration is used. The speed of light to ion sound speed ratio has a bigger impact on the computational time than the mass ratio. The explicit DG method requires that the time step size be decreased as the speed of light increases to satisfy the CFL stability condition given by
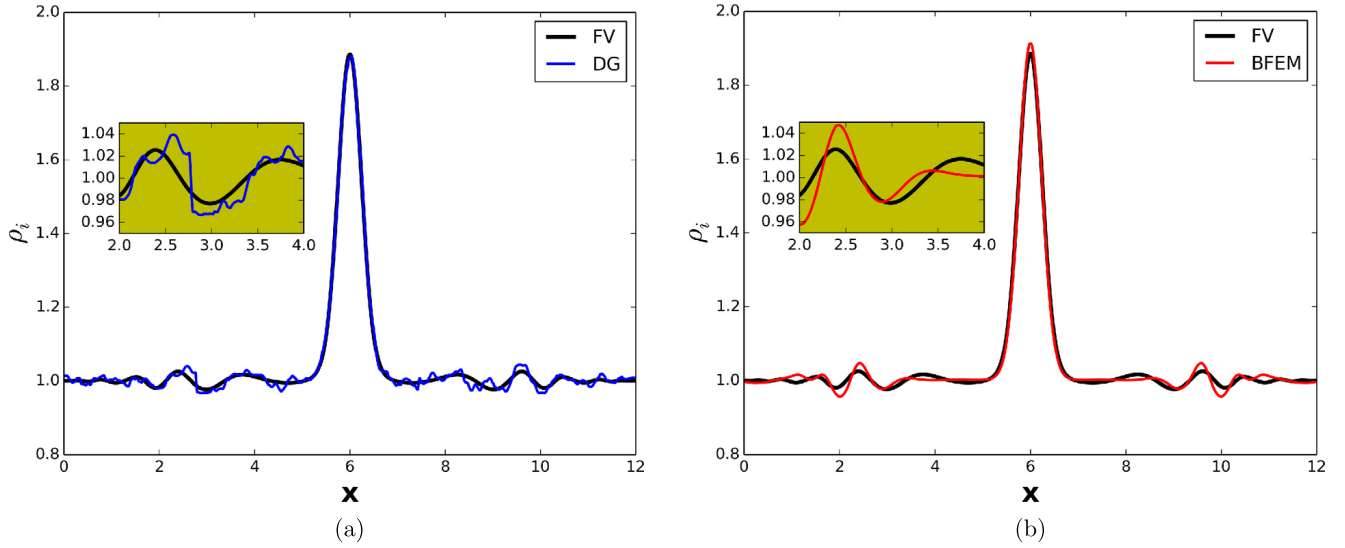
Fig. 3. Ion density profiles for the plasma soliton problem at $t = \sqrt{2}/30L/c_{si}$ are shown for the explicit DG solution and the BFEM solution using 512 second-order elements. The simulations use a realistic mass ratio and normalized speed of light. The solutions are compared to a converged FV solution of 5000 cells. Ion density fluctuations propagate from the center of the domain towards the boundaries. Both methods resolve the oscillations of the problem, but the BFEM exhibits phase error since it does not resolve the electron plasma frequency. Second-order BFEM is used.
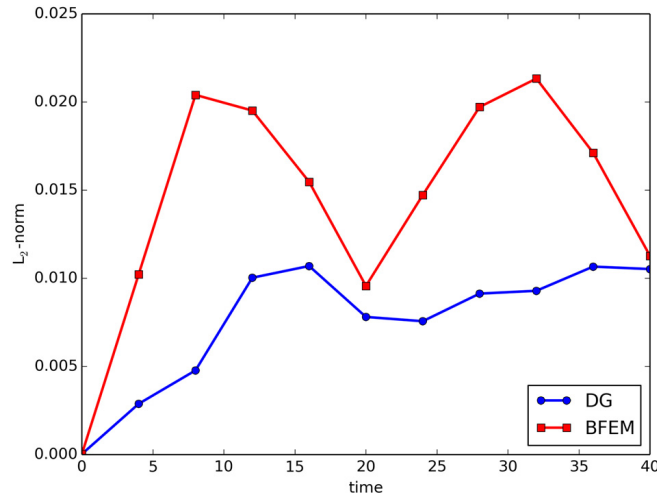
Fig. 4. L_2-norm of the relative error, see Eq. (50), in the ion density solutions for the plasma soliton problem from the DG method and the BFEM as a function of time. Realistic values for the ion to electron mass ratio and the speed of light to ion sound speed ratio are used. The DG method produces a more accurate solution than the BFEM. The BFEM error relative to the converged solution – as measured by the L_2-norm – is only about 1.5%, this corresponds to case 8 from Table 1.

Eq. (47). Therefore, as the ratio of speed of light to ion sound speed approaches realistic values, the BFEM computational time becomes considerably less than that of the DG method.

The ion density solutions at $t = \sqrt{2}/30L/c_{si}$ from the DG method and the BFEM using 512 second-order elements are shown in Fig. 3 and compared to a converged solution with 5000 cells using a finite-volume high-resolution wave propagation method [18]. In this case the plasma soliton is initialized with $m_i/m_e = 1836$ and $c/c_{si} = 1000/\sqrt{2}$. The DG solution exhibits a large amount of dispersion, which appears when a realistic mass ratio is used. The reason for the dispersion on the DG method is not well understood at this point, further studies are need. The BFEM has a higher peak value than the other methods because both the DG method and the FV method can be more dissipative even for smooth solutions. This is due to the fact that both the FV and DG method use flux limiters that tend to decrease value on those cases. Fig. 3 also shows that the BFEM solution has phase errors due to the fact that the electron plasma frequency is not resolved. The phase error is evidenced by the BFEM solution being spatially shifted relative to the converged FV solution. Phase error is expected whenever high-frequency dynamics are not resolved by implicit time integrators. The dissipation in the BFEM method comes from the artificial dissipation term, Eq. (26), but for smooth solutions the value of κ can be small as in this case where $\kappa = 10^{-10}$.

Fig. 4 plots the evolution over time of the L_2-norm of the relative error for the DG method and the BFEM when using physical values for the ion to electron mass ratio and the speed of light to ion sound speed ratio. The relative error is
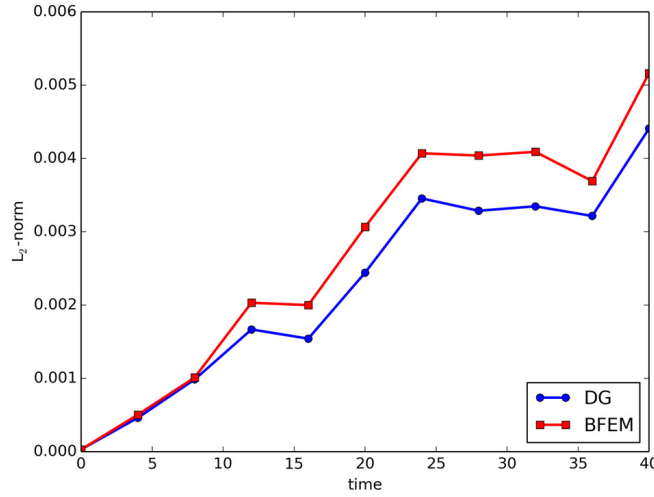
Fig. 5. L_2-norm of the relative error for the plasma soliton solution from the DG method and the BFEM as a function of time for a case where $m_i/m_e = 1$. The L_2-norms for the DG method and the BFEM are comparable since both methods use the same time step size and resolve the electron plasma frequency.

defined as

$$\frac{\rho_i^k - \rho_i^c}{\rho_i^c}, \tag{50}$$

where ρ_i^c is the mass density for the converged solution and ρ_i^k represents the solution given by the DG method or BFEM. The error is evaluated at each quadrature point (DG) or the nodal values (BFEM), and compared to the corresponding cell average (FV) at the same physical location. The L_2-norm of the DG error is lower than that of the BFEM error, and the BFEM error relative to the converged solution is approximately 1.5%. It is important to note that the BFEM resolution is only 10% of the converged solution resolution. The BFEM solution has a larger error because the DG and converged solutions are obtained using explicit time integration, which resolves the electron plasma frequency, whereas the BFEM does not resolve the electron plasma frequency. A fully explicit treatment is expected to be more accurate, but it is not always feasible or desired for stiff problems. The oscillatory behavior of the L_2-norm for the BFEM continues even for longer time intervals.

Fig. 5 compares the L_2-norm of the relative error for the DG method and the BFEM for a plasma soliton simulation in which the ion to electron mass ratio is one. The errors for the DG method and BFEM are comparable since the time step sizes are the same, and both methods resolve the electron and ion plasma frequencies.

The soliton problem demonstrates that the BFEM is less computationally costly than the DG method for problems where realistic ion to electron mass ratio and speed of light to ion sound speed ratio are used. In an hydrogen plasma, a realistic ion to electron mass ratio is 1836 (Table 1, case 5), which is at the lowest limit of mass ratios. For realistic fusion plasmas, the explicit time step limitation is even more restrictive because the ion to electron mass ratio is two or three times larger (see Table 1, case 8). Thus for fusion-relevant plasmas the BFEM offers considerable computational cost savings over the DG method, and it offers an even bigger advantage in plasma applications that use non-hydrogen plasmas where mass ratios would be even larger.

4.3. Electromagnetic plasma shock problem

The BFEM is applied to the two-fluid version of the electromagnetic plasma shock problem [55] as presented in Refs. [1, 35,50]. The electromagnetic plasma shock problem offers a comprehensive physics test for the BFEM because it exhibits the different limits of MHD behavior and of multi-fluid plasma effects by changing the ion Larmor radius, r_L. Note that MHD assumes the limit of $r_L \to 0$, and multi-fluid plasma model allows for arbitrary values of r_L.

The electromagnetic plasma shock is initialized with a discontinuity in the variables such that half of the domain is at one state and the other half is at another state. For the test case presented here, the mass ratio $m_i/m_e = 1836$. The problem is described in detail in Ref. [1]. The solution features are shown in Fig. 6 for the case with $r_L = 0.73$. From left to right the structures are: a fast rarefaction wave (FR), a slow compound wave (SC), a contact discontinuity (CD), a slow shock (SS), and another fast rarefaction wave (FR). For ion Larmor radii comparable to or smaller than the domain size, the ion fluid is tightly bound to the magnetic field and the solution contains wave-like structures. These structures are fast electromagnetic waves, which propagate faster than MHD waves and can be seen at the left of the first FR in Fig. 6. The fast waves, which include the whistler wave, correspond to the right-hand and left-hand circularly polarized plasma waves that propagate parallel to the magnetic field.
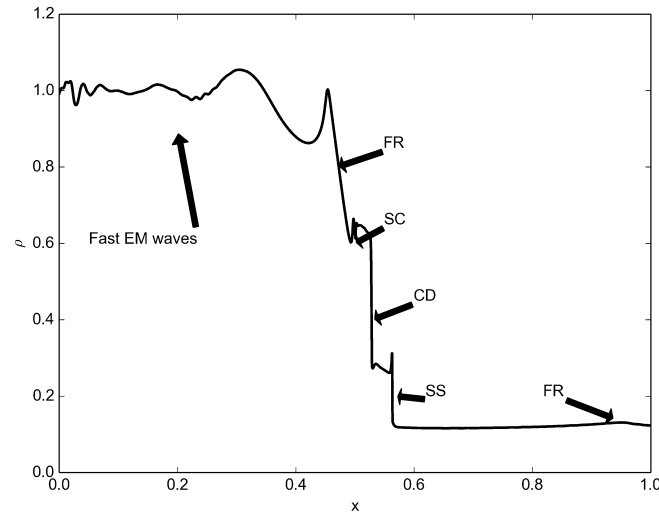
Fig. 6. The solution features of the electromagnetic plasma shock for $r_L = 0.73$ are a fast rarefaction wave (FR), a slow compound wave (SC), a contact discontinuity (CD), a slow shock (SS), and another fast rarefaction wave (FR). The solution also shows fast electromagnetic waves (including the whistler wave) that propagate faster than MHD waves [1].

The electromagnetic plasma shock is initialized by setting the two-fluid plasma variables to

$$
\begin{bmatrix}
n_e \\ u_e \\ v_e \\ w_e \\ p_e \\ n_i \\ u_i \\ v_i \\ w_i \\ p_i \\ B_x \\ B_y \\ B_z \\ E_x \\ E_y \\ E_z
\end{bmatrix}_{\text{left}}
=
\begin{bmatrix}
1.0 \\ 0 \\ 0 \\ 0 \\ 0.5 \times 10^{-4} \\ 1.0 \\ 0 \\ 0 \\ 0 \\ 0.5 \times 10^{-4} \\ 0.75 \times 10^{-2} \\ 1.0 \times 10^{-2} \\ 0 \\ 0 \\ 0 \\ 0
\end{bmatrix}, \quad \text{and} \quad
\begin{bmatrix}
n_e \\ u_e \\ v_e \\ w_e \\ p_e \\ n_i \\ u_i \\ v_i \\ w_i \\ p_i \\ B_x \\ B_y \\ B_z \\ E_x \\ E_y \\ E_z
\end{bmatrix}_{\text{right}}
=
\begin{bmatrix}
0.125 \\ 0 \\ 0 \\ 0 \\ 0.05 \times 10^{-4} \\ 0.125 \\ 0 \\ 0 \\ 0 \\ 0.05 \times 10^{-4} \\ 0.75 \times 10^{-2} \\ -1.0 \times 10^{-2} \\ 0 \\ 0 \\ 0 \\ 0
\end{bmatrix}, \tag{51}
$$

for the left and right halves of the domain. The parameters used for the problem are obtained from Ref. [1], and are $c/c_{si} = 110$, $r_L = 0.73$, $\Gamma_e = \Gamma_i = \frac{5}{3}$ and the ion to electron mass ratio is $m_i/m_e = 1836$. A grid resolution of 512 second-order elements is used. Time is normalized to the ion cyclotron time $\tau_c = 1/\omega_{ci}$.

The solution from the BFEM is compared to a solution from the DG method [50] and to the finite-volume wave propagation method [18]. Fig. 7(a) shows the mass density profile at time $t = 0.05\tau_c$ for all three methods. The BFEM solution smooths the physical oscillations in the solution due to the artificial dissipation and is discussed in more detail in Sec. 4.3.2. The BFEM also does not resolve the fast electromagnetic waves, which are driven by electron dynamics. Fig. 7(b) shows B_y which is smooth and represented by the CG portion of the BFEM, showing that there is good agreement between all the methods where the electron dynamics is not very relevant.

4.3.1. Implicit and explicit time integration comparison

As evident in Eq. (47), the CFL condition depends on the characteristic speeds of the system, the species speeds of sound, $c_{s\alpha}$, and the speed of light, c. Moreover, the temporal discretization must also resolve the species cyclotron frequencies $\omega_{c\alpha} = q_\alpha B/m_\alpha$, and the species plasma frequencies $\omega_{p\alpha} = \sqrt{n_\alpha q_\alpha^2/\epsilon_0 m_\alpha}$, as described in Sec. 2. The initialization parameters for the electromagnetic plasma shocks studied are shown in Table 2.

The maximum explicit time step size is determined from these parameters by the following expression,

$$
\Delta t_{max} = \min\left(\frac{\Delta x}{c_{se}}, \frac{\Delta x}{c_{si}}, \frac{\Delta x}{c}, \frac{\beta}{\omega_{ce}}, \frac{\beta}{\omega_{ci}}, \frac{\beta}{\omega_{pe}}, \frac{\beta}{\omega_{pi}} \right), \tag{52}
$$

B-21
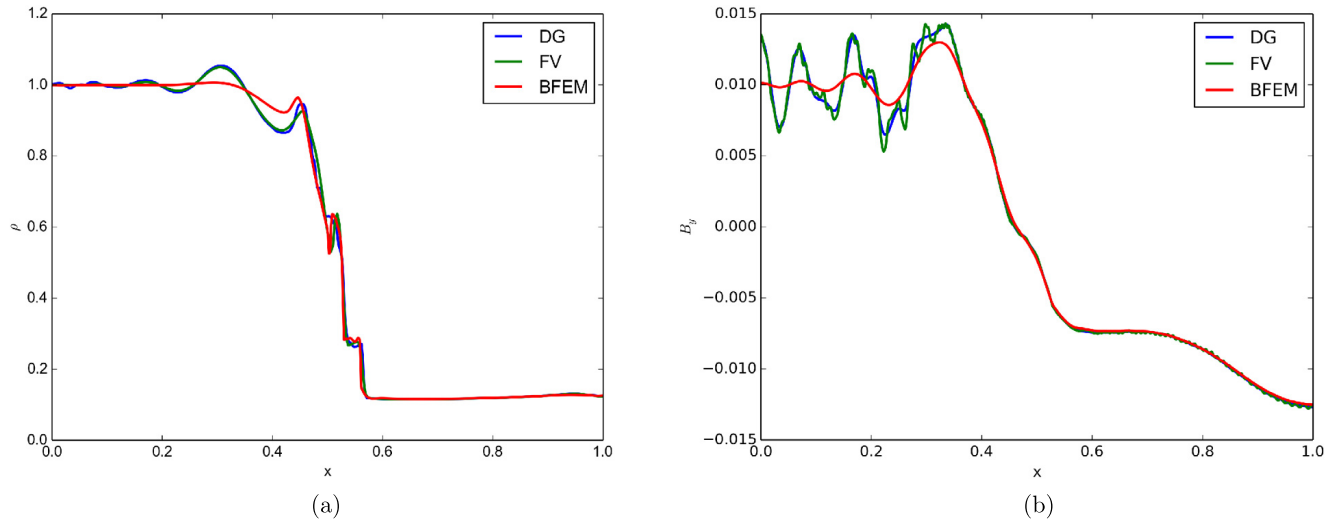
Fig. 7. The total mass density, $m_i n_i + m_e n_e$, and y-component of magnetic field are plotted for the electromagnetic plasma shock problem at $t = 0.05\tau_c$, when $c/c_{si} = 110$ and $m_i/m_e = 1836$. Second-order BFEM is used. The main features of the problem are captured by all three methods, but the BFEM does not properly resolve the fast electromagnetic waves, which require accurately resolving the electron dynamics by using a fully explicit treatment.

Table 2
Characteristic speeds and frequencies for the electromagnetic shock problem.

	Electron	Ion
c	1.0	1.0
$c_{s\alpha}$	3.9×10^{-1}	9.1×10^{-3}
$\omega_{c\alpha}$	1.8×10^{2}	1.0×10^{-1}
$\omega_{p\alpha}$	4.3×10^{2}	1.0×10^{1}
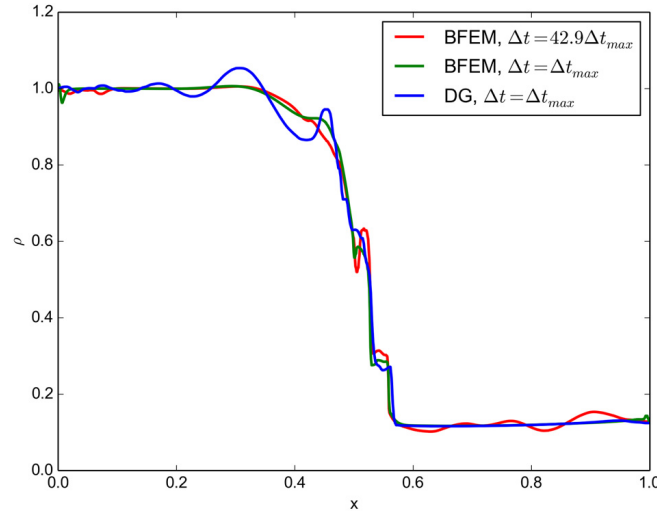
Fig. 8. The total mass density, $m_i n_i + m_e n_e$, is plotted for the electromagnetic plasma shock problem at $t = 0.05\tau_c$ using different time step size Δt. Second-order BFEM is used. The time step size is expressed relative to Δt_{max}, which corresponds to the maximum value allowed for explicit methods based on the CFL condition. Note that $\Delta t = 42.9\Delta t_{max}$ is the maximum time step allowed by the BFEM, where the ion dynamics restrict the time step size.

where β is the number of time points required to resolve an oscillation, typically, $\beta = 1/10$. The electron plasma frequency imposes the most stringent restriction on the time step size, $\Delta t_{max} = 2.33 \times 10^{-4}$. This restriction is particularly severe for methods that use fully explicit time integration. Since in the BFEM the electron fluid and the electromagnetic fields are advanced implicitly, the time step restrictions only depend on the slower ion and neutral fluids. Therefore, the BFEM permits larger time steps.

Fig. 8 compares the total mass density solution for BFEM using a time step equal to the explicit time step limit, $\Delta t = \Delta t_{max}$, with a solution using a larger implicit time step, $\Delta t = \sqrt{m_i/m_e}\,\Delta t_{max} = 42.9\Delta t_{max}$. The implicit time step is limited by the ion plasma frequency. The solution attained using the implicit Δt resolves all the main features of the problem
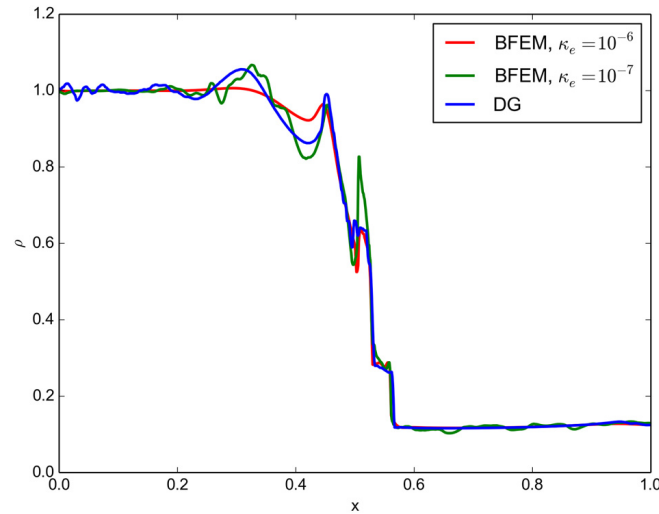
Fig. 9. The total mass density, $m_i n_i + m_e n_e$, is plotted for the electromagnetic plasma shock problem to demonstrate the effect of varying the artificial dissipation on the electron fluid, κ_e, for fixed electromagnetic artificial dissipation $\kappa_{EM} = 10^{-4}$. The solution for $\kappa_e = 10^{-7}$ captures the wave-like behavior of the electromagnetic plasma shock problem. The amplitude of the compound wave increases, and the right fast rarefaction wave is not visible. Second-order BFEM is used.
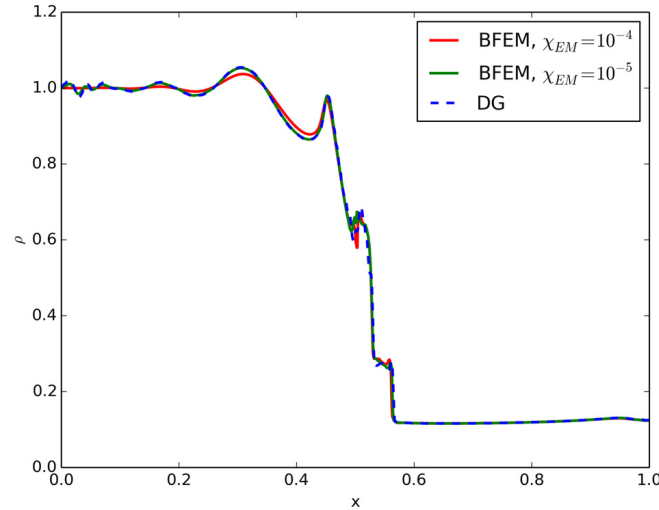
Fig. 10. The total mass density, $m_i n_i + m_e n_e$, is plotted for the electromagnetic plasma shock problem where the artificial dissipation on the electromagnetic fields is decreased from $\kappa_{EM} = 10^{-4}$ to 10^{-5}, and second-order BFEM is used. The electron fluid artificial dissipation is fixed at $\kappa_e = 10^{-6}$. The reduced dissipation solution agrees better with the solution from the DG method, reinforcing the point that the wave-like behavior arises from the interaction of the electron fluid with the electromagnetic fields. Second-order BFEM is used.

except the fast rarefaction wave, which should be ahead of the slow shock, but instead there are small oscillation ahead of the SS. The slow compound wave (SC) is better resolved with the larger time step of the BFEM because this wave is a feature of the ion dynamics.

4.3.2. Effects of artificial dissipation

As described in Sec. 3.1, an artificial dissipation term is added to the governing equations for the electron fluid and electromagnetic fields to damp numerical oscillations that are produced by the CG method in regions of sharp gradients in the solution. The artificial diffusivity coefficient κ scales the amount of artificial dissipation applied to the electron fluid and electromagnetic fields. If κ is too small the solution develops high amplitude node-to-node oscillations that grow over time, making the solution of the nonlinear Newton solver more stiff and requiring more iterations to converge [35]. On the other hand, if κ is too big the solution smooths relevant features of the solution producing an inaccurate result.

It is possible to apply different values of κ for the electron equations and electromagnetic field equations, e.g. κ_e and κ_{EM}. Reducing the artificial dissipation coefficient in the electron fluid (κ_e) from 10^{-6} to 10^{-7} while keeping κ_{EM} fixed makes the compound wave more distinct as shown in Fig. 9. The oscillations due to Langmuir and whistler waves are also more visible. However, the second fast rarefaction wave (right-most FR) is not resolved, and small oscillations are present instead. Decreasing the artificial dissipation applied to Maxwell's equations while keeping κ_e fixed allows the BFEM solution to better resolve the oscillations due to the fast electromagnetic waves. Fig. 10 shows the total mass density for

the electromagnetic plasma shock problem when the electron fluid dissipation is $\kappa_e = 10^{-6}$ and the electromagnetic field artificial dissipation is varied from $\kappa_{EM} = 10^{-4}$ to $\kappa_{EM} = 10^{-5}$. In addition, the fast rarefaction wave is better resolved with the smaller value of κ_{EM}.

Overall there is remarkable agreement between the BFEM solution and the computationally more expensive DG method solution. It is evident from the electromagnetic plasma shock results presented in Figs. 9 and 10 that artificial dissipation plays an important role in the accuracy of the BFEM solution. Thus the BFEM can be further improved by devising a systematic means of calculating the parameter κ or using a different form of artificial dissipation.

4.4. Species separation in fusion capsule implosions

The multi-fluid plasma model is applicable to problems where the plasma is composed of multiple species that exhibit dynamics at different scales. A motivating problem is the species separation [42] that can occur during the implosion phase of inertial confinement fusion (ICF) capsules, where deuterium and tritium are heated and compressed to fusion conditions. The compression process uses laser-driven shocks that produce electric fields [56], which can cause the deuterium to accelerate faster than the tritium. The phenomenon is not captured by single-fluid plasma models. Low neutron yield measurements [57] point to the possibility of fuel stratification caused by baro-diffusion [56] (pressure gradient-driven diffusion) that causes the separation of the ion species during the implosion.

The multi-fluid plasma for this problem is composed of two ion fluids, deuterium and tritium, and an electron fluid. The dynamics of the ions, electrons, and electromagnetic fields occur at a vastly different timescales, which introduces numerical stiffness making this problem ideally suited for the BFEM. The different timescales in the ICF fuel species separation problem result from the characteristic speeds and frequencies for the constituent species. The differences are particularly large when realistic speed of light and species masses are used.

Following the problem setup in Ref. [42], a Cartesian geometry is used and the plasma is initialized with a discontinuity in the parameters. The left half of the domain ($x < 0$) has a total ion density given by $\sum_\alpha n_\alpha = 4 \times 10^{19}$ cm^{-3}, where the sum is only over the ion species, with all species having a temperature of $T_\alpha = 100$ eV. The right half of the domain ($x \geq 0$) has a total ion density given by $\sum_\alpha n_\alpha = 1 \times 10^{19}$ cm^{-3} with all species having a temperature of $T_\alpha = 10$ eV. The plasma is initialized to be charge neutral everywhere, $n_e = \sum_\alpha Z_\alpha n_\alpha$, where the sum is again only over the ion species. Heat flux and viscous effects are neglected. The computational domain is $x \in [-30 \text{ μm}, 30 \text{ μm}]$, and zero normal gradient boundary condition are applied at the boundaries. The speed of light to proton sound speed ratio (c/c_{sp}) is 3065 and the proton to electron mass ratio is 1836. The ion species are characterized by ion mass ratio in relation to a proton mass, $\mu = m_\alpha/m_p$ and by the ionization state, $Z = q_\alpha/e$. The species separation from the deuterium is magnified by using a heavier second ion species with $\mu = 10$, instead of $\mu = 3$ corresponding to tritium.

Fig. 11 compares the ion number densities at $t = 150$ ps for simulations with an electron CFL number of 1 and an electron CFL number of 20. An electron CFL number of 1 restricts the time step size to resolve all electron characteristic timescales. The ion species separation is the same for both cases but the oscillations behind the shock front differ. This may be due to the fact that the electron dynamics are not fully resolved with an electron CFL number of 20. The effect of electron CFL number on the required computational time (defined as the total elapsed time) and solution accuracy is shown in Fig. 11(c). There it can be seen that there are considerable CPU cost saving as the CFL number is increased, although the gains are minimal after CFL = 10. The L_2-norm (Eq. (49)) increases after an electron CFL number of 10 but remains small.

5. Conclusion

A blended finite element method (BFEM) is presented for the multi-fluid plasma model. The method uses a DG spatial discretization combined with explicit Runge–Kutta time integration to describe the ion and neutral fluids and a CG spatial discretization combined with implicit Crank–Nicolson time integration for the electron fluid and electromagnetic fields. The DG method accurately captures shocks and discontinuities that can occur in the ion and neutral fluids, and the CG method efficiently and robustly computes smooth solutions for the electron fluid and electromagnetic fields. The physics-based decomposition of the algorithm into implicit CG and explicit DG portions yields numerical solutions that resolve the desired timescales and match the expected solution structure.

Each component of the numerical method is independently verified to converge at the expected order of accuracy. The two-fluid soliton problem is used to compare the computational cost of the BFEM to an explicit DG method. For unphysical values of the ion to electron mass ratio and speed of light to ion thermal speed ratio, the DG method is more computationally efficient than the BFEM. However, for realistic values of the mass ratio and normalized speed of light, the BFEM is less costly than the DG method. It is worth noting that for non-hydrogen plasmas, the mass ratio for the ion species relative to electrons can be many times greater than 1836, and even for fusion hydrogen plasmas the ion fluids are deuterium and tritium, so the mass ratio is 3672. In these cases the computational cost savings offered by the BFEM over the DG method are considerable.

The BFEM and DG method are further compared using the electromagnetic plasma shock problem. The total mass density from DG and BFEM solutions are compared to solutions given by a finite-volume high-resolution wave propagation method. The electron fluid and the electromagnetic field equations are advanced implicitly using a time step 42.9 times larger than the time step required for an explicit method. The fast electromagnetic waves and the fast rarefaction wave are not

(a) Electron CFL=1

(b) Electron CFL=20

(c) Cost vs. Accuracy
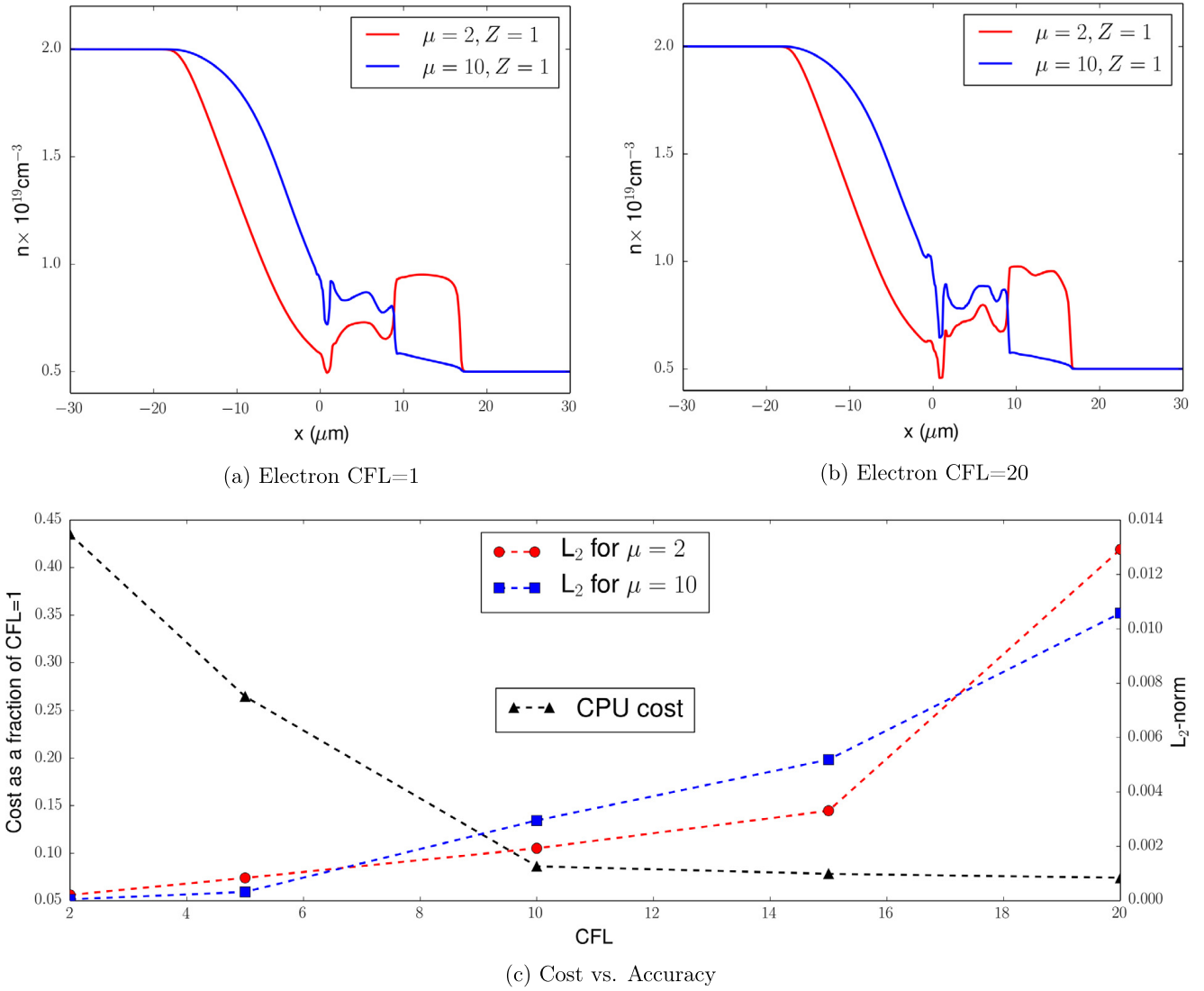
Fig. 11. Depicted are the ion densities from a multi-fluid plasma simulation of the species separation problem composed of two ion fluids ($\mu = 2$ and $\mu = 10$) and an electron fluid using (a) an electron CFL number of 1, a time step size that resolves all electron characteristic timescales, and (b) an electron CFL number of 20. The ion species separation in both cases is the same although the solution behind the shock fronts differ. (c) The L_2-norm of the densities and the computational time for different electron CFL numbers are shown. The CPU time is calculated as a fraction of the computational time used for the case with electron CFL number of 1. The solution error increases as the computational time decreases.

resolved, but the location of the shock, contact discontinuity, and compound wave are accurately computed. The artificial dissipation added to the CG portion of the BFEM is adjusted for each equation system independently to produce more physically accurate results. When the artificial dissipation for Maxwell's equations is reduced by a factor of ten, there is remarkable agreement between the DG and BFEM results. This shows that artificial dissipation plays an important role in BFEM solutions.

Application of the BFEM to the multi-fluid plasma problem of species separation in ICF capsules demonstrates the ability of the method to take time step sizes that are much larger than the electron timescales. The method generates stable solutions that capture the overall ion structures but at a significantly lower computational cost.

The BFEM has large potential to be useful in problems where the slow dynamics are of primary interest, but the fast dynamics still play an important role, i.e. problems that span a multitude of temporal and spatial scales. The method offers a computationally efficient means of modeling plasma dynamics using realistic parameters. The BFEM can be further improved by dynamically adjusting the artificial dissipation. While the results presented are for one-dimensional applications, the extension to multiple dimensions is straightforward. The reduction in computational cost achieved by the BFEM is due to fast dynamics being treated implicitly. This means that the cost savings are expected to hold for higher dimensions. The DG method takes less computational time to advance the solution by one time step, however Δt is much smaller than that of the BFEM. Thereby a fully explicit DG solution takes many more time steps, independent of the dimensionality, which also means that the computational cost savings using the BFEM only occur for relatively large implicit time-steps compared to

explicit time-steps. The physics-informed blending of the CG and DG representations offers a way to reduce computational cost while retaining the generalized physics of the multi-fluid plasma model.

Acknowledgements

References

[1] U. Shumlak, J. Loverich, Approximate Riemann solver for the two-fluid plasma model, J. Comput. Phys. 187 (2003) 620–638.
[2] B. Srinivasan, U. Shumlak, Analytical and computational study of the ideal full two-fluid plasma model and asymptotic approximations for Hall-magnetohydrodynamics, Phys. Plasmas (ISSN 1070-664X) 18 (9) (2011) 092113, http://dx.doi.org/10.1063/1.3640811.
[3] J.P. Freidberg, Ideal magnetohydrodynamic theory of magnetic fusion systems, Rev. Mod. Phys. 54 (3) (1982) 801–902.
[4] U. Shumlak, R. Lilly, N. Reddell, E. Sousa, B. Srinivasan, Advanced physics calculations using a multi-fluid plasma model, Comput. Phys. Commun. 182 (9) (2011) 1767–1770.
[5] E.T. Meier, U. Shumlak, A general nonlinear fluid model for reacting plasma-neutral mixtures, Phys. Plasmas 19 (7) (2012) 072508, http://link.aip.org/link/?PHP/19/072508/1.
[6] R.J. LeVeque, Finite Volume Methods for Hyperbolic Problems, 1st edn., Cambridge University Press, 2002.
[7] T. Barth, M. Ohlberger, Finite Volume Methods: Foundation and Analysis, John Wiley & Sons, Ltd, ISBN 9780470091357, 2004.
[8] P. Colella, M. Dorr, J. Hittinger, D. Martin, P. McCorquodale, High-order finite-volume adaptive methods on locally rectangular grids, J. Phys. 180 (2009) 012010.
[9] S.C. Jardin, A triangular finite element with first-derivative continuity applied to fusion MHD applications, J. Comput. Phys. 200 (1) (2004) 133–152.
[10] C. Sovinec, A. Glasser, T. Gianakon, D. Barnes, R. Nebel, S. Kruger, D. Schnack, S. Plimpton, A. Tarditi, M. Chu, Nonlinear magnetohydrodynamics simulation using high-order finite elements, J. Comput. Phys. 195 (1) (2004) 355–386.
[11] B. Cockburn, C.W. Shu, TVB Runge–Kutta local projection discontinuous Galerkin finite element for conservation laws II – general framework, Math. Comput. 52 (186) (1989) 411–435.
[12] F. Li, L. Xu, S. Yakovlev, Central discontinuous Galerkin methods for ideal MHD equations with the exactly divergence-free magnetic field, J. Comput. Phys. 230 (12) (2011) 4828–4847.
[13] V. Wheatley, H. Kumar, P. Huguenot, On the role of Riemann solvers in discontinuous Galerkin methods for magnetohydrodynamics, J. Comput. Phys. 229 (3) (2010) 660–680.
[14] B. Srinivasan, A. Hakim, U. Shumlak, Numerical methods for two-fluid dispersive fast MHD phenomena, Commun. Comput. Phys. 10 (1) (2011) 183–215.
[15] J.U. Brackbill, W.E. Pracht, An implicit, almost-Lagrangian algorithm for magnetohydrodynamics, J. Comput. Phys. 13 (1973) 455.
[16] R.E. Peterkin Jr., M.H. Frese, C.R. Sovinec, Transport of magnetic flux in an arbitrary coordinate ALE code, J. Comput. Phys. 140 (1) (1998) 148–171.
[17] U. Shumlak, T.W. Hussey, R.E. Peterkin Jr., Three-dimensional magnetic field enhancement in a liner implosion system, IEEE Trans. Plasma Sci. 23 (1) (1995) 83–88.
[18] A. Hakim, J. Loverich, U. Shumlak, A high resolution wave propagation scheme for ideal two-fluid plasma equations, J. Comput. Phys. 219 (2006) 418–442.
[19] N. Murphy, A. Young, C. Shen, J. Lin, L. Ni, The plasmoid instability during asymmetric inflow magnetic reconnection, Phys. Plasmas 20 (6) (2013) 061211.
[20] V.A. Izzo, Impurity mixing and radiation asymmetry in massive gas injection simulations of DIII-D, Phys. Plasmas 20 (5) (2013) 056107.
[21] J. Slough, R. Milroy, High flux FRC facility for stability and confinement studies, J. Fusion Energy 29 (6) (2010) 567–570.
[22] A.I. Macnab, S. Woodruff, Extended MHD simulations of the compression and stability of spheromaks for current drive, J. Fusion Energy 28 (2) (2009) 183–186.
[23] O.C. Zienkiewics, R.L. Taylor, P. Nithiarasu, The Finite Element Method for Fluid Dynamics, seventh edition, Elsevier, 2014.
[24] S. Jardin, J. Breslau, N. Ferraro, A high-order implicit finite element method for integrating the two-fluid magnetohydrodynamic equations in two dimensions, J. Comput. Phys. 226 (2) (2007) 2146–2174.
[25] L. Chacón, D. Knoll, J. Finn, An implicit, nonlinear reduced resistive MHD solver, J. Comput. Phys. 178 (1) (2002) 15–36.
[26] H.W. Reed, T.R. Hill, Triangular mesh methods for the neutron transport equation, Los Alamos Scientific Laboratory Report LA-UR-73-479, 1973.
[27] F. Bassi, S. Rebay, A high-order accurate discontinuous finite element method for the numerical solution of the compressible Navier–Stokes equations, J. Comput. Phys. 131 (1997) 267–279.
[28] F. Bassi, L. Botti, A. Colombo, S. Rebay, Agglomeration based discontinuous Galerkin discretization of the Euler and Navier–Stokes equations, Comput. Fluids 61 (2012) 77–85.
[29] E. Ferrer, R. Willden, A high-order discontinuous Galerkin finite element solver for the incompressible Navier–Stokes equations, Comput. Fluids 46 (1) (2011) 224–230.
[30] P. Birken, G. Gassner, M. Haas, C.-D. Munz, Preconditioning for modal discontinuous Galerkin methods for unsteady 3D Navier–Stokes equations, J. Comput. Phys. 240 (2013) 20–35.
[31] T. Warburton, G. Karniadakis, A discontinuous Galerkin method for the viscous MHD equations, J. Comput. Phys. (ISSN 0021-9991) 152 (2) (1999) 608–641.
[32] J.A. Rossmanith, D.C. Seal, A positivity-preserving high-order semi-Lagrangian discontinuous Galerkin scheme for the Vlasov–Poisson equations, J. Comput. Phys. 230 (16) (2011) 6203–6232.
[33] B. Cockburn, C.W. Shu, Runge–Kutta discontinuous Galerkin methods for convection-dominated problems, J. Sci. Comput. 16 (3) (2001) 173–261.
[34] U. Shumlak, R. Lilly, N. Reddell, E. Sousa, B. Srinivasan, Advanced physics calculations using a multi-fluid plasma model, Comput. Phys. Commun. 18 (2011) 1767–1770.
[35] B. Srinivasan, Numerical methods for 3-dimensional magnetic confinement configurations using two-fluid plasma equations, Ph.D. thesis, University of Washington, 2010.
[36] U. Ascher, S. Ruuth, R. Spiteri, Implicit–explicit Runge–Kutta methods for time-dependent partial differential equations, Appl. Numer. Math. 25 (1997) 151–167.
[37] A. Kanevsky, M. Carpenter, D. Gottlieb, J. Hesthaven, Application of implicit–explicit high order Runge–Kutta methods to discontinuous-Galerkin schemes, J. Comput. Phys. 225 (2007) 1753–1781.
[38] M.G. Haines, A review of the dense Z-pinch, Plasma Phys. Control. Fusion 53 (9) (2011) 093001.
[39] S. Hirshman, D. Sigmar, Neoclassical transport of impurities in tokamak plasmas, Nucl. Fusion 21 (9) (1981) 1079.

[40] P. Helander, C.D. Beidler, T.M. Bird, M. Drevlak, Y. Feng, R. Hatzky, F. Jenko, R. Kleiber, J.H.E. Proll, Y. Turkin, P. Xanthopoulos, Stellarator and tokamak plasmas: a comparison, Plasma Phys. Control. Fusion 54 (12) (2012) 124009.

[41] J.D. Lindl, P. Amendt, R.L. Berger, S.G. Glendinning, S.H. Glenzer, S.W. Haan, R.L. Kauffman, O.L. Landen, L.J. Suter, The physics basis for ignition using indirect-drive targets on the National Ignition Facility, Phys. Plasmas 11 (2004) 339.

[42] C. Bellei, P.A. Amendt, S.C. Wilks, M.G. Haines, D.T. Casey, C.K. Li, R. Petrasso, D.R. Welch, Species separation in inertial confinement fusion fuels, Phys. Plasmas 20 (2013) 012701.

[43] C. Munz, P. Omnes, R. Schneider, E. Sonnendruer, U. Voss, Divergence correction techniques for Maxwell solvers based in a hyperbolic model, J. Comput. Phys. 161 (2000) 484–511.

[44] E.M. Sousa, A blended finite element method for multi-fluid plasma modeling, Ph.D. thesis, University of Washington, Seattle, WA 98195, 2014.

[45] J.N. Reddy, An Introduction to the Finite Element Method, 3rd edn., McGraw-Hill, 2006.

[46] D.F. Griffiths, D.J. Higham, Numerical Methods for Ordinary Differential Equations, Springer, 2010.

[47] J. Crank, P. Nicolson, A partial method for numerical evaluation of solutions of partial differential equations of the heat-conduction type, Adv. Comput. Math. 6 (1996) 207–226.

[48] T.J. Ypma, Historical development of the Newton–Raphson method, SIAM Rev. 37 (4) (1995) 531–551.

[49] J. Loverich, U. Shumlak, A discontinuous Galerkin method for the full two-fluid plasma model, Comput. Phys. Commun. (ISSN 0010-4655) 169 (1–3) (2005) 251–255, http://www.sciencedirect.com/science/article/B6TJ5-4FWV2KT-5/2/e932f6ea4ea9a11dfad06528fb6b71f0.

[50] J. Loverich, A. Hakim, U. Shumlak, A discontinuous Galerkin method for ideal two-fluid plasma equations, Commun. Comput. Phys. 9 (2) (2011) 240–268.

[51] P.L. Roe, Approximate Riemann solvers, parameter vectors and difference schemes, J. Comput. Phys. 43 (1981) 357.

[52] J.S. Hesthaven, T. Warburton, Nodal Discontinuous Galerkin Methods: Algorithms, Analysis, and Applications, Springer, 2008.

[53] S. Baboolal, Finite-difference modeling of solitons induced by a density hump in a plasma multi-fluid, Math. Comput. Simul. 55 (2001) 309–316.

[54] J. Birn, J.F. Drake, M.A. Shay, B.N. Rogers, R.E. Denton, M. Hesse, M. Kuznetsova, Z.W. Ma, A. Bhattacharjee, A. Otto, P.L. Pritchett, Geospace Environmental Modeling (GEM) magnetic reconnection challenge, J. Geophys. Res. 106 (A3) (2001) 3715–3719.

[55] M. Brio, C.C. Wu, An upwind differencing scheme for the equations of ideal magnetohydrodynamics, J. Comput. Phys. 75 (1988) 400–422.

[56] P. Amendt, S.C. Wilks, C. Bellei, C.K. Li, R.D. Petrasso, The potential role of electric fields and plasma barodiffusion on the inertial confinement fusion database, Phys. Plasmas 18 (2011) 056308.

[57] D.T. Casey, J.A. Frenje, M.G. Johnson, M.J.E. Manuel, H.G. Rinderknecht, N. Sinenian, F.H. Séguin, C.K. Li, R.D. Petrasso, P.B. Radha, J.A. Delettrez, V.Y. Glebov, D.D. Meyerhofer, T.C. Sangster, D.P. McNabb, P.A. Amendt, R.N. Boyd, J.R. Rygg, H.W. Herrmann, Y.H. Kim, A.D. Bacher, Evidence for stratification of deuterium-tritium fuel in inertial confinement fusion implosions, Phys. Rev. Lett. 108 (2012) 075002.

B-27

This Page Intentionally Left Blank

Appendix C Collision Models C-1

Conservative Bin-to-Bin Fractional Collisions

Robert Martin[1,a)]

[1]*ERC Inc., In-Space Propulsion Branch, Air Force Research Laboratory, Edwards AFB, CA 93524 USA.*

a)robert.martin.101@us.af.mil

Abstract. Particle methods such as direct simulation Monte Carlo (DSMC) and particle-in-cell (PIC) are commonly used to model rarefied kinetic flows for engineering applications because of their ability to efficiently capture non-equilibrium behavior. The primary drawback to these methods relates to the poor convergence properties due to the stochastic nature of the methods which typically rely heavily on high degrees of non-equilibrium and time averaging to compensate for poor signal to noise ratios. For standard implementations, each computational particle represents many physical particles which further exacerbate statistical noise problems for flow with large species density variation such as encountered in flow expansions and chemical reactions. The stochastic weighted particle method (SWPM) introduced by Rjasanow and Wagner overcome this difficulty by allowing the ratio of real to computational particles to vary on a per particle basis throughout the flow. The DSMC procedure must also be slightly modified to properly sample the Boltzmann collision integral accounting for the variable particle weights and to avoid the creation of additional particles with negative weight.

In this work, the SWPM with necessary modification to incorporate the variable hard sphere (VHS) collision cross section model commonly used in engineering applications is first incorporated into an existing engineering code, the Thermophysics Universal Research Framework. The results and computational efficiency are compared to a few simple test cases using a standard validated implementation of the DSMC method along with the adapted SWPM/VHS collision using an octree based conservative phase space reconstruction.

The SWPM method is then further extended to combine the collision and phase space reconstruction into a single step which avoids the need to create additional computational particles only to destroy them again during the particle merge. This is particularly helpful when oversampling the collision integral when compared to the standard DSMC method. However, it is found that the more frequent phase space reconstructions can cause added numerical thermalization with low particle per cell counts due to the coarseness of the octree used. However, the methods are expected to be of much greater utility in transient expansion flows and chemical reactions in the future.

INTRODUCTION

Stochastic particle methods such as direct simulation Monte Carlo (DSMC) and particle in cell (PIC) have been the primary engineering tools for rarefied gas and plasma dynamics for decades. The computational cost of suppressing statistical noise in these methods has long been a hindrance for flows with high dynamic range in densities and in length-scales such as ionizing breakdown, chemical reactions with trace species, and spacecraft plume interaction models. The noise is further exacerbated by unsteady flows where time averaging is inappropriate and in cases where fluctuations can non-linearly feed back through the system as in the case of evaluating electron mobility in hybrid Fluid/PIC models used for modeling Hall effect thrusters [1]. To address the issue of poor statistical power, models that relax the constraint on uniform physical to computational particle ratio have been developed. The addition of conservative local dynamic phase space reconstruction using these weighted particles enables direct control over the number of particles per cell, a key parameter influencing statistical noise, while simultaneously preserving velocity distribution shape so that numerical thermalization and artificial entropy growth are inhibited [2, 3].

The development of robust phase space reconstruction has also opened the door to a new class of collision models for particle codes based on fractional particle jumps. This change enables much more direct control over the statistical noise due to collisions through a finer stochastic sampling of the collision integral than was previously possible. Such fractional collision methods replacing MCC ionization as well as DSMC elastic collisional relaxation

have been demonstrated in conjunction with octree phase space reconstruction methods in References [2, 3]. For the DSMC replacement, fractional collision methods are particularly critical because the standard all-or-nothing collision of the DSMC method is inherently incompatible with variable computational weight particles. Even compensating for the dynamic range of relatively simple axii-symmetric flows can cause significant on-axis issues related to variable radial weighting procedures that simply use cell averaged weights in the collision routines [4]. Without global phase space reconstruction, merging the fractional pre- and post-collision fragments within the collision step is a particularly poor choice because it necessarily violates energy conservation, merges particles far apart in velocity space causing artificial thermalization, directly violates detailed balance, and fails to converge to the physical solution even with refinement of increased particle count.

Though fractional collision methods with phase space reconstruction have been demonstrated to reproduce results based off the original fixed weight methods, in this work, the stochasitc weight particle method is first adapted to use standard engineering cross sections and combined with the octree phase space reconstruction. These ideas are then extended to fuse the fractional collision and the reconstruction process into a single step. This is done as a means of reducing the memory overhead from storing extra fractional collision particle information which is only destroyed in the subsequent conservative merging reconstruction process. The combined collision process then becomes conservative non-local fluxes of mass, momentum, and energy between phase space bins used to update the quantities required for generation of the reconstructed particles. The modified and fused algorithms are then shown to reproduce results from the standard DSMC model when sufficient numbers of computational particles are used.

STOCHASTIC WEIGHT PARTICLE ALGORITHMS

The Boltzmann equation, $\frac{\partial f}{\partial t} + \nabla_x \cdot (vf) + \nabla_v \cdot (af) = \left[\frac{df}{dt}\right]^{Coll.}$, for the evolution in time, t, and space, x, of the velocity distribution function, $f = f(x, v; t)$ represents the fundamental evolution equation for kinetic rarefied dilute gasses where v and a are the velocity and acceleration in phase space. The collision term is $\left[\frac{df}{dt}\right]^{Coll.} = \int_{\mathbb{R}^3} \int_{S^2} B(v, w, \hat{e}) \left(f(v')f(w') - f(v)f(w)\right) d\hat{e} \, dw$, where the collision kernel $B(v, w, \hat{e})$ is the differential probability of collisions between particles of velocities u and v scattering on to a momentum and energy conserving sphere $\hat{e} \in S^2$ centered at the pair's center of mass, $(v + w)/2$, with radius $|v - w|/2$.

Though used in engineering applications for several decades preceding formal proof, Wagner demonstrated that Bird's direct simulation Monte Carlo (DSMC) method converges to the solution of the Boltzmann equation in the limit of infinite particles using a Markov jump process using a random time transformation in Reference [5]. The DSMC method therefore represents a relatively computationally efficient stochastic sampling of the Boltzmann collision integral. This enables solution of the Boltzmann equation when coupled with an operator split particle advection scheme between spatial cells used to localize collision partner selection. However, for finite cost realizations of the method, the signal to noise ratio in the solution resulting from the stochastic nature of the method represents a significant limitation on the method which is particularly exacerbated by solutions with large dynamic range in density and in transient solutions where time averaging is inappropriate.

Fractional Weight Collisions

Relaxing the constraint on the model that each computational particle represents the same number of physical particles helps address the issue of poor dynamic range. This modification does not affect the representation of the spatial transport side of the Boltzmann equation, but it does complicate the sampling of the collision process. The necessary adjustments for the the collision algorithms were addressed as the the stochastic weight particle method (SWPM) introduced by Rjasanow and Wagner in Reference [6]. The method revisits the Markov process relaxing the constant weight assumption assuming the N_p-particle distribution jumps from one computational particle configuration, $z^t = \{(x_1, v_1, w_1), ..., (x_{N_p}, v_{N_p}, w_{N_p})\}$, to the next, z^{t+1}, through a series of k-infinitesimal jumps as shown in Equation 1.

$$z^{t+1} = J(z^t, i, j, \hat{e}) = \begin{cases} (x_k, v_k, w_k), & \text{if } k \leq N_p, k \neq i, j, \\ (x_i, v_i, w_i - W(z^t, i, j, \hat{e})), & \text{if } k = i, \\ (x_j, v_j, w_j - W(z^t, i, j, \hat{e})), & \text{if } k = j, \\ (x_i, v'_i, W(z^t, i, j, \hat{e})), & \text{if } k = N_p + 1, \\ (x_j, v'_j, W(z^t, i, j, \hat{e})), & \text{if } k = N_p + 2 \end{cases} \tag{1}$$

Here, the function $W(z^t, i, j, \hat{e}))$ is the "weight transfer function" which transfers a portion of the ith-particle weight, $w_i = f_i \, \delta\Omega$, to a new, $(n + 1)$, particle as defined in Reference [6]. Algorithm 1 shows pseudocode to adapt the DSMC method to use variable particle weights via the weight transfer function with associated modification to reject fictitious collisions and account for the weight variation in the monte carlo acceptance-rejection procedure.

Algorithm 1: Stochastic Weight Particle Cell Collision Algorithm (Modifications to Standard DSMC in red)

```
1   n ← N_p   // Variable to Account for Growth in Computational Particles
2   w_min/max ← min/max(w_i ∈ {w})   // Find Particle Weight Bounds
3   w̄ ← ∑(w_i ∈ {w})/N_p   // Calculate Average Particle Weight
4   Attempted Collisions/Cell:
5       N_collide ← Poisson(c_m(2w̄ − w_min)N_p(N_p − 1)⟨σv⟩^max dt)   // Collison Rate from Poisson Sample of ⟨σv⟩^max Frequency
6       For k ∈ [1 : N_collide]:
7           Select Random i and j∈n While:   // Adapted from Eq 2.24 in Reference [10]
8               Rand(1) < (w_i + w_j − w_min)/(2w_max − w_min)   // Eliminate Excess Rejection by Maximum Probability
9           -AND-
10              i ≠ j   // Equal Velocity Particles Never Collide
11          Collide If:
12              Rand(1) < (c_m max(w_i, w_j))/(w_i + w_j − w_min)⟨σv⟩_ij / ⟨σv⟩^max   // Adjusted Monte Carlo Probability
13              Perform Standard VHS Collisions:
14                  (x_{n+1}, x_{n+2}) ← (x_i, x_j)   // New Particles at Old Positions
15                  (v_{n+1}, v_{n+2}) ← VHS(v_i, v_j, ê)   // Isotropic Scatter with Velocity Dependent Cross Section of Reference [4]
16              Generate/Modify Particles with:
17                  Δw ← min(w_i, w_j)/c_m   // Guarantees Positive Particles for c_m ≥ 1 Collision Integral Sampling
18                  (w_i, w_j) -= Δw   // Adjust Original Weights
19                  (w_{n+1}, w_{n+2}) ← Δw   // Transfer Weight to New Particles
20              Update:
21                  ⟨σv⟩^temp ← Max(⟨σv⟩_ij, ⟨σv⟩^max)   // Track ⟨σv⟩^max for Subsequent Iterations
22                  n ← n + 2   // Allow New Particles to Subsequently Collide
23  Update Maximum Cross Section:
24      ⟨σv⟩^max ← ⟨σv⟩^temp   // Modify ⟨σv⟩^max for Efficiency
25  Remove all particle i ∈ n such that w_i = 0
```

For variable weight particles, this results in a growth of the number of computational particles as only a fraction of each original computational particle is collided with its collision partner. When the collision multiplier is unity, $c_m = 1$, the transferred weight is equal to the lesser of the two particles colliding such that the smaller particle is completely eliminated and only one particle is effectively added to z. In the special case that all the particles have the same weight, $w_i = w_j =$ constant, and the collision multiplier is unity, the standard DSMC method is recovered as all terms highlighted in red in the algorithm vanish or are unity with the exception that instead of replacing the original i & j particles with the post collision velocities, the original particles are essentially deleted by zeroing the weight. In standard DSMC, the new particles $(n + 1)$ and $(n + 2)$ would simply replace i and j respectively to avoid the need to remove 0-weight particles. If the collision multiplier is greater than unity, $c_m > 1$, only a fraction of both original particles is transferred to new particles which over-samples the Boltzmann collision integral when compared to standard DSMC but at the expense of two new computational particles per collision.

The growth in the number of computational particles per cell of the basic SWPM is unsustainable. The problem of differing particle weight and computational particle growth have been encountered in the past, particularly with respect to so-called radial weighting schemes for axii-symmetric flows [4] and flows involving trace species [7]. Generally in the particle method community, these errors have been simply accepted with attempts to produce the correct asymptotic behavior as in the case of the radial variation of weight within a cell, or the pre- and post-collision pieces are non-conservatively combined in a manner that either violated energy or momentum conservation as well as detailed balance as in common binary merge algorithms [8]. In fact, non-conservative merging of pre- and post-collision fragments within the collision step is particularly problematic as in general the isotropic elastic collision models commonly used in rarefied flow have significant non-local behavior in velocity-space that exacerbates the conservation errors.

Phase Space Resampling

In the original method of Reference [6], the number of particles is controlled by merging subgroups of m-particles into two particles preserving mass, momentum, and energy. This approach to particle merging has been periodically rediscovered throughout the literature on stochastic particle methods [8, 9], but is often disregarded due to the impact of distribution thermalization despite conservation of mass, momentum, and energy as in Reference [8].

In a subsequent work on the SWPM algorithms [10], Rjasanow, Schreiber, and Wagner analyze the importance of particle clustering in phase space to minimize the product of cluster root mean square velocity (RMS) and weight to inhibit the error resulting from the merge as well as the advantage of approximately uniform cluster weights. Because optimal clustering is known to be np-complete, they avoid attempting to find a global optimal clustering in favor a binary space subdivision method along the plane of maximum variance efficient enough to be run several times on a large database.

In prior work by Martin and Cambier [2, 11, 3], these issues were again encountered with respect to particle merging and fractional particle collisions. In these References, particles within a spatial cell were first sorted into approximately uniform weight octree-bins in velocity space prior to (m:2) merging within the leaves of the octree for leaves containing more than two particles. This algorithm was efficient enough to be applied continuously and when coupled with an analogous particle split, it was also shown to maintain a stable weight distribution among particles through repeated merging and splitting [3]. In the algorithm, both the target leaf weight and adaptive velocity cell scale shrink automatically with increasing target number of computational particles per cell suggesting that, combined with the Lipschitz metric of Reference [10], the method converges with increased particles/cell and decreased cell size.

Fused Bin-to-Bin Collide and Merge

Preliminary investigation of the fractional collisions suggested that oversampling the Boltzmann collision integral could result in lower fluctuations in the directional components of kinetic energy (i.e. kinetic temperature components) during a thermalization process [11]. In the current notation, this is equivalent to increasing the c_m multiplier. In doing so, more collisions are sampled with a smaller fraction of each particle being transferred to new locations in velocity space which reduces the impact of large rare scattering events of outlier particles that disproportionately impact the kinetic temperature. However, increasing c_m also increases the number of particles created per step by the collision algorithm. This increases memory requirements as well as increases the cost of particle sorting while the particles are immediately eliminated by the merge algorithm anyway as large c_m rapidly increases particle counts per cell beyond the target values. To avoid this step, a combined collide/merge step is investigated.

The algorithm is quite similar to the merge algorithm as described in Reference [3]. One key difference is that instead of discarding octree cells during the velocity space sort such that only active velocity cells with non-zero weight are retained, in the fused collide/merge algorithm, the inactive cells are flagged and retained along with pointers from parent to child octree cells. These links are used to rapidly identify the cell in which the post-collision velocities, v', w', land. After the particles have been sorted into octree velocity cells, the active cell 0th moment as well as the 1st and diagonal 2nd moments of velocity and position are accumulated for particles within the cell as $\bar{M}^t = \bigcup_{ci=1:N_c} \bar{M}^{(ci)} = \left((w)^{(ci)}, (wx_d)^{(ci)}, (wx_d^2)^{(ci)}, (wv_d)^{(ci)}, (wv_d^2)^{(ci)} \right)$. These moments are the same used to construct the merge particle pairs in the original merge algorithm. Note that subscript $d = \{x, y, x\}$ denotes directions for the position and velocity vectors such that 13 total moments are conserved.

To avoid storing new particles, the fused algorithm then jumps to a collision phase analogous to the SWPM collision algorithm. Instead of collisions between the variable weight particles, the collisions are sampled using the velocity cell weights and cross section for collision between pairs, $p = [a, b]$, of randomly generated particles from the bin moments created as they are in the original merge algorithm. If the collision is accepted, both "$a - a$" and "$b - b$" collisions are performed. This means the "a" particle of velocity cell "ci" collides with the "a" particle of cell "cj" to new "a'" velocity locations. The same process is repeated for the "b" particles such that the independent random orientations of "a" with respect to "b" collide all combinations of "a/b" orientations and the original cell moments are decremented proportionally. The collision is sampled using acceptance rejection and the bin moments of the original particle locations are decremented by the fraction of weight collided out of the bin. The binary elastic collisions are performed just as described by Equation 1, but the octree is traversed to find the most appropriate cell in which to transfer the weight, $\Delta^t w = W(\bar{M}^t, ci, cj, \hat{e}, p = [a, b])$, such that the fragments of computational particle are mixed with other fragments localized in velocity space. Instead of creating new particles at $v_d^{p'(ci)}$ and $v_d^{p'(cj)}$, a fraction of the conserved moments proportional to $\Delta^t w$ are then transferred from the ci and cj velocity cells to the

ci', cj' velocity cells respectively. The modified jump process for velocity cell moments is shown in Equation 2. The modified algorithm is equivalent to a stochastically sampled flux of mass, momentum, directional kinetic energy, center of mass, and directional RMS position due to the Boltzmann collision integral.

$$\bar{M}^{t+1} = J(\bar{M}^t, ci, cj, \hat{e}) = \sum_{p=[a,b]} \begin{cases} \bar{M}^{(k)}, & \text{if } k \leq N_c, k \neq ci, cj, ci', cj', \\ \bar{M}^{(ci)} - \Delta^t w\left(1, x_d^{p(ci)}, (x_d^2)^{p(ci)}, v_d^{p(ci)}, (v_d^2)^{p(ci)}\right), & \text{if } k = ci, \\ \bar{M}^{(cj)} - \Delta^t w\left(1, x_d^{p(cj)}, (x_d^2)^{p(cj)}, v_d^{p(cj)}, (v_d^2)^{p(cj)}\right), & \text{if } k = cj, \\ \bar{M}^{(ci')} + \Delta^t w\left(1, x_d^{p(ci)}, (x_d^2)^{p(ci)}, v_d^{p'(ci)}, (v_d^2)^{p'(ci)}\right), & \text{if } k = ci', \\ \bar{M}^{(cj')} + \Delta^t w\left(1, x_d^{p(cj)}, (x_d^2)^{p(cj)}, v_d^{p'(cj)}, (v_d^2)^{p'(cj)}\right), & \text{if } k = cj' \end{cases} \quad (2)$$

Each individually sampled collision preserves mass, momentum, and energy such that the fluxes of the moments maintain conservation of these conserved quantities within a spatial cell as well. The method does thermalize the distribution within local velocity bins as does the original merge algorithm. This has implications on detailed balance, but in the limit as $\Delta v \rightarrow 0$ for the velocity space cells, with increased number of particles per cell, the method should at least consistently converge to the solution of the Boltzmann equation as does the un-fused collide and merge algorithms. The convergence properties will be investigated qualitatively in the results section though a more rigorous analysis is left to future work.

RESULTS

This section will compare the performance of the SWPM using Octree merge and fused bin-to-bin Octree collisions to the standard DSMC method. Test cases include a 0D thermalization of a bi-Maxwellian distribution, a 1D Mach 2 shock in Argon gas, and a 2D Mach 8 flow around a flat plate. All the cases use the VHS model described in Reference [4] using the parameters d_{ref}=4.17Å, α=0.31, T_{ref}=273K.

The first case is the homogeneous thermalization of a bi-Maxwellian distribution of Argon. Each half Maxwellian has a number density of 5e21/m^3 initially at 293K with ±sound speed (246.948m/s) drift velocities aligned along the x-axis. A baseline case was run using standard DSMC with a real to computational particle weight fraction of 1.314e8 in a 2mm^3 cube. Time is stepped in 10ns increments for 500 time-steps. Table 1 lists computational performance of the SWPM+Octree and Bin-to-Bin model implementations for a range of collision multipliers. All the weighted particle cases use the same target number of particles though the range shown is the particle count range for the last 0.4μs. Figure 1 shows the relaxation results for the 3 cases each of SWPM+Octree and Bin-to-Bin method.

TABLE 1: Runtime and Particle Count for 0D-Thermalization.

Method	Multiplier	Runtime (s)	Particle Count (x1e3)
DSMC	n/a	48.8	609
Octree	1x	2.51	14.9-25.1
Octree	4x	3.75	15.5-25.5
Octree	16x	6.99	15.1-15.9
Bin-to-Bin	1x	2.59	17.1-25.9
Bin-to-Bin	4x	3.71	15.8-18.7
Bin-to-Bin	16x	6.53	17.1-18.6

As expected from prior work [11], increasing the collision multiplier results in a smoother thermalization. In general, the results approach those of the basline DSMC case with increased multiplier, with a notable exception in the SWPM+Octree case with 16x multiplier. For the high multiplier SWPM+Octree method, the relaxation rate noticeably deviates from the baseline solution. The deviation for the high multiplier SWPM+Octree method is likely the result of the same particles colliding repeatedly within a single time-step between merges. If the time-step is reduced by an order of magnitude to 1ns, the correct relaxation rate is recovered. The method is still convergent, but has a maximum fraction of particle collision per iteration. This error may be correctable in the future, but further analysis is required.

It is interesting to note that the Bin-to-Bin method appears to remain stable for large multipliers (up to 1024 was tested). This did require an additional modification to skip collisions such that the resulting fractional particle would have a real to computational weight ratio less than 1. With very high collision multiplier values, particles are scattered
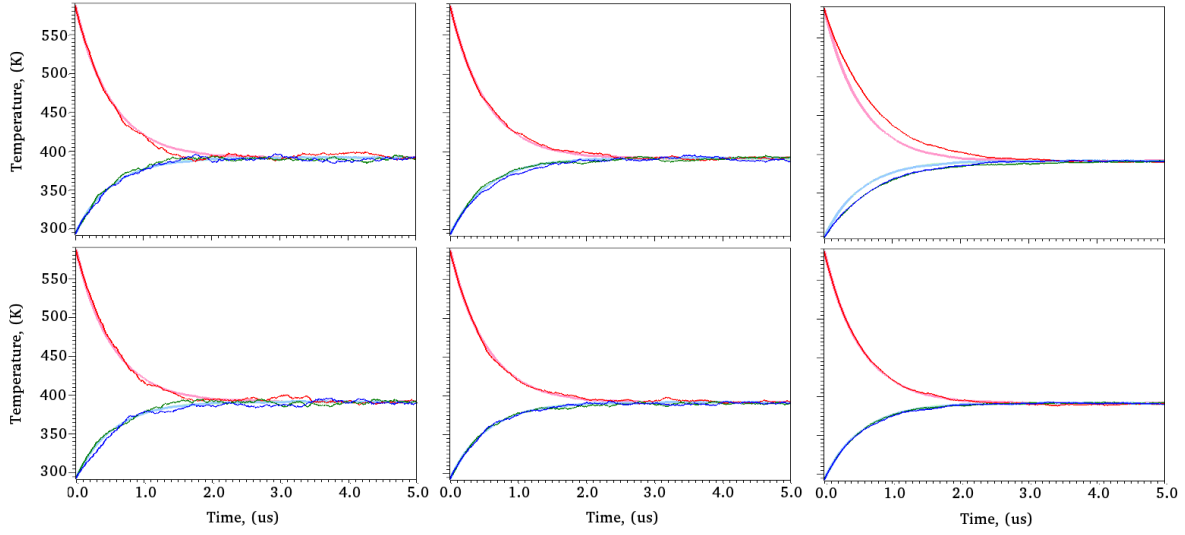
FIGURE 1: Comparison of 0D Thermalization Cases. Top row is SWPM+Octree method and bottom row is Bin-to-Bin method. Red is T_x while Green and Blue are T_y and T_z. Lighter thicker lines are baseline DSMC results. Collision multipliers are [1x,4x,16x] from left to right.
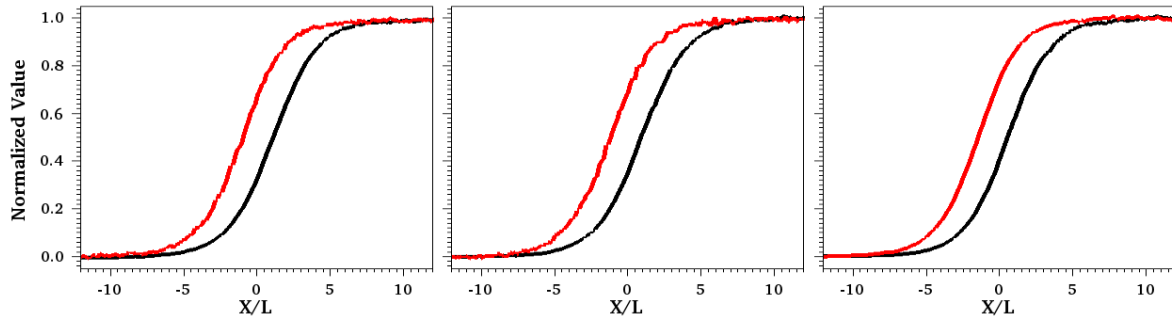
FIGURE 2: Comparison of DSMC, SWPM+Octree, and Bin-to-Bin results for 1D Mach 2.0 argon shock scaled by the upstream mean free path, L. Red line is the normalized temperature jump and black is normalized density jump. Results are for the 1x collision multiplier.

far into the tail of the distribution. Some limit is required to avoid floating point precision roundoff issues. Considering this weight ratio is approximately eight orders of magnitude lower than the particle weight of the baseline DSMC case, this is expected to have a minor impact of the results and enabled collision multipliers significantly beyond where the algorithm would otherwise run into precision issues. Though all these cases run considerably faster than the baseline DSMC case, the "error" and computational efficiency have yet to be quantified and measured. The results only indicate qualitative convergence towards the baseline solution. Further analysis of results across a broader range of parameter space is needed.

For the 1D example, the flow is setup as a stationary Mach 2 shock case from Chapter 12 of Reference [4]. Again argon gas is used with an initial (pre-shock) density and Temperature of 1e22/m³ and 293K respectively. Based off the VHS cross section, the upstream mean free path is 13.2μm. The right half of the domain is initialized with the post-shock conditions of 2.229e22/m³ and 608.891K. To maintain a stationary shock, the left side flow enters at 637.411m/s and exits to the right at 278.878m/s. Left and right boundary conditions are enforced through 3-cells worth of ghost cells with the initial left and right states. The domain used is (2cm x 2mm x 2mm) with grid spacing, dx=20μm. A time step of 10ns is again used with the flow stabilizing over 8μs and then the solution is averaged over the following 2μs.

The solutions as shown converge to the baseline CPU DSMC case when more particles are used, but the full
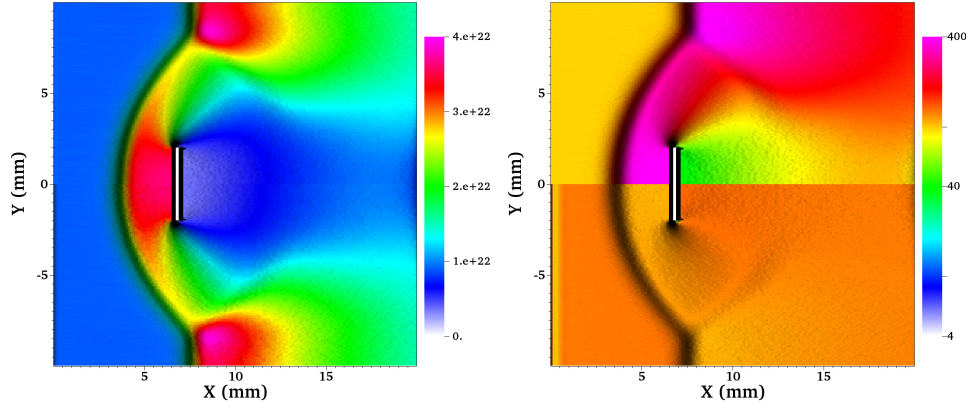
FIGURE 3: Comparison of Mach 8 Argon Shock Case for Standard DSMC (top half) and SWPM+Octree Merge (bottom half). The left figure shows argon number density and the right shows the number of computational particles per cell.

convergence properties with octree depth and particle count are beyond the scope of this work. Though the standard DSMC method can converge to the correct solution with only a few 10s of particles per cell in long time averages, the adapted algorithms introduce large errors likely resulting from the coarseness of the velocity bins below several hundred particles per cell though the results are considerably smoother than a DSMC solution with equivalent particle count. The impact of octree resolution on the higher moments that are only approximately conserved as a result of the velocity space binning should be investigated further. Based off the error analysis in Reference [10], rather than simply aiming for bins with approximately equal weight, it may also be advantageous to adapt the octree refinement to select for cells with approximately uniform product of weight multiplied by bin size. This too is left to future work.

For a final multidimensional example, a Mach 8.0 argon flow is impinged on a stationary plate. The same temperature and density of 293K and $1e22/m^3$ are used, but the inflow velocity is increased to 2550.455m/s. For the simulation, the domain size is increased to (2cm x 1cm x 2mm) using (dx=dy=80μm), and a time-step of 20ns was used. Specular ±y and ±z boundary conditions were used, and the left inflow boundary was set through filled ghost cells as in the Mach 2 case. The outflow boundary was also set to the inflow condition which does not account for the flow variation, but as the flow is supersonic at the exit, the results are reasonably independent of outflow boundary condition. In addition to the boundary conditions on the edges of the domain, a plate is added that extends 2mm into the flow from the lower y-boundary. This is simply a 0.4mm thick region with specular reflection boundaries that faces the flow to standoff into a curved bow-shock configuration. With the specular boundary conditions, this flow approximates flow through an array of plates blocking 20% of the flow. In the figures, the methods are compared to the mirrored version of the DSMC results. As in the 1D case, the method seems to converge to the baseline DSMC result, but again only with sufficiently high numbers of particles per cell. Quantifying the necessary particle counts for a given error level is therefore a critical next step in the development of these methods.

CONCLUSION

This work demonstrates the ability of conservative fractional weight collision schemes to converge to the baseline DSMC solution for a few simple flows. For accurate results, the number of particles per cell must be sufficiently high to control merge errors due to continuous splitting and merging of particles. This means that the methods will likely have trouble outperforming the standard DSMC method for steady state problems with relatively modest density jumps as in the cases shown here.

However, these cases were selected to be accessible DSMC baseline benchmark cases to demonstrate convergence of the fractional collision models. These new models are more likely to provide significant performance improvements for time accurate non-equilibrium flows where high particle/cell counts are already required to extract the transient signal from noise. The methods are also likely to be more useful for mixtures with large mass ratios
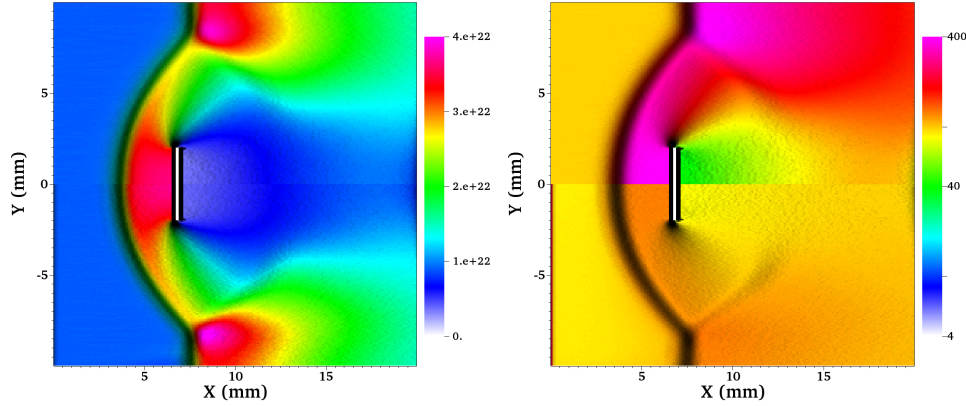
FIGURE 4: Comparison of Mach 8 Argon Shock Case for Standard DSMC (top half) and Fused Bin-to-Bin Collide and Merge (bottom half). The left figure shows argon number density and the right shows the number of computational particles per cell.

between species once adapted to the mixture case. Conservation of mass, momentum, and energy is enforced while higher moments and detailed balance are recovered in the many-particle/small octree bin limits. Detailed analysis of the sources of these errors is needed but left to future work. The method's ability to control particle/cell count and statistical fluctuations may prove particularly helpful in high density dynamic range flows such as plume expansion.

Another particularly noteworthy feature of the Bin-to-Bin method is that the collision integral can be sampled up to the velocity octree space quadrature accuracy with increased collision multiplier without a dramatically larger memory footprint. This highly adaptive binning and collision sampling could even find application in efficiently accelerating the Boltzman integral calculation in models that use Vlasov advection schemes in the future. More accurate solutions with fewer particles would be particularly advantageous for memory bandwidth bound applications and early results indicate improved parallel efficiency for an 8-processor version of the 2D plate case as the collision work increases relative to the communication overhead.

Because the collision multiplier is a local parameter, if coupled with an error estimate, it could also be used for adaptive refinement. In the future, it would also be particularly interesting to attempt to adapt the stochastic weight models to the positive/negative deviational particle methods as in Reference [12] so that collision work is only performed on positive and negative weight particles sampled from the deviation of the velocity distribution from a local Maxwellian.

REFERENCES

[1]   J. W. Koo, "2D electrostatic potential solver for Hall thruster simulation," in *42nd AIAA/ASME/SAE/ASEE Joint Propulsion Conference and Exhibit* (2006).
[2]   R. Martin and J.-L. Cambier, "Moment preserving adaptive particle weights using octree velocity distributions for PIC simulations," in *Proc. 28th Int. Symp. on Rarefied Gas Dynamics* (2012), pp. 872–879.
[3]   R. Martin and J.-L. Cambier, Journal of Computational Physics, **In-Press** (2016), DOI://10.1016/j.jcp.2016.01.020.
[4]   G. Bird, *Molecular Gas Dynamics and the Direct Simulation of Gas Flows* (Oxford University Press, 1994).
[5]   W. Wagner, Journal of Statistical Physics **66**, 1011–1044 (1992).
[6]   S. Rjasanow and W. Wagner, Journal of Computational Physics **124**, 243 – 253 (1996).
[7]   I. Boyd, Journal of Thermophysics and Heat Transfer **10**, 579–585 (1996).
[8]   G. Lapenta and J. U. Brackbill, J. Comp. Phys. **115**, 213 – 227 (1994).
[9]   J.-L. Cambier, "AFOSR Computational Mathematics Program Contractor's Review," August (2006).
[10]   S. Rjasanow, T. Schreiber, and W. Wagner, Journal of Computational Physics **145**, 382 – 405 (1998).
[11]   R. Martin and J.-L. Cambier, "Low noise fractional NTC collisions for DSMC," in *Proc. 28th Int. Symp. on Rarefied Gas Dynamics* (2012), pp. 615–620.
[12]   B. Yan, Journal of Computational Physics **309**, 18 – 36 (2016).

Analysis and Simulation for a Model of Electron Impacted Excitation/Deexcitation and Ionization/Recombination [*]

Bokai Yan[†], Russel E. Caflisch[†], Farzin Barekat[†] and Jean-Luc Cambier[‡]

February 25, 2015

Abstract

This paper describes a kinetic model and a corresponding Monte Carlo simulation method for excitation/deexcitation and ionization/recombination by electron impact in a plasma free of external fields. The atoms and ions in the plasma are represented by continuum densities and the electrons by a particle distribution. A Boltzmann type equation is formulated and an H-theorem is derived. The stationary states, which could be the Maxwell-Boltzmann distributions or not, are studied. An efficient Monte Carlo method is then developed for an idealized analytic model of the excitation and ionization collision cross sections. To accelerate the simulation, the reduced rejection method and binary search method are used to overcome the singular rate in the recombination process. Numerical results are presented to demonstrate the efficiency of the method on spatially homogeneous problems.

Keywords. Monte Carlo Method, Excitation-deexcitation, Ionization-recombination, Boltzmann equation, H theorem, Singular reaction rates.

[†]Mathematics Department, University of California at Los Angeles, Los Angeles, CA 90095-1555, USA. byan@math.ucla.edu, caflisch@math.ucla.edu, fbarekat@math.ucla.edu

[‡]Air Force Research Laboratory, Edwards AFB, CA 93524, USA. jean_luc.cambier@us.af.mil

Contents

1 Introduction

Simulations of plasma dynamics can be computationally challenging due to the large number of relevant physical processes and the wide range of space/time scales over which they operate. This is particularly true when accounting for inelastic collisional processes such as excitation/deexcitation and ionization/recombination in an atomic plasma, due to the large number of electronic states and reaction pathways. The relative significance of collisional interactions is determined by examining the respective strengths of the various terms of the Boltzmann equation for the distribution function f:

$$\partial_t f + \mathbf{v}\cdot\nabla_\mathbf{x} f + \mathbf{a}\cdot\nabla_\mathbf{v} f = Q(f) \tag{1}$$

where Q is the collision operator, with a stationary state f^{eq} being the equilibrium, Maxwellian distribution. The left-hand-side of (1) is the streaming operator in physical (x) and velocity (v) space, and $\mathbf{a}(E, B)$ is the acceleration due to the electric (E) and magnetic (B) fields. Thus, the Knudsen number $K_n = L_c/L_0$, in which L_c is the mean free path between collisions and L_0 is a characteristic length scale of the gradient operator, determines the relative strength of collisions versus advection. In the limit of small Knudsen number and weak fields, the energy distribution function f for each of the particle species is close to an Maxwellian equilibrium, and the evolution of the plasma can be described by fluid-like equations, in which individual particle interactions do not need to be resolved. On the other hand, for $K_n \gtrsim 1$ and/or large fields, the distribution f can be far from equilibrium, in which case particle representations and a Monte Carlo simulation procedure are appropriate. In this work, we consider the electron-induced inelastic collisions for excitation, ionization, and their reverse processes (deexcitation and recombination) for a dilute atomic plasma. For simplicity, we consider the simplest atomic species, Hydrogen, using a Bohr model of the Atomic State Distribution Function (ASDF); this is sufficient to examine the effects of multiple scales in the energies exchanged, as well as time-scales of reactions, while focusing on some mathematical and algorithmic aspects of the solution. For the same reason, other physical processes such as radiative transitions, atomic (heavy-particle) collisions, charge-exchange and elastic (Coulomb) collisions are also not considered. Note that we are solving for the local inelastic collision operator, and other effects due to transport in physical and velocity space, i.e. left-hand-side of (1), would be treated separately.

This paper consists of two parts. The first part (Section 2 - 4) reviews the mathematical description of excitation/deexcitation and ionization/recombination, in terms of the differential cross sections for each process. The modeling of the ionization cross sections by electron impact has been started from the early quantum models in the 1920s (see for example a recent review [1]). In this work, as a platform for development of numerical methods, our model uses the semi-classical cross section (for example, see [2]) for the energetic cross section of ionization and an extension of this cross section for excitation. The cross sections for the reverse processes are then found through detailed balance. A Boltzmann equation is also formulated for the evolution of the electron distribution and for the atom and ion densities. Using this Boltzmann equation, we formulate and derive a version of Boltzmann's H-Theorem for excitation/deexcitation and ionization/recombination, originating from the classical definition of physical entropy. Although not unexpected, the H function is new in this context to the best of our knowledge.

The second part (Section 5 and 6) of this paper describes the development of a particle simulation method for these kinetic processes. Ionization and recombination processes have been included in the kinetic equations describing particles collisions in, for example, [3–5]. In those work the reaction rates depend on the macroscopic number density and temperature, since they were computed by assuming the electron distribution to be a Maxwellian. For non-equilibrium conditions, (see for

example [6]), more realistic reaction rates depend on the electron velocity (or energy) rather than temperature. The recombination rates are particularly difficult to treat, since they are singular as the electron velocity goes to 0; thus, an electron with lower energy can more easily be recombined, see for example [7]. This singularity presents a new numerical challenge that we overcome in this work, using either the Reduced Rejection method of [8] or a binary search method. We employ here the framework of the Kinetic Monte Carlo (KMC) method ([9, 10]), or equivalently the Gillespie method [11]. Simulations are performed by random sampling from all of the relevant kinetic processes. We would also like to mention that [12] gives a deterministic method to solve the same system.

The remainder of this paper is organized as follows. The formulation of the kinetic processes and their rates and the resulting Botlzmann equations, along with some preliminaries, are presented in Section 2. The analogue of Boltzmann's H-theorem is formulated in Section 3. The models for the cross sections are described in Section 4, and the Monte Carlo simulation method, using a particle representation for the electrons, is presented in Section 5. Computational results from this simulation method are presented in Section 6. Finally, conclusions and future directions are discussed in Section 7, while some technical details are presented in Appendices A-E.

2 Formulation

2.1 The Distribution Function

The plasma is assumed to consist of electrons (e), a single type of ion, of unit charge, and neutral atoms in various electronic states. The atoms and ions are modeled as a continuum with uniform density; the electrons are modeled through an energy distribution function, which is simulated using a discrete set of particles. Throughout this paper, the temperature T_e will have units of energy so that the Boltzmann constant $k_B = 1$ (i.e., it can be omitted).

The problems solved here will be spatially homogeneous (no spatial gradients and no transport) and isotropic in velocity. Thus, we can describe the system in terms of a time-dependent electron energy distribution function (EEDF) for the free electrons, $f(E, t)$ (E is the energy of the particle). The normalization is such that macroscopic electron number density n_e and temperature T_e can be obtained from by taking the first two moments:

$$n_e = \int_0^\infty f(E)\, \mathrm{d}E, \tag{2a}$$

$$\frac{3}{2} n_e T_e = \int_0^\infty E f(E)\, \mathrm{d}E. \tag{2b}$$

Here, T_e defines the scale of the macroscopic energy of the electrons, without necessarily assuming an equilibrium, Maxwellian distribution. Note that the energy distribution function f and the velocity distribution function F (under the assumption that F is isotropic, i.e., $F = F(v)$ for $v = |\mathbf{v}|$) are related by

$$f(E) = \frac{4\pi}{m_e} \left(\frac{2E}{m_e} \right)^{\frac{1}{2}} F, \tag{3}$$

since $E = m_e v^2 / 2$ and $\mathrm{d}\mathbf{v} = 4\pi v^2\, \mathrm{d}v$.

We use the following notation for the other variables.

$k_{\max}$: the total number of levels included in atoms,

$n_k(t)$: the number density of atoms at excitation level, $k = 1, \ldots, k_{\max}$,

n_a : number density of all neutral atoms $\left(= \sum_k n_k \right)$,

n_i : number density of ions $(\equiv n_e)$,

L_k : the energy of atoms at the k-th excitation level, $k = 1, \ldots, k_{\max}$,

L_i : the ionization energy of an unexcited atom,

g_k : the degeneracy of level k,

g_i : the degeneracy of an ion,

g_e : the (spin) degeneracy of the electron$(= 2)$.

The subscript i is this work always refer to "ion". The subscript k always refer to the atomic level. As mentioned earlier, we use the simple Bohr model for Hydrogen, such that:

$$L_k = (1 - k^{-2})I_H, \qquad L_i = I_H = L_\infty, \qquad g_k = 2k^2, \qquad g_i = 2, \tag{4}$$

where I_H is the Rydberg unit of energy (13.6eV). By definition, the atomic ground state, from which all energy levels are measured, corresponds to $k = 1$, i.e. $L_1 \equiv 0$. Without transport of particles, charge neutrality of the system is assured, i.e. $n_i \equiv n_e$, while mass and energy conservation imply $\frac{\mathrm{d}}{\mathrm{d}t}n_{tot} = \frac{\mathrm{d}}{\mathrm{d}t}\varepsilon_{tot} = 0$, with n_{tot} the total number density of (bound and free) electrons and ε_{tot} the total energy of the system defined by

$$n_{\mathrm{tot}} = n_e + n_a = n_i + n_a, \tag{5a}$$

$$\varepsilon_{tot} = \varepsilon_e + \varepsilon_a + \varepsilon_i = \int E f(E)\,\mathrm{d}E + \sum_k n_k L_k + n_i L_i. \tag{5b}$$

Note that momentum conservation is not used here, since it leads to terms of order of the ratio of masses, $m_e/M_i \lessgtr 1/2000$, which are neglected. At equilibrium, the electron distribution is the (isotropic) Maxwell-Boltzmann distribution

$$f^{eq}(E) = n_e 2(\pi T_e^3)^{-\frac{1}{2}}\sqrt{E}\,e^{-E/T_e}. \tag{6}$$

The equilibrium densities n_k^{eq} and n_i^{eq} for atomic level populations and ions are given by the Boltzmann and Saha distributions respectively [13]. The former describes the ratio of number densities between two levels (e.g. l, u), and the latter is the ratio between electron and ion densities and that of the atomic level from which ionization takes place [1]

$$\text{Boltzmann}: \quad \mathcal{B}_{lu}(T_e) = \frac{n_u^{eq}}{n_l^{eq}} = \frac{g_u}{g_l}e^{-\Delta E_{lu}/T_e}, \tag{7a}$$

$$\text{Saha}: \quad \mathcal{S}_k(T_e) = \frac{n_i^{eq}n_e^{eq}}{n_k^{eq}} = \frac{g_i}{g_k}\mathbb{Z}_e e^{-B_k/T_e}, \tag{7b}$$

where h is the Planck constant, and

$$\mathbb{Z}_e = g_e \left(\frac{2\pi m_e T_e}{h^2} \right)^{3/2} = g_e \lambda_e^{-3}, \tag{8}$$

is the electron partition function (we recall that $g_e \equiv 2$). Here λ_e is the de Broglie wavelength of an electron (see [13] for example). We have also defined the energy gap $\Delta E_{lu} = L_u - L_l$ and the binding

---

[1]We emphasize that only electron-impact collisions are examined here, and therefore both functions depend only on T_e. The equilibrium distributions being used here only to express equilibrium relations and verify the H-theorem, no assumption is made about the actual thermodynamic state of the plasma.

energy $B_k = L_i - L_k$. These expressions are equivalent (under the assumption that $n_e = n_i$; i.e., charge neutrality) to the following:

$$n_k^{eq} = \frac{n_a}{\mathbb{Z}_a} g_k e^{-L_k/T_e}, \tag{9a}$$

$$n_i^{eq} = c_i e^{-L_i/2T_e}, \tag{9b}$$

where $\mathbb{Z}_a$ and c_i are:

$$\mathbb{Z}_a = \sum_{k=1}^{k_{\max}} g_k e^{-L_k/T_e}, \tag{10a}$$

$$c_i = \left[2 g_i \mathbb{Z}_a^{-1} n_a \left(\frac{2\pi m_e T_e}{h^2} \right)^{\frac{3}{2}} \right]^{1/2}. \tag{10b}$$

Here $\mathbb{Z}_a$ is the atomic partition function. Note that T_e used here is also the equilibrium temperature of the electrons, i.e. that of the Maxwellian distribution (6).

We end this section with a lemma, which shows that specification of temperature is equivalent to specification of total energy:

Lemma 2.1. *Suppose $n_{tot} > 0$ is the total number of free and bound electrons, and $\varepsilon_{tot} > 0$ is the total energy of the system. Then there are unique values of T_e, n_e and n_a satisfying*

$$n_e + n_a = n_{tot},$$
$$\frac{3}{2} n_e T_e + \sum_k n_k^{eq} L_k + n_i^{eq} L_i = \varepsilon_{tot},$$

with n_k^{eq} and $n_i^{eq} = n_e$ obtained using (7a)-(7b).

The proof is given in Appendix A for completeness.

2.2 Interaction Types and Rates

We consider here a thermal (single-fluid) plasma; because of the small electron/atom mass ratio, the relative velocity and relative energy of the collision is well approximated by electron velocity and kinetic energy. We also assume also that the differential cross sections are independent of the angular variables and only depend on the collision energy. We consider four types of collisions, ordered in pairs of forward and backward processes:

1. The excitation of a lower state l to an upper-state u by an electron of energy E_0 with $E_0 > \Delta E_{lu}$ leaves a post-collision electron with energy $E_1 = E_0 - \Delta E_{lu}$. We write this process as $(l, E_0) \to (u, E_1)$, with a cross section $\sigma_{lu}^{exc}(E_0; E_1)$.
2. The reverse process is deexcitation from the upper-state u down to a lower-state l after collision with an electron of energy E_1, leaving a post-collision electron with energy $E_0 = E_1 + \Delta E_{lu}$. We write this process as $(u, E_1) \to (l, E_0)$, with cross section $\sigma_{ul}^{dex}(E_1; E_0)$.
3. Ionization from an atomic level k, by a free electron with energy $E_0 > B_k$, which generates a scattered electron with energy of $E_1 = E_0 - E_t$, a new electron with energy $E_2 = E_t - B_k$, and an ion. The transferred energy E_t satisfies $B_k \leqslant E_t \leqslant E_0$. We write this process as $(k, E_0, E_t) \to (E_1, E_2)$, with $\sigma_k^{ion}(E_0; E_1, E_2)$.
4. The reverse process is three-body recombination, where a free electron (E_1) and an ion recombine into an atomic state k, after collision with a second free electron (E_2). This second electron gains energy from the collision, with post-collisional energy $E_0 = E_2 + E_1 + B_k$. We write this process as $(E_1, E_2) \to (k, E_0)$ and $\sigma_k^{rec}(E_1, E_2; E_0)$.

Explicit formulae for these cross sections are presented in Section 4. For each process, we can define a rate r per electron (more precisely, per electron pair for recombination):

$$r^{\text{ion}}(k, E_0, E_t) = n_k v(E_0) \sigma_k^{\text{ion}}(E_0; E_1, E_2), \tag{11a}$$

$$r^{\text{rec}}(k, E_1, E_2) = n_i v(E_1) v(E_2) \sigma_k^{\text{rec}}(E_1, E_2; E_0), \tag{11b}$$

$$r^{\text{exc}}(l, u, E_0) = n_l v(E_0) \sigma_{lu}^{\text{exc}}(E_0; E_1), \tag{11c}$$

$$r^{\text{dex}}(u, l, E_1) = n_u v(E_1) \sigma_{ul}^{\text{dex}}(E_1; E_0) \tag{11d}$$

where $v(E) = \sqrt{2E/m_e}$ is the electron velocity and only depends on the energy. An integrated ionization rate per electron is:

$$r_{tot}^{\text{ion}}(k, E_0) = \int_{B_k}^{E_0} r^{\text{ion}}(k, E_0, E_t) \, \mathrm{d}E_t = n_k v(E_0) \sigma_{tot}^{\text{ion}}(k, E_0). \tag{12}$$

The total, macroscopic rates are (in units of $(\text{volume} \cdot \text{time})^{-1}$):

$$R^{ion} = \sum_k \int_{B_k}^{\infty} r_{tot}^{\text{ion}}(k, E_0) f(E_0) \, \mathrm{d}E_0, \tag{13a}$$

$$R^{rec} = \sum_k \int_0^{\infty} \int_0^{\infty} r^{\text{rec}}(k, E_1, E_2) f(E_1) f(E_2) \, \mathrm{d}E_1 \, \mathrm{d}E_2, \tag{13b}$$

$$R^{exc} = \sum_l \sum_{u>l} \int_{\Delta E_{lu}}^{\infty} r^{\text{exc}}(l, u, E_0) f(E_0) \, \mathrm{d}E_0, \tag{13c}$$

$$R^{dex} = \sum_u \sum_{l<u} \int_0^{\infty} r^{\text{dex}}(u, l, E_1) f(E_1) \, \mathrm{d}E_1 \tag{13d}$$

2.3 The Principle of Detailed Balance

The principle of detailed balance determines the relations between the rates of different processes [13], by asserting that, at thermal equilibrium, each reaction $p \to q$ is exactly counterbalanced by its inverse $q \to p$. In other words, $r_{p \to q} = r_{q \to p}$ for all pairs of states p and q. Hereafter, to simply expressions and unless specified otherwise, we will use the short notations

$$v_p = v(E_p), \quad f_p = f(E_p), \quad \text{for } p = 0, 1, 2 \tag{14}$$

and

$$\sigma^{\text{ion}} = \sigma_k^{\text{ion}}(E_0; E_1, E_2), \tag{15a}$$

$$\sigma^{\text{rec}} = \sigma_k^{\text{rec}}(E_1, E_2; E_0), \tag{15b}$$

$$\sigma^{\text{exc}} = \sigma_{lu}^{\text{exc}}(E_0; E_1), \tag{15c}$$

$$\sigma^{\text{dex}} = \sigma_{ul}^{\text{dex}}(E_1; E_0), \tag{15d}$$

For the ionization and recombination processes, the principle of detailed balance states that:

$$n_k^{eq} f_0^{eq} v_0 \sigma^{\text{ion}} = n_i^{eq} f_1^{eq} f_2^{eq} v_1 v_2 \sigma^{\text{rec}}. \tag{16}$$

Note that n_k^{eq}, f^{eq} and n_i^{eq} are temperature dependent, describing the statistical properties of the reactants (average over initial states), while the microscopic quantities v_p, σ^{ion} and σ^{rec} are independent of temperature. Using the Saha equilibrium relation (7b), we obtain the Fowler-Nordheim relation between microscopic variables [13]:

$$g_k E_0 \sigma^{\text{ion}} = \frac{16 \pi m_e}{h^3} g_i E_1 E_2 \sigma^{\text{rec}}. \tag{17}$$

Similarly, for the excitation and deexcitation processes, detailed balance implies:

$$n_l^{eq} f_0^{eq} v_0 \sigma^{\text{exc}} = n_u^{eq} f_1^{eq} v_1 \sigma^{\text{dex}}. \tag{18}$$

Using the equilibrium Boltzmann relation (7a), we then obtain a similar relationship between microscopic variables, the Klein-Rosseland relation [13]:

$$g_l\, E_0\, \sigma^{\text{exc}} = g_u\, E_1\, \sigma^{\text{dex}}. \tag{19}$$

The fact that the cross-sections for forward and reverse processes are not independent is to be expected from invariance under time-reversal of the microscopic, quantum interactions. Thus, eqs. (17,19) are more fundamental than (16,18) and in turn, can be used to relate the rates of forward and backward processes, independently of thermodynamic equilibrium conditions.

2.4 The Boltzmann equation

Now we formulate the Boltzmann type equations for the electron energy distribution $f(E,t)$ and the atom density function $n_k(t)$, for inelastic collisions only. We present the results here and go through the details for ionization/recombination processes in Section 2.4.1 and excitation/deexcitation processes in Section 2.4.2. Since we are only examining here the collisional processes, we can restrict ourselves to a homogeneous system with no electro-magnetic fields, so that the streaming operators on the left-side of (1) vanish. Thus, the reduced Boltzmann equations for ionization / recombination and excitation / deexcitation are:

$$
\begin{aligned}
\partial_t f(E) &= Q^e_{IR} + Q^e_{ED}, \\
\partial_t n_k &= Q^k_{IR} + Q^k_{ED}, \\
\partial_t n_i &= Q^i_{IR} + Q^i_{ED},
\end{aligned}
\tag{20}
$$

with the ionization/recombination collision operators

$$
\begin{aligned}
Q^e_{IR} &= \sum_k \iint (\delta_1 + \delta_2 - \delta_0)\left(n_k f_0 v_0 \sigma^{ion} - n_i f_1 f_2 v_1 v_2 \sigma^{rec}\right)\, \mathrm{d}E_0\, \mathrm{d}E_t, \\
Q^k_{IR} &= -\iint \left(n_k f_0 v_0 \sigma^{ion} - n_i f_1 f_2 v_1 v_2 \sigma^{rec}\right)\, \mathrm{d}E_0\, \mathrm{d}E_t, \\
Q^i_{IR} &= \sum_k \iint (n_k f_0 v_0 \sigma^{ion} - n_i f_1 f_2 v_1 v_2 \sigma^{rec})\, \mathrm{d}E_0\, \mathrm{d}E_t,
\end{aligned}
\tag{21}
$$

and the excitation/deexcitation collision operators

$$
\begin{aligned}
Q^e_{ED} &= \sum_u \sum_{l<u} \int (\delta_1 - \delta_0)\left(n_l f_0 v_0 \sigma^{exc} - n_u f_1 v_1 \sigma^{dex}\right)\, \mathrm{d}E_0, \\
Q^k_{ED} &= \sum_u \sum_{l<u} (\delta_{uk} - \delta_{lk}) \int \left(n_l f_0 v_0 \sigma^{exc} - n_u f_1 v_1 \sigma^{dex}\right)\, \mathrm{d}E_0, \\
Q^i_{ED} &= 0.
\end{aligned}
\tag{22}
$$

Here E_1 and E_2 in the ionization/recombination equations (21) are defined by

$$E_1 = E_0 - E_t, \quad E_2 = E_t - B_k, \tag{23}$$

and E_1 in the excitation/deexcitation equations (22) is defined by

$$E_1 = E_0 - \Delta E_{lu}. \tag{24}$$

The short notations (14), (15) and

$$\delta_p = \delta(E - E_p), \quad p = 0, 1, 2, \tag{25}$$

are used. In Q^k_{ED} the Kronecker delta function $\delta_{ij} = 1$ if the two subscripts i, j are equal, and 0 otherwise.

2.4.1 Ionization and recombination

Considering ionization and recombination from and to a single level k only, the kinetic equation for electrons includes a source term:

$$
\begin{aligned}
\partial_t f(E)|_k = Q^e_{IR}|_k = n_k \int & f_0 v_0 \, \sigma^{ion}_k(E_0; E_1, E_2)\delta(E_1 - E) \, \mathrm{d}E_t \, \mathrm{d}E_0 \\
+ n_k \int & f_0 v_0 \, \sigma^{ion}_k(E_0; E_1, E_2)\delta(E_2 - E) \, \mathrm{d}E_t \, \mathrm{d}E_0 \\
- n_k \int & f_0 v_0 \, \sigma^{ion}_k(E_0; E_1, E_2)\delta(E_0 - E) \, \mathrm{d}E_t \, \mathrm{d}E_0 \\
- n_i \int & f_1 f_2 v_1 v_2 \, \sigma^{rec}_k(E_1, E_2; E_0)\delta(E_1 - E) \, \mathrm{d}E_1 \, \mathrm{d}E_2 \\
- n_i \int & f_1 f_2 v_1 v_2 \, \sigma^{rec}_k(E_1, E_2; E_0)\delta(E_2 - E) \, \mathrm{d}E_1 \, \mathrm{d}E_2 \\
+ n_i \int & f_1 f_2 v_1 v_2 \, \sigma^{rec}_k(E_1, E_2; E_0)\delta(E_0 - E) \, \mathrm{d}E_1 \, \mathrm{d}E_2.
\end{aligned}
$$

The first three lines describe respectively the gain/gain/loss of electrons during an ionization process, the next three lines describe the loss/loss/gain of electrons during a recombination process, and the integration takes place over the initial states. These expressions implicitly contain the relationships between the electron energies, i.e. (23) from energy conservation, and such that $\mathrm{d}E_0 \, \mathrm{d}E_t = \mathrm{d}E_1 \, \mathrm{d}E_2$. Summing over all excitation levels, we obtain:

$$
\partial_t f(E) = Q^e_{IR} = \sum_{k=1}^{k_{max}} \iint (\delta_1 + \delta_2 - \delta_0) \left(n_k f_0 v_0 \sigma^{ion} - n_i f_1 f_2 v_1 v_2 \sigma^{rec} \right) \, \mathrm{d}E_0 \, \mathrm{d}E_t, \tag{26}
$$

with δ_p defined in (25). Similarly, the equation for the atomic state is:

$$
\begin{aligned}
\partial_t n_k = Q^k_{IR} &= \iint n_i f_1 f_2 v_1 v_2 \, \sigma^{rec}_k(E_1, E_2; E_0) \, \mathrm{d}E_t \, \mathrm{d}E_0 \\
&\quad - \iint n_k f_0 v_0 \, \sigma^{ion}_k(E_0; E_1, E_2) \, \mathrm{d}E_t \, \mathrm{d}E_0 \\
&= - \iint \left(n_k f_0 v_0 \sigma^{ion} - n_i f_1 f_2 v_1 v_2 \sigma^{rec} \right) \, \mathrm{d}E_0 \, \mathrm{d}E_t.
\end{aligned} \tag{27}
$$

The first term describes the gain of atomic level density in the recombination process, while the second term describes the loss of neutral density in the kth level due to the ionization. The equation for the ions is

$$
\begin{aligned}
\partial_t n_i = Q^i_{IR} = \partial_t \int f(E) \, \mathrm{d}E &= - \sum_k \partial_t n_k \\
&= \sum_k \iint (n_k f_0 v_0 \sigma^{ion} - n_i f_1 f_2 v_1 v_2 \sigma^{rec}) \, \mathrm{d}E_t \, \mathrm{d}E_0.
\end{aligned} \tag{28}
$$

2.4.2 Excitation and deexcitation

Consider now an excitation and deexcitation process between two levels (l, u) only. The kinetic equation for the electrons is

$$
\begin{aligned}
\partial_t f(E)]_{lu} = Q^e_{ED}]_{lu} = & \int n_l f(E_0) v(E_0) \sigma^{exc}_{lu}(E_0; E_1) \delta(E_1 - E) \, \mathrm{d}E_1 \\
& - \int n_l f(E_0) v(E_0) \sigma^{exc}_{lu}(E_0; E_1) \delta(E_0 - E) \, \mathrm{d}E_0 \\
& + \int n_u f(E_1) v(E_1) \sigma^{dex}_{ul}(E_1; E_0) \delta(E_0 - E) \, \mathrm{d}E_0 \\
& - \int n_u f(E_1) v(E_1) \sigma^{dex}_{ul}(E_1; E_0) \delta(E_1 - E) \, \mathrm{d}E_1.
\end{aligned}
\tag{29}
$$

The first two lines correspond respectively to the gain/loss of electrons in the excitation processes, while the next two lines correspond to the gain/loss of electrons in the deexcitation processes. Summing over all pairs of levels (l, u) and using short notations again, we obtain the compact form:

$$
\partial_t f(E) = Q^e_{ED} = \sum_u \sum_{l<u} \int (\delta_1 - \delta_0) \left(n_l f_0 v_0 \sigma^{exc} - n_u f_1 v_1 \sigma^{dex} \right) \mathrm{d}E_0.
\tag{30}
$$

Here E_0 and E_1 are related by (24). Similarly the equation for the density function of atoms is

$$
\begin{aligned}
\partial_t n_k = Q^k_{ED} = & \sum_{l<k} \int n_l f(E_0) v(E_0) \sigma^{exc}_{kl}(E_0; E_1) \, \mathrm{d}E_0 - \sum_{u>k} \int n_k f(E_0) v(E_0) \sigma^{exc}_{uk}(E_0; E_1) \, \mathrm{d}E_0 \\
& + \sum_{u>k} \int n_u f(E_1) v(E_1) \sigma^{dex}_{ku}(E_1; E_0) \, \mathrm{d}E_1 - \sum_{l<k} \int n_k f(E_1) v(E_1) \sigma^{dex}_{lk}(E_1; E_0) \, \mathrm{d}E_1 \\
& = \sum_u \sum_{l<u} \int \left(n_l f_0 v_0 \sigma^{exc} - n_u f_1 v_1 \sigma^{dex} \right) (\delta_{uk} - \delta_{lk}) \, \mathrm{d}E_0.
\end{aligned}
\tag{31}
$$

The first two tems correspond to the gain and loss of atoms at k-th level in excitation processes, and the next two terms corresponds to the deexcitation processes. In the last line, the summation is over all pairs of (l, u) with $l < u$ by introducing the Kronecker delta function.

3 Entropy and the H-Theorem

3.1 Entropy

The Boltzmann entropy of a macroscopic system of $\mathbb{N}_p$ particles of type p is defined as

$$
S_p = k_B \log \mathbb{W}_p,
$$

where $\mathbb{W}_p$ is the number of independent micro-states available and compatible with a given total energy of the system. The total phase space available to the system can be divided into unit cells, such that the number of possible arrangements of $\mathcal{N}_p(n)$ particles distributed into $\mathcal{G}_p$ available quantum states in the nth cell is

$$
\mathbb{W}_p(n) = \frac{\mathcal{G}_p^{\mathcal{N}_p}}{\mathcal{N}_p!}.
$$

We have assumed here a *classical* approximation $(\mathcal{G}_p \gg \mathcal{N}_p)$, since the studied conditions are such that no quantum statistical effects need to be considered. The $\mathcal{N}_p!$ factor is a correction for the fact that particles in the same unit phase space are indistinguishable. The number of particles being variable, the total number of possible arrangements for a given macro state (in units of $k_B = 1$) is

$$
S_p = \log \prod_n \mathbb{W}_p(n) = \sum_n \log \frac{\mathcal{G}_p^{\mathcal{N}_p}}{\mathcal{N}_p!},
\tag{32}
$$

in which the dependence of $\mathcal{G}_p$ and $\mathcal{N}_p$ on n is implicit. Using the Stirling approximation $\log(\mathcal{N}!) \approx \mathcal{N}\log\mathcal{N} - \mathcal{N}$, the entropy (32) becomes

$$S_p = -\sum_n \mathcal{N}_p \left[\log \frac{\mathcal{N}_p}{\mathcal{G}_p} - 1 \right]. \tag{33}$$

For a very large number of cells (continuous distributions), we can approximate the discrete summation by an integral, yielding

$$S_p = -\int N_p(E) \left[\log \frac{\mathcal{N}_p(E)}{\mathcal{G}_p(E)} - 1 \right] dE. \tag{34}$$

We introduce now the definition of the occupation number

$$\zeta_p(E) = \frac{\mathcal{N}_p(E)}{\mathcal{G}_p(E)}. \tag{35}$$

The occupation number ζ_p is a temperature-dependent, intensive variable.

For electrons, consider a small (or infinitesimal) volume $d^3\mathbf{v}\, d^3\mathbf{p}$ in phase space. The number of possible micro-states in this phase space cell is

$$\mathcal{G}_e \equiv g_e \frac{d^3\mathbf{x}\, d^3\mathbf{p}}{h^3} = g_e \frac{m_e^3}{h^3} d^3\mathbf{x}\, d^3\mathbf{v},$$

where $g_e = 2$ is the spin degeneracy, and the remainder is the elementary volume in phase space. Assuming that the distributions are spatially homogeneous, we can replace $d^3\mathbf{x}$ by a spatial cell of volume 1. After a change of variable from velocity $\mathbf{v}$ to energy E (assuming isotropic distributions), one has

$$\mathcal{G}_e \equiv g_e \left[\frac{4\pi m_e^2}{h^3} \left(\frac{2E}{m_e} \right)^{1/2} \right] dE = g_e g_{\mathrm{tr}}(E)\, dE, \tag{36}$$

in which $g_{\mathrm{tr}}(E)$ is the energy-dependent degeneracy per unit volume due to the *translational* modes only. Similarly, the number of particles in a unit spatial volume with energy in an interval of size dE can be written as

$$\mathcal{N}_e(E) = F(v)\, d^3v = f(E)\, dE$$

The occupation number (35) becomes

$$\zeta_e(E) = \frac{\mathcal{N}_e(E)}{\mathcal{G}_e(E)} = \frac{f(E)}{g_e g_{\mathrm{tr}}(E)}. \tag{37}$$

From (34), we can write down the entropy for the free electrons:

$$S_e = -\int f(E)\, (\log \zeta_e(E) - 1)\, dE = -\int f(E) \left(\log \frac{f(E)}{g_e g_{\mathrm{tr}}(E)} - 1 \right) dE. \tag{38}$$

For atoms in a specified atomic state k, the same definition applies; i.e.,

$$\mathcal{G}_k = g_k \left[\frac{4\pi M_A^2}{h^3} \left(\frac{2E_A}{M_A} \right)^{1/2} \right] dE_A = g_k g_{\mathrm{tr},A}\, dE_A,$$

where g_k is now the level degeneracy, E_A, M_A are respectively the kinetic energy and mass of the atom, and $\mathcal{N}_k = n_k\, dE_A$. Combining with (36), the occupation number for atoms at level k is

$$\zeta_k = \frac{\mathcal{N}_k}{\mathcal{G}_k} = \frac{n_k}{g_k g_{\mathrm{tr},A}}, \tag{39}$$

and the entropy for the atoms is

$$S_a = \sum_k S_k = -\sum_k n_k (\log \zeta_k - 1) = -\sum_k n_k \left(\log \frac{n_k}{g_k g_{\mathrm{tr},A}} - 1 \right). \tag{40}$$

Similarly the occupation number for ions is

$$\zeta_i = \frac{n_i}{g_i g_{\mathrm{tr},i}}, \tag{41}$$

with the translational degeneracy

$$g_{\mathrm{tr},i} = \frac{4\pi M_i^2}{h^3}\left(\frac{2E_i}{M_i}\right)^{1/2}.$$

Because of the small electron/atom mass ratio, the kinetic energy of the atom is approximately constant during collisions, i.e. $M_i \approx M_a$ and $E_i \approx E_a$. Therefore $g_{\mathrm{tr},i} \approx g_{\mathrm{tr},A}$. The entropy for the ions is then:

$$S_i = -n_i\left(\log\zeta_i - 1\right) = -n_i\left(\log\frac{n_i}{g_i g_{\mathrm{tr},i}} - 1\right). \tag{42}$$

The total entropy of the system is the sum of that of its constituents,

$$S = S_e + S_a + S_i, \tag{43}$$

with S_e, S_a and S_i defined by (38)(40)(42).

3.2   Relation to H theorem

It is traditional to define a H function[2] to describe the constrained evolution of the system towards equilibrium. The definition of a H function includes the equilibrium distribution,

$$
\begin{aligned}
H^* = \int &\left\{ f(E)\log\frac{f(E)}{f^{eq}(E)} - (f(E) - f^{eq}(E))\right\}\mathrm{d}E \\
&+ \sum_k \left\{ n_k\log\frac{n_k}{n_k^{eq}} - (n_k - n_k^{eq})\right\} \\
&+ n_i\log\frac{n_i}{n_i^{eq}} - (n_i - n_i^{eq}).
\end{aligned}
\tag{44}
$$

This expression is commonly referred to as the *relative* entropy, since it is identically zero at equilibrium. One can recognize it as the Kullback-Leibler divergence between the two probability density functions f, f^{eq}. Using (6)(8) and (37), we can express the two distribution functions for the electrons as

$$f(E) = g_e g_{\mathrm{tr}}(E)\zeta_e(E), \tag{45a}$$

$$f^{eq}(E) = n_e^{eq}\frac{g_e g_{\mathrm{tr}}(E)}{\mathbb{Z}_e(T)}e^{-E/T}. \tag{45b}$$

The electron contribution to the H function is therefore

$$H_e^* = \int f(E)\log\zeta_e(E)\,\mathrm{d}E + \left(\log\frac{\mathbb{Z}_e(T)}{n_e^{eq}}\right)\int f(E)\,\mathrm{d}E + \frac{1}{T}\int E f(E)\,\mathrm{d}E - n_e + n_e^{eq}.$$

Note that $\int f(E)\,\mathrm{d}E = n_e$ and $\int E f(E)\,\mathrm{d}E = \varepsilon_e$ are the electron density and energy. For atoms at level k, (39) leads to $n_k = g_k g_{\mathrm{tr},A}\zeta_k$. Combining with (9a), the contribution by atomic states is

$$H_a^* = \sum_k n_k\log\zeta_k + \left(\log\frac{g_{\mathrm{tr},A}\mathbb{Z}_a}{n_a^{eq}}\right)\sum_k n_k + \frac{1}{T}\sum_k n_k L_k - n_a + n_a^{eq}.$$

The last term is the total energy of the atoms $\varepsilon_a = \sum_k n_k L_k$. For ions, (41) leads to $n_i = g_i g_{\mathrm{tr},i}\zeta_i$. (9b) gives

$$(n_i^{eq})^2 = 2n_a^{eq}\frac{g_i}{g_e}\frac{\mathbb{Z}_e}{\mathbb{Z}_a}e^{-L_i/T}.$$

---

[2]In most cases, this function is equivalent to the negative entropy, and therefore is *minimized* at equilibrium.

The contribution by ions is

$$H_i^* = n_i \log \zeta_i - n_i + n_i^{eq} + n_i \log \frac{g_i g_{\mathrm{tr},i} n_i^{eq}}{(n_i^{eq})^2}$$

$$= n_i \log \zeta_i - n_i + n_i^{eq} + \left(\log \frac{g_{\mathrm{tr},i} n_i^{eq} \mathbb{Z}_a}{n_a^{eq} \mathbb{Z}_e} \right) n_i + \frac{n_i L_i}{T}.$$

The last term is the total energy of the ions $\varepsilon_i = n_i L_i$. Combining, we find

$$H^* = \int f(E) \log \zeta_e(E) \, \mathrm{d}E - n_e + \sum_k n_k \log \zeta_k - n_a + n_i \log \zeta_i - n_i$$

$$+ n_e \log \frac{\mathbb{Z}_e}{n_e^{eq}} + n_a \log \frac{g_{\mathrm{tr},A} \mathbb{Z}_e}{n_a^{eq}} + n_i \log \frac{g_{\mathrm{tr},i} n_i^{eq} \mathbb{Z}_a}{n_a^{eq} \mathbb{Z}_e}$$

$$+ \frac{\varepsilon_e}{T} + \frac{\varepsilon_a}{T} + \frac{\varepsilon_i}{T} + n_e^{eq} + n_a^{eq} + n_i^{eq}.$$

Using $n_i = n_e = n_{tot} - n_a$, $\varepsilon_{tot} = \varepsilon_e + \varepsilon_a + \varepsilon_i$, and $g_{\mathrm{tr},A} \approx g_{\mathrm{tr},i}$, we have

$$H^* = \int f(E) \log \zeta_e(E) \, \mathrm{d}E - n_e + \sum_k n_k \log \zeta_k - n_a + n_i \log \zeta_i - n_i + C, \tag{46}$$

with C a constant term in time

$$C = n_{tot} \log \frac{g_{\mathrm{tr},A} \mathbb{Z}_e}{n_a^{eq}} + \frac{\varepsilon_{tot}}{T} + n_e^{eq} + n_a^{eq} + n_i^{eq}.$$

Thus, the relative entropy provides the same dynamics as the true entropy (43) since $H^* = -S + C$.

3.3   H-Theorems

In this section we show the H-Theorems for the Boltzmann equations ((20)(21)(22), based on the relative entropy. We first summarize the results on moments conservations. The proof is left in Appendix C.

Proposition 3.1 (Conservation of density and energy.)**.**

(a) *Suppose* $\{f, n_k, n_i\}$ *is the solution to the ionization/recombination kinetic equations, i.e.* (20)(21) *with* $Q_{ED}^e = Q_{ED}^k = Q_{ED}^i = 0$. *Then the total density and total energy are conserved, i.e.,*

$$\frac{\mathrm{d}}{\mathrm{d}t} n_{tot} = \frac{\mathrm{d}}{\mathrm{d}t} \varepsilon_{tot} = 0,$$

where n_{tot} *and* ε_{tot} *are defined by* (5a) *and* (5b)*.*

(b) *Suppose* $\{f, n_k, n_i\}$ *is the solution to the excitation/deexcitation kinetic equations, i.e.* (20) (22) *with* $Q_{IR}^e = Q_{IR}^k = Q_{IR}^i = 0$. *Then the densities for each species and the total energy are conserved, i.e.,*

$$\frac{\mathrm{d}}{\mathrm{d}t} \int f(E) \, \mathrm{d}E = \frac{\mathrm{d}}{\mathrm{d}t} \sum_k n_k = \frac{\mathrm{d}}{\mathrm{d}t} \varepsilon_{tot} = 0,$$

where ε_{tot} *is defined by* (5b)*.*

(c) *Suppose* $\{f, n_k, n_i\}$ *is the solution to the ionization/recombination and excitation/deexcitation kinetic equations* (20)(21)(22)*. Then the total density and total energy are conserved,*

$$\frac{\mathrm{d}}{\mathrm{d}t} n_{tot} = \frac{\mathrm{d}}{\mathrm{d}t} \varepsilon_{tot} = 0.$$

Now we give the stationary states:

Proposition 3.2 (Stationary states)**.**

- *If the ionization and recombination processes are included, the stationary solutions $\{f^\infty, n_k^\infty, n_i^\infty\}$ are given by*

$$f^\infty = f^{eq}, \quad n_i^\infty = n_i^{eq}, \quad n_k^\infty = n_k^{eq}, \quad for\ k = 1,\ldots,k_{\max}. \tag{47}$$

  Here f^{eq}, n_k^{eq} and n_i^{eq} are the equilibria with temperature T_e determined by the total number density n_{tot} and the total energy ε_{tot}.
- *If only the excitation and deexcitation processes are included, i.e. without the ionization and recombination processes, the stationary solutions $\{f^\infty, n_k^\infty, n_i^\infty\}$ are given by*

$$f^\infty = f^{eq}(E; T_e)\eta(E), \quad n_i^\infty = n_i^0, \quad n_k^\infty = n_k^{eq}(T_e), \quad for\ k = 1,\ldots,k_{\max}, \tag{48}$$

  where $\eta(E)$ is a periodic function in E, defined by

$$\eta(E) = \frac{\sum_j f(E + j\Delta E, t = 0)}{\sum_j f^{eq}(E + j\Delta E; T_e)}. \tag{49}$$

  with $f(E, t = 0)$ the initial electron distribution and T_e the equilibrium temperature determined from energy conservation

$$\int E f^{eq}(E; T_e)\eta(E)\,\mathrm{d}E + \sum_k n_k^{eq}(T_e)L_k = \int E f(E, t = 0)\,\mathrm{d}E + \sum_k n_k^0 L_k. \tag{50}$$

  where n_i^0 is the initial ion density and $n_k^{eq}(T)$ is the k-level equilibrium atom density (9a) at temperature T_e. The summation in (49) is over all integers $j = j(E)$, such that $E + j\Delta E \geqslant 0$.

This proposition is a direct result of the following H-theorem on the relative entropy. We define:

Definition 3.3 (Relative entropy). Define the relative entropy of the system

$$H = H_e + H_a + H_i, \tag{51}$$

with H_e, H_a and H_i the relative entropy of electrons, atoms and ions respectively

$$
\begin{aligned}
H_e &= \int f \log \frac{f}{f^\infty}\,\mathrm{d}E - n_e + n_e^\infty, \\
H_a &= \sum_k \left(n_k \log \frac{n_k}{n_k^\infty} - n_k + n_k^\infty \right), \\
H_i &= n_i \log \frac{n_i}{n_i^\infty} - n_i + n_i^\infty,
\end{aligned}
\tag{52}
$$

where $n_e = \int f\,\mathrm{d}E$ and $n_e^\infty = \int f^\infty\,\mathrm{d}E$; $\{f^\infty, n_k^\infty, n_i^\infty\}$ are the the stationary solutions given in Proposition 3.2.

Note that $(\sum n_k + n_i)$ is constant and $n_e = n_i$, the total relative entropy (51) can be rewritten as

$$H = \int f \log \frac{f}{f^\infty}\,\mathrm{d}E + \sum_k \left(n_k \log \frac{n_k}{n_k^\infty} + n_k - n_k^\infty \right) + n_i \log \frac{n_i}{n_i^\infty}. \tag{53}$$

The H-theorem can be presented as follows:

Theorem 3.4 (H-theorem). *One always has $H_e \geqslant 0$, $H_a \geqslant 0$ and $H_i \geqslant 0$ in (52), hence $H \geqslant 0$ in (51). If one further assumes the solution f to the kinetic system (20)(21)(22) is smooth, then for the entropy defined by (51)(52), one has $\frac{\mathrm{d}}{\mathrm{d}t}H \leqslant 0$. The equality holds if and only if $H = 0$, which is equivalent to the fact that $f(E)$, n_k and n_i are the stationary solutions given in Proposition 3.2. This result is also valid for the solely ionization/recombination process (with $Q_{ED}^e = Q_{ED}^k = Q_{ED}^i = 0$) or the excitation/deexcitation process (with $Q_{IR}^e = Q_{IR}^k = Q_{IR}^i = 0$).*

The non-negativity of H_e, H_a and H_i comes from the inequality $y \log \frac{y}{x} \geqslant (y - x)$, for $x, y > 0$. We prove the decay of the relative entropy for different processes in the following sections.

3.3.1 Ionization and recombination

We first prove the H-theorem for the ionization/recombination process, i.e., the equations (20) (21) with $Q_{ED}^e = Q_{ED}^k = Q_{ED}^i = 0$. To start, we derive the weak form of the Boltzmann equations.

For any smooth function $\phi = \phi(E)$, one has for electrons,

$$
\begin{aligned}
\partial_t \int \phi f \, \mathrm{d}E &= \int \phi \, Q_{IR}^e \, \mathrm{d}E \\
&= \sum_k \iint (\phi_1 + \phi_2 - \phi_0) \left(n_k f_0 v_0 \sigma^{ion} - n_i f_1 f_2 v_1 v_2 \sigma^{rec} \right) \, \mathrm{d}E_0 \, \mathrm{d}E_t \\
&= \sum_k \iint (\phi_1 + \phi_2 - \phi_0) \left(\frac{n_k}{n_k^{eq}} \frac{f_0}{f_0^{eq}} - \frac{n_i}{n_i^{eq}} \frac{f_1}{f_1^{eq}} \frac{f_2}{f_2^{eq}} \right) n_k^{eq} f_0^{eq} v_0 \sigma^{ion} \, \mathrm{d}E_0 \, \mathrm{d}E_t,
\end{aligned}
\tag{54}
$$

using the detailed balance relation (16). Similarly, for atoms and ions,

$$
\partial_t n_k = Q_{IR}^k = - \iint \left(\frac{n_k}{n_k^{eq}} \frac{f_0}{f_0^{eq}} - \frac{n_i}{n_i^{eq}} \frac{f_1}{f_1^{eq}} \frac{f_2}{f_2^{eq}} \right) n_k^{eq} f_0^{eq} v_0 \sigma^{ion} \, \mathrm{d}E_0 \, \mathrm{d}E_t,
\tag{55}
$$

$$
\partial_t n_i = Q_{IR}^i = \sum_k \iint \left(\frac{n_k}{n_k^{eq}} \frac{f_0}{f_0^{eq}} - \frac{n_i}{n_i^{eq}} \frac{f_1}{f_1^{eq}} \frac{f_2}{f_2^{eq}} \right) n_k^{eq} f_0^{eq} v_0 \sigma^{ion} \, \mathrm{d}E_0 \, \mathrm{d}E_t.
\tag{56}
$$

The following lemma, proven in Appendix B, will be used in the derivation of the H-theorem.

Lemma 3.5. *Suppose $f(E)$ is a smooth function and f^{eq}, $\{n_k^{eq}\}$, n_i^{eq} are the equilibrium functions defined by (6)-(9b), sharing the same total number density and total energy with f, $\{n_k\}$ and n_i. If*

$$
\frac{n_k}{n_k^{eq}} \frac{f_0}{f_0^{eq}} = \frac{n_i}{n_i^{eq}} \frac{f_1}{f_1^{eq}} \frac{f_2}{f_2^{eq}},
\tag{57}
$$

for every E_0 and E_t, then

$$
f = f^{eq}, \quad n_k = n_k^{eq}, \quad n_i = n_i^{eq}.
$$

Now we are ready to give the H-theorem for the ionization/recombination process,

Theorem 3.6 (H-theorems for ionization/recombination)**.** *Assume the solution f to the ionization/recombination kinetic equations ((20) (21) with $Q_{ED}^e = Q_{ED}^k = Q_{ED}^i = 0$) is smooth. Then for the entropy H defined by (51)(52) with the stationary solution (47), one has $\frac{\mathrm{d}}{\mathrm{d}t} H \leqslant 0$. The equality holds if and only if $H = 0$, which is equivalent to say $f(E)$, n_k and n_i are the equilibrium values.*

Proof. Utilizing the weak forms (54)-(56), a straightforward computation gives

$$
\begin{aligned}
\partial_t H &= \int \partial_t f \log \frac{f}{f^{eq}} \, \mathrm{d}E + \sum_k \partial_t n_k \log \frac{n_k}{n_k^{eq}} + \partial_t n_i \log \frac{n_i}{n_i^{eq}} + 2\partial_t n_{tot} \\
&= -\sum_k \iint \left(\log \left(\frac{n_k}{n_k^{eq}} \frac{f_0}{f_0^{eq}} \right) - \log \left(\frac{n_i}{n_i^{eq}} \frac{f_1}{f_1^{eq}} \frac{f_2}{f_2^{eq}} \right) \right) \\
&\qquad \cdot \left(\frac{n_k}{n_k^{eq}} \frac{f_0}{f_0^{eq}} - \frac{n_i}{n_i^{eq}} \frac{f_1}{f_1^{eq}} \frac{f_2}{f_2^{eq}} \right) n_k^{eq} f_0^{eq} v_0 \sigma^{ion} \, \mathrm{d}E_0 \, \mathrm{d}E_t \\
&\leqslant 0.
\end{aligned}
$$

The equality holds if and only if

$$
\frac{n_k}{n_k^{eq}} \frac{f_0}{f_0^{eq}} = \frac{n_i}{n_i^{eq}} \frac{f_1}{f_1^{eq}} \frac{f_2}{f_2^{eq}},
$$

for every E_0 and E_t. Lemma 3.5 then implies

$$f = f^{eq}, \qquad n_k = n_k^{eq}, \qquad n_i = n_i^{eq},$$

which is equivalent to $H = 0$. $\qquad\qquad\qquad\qquad\qquad\qquad\qquad\qquad\qquad\qquad\qquad$ $\square$

3.3.2 Excitation and deexcitation

We then prove the H-theorem for the excitation/deexcitation process, i.e., the equations (20) (22) with $Q_{IR}^e = Q_{IR}^k = Q_{IR}^i = 0$. Again we derive the weak form of the Boltzmann equations.

For any smooth function $\phi = \phi(E)$, one has for electrons

$$
\begin{aligned}
\partial_t \int \phi f \, \mathrm{d}E &= \iint \phi \, Q_{ED}^e \, \mathrm{d}E \\
&= \sum_{l<u} \int (\phi_1 - \phi_0) \left(n_l f_0 v_0 \sigma^{exc} - n_u f_1 v_1 \sigma^{dex} \right) \, \mathrm{d}E_0 \\
&= \sum_{l<u} \int (\phi_1 - \phi_0) \left(\frac{n_l}{n_l^{eq}} \frac{f_0}{f_0^{eq}} - \frac{n_u}{n_u^{eq}} \frac{f_1}{f_1^{eq}} \right) n_l^{eq} f_0^{eq} v_0 \sigma^{exc} \, \mathrm{d}E_0,
\end{aligned}
\tag{58}
$$

using the detailed balance relation (18). Similarly for atoms

$$
\partial_t n_k = Q_{ED}^k = \sum_{l<u} \int \left(\frac{n_l}{n_l^{eq}} \frac{f_0}{f_0^{eq}} - \frac{n_u}{n_u^{eq}} \frac{f_1}{f_1^{eq}} \right) (\delta_{uk} - \delta_{lk}) n_l^{eq} f_0^{eq} v_0 \sigma^{exc} \, \mathrm{d}E_0.
\tag{59}
$$

Note that for any sequence $\{\phi_k\}$,

$$
\begin{aligned}
\partial_t \sum n_k \phi_k &= \sum_{l<u} \int \left(\frac{n_l}{n_l^{eq}} \frac{f_0}{f_0^{eq}} - \frac{n_u}{n_u^{eq}} \frac{f_1}{f_1^{eq}} \right) \sum_k \phi_k (\delta_{uk} - \delta_{lk}) n_l^{eq} f_0^{eq} v_0 \sigma^{exc} \, \mathrm{d}E_0 \\
&= \sum_{l<u} \int \left(\frac{n_l}{n_l^{eq}} \frac{f_0}{f_0^{eq}} - \frac{n_u}{n_u^{eq}} \frac{f_1}{f_1^{eq}} \right) (\phi_u - \phi_l) n_l^{eq} f_0^{eq} v_0 \sigma^{exc} \, \mathrm{d}E_0.
\end{aligned}
\tag{60}
$$

With only excitation/deexcitation, the equilibria f^{eq} and n_k^{eq} defined in Section 2.1 are not the only stationary solutions. The proof of this uses the following results.

Lemma 3.7. *(i). Suppose f is a solution to the excitation/deexcitation kinetic equations (20) (22) with initial value $f(E, t = 0)$. Then*

$$
\frac{\mathrm{d}}{\mathrm{d}t} \sum_j f(E + j\Delta E, t) = 0, \quad \text{for any } E \geqslant 0,
\tag{61}
$$

where the summation is over all integers j such that $(E + j\Delta E) \geqslant 0$.

(ii). If f is in the form $f(E) = f^{eq}(E; T_e) \eta(E; T_e)$, for some temperature T_e and some periodic function $\eta(E; T_e)$ in E with the period ΔE, then η is given by (49).

(iii). There is a unique value of T_e satisfying the energy conservation (50).

The detailed proof is given in Appendix D. The equation (61) describes the fact that an electron can only gain or lose an energy of integer multiplication of ΔE with only excitation/deexcitation included. (ii) gives the formula of η, as a result of (61). (iii) shows the uniqueness of the equilibrium temperature, as an analogy to Lemma 2.1 where the ionization/recombination processes are included.

Theorem 3.8. *Assume there is $\Delta E > 0$, such that ΔE_{lu} is an integer multiplication of ΔE, for every l, u. Suppose $f(E)$ is a smooth function such that*

$$\frac{n_l}{n_l^{eq}} \frac{f_0}{f_0^{eq}} = \frac{n_u}{n_u^{eq}} \frac{f_1}{f_1^{eq}} \tag{62}$$

holds for every l, u and E_0, in which $f^{eq} = f^{eq}(E; T_e)$, $\{n_k^{eq}\} = \{n_k^{eq}(T_e)\}$ are of the form (6) and (9a)(9b) for the temperature T_e determined from (50). Then

$$\begin{aligned} f(E) &= f^{eq}(E; T_e)\eta(E), \\ n_k &= n_k^{eq}(T_e), \end{aligned} \tag{63}$$

where $\eta(E)$ is the periodic function (49), with period ΔE.

A detailed proof is given in Appendix D. Here we would like to point out several facts.

- ΔE_{lu} is a rational multiple of I_H in our model, so that ΔE exists.
- The period ΔE decreases to 0 very fast as the number of excitation levels increase. As $\Delta E \to 0$, η becomes a constant function and the stationary solutions are given by the Boltzmann distribution (6) and (9a), with temperature determined by energy conservation.

Now we are ready to give the H-theorem for the excitation/deexcitation process,

Theorem 3.9 (H-theorems for excitation/deexcitation). *Assume the solution f to the excitation/deexcitation kinetic equations ((20) (22) with $Q_{IR}^e = Q_{IR}^k = Q_{IR}^i = 0$) is smooth. Then for the entropy H defined by (51)(52) with the stationary solution (48), one has $\frac{d}{dt} H \leqslant 0$. The equality holds if and only if $H = 0$, which is equivalent to say f and $\{n_k\}$ are given by (63).*

Proof. Note that with only excitation and deexcitation, one has

$$\sum_k (n_k - n_k^{\infty}) = n_i \log \frac{n_i}{n_i^{\infty}} = 0.$$

The entropy becomes

$$H = \int f(E) \log \frac{f(E)}{f^{eq}(E; T)\eta(E)} \, \mathrm{d}E + \sum_k \left(n_k \log \frac{n_k}{n_k^{eq}(T)} \right).$$

Utilizing the weak forms (58)(59), a straightforward computation gives

$$\begin{aligned} \partial_t H &= \int \partial_t f \log \frac{f}{f^{eq}\eta} \, \mathrm{d}E + \sum_k \partial_t n_k \log \frac{n_k}{n_k^{eq}} + \partial_t \int f \, \mathrm{d}E + \partial_t \sum_k n_k \\ &= -\sum_{l<u} \int \left(\log \left(\frac{n_l}{n_l^{eq}} \frac{f_0}{f_0^{eq}\eta_0} \right) - \log \left(\frac{n_u}{n_u^{eq}} \frac{f_1}{f_1^{eq}\eta_1} \right) \right) \left(\frac{n_l}{n_l^{eq}} \frac{f_0}{f_0^{eq}} - \frac{n_u}{n_u^{eq}} \frac{f_1}{f_1^{eq}} \right) n_l^{eq} f_0^{eq} v_0 \sigma^{exc} \, \mathrm{d}E_0 \\ &= -\sum_{l<u} \int \left(\log \left(\frac{n_l}{n_l^{eq}} \frac{f_0}{f_0^{eq}} \right) - \log \left(\frac{n_u}{n_u^{eq}} \frac{f_1}{f_1^{eq}} \right) \right) \left(\frac{n_l}{n_l^{eq}} \frac{f_0}{f_0^{eq}} - \frac{n_u}{n_u^{eq}} \frac{f_1}{f_1^{eq}} \right) n_l^{eq} f_0^{eq} v_0 \sigma^{exc} \, \mathrm{d}E_0 \\ &\leqslant 0. \end{aligned}$$

This inequality used

$$\eta(E_1) = \eta(E_0 - \Delta E_{lu}) = \eta(E_0),$$

since ΔE_{lu} is an integer multiplication of ΔE, the period of η. The equality holds if and only if

$$\frac{n_l}{n_l^{eq}} \frac{f_0}{f_0^{eq}} = \frac{n_u}{n_u^{eq}} \frac{f_1}{f_1^{eq}},$$

for every l, u and E_0. By Theorem 3.8 and 3.7, f and $\{n_k\}$ are given by (63), which is equivalent to $H = 0$. □

The stationary solution is unique for any specified initial data as a result of this theorem.

3.3.3 Full Kinetic Equations

Finally consider the full kinetic equations including all four processes (20)(21)(22). We are ready to give:

Proof of Theorem 3.4. The proof of the non-negativity of H is the same as the one in Theorem 3.6. Then it is straightforward to obtain

$$
\begin{aligned}
\partial_t H = -\sum_k \iint & \left(\log\left(\frac{n_k}{n_k^{eq}} \frac{f_0}{f_0^{eq}} \right) - \log\left(\frac{n_i}{n_i^{eq}} \frac{f_1}{f_1^{eq}} \frac{f_2}{f_2^{eq}} \right) \right) \\
& \cdot \left(\frac{n_k}{n_k^{eq}} \frac{f_0}{f_0^{eq}} - \frac{n_i}{n_i^{eq}} \frac{f_1}{f_1^{eq}} \frac{f_2}{f_2^{eq}} \right) n_k^{eq} f_0^{eq} v_0 \sigma^{ion} \, \mathrm{d}E_0 \, \mathrm{d}E_t \\
- \sum_{l<u} \int & \left(\log\left(\frac{n_l}{n_l^{eq}} \frac{f_0}{f_0^{eq}} \right) - \log\left(\frac{n_u}{n_u^{eq}} \frac{f_1}{f_1^{eq}} \right) \right) \left(\frac{n_l}{n_l^{eq}} \frac{f_0}{f_0^{eq}} - \frac{n_u}{n_u^{eq}} \frac{f_1}{f_1^{eq}} \right) n_l^{eq} f_0^{eq} v_0 \sigma^{exc} \, \mathrm{d}E_0 \\
\leqslant 0. &
\end{aligned}
$$

The equality holds if and only if both (57) and (62) hold. Then by (57) and Lemma 3.5,
$$
f = f^{eq}, \qquad n_k = n_k^{eq}, \qquad n_i = n_i^{eq},
$$

which is consistent with (62) with the periodic function $\eta = 1$. $\qquad\square$

4 Idealized Energetic Cross Sections

This section describes semi-classical cross sections, which have explicit analytic formulas.

4.1 Ionization

For ionization events $(k, E_0, E_t) \to (E_1, E_2)$, experimental measurements and numerical calculations of the differential cross section have been performed (e.g., [14], [15]) but the results are rather complicated. As a simpler alternative, the semi-classical cross section [2] is used. This is sufficient for demonstrating the Monte-Carlo procedure, while highlighting some key difficulties due to the scaling of the cross-sections with energy – an issue which remains for any physically realistic cross-section model. In the semi-classical approximation, we have the differential cross section

$$
\sigma_k^{ion}(E_0; E_1, E_2) = 4\pi a_0^2 I_H^2 \frac{1}{E_0} \frac{1}{E_t^2} \mathbf{1}_{B_k \leqslant E_t \leqslant E_0}. \tag{64}
$$

where $\mathbf{1} \equiv 1$ if the conditional argument is satisfied, $\equiv 0$ otherwise. The total ionization cross section for a given initial atomic energy level k, and electron energy E_0, is

$$
\begin{aligned}
\sigma_{tot}^{ion}(k, E_0) &= \int_{B_k}^{E_0} \sigma_k^{ion}(E_0; E_1, E_2) \, \mathrm{d}E_t \\
&= 4\pi a_0^2 I_H^2 \frac{1}{E_0} \left(\frac{1}{B_k} - \frac{1}{E_0} \right) \mathbf{1}_{E_0 > B_k}.
\end{aligned} \tag{65}
$$

The corresponding ionization rate per electron E_0 from (12) is

$$
\begin{aligned}
r_{tot}^{ion}(k, E_0) &= n_k v(E_0) \sigma_{tot}^{ion}(k, E_0) \\
&= 4\pi a_0^2 I_H^2 \sqrt{\frac{2}{m_e}} \frac{n_k}{\sqrt{E_0}} \left(\frac{1}{B_k} - \frac{1}{E_0} \right) \mathbf{1}_{E_0 > B_k}.
\end{aligned} \tag{66}
$$

In simulation of ionization from level k, the incident energy E_0 is sampled according to (65), then the energy transfer E_t is chosen from the energy interval $B_k < E_t < E_0$ according to the probability density

$$p_{ion}(E_t) = \frac{\sigma_k^{ion}(E_0; E_1, E_2)}{\sigma_{tot}^{ion}(k, E_0)} = \frac{E_0 B_k}{E_0 - B_k} \frac{1}{E_t^2} \mathbf{1}_{B_k \leqslant E_t \leqslant E_0}. \tag{67}$$

Note that this expression diverges rapidly when the excess energy $E_0 - B_k \to 0$.

4.2 Recombination

The cross section for a recombination event $(E_1, E_2) \to (k, E_0)$ is obtained from the relation (17), using $E_t = E_2 + B_k$,

$$\begin{aligned}
\sigma_k^{rec}(E_1, E_2; E_0) &= \frac{1}{16\pi m_e h^{-3}} \frac{g_k}{g_i} \frac{E_0}{E_1 E_2} \sigma_k^{ion}(E_0; E_1, E_2) \\
&= \frac{4\pi a_0^2 I_H^2}{16\pi m_e h^{-3}} \frac{g_k}{g_i} \frac{1}{E_1 E_2} \frac{1}{(E_2 + B_k)^2}.
\end{aligned} \tag{68}$$

The corresponding recombination rate per pair of electrons E_1, E_2 from (11) is

$$\begin{aligned}
r^{rec}(k, E_1, E_2) &= n_i v(E_1) v(E_2) \sigma_k^{rec}(E_1, E_2; E_0) \\
&= \frac{a_0^2 I_H^2}{2 m_e^2 h^{-3}} \frac{n_i}{\sqrt{E_1}\sqrt{E_2}} \frac{g_k}{g_i} \frac{1}{(E_2 + B_k)^2}.
\end{aligned} \tag{69}$$

Both cross-sections are divergent as $E_1 \to 0$ or $E_2 \to 0$, conditions obtained at either end of the allowed range of energy transferred, i.e. near threshold $(E_t \simeq B_k)$ or near maximum $(E_t \simeq E_0)$.

4.3 Excitation

For the energetic cross section of excitation $(l, E_0) \to (u, E_1)$, the semi-classical cross section is [2]

$$\sigma_{lu}^{exc}(E_0; E_1) = (4\pi a_0^2 I_H^2)(3\mathrm{f}_{ul}) \frac{1}{E_0} \left(\frac{1}{\Delta E_{lu}} - \frac{1}{E_0} \right) \mathbf{1}_{E_0 > \Delta E_{lu}}, \tag{70}$$

where the absorption oscillator strength is

$$\mathrm{f}_{ul} = \frac{32}{3\pi\sqrt{3}} \frac{1}{l^5 u^3} \frac{1}{(l^{-2} - u^{-2})^3}. \tag{71}$$

The corresponding excitation rate per electron E_0 from (11) is

$$r^{exc}(l, u, E_0) = 12\pi a_0^2 I_H^2 \mathrm{f}_{ul} \sqrt{\frac{2}{m_e}} \frac{n_l}{\sqrt{E_0}} \left(\frac{1}{\Delta E_{lu}} - \frac{1}{E_0} \right) \mathbf{1}_{E_0 > \Delta E_{lu}}. \tag{72}$$

4.4 Deexcitation

For the cross section of the deexcitation $(u, E_1) \to (l, E_0)$, the Klein-Rosseland relation (19) is used:

$$\begin{aligned}
\sigma_{ul}^{dex}(E_1; E_0) &= \frac{g_l}{g_u} \frac{E_0}{E_1} \sigma_{lu}^{exc}(E_0; E_1) \\
&= 12\pi a_0^2 I_H^2 \mathrm{f}_{ul} \frac{g_l}{g_u} \frac{1}{E_1} \left(\frac{1}{\Delta E_{lu}} - \frac{1}{E_1 + \Delta E_{lu}} \right).
\end{aligned} \tag{73}$$

The corresponding deexcitation rate per electron E_1 from (11) is

$$r^{dex}(u, l, E_1) = 12\pi a_0^2 I_H^2 \mathrm{f}_{ul} \sqrt{\frac{2}{m_e}} n_u \frac{g_l}{g_u} \frac{1}{\sqrt{E_1}} \left(\frac{1}{\Delta E_{lu}} - \frac{1}{E_1 + \Delta E_{lu}} \right). \tag{74}$$

5 Monte Carlo Particle Method

Using the rates detailed in the previous sections, we now formulate a Monte Carlo simulation method for plasma dynamics, including ionization, recombination, excitation and deexcitation interactions between electrons and atoms/ions. The simulation is performed using a method like that of Direct Simulation Monte Carlo (DSMC) [16] designed for binary elastic collisions. Coulomb collisions and other physical processes are not included here, but could be easily added to the method.

There are several difficulties in simulation of excitation/deexcitation and ionization/recombination:

1. There are many processes to be simulated, including $(k_{\max}(k_{\max}-1))$ excitation/deexcitation processes and $(2k_{\max})$ ionization/recombination processes. One needs to pick the processes and sample corresponding electrons with the right rates.
2. The recombination rate depends in a singular way on the electron energies, so that efficient and correct sampling of the electrons for recombination events is difficult.
3. The rates for different interactions are widely varying, so that it is difficult to efficiently include all of the interactions.

In this section we mainly focus on dealing with the first two difficulties. The third involves the multiscale properties which will be investigated in future work.

5.1 The Framework of Algorithm

We employ a Kinetic Monte Carlo (KMC) method to deal with the first difficulty. The method can be summarized as

Step 1. Find upper bounds for the total rates of each of the four collision types, denoted as $\tilde{r}^j$ with the superscript $j = exc, dex, ion, rec$. The total rate of all types of collisions is given by $\tilde{R} = \sum_j \tilde{r}^j$.
Step 2. Choose collision type j with rate $\tilde{r}^j/\tilde{R}$. Update the time with $t = t + \Delta t$, where $\Delta t = 1/\tilde{R}$, so that there is only one virtual collision in one time step.
Step 3. For the selected collision type, choose the participating particles, including electrons and atom levels before and/or after the collision, with the rate used in computing the upper bound $\tilde{r}^j$. Denote this rate to be $\tilde{r}^j_P$, with the subscript P representing the particles.
Step 4. For the selected collision type and particles, compute the actual rate r^j_P of this collision. Accept and perform the collision with probability $r^j_P/\tilde{r}^j_P$.

5.2 Sample Electrons from a Singular Distribution

In step 3 of the framework, electrons for excitation, deexcitation and ionization processes are uniformly chosen from the numerical particles. For the recombination process, the actual rate r^j_P scales like $(E_1 E_2)^{-1/2}$, if two electrons with energy E_1 and E_2 are *uniformly chosen* from the numerical particles. This makes the upper bound $\tilde{r}^{rec}$ extremely large and the acceptance/rejection procedure in step 4 very inefficient. This is the second difficulty mentioned above.

To avoid this singularity, we choose electrons E with rate $p(E)$, in which the distribution $p(E)$ scales like $E^{-1/2}$ as $E \to 0$. As described in the following sections, the two electrons E_1 and E_2 in the recombination are chosen with probabilities

$$
\begin{aligned}
\mathrm{p}_1(E) &= \frac{1}{\sqrt{E}}, \\
\mathrm{p}_2(E) &= \frac{1}{\sqrt{E}} \sum_l \frac{g_l}{(E + B_l)^2}.
\end{aligned}
\tag{75}
$$

Suppose in each time step one needs to choose an electron E_j with probability $p_j = p(E_j)$ from N_e electrons with energy $\{E_j, j = 1, \ldots, N_e\}$. To simulate over a time interval $[0, t_{\max}]$, a total number of $\mathcal{O}(N_e)$ collisions are needed. We propose four different methods here and give a numerical comparison in Section 6.4.

5.2.1 Acceptance/Rejection Method

For this method, first compute

$$p_{\max} = \max_{1 \leqslant j \leqslant N_e} p_j, \tag{76}$$

then uniformly choose an electron E_j and accept it with rate $\frac{p_j}{p_{\max}}$. Keep sampling until one electron is accepted. The value $p_{\max}$ can be updated after each collision.

This method is used for the excitation, deexcitation and ionization. But it is very inefficient for the recombination due to the singularity as $E \to 0$. To see this, consider the case when the system is at equilibrium. At equilibrium for small E_*, using equation (6), the fraction of electrons with $E < E_*$ is

$$P(E < E_*) = C \int_0^{E_*} \sqrt{E} e^{-E/T_e} \, dE = \mathcal{O}(E_*^{3/2}), \tag{77}$$

so that

$$P\left(\min_{1 \leqslant j \leqslant N_e} E_j \leqslant E_*\right) = 1 - (1 - P(E < E_*))^{N_e} = \mathcal{O}(N_e E_*^{3/2}).$$

Hence the minimum of E is $\mathcal{O}(N_e^{-2/3})$ and $p_{\max} = \frac{1}{\sqrt{E}} = \mathcal{O}(N_e^{1/3})$. The acceptance rate is

$$r_{AR} = \frac{1}{p_{\max}} = \mathcal{O}(N_e^{-1/3}).$$

To simulate over $[0, t_{\max}]$, the total cost is

$$C_{AR} = \mathcal{O}\left(\frac{N_e}{r_{AR}}\right) = \mathcal{O}(N_e^{4/3}).$$

However, in simulation the cost is usually much larger than $\mathcal{O}(N_e^{4/3})$. This is due to two reasons. First, the simulations may not start from the equilibrium, making the estimate (77) invalid. Second, the way we update $p_{\max}$ in (76) may lead to an overly large $p_{\max}$. Consider the case that the electron with smallest energy gains energy from a deexcitation or recombination. This leads to the increment of $\min_j E_j$, hence the decrement of $p_{\max}$. However, as we are not lessening $p_{\max}$ accordingly, the actual cost is larger than the expected. In Section 6.4, we show that the actual cost may increase as large as $\mathcal{O}(N_e^2)$.

5.2.2 Direct Search Method

A direct search method is to sample a number r uniformly from $[0, 1]$ and look for

$$j = \min\left\{\xi, \, s.t. \sum_{i=1}^{\xi} p_i \geqslant r \sum_{i=1}^{N_e} p_i\right\}. \tag{78}$$

Here the summation $s = \sum_{i=1}^{N_e} p_i$ can be updated after each collision. In this method the singularity is not a problem. However the searching for j takes $\mathcal{O}(N_e)$ operations. The total cost to simulate over $[0, t_{\max}]$ is

$$C_{direct} = \mathcal{O}(N_e^2).$$

C-31

5.2.3 Binary Search Method

The direct search method can be accelerated by a binary search method to find j in (78). Divide $[0, N_e]$ into two equal size subdivisions and first locate which division E_j is in. If this idea is applied iteratively to each subdivision, the total cost can be reduced to $\mathcal{O}(\log_2 N_e)$. This is the widely used binary search method. For this method the sum $s = \sum p_i$ in each subdivision can be updated after each collision. A total number of $\mathcal{O}(\log_2 N_e)$ updates is need for each collision. For completeness a detailed algorithm is given in Appendix E. The total cost to simulate over $[0, t_{\max}]$ is

$$C_{binary} = \mathcal{O}(N_e \log_2 N_e).$$

5.2.4 Reduced Rejection Method

The recently developed reduced rejection method [8] can be applied, by combining with the Marsaglia table method [17]. See Section 6 in [8] for a detailed description.

There are two sources of computation costs. Suppose the Marsaglia table is re-created after K collisions. Then there are $\mathcal{O}(K)$ particles in the L-region, where a regular acceptance/rejection method is applied. According to Section 5.2.1, the cost of sampling one electron is $\mathcal{O}(K^{1/3})$ in the L-region. Hence the total cost of sampling $\mathcal{O}(N_e)$ particles is $\mathcal{O}(N_e K^{1/3})$. A total number of $\mathcal{O}(N_e/K)$ Marsaglia tables are re-created, since the cost of creating one table is $\mathcal{O}(N_e)$, the resulting total cost in this part is $\mathcal{O}\left(\frac{N_e}{K} N_e\right)$. Therefore the total cost of the reduced rejection method to simulate over $[0, t_{\max}]$ is

$$C_{RR} = \mathcal{O}\left(N_e K^{1/3} + \frac{N_e^2}{K}\right) = \mathcal{O}(N_e^{5/4}),$$

if $K = N_e^{3/4}$. Note that to minimize the total cost, we need the costs in the two sources to be approximately equal, i.e., $N_e K^{1/3} \approx \frac{N_e^2}{K}$. In practice, we use a simple technique to make the cost of re-creating Marsaglia tables and the cost of sampling from L-regions approximately equal:

- Step 1. Create the Marsaglia table. Record the computation time as t_{table}.
- Step 2. Perform collisions. Keep track of the total time t_{sample} used in sampling particles for recombination. When

$$t_{sample} > t_{table},$$

set $t_{sample} = 0$ and go to step 1.

5.3 Large Scale Variation in the Rates

This section illustrates the large variation in the rates of different processes. Efficient multiscale algorithms will be investigated in future works.

The total rate of excitation from level l to level u at equilibrium is

$$R^{exc}(l, u) = \int r^{exc}(l, u, E_0) f^{eq}(E_0) \, \mathrm{d}E_0 = 3\mathrm{f}_{ul} n_l C(n_e, T_e) \psi\left(\frac{\Delta E_{lu}}{T_e}\right),$$

where f_{ul} is the absolute oscillatory strength (71), $C(n_e, T_e)$ is a function of n_e and T_e, and

$$\psi(x) = \int_x^\infty \left(\frac{1}{x} - \frac{1}{y}\right) e^{-y} \, \mathrm{d}y.$$

One can easily check

$$\psi(x) = \mathcal{O}\left(\frac{1}{x}\right), \quad \text{as } x \to 0.$$

For large l, the value of f_{ul} is maximized at $u = l + 1$, for which

$$f_{l+1,l} \approx \frac{4}{3\pi\sqrt{3}}l.$$

ΔE_{lu} is minimized at the same post-collisional level $u = l + 1$,

$$\Delta E_{l,l+1} \approx \frac{2}{l^3}I_H.$$

Therefore, since $n_l = \mathcal{O}(l^2)$,

$$R^{\text{exc}}(l, l + 1) = n_l f_{l+1,l} \cdot \mathcal{O}\left(\frac{1}{\Delta E_{l,l+1}}\right) = \mathcal{O}(l^6). \tag{79}$$

Similarly, at equilibrium the total rate of ionization from level l is

$$R^{\text{ion}}(l) = n_l \cdot \mathcal{O}\left(\frac{1}{B_l}\right) = n_l \cdot \mathcal{O}(l^2) = \mathcal{O}(l^4). \tag{80}$$

(79) and (80) indicate that there are two different scales in the excitation/ionization problem.

First, the scales of excitation and ionization vary dramatically as the atom level l increases. The rate of ionization increases as $\mathcal{O}(l^4)$ and the rate of excitation increases as $\mathcal{O}(l^6)$, a range of $10^4 \sim 10^6$ for typical values of $k_{\max} = 10$.

Second, the rate of excitation is much larger than that of ionization for large excitation level, with ratio

$$\frac{R^{\text{exc}}(l, l + 1)}{R^{\text{ion}}(l)} = \mathcal{O}(l^2).$$

Some numerical examples are presented in Section 6.5.

5.4 Particle/Continuum Representation

The plasma is described by a discrete set of particles for the electron diestribution $f(E, t)$ and a continuum description for the atoms $n_k(t)$ and ions $n_i(t)$. The electron distribution function $f(E, t)$ is represented by the following discrete distribution

$$f(E, t) = N_{\text{eff}} \sum_{j=1}^{N_e} \delta(E - E_j(t)). \tag{81}$$

The number $N_e = N_e(t)$ of electrons is not constant because of ionization and recombination. The units of f are (number of particles) per energy per volume, and the constant N_{eff} is the effective number which represents the number of physical particles per numerical particle per volume.

5.5 A No Time Counter DSMC method

This section describes in detail a Direct Simulation Monte Carlo method without time counter. The method follows the framework illustrated in Section 5.1. It preserves the total electron density n_{tot} (including the free and bound electrons) and the total energy ε_{tot}, due to the fact that n_{tot} and ε_{tot} are preserved in each collision. Moreover, since the algorithm satisfies detailed balance, if initially the system is in an equilibrium state, then it is always in equilibrium. This is numerically tested in Section 6.1.

Step 1 : **Decide the rates of virtual collisions.**

First find upper bounds on the total rates of collisions of each type. The upper bounds need to be not too large, while at the same time easy to compute. The actual total rates of collisions

in each type can be derived by taking the summation of the rates (66), (69), (72), (74) over all electrons and atom levels:

$$\overline{r^{\text{exc}}} = N_{\text{eff}} \sum_l \sum_{u>l} \sum_k r^{\text{exc}}(l, u, E_k)$$

$$= 12\pi a_0^2 I_H^2 \sqrt{\frac{2}{m_e}} N_{\text{eff}} \sum_l \sum_{u>l} \sum_k \frac{n_l}{\sqrt{E_k}} \text{f}_{ul} \left(\frac{1}{\Delta E_{lu}} - \frac{1}{E_k}\right) \mathbf{1}_{E_k > \Delta E_{lu}},$$

$$\overline{r^{\text{dex}}} = N_{\text{eff}} \sum_u \sum_{l<u} \sum_k r^{\text{dex}}(u, l, E_k)$$

$$= 12\pi a_0^2 I_H^2 \sqrt{\frac{2}{m_e}} N_{\text{eff}} \sum_u \sum_{l<u} \sum_k \frac{n_u g_l}{g_u} \frac{\text{f}_{ul}\sqrt{E_k}}{\Delta E_{lu}(\Delta E_{lu} + E_k)},$$

$$\overline{r^{\text{ion}}} = N_{\text{eff}} \sum_l \sum_k r_{tot}^{\text{ion}}(l, E_k)$$

$$= 4\pi a_0^2 I_H^2 \sqrt{\frac{2}{m_e}} N_{\text{eff}} \sum_l \sum_k \frac{n_l}{\sqrt{E_k}} \left(\frac{1}{B_l} - \frac{1}{E_k}\right) \mathbf{1}_{E_k > B_l},$$

$$\overline{r^{\text{rec}}} = N_{\text{eff}}^2 \sum_{i \neq j} \sum_l r^{\text{rec}}(l, E_i, E_j)$$

$$= \frac{a_0^2 n_i}{4 m_e^2 h^{-3} g_+} I_H^2 N_{\text{eff}}^2 \left(\sum_{i,j} \frac{1}{\sqrt{E_i E_j}} \sum_l \frac{g_l}{(E_i + B_l)^2} - \sum_i \frac{1}{E_i} \sum_l \frac{g_l}{(E_i + B_l)^2}\right)$$

$$= \frac{a_0^2 n_i}{4 m_e^2 h^{-3} g_+} I_H^2 N_{\text{eff}}^2 \left(\sum_j \frac{1}{\sqrt{E_j}} \sum_i \left(\frac{1}{\sqrt{E_i}} \sum_l \frac{g_l}{(E_i + B_l)^2}\right) - \sum_i \frac{1}{E_i} \sum_l \frac{g_l}{(E_i + B_l)^2}\right). \tag{82}$$

Note that these are just a numerical approximation of (13). They have the following upper bounds:

$$\overline{r^{\text{exc}}} \leqslant r^{\tilde{\text{exc}}} = 12\pi a_0^2 I_H^2 \sqrt{\frac{2}{m_e}} N_e N_{\text{eff}} \sum_l n_l \sum_{u>l} \frac{2}{3\sqrt{3}} \frac{\text{f}_{ul}}{(\Delta E_{lu})^{3/2}},$$

$$\overline{r^{\text{dex}}} \leqslant r^{\tilde{\text{dex}}} = 12\pi a_0^2 I_H^2 \sqrt{\frac{2}{m_e}} N_e N_{\text{eff}} \sum_u n_u \sum_{l<u} \frac{g_l}{g_u} \frac{\text{f}_{ul}}{2(\Delta E_{lu})^{3/2}},$$

$$\overline{r^{\text{ion}}} \leqslant r^{\tilde{\text{ion}}} = 4\pi a_0^2 I_H^2 \sqrt{\frac{2}{m_e}} N_e N_{\text{eff}} \sum_l \frac{2}{3\sqrt{3}} \frac{n_l}{(B_l)^{3/2}},$$

$$\overline{r^{\text{rec}}} \leqslant r^{\tilde{\text{rec}}} = \frac{a_0^2 n_i}{4 m_e^2 h^{-3} g_+} \frac{2}{m_e} I_H^2 N_{\text{eff}}^2 \sum_j \frac{1}{\sqrt{E_j}} \sum_i \left(\frac{1}{\sqrt{E_i}} \sum_l \frac{g_l}{(E_i + B_l)^2}\right),$$

using the inequalities $x^{-1/2}(1/a - 1/x) \leqslant \frac{2}{3\sqrt{3}} a^{-3/2}$, for $x \geqslant a$, and $\frac{2\sqrt{x}}{a(a+x)} \leqslant a^{-3/2}$. Then

$$\tilde{R} = r^{\tilde{\text{exc}}} + r^{\tilde{\text{dex}}} + r^{\tilde{\text{ion}}} + r^{\tilde{\text{rec}}}$$

is an upper bound on the total rate of all collisions.

Evaluation of $\tilde{R}$ requires total computational cost of $\mathcal{O}((k_{\max})^2 + N_e)$ at beginning, with $k_{\max}$ the number of excitation levels. Since only one or two electrons and one or two atom levels are updated after each collision, it is easy to update $\tilde{R}$ in each step.

Step 2 : **Update time and choose collision type.**

For a time step Δt, there are $\tilde{R}\Delta t$ virtual collisions. For the space homogeneous problem, one can take

$$\Delta t = \frac{1}{\tilde{R}}.$$

This eliminates the time error.

An equivalent choice is to take

$$\Delta t = \frac{1}{\tilde{R}} \ln(1/u),$$

with u a number uniformly sampled from $[0, 1]$. This has been widely used in the simulation of chemical reactions since Gillespie's work [11]

Then update the time $t = t + \Delta t$. The collision type is chosen with probability

$$\frac{\tilde{r}^j}{\tilde{R}}, \quad \text{for } j \in \{exc, dex, ion, rec\}.$$

Step 3 and 4 : Perform one virtual collision

We combined the steps 3 and 4 in Section 5.1. For the different collision types, the algorithms are slightly different.

- **For excitation:**

  Step 3.1 Choose a free electron E_0 uniformly.

  Step 3.2 Choose a prior-collisional level l and post-collisional level $u > l$ with rate

  $$\frac{n_l \frac{f_{ul}}{(\Delta E_{lu})^{3/2}}}{\sum_l n_l \sum_{u>l} \frac{f_{ul}}{(\Delta E_{lu})^{3/2}}},$$

  by the following method: Denote $a_{lu} = \frac{f_{ul}}{(\Delta E_{lu})^{3/2}}$ and $b_l = \sum_{u>l} a_{lu}$. $\{a_{lu}\}$ and $\{b_l\}$ are pre-computed. Then apply the direct search method described in Section 5.2.2) to choose first l with rate $\frac{n_l b_l}{\sum_l n_l b_l}$, then u with rate $\frac{a_{lu}}{b_l}$. The total cost in this step is $\mathcal{O}(k_{\max})$.

  Step 3.3 Sample a number q uniformly from $[0, 1]$. If

  $$q \leqslant \frac{\frac{1}{\sqrt{E_0}} \left(\frac{1}{\Delta E_{lu}} - \frac{1}{E_0} \right) \mathbf{1}_{E_0 > \Delta E_{lu}}}{\frac{2}{3\sqrt{3}} \frac{1}{(\Delta E_{lu})^{3/2}}},$$

  accept the collision and perform the excitation

  $$(l, E_0) \rightarrow (u, E_1 = E_0 - \Delta E_{lu}).$$

  Otherwise reject it.

- **For deexcitation:**

  Step 3.1 Choose a free electron E_1 uniformly.

  Step 3.2 Choose a prior-collisional level u and post-collisional level $l < u$ with rate

  $$\frac{n_u \frac{g_l}{g_u} \frac{f_{ul}}{2(\Delta E_{lu})^{3/2}}}{\sum_u n_u \sum_{l<u} \frac{g_l}{g_u} \frac{f_{ul}}{2(\Delta E_{lu})^{3/2}}},$$

  by a method similar to Step 3.2 in the case of excitation.

  Step 3.3 Sample a number q uniformly from $[0, 1]$. If

  $$q \leqslant \frac{\frac{\sqrt{E_1}}{\Delta E_{lu} + E_1}}{\frac{1}{2(\Delta E_{lu})^{1/2}}},$$

C-35

accept the collision and perform the deexcitation
$$(u, E_1) \to (l, E_0 = E_1 + \Delta E_{lu}).$$

Otherwise reject it.

- **For ionization:**

  Step 3.1 Choose a free electron E_0 uniformly.

  Step 3.2 Choose a prior-collisional level l with rate
  $$\frac{\frac{n_l}{(B_l)^{3/2}}}{\sum_l \frac{n_l}{(B_l)^{3/2}}}.$$

  Step 3.3 Sample a number q uniformly from $[0, 1]$. If
  $$q \leqslant \frac{\frac{1}{\sqrt{E_0}} \left(\frac{1}{B_l} - \frac{1}{E_0} \right) \mathbf{1}_{E_0 > B_l}}{\frac{2}{3\sqrt{3}} \frac{1}{(B_l)^{3/2}}},$$

  accept the collision and sample the transfer energy E_t according to
  $$\frac{E_0 B_k}{E_0 - B_k} \frac{1}{E_t^2} \mathbf{1}_{B_k \leqslant E_t \leqslant E_0}.$$

  and perform the ionization
  $$(l, E_0) \to (E_1 = E_0 - E_t, E_2 = E_t - B_l).$$

  Otherwise reject it.

- **For recombination:**

  Step 3.1 Pick up one free electron with with
  $$\frac{\frac{1}{\sqrt{E_j}}}{\sum_j \frac{1}{\sqrt{E_j}}},$$

  and denote it by E_1. Pick up a second electron with rate
  $$\frac{\frac{1}{\sqrt{E_i}} \sum_l \frac{g_l}{(E_i + B_l)^2}}{\sum_i \left(\frac{1}{\sqrt{E_i}} \sum_l \frac{g_l}{(E_i + B_l)^2} \right)},$$

  and denote it by E_2. As described in Section 5.2, this step can be accomplished by several different methods. In the numerical section part, we apply four different methods and compare their efficiencies.

  Step 3.2 If the two electrons are the same, reject the collision. Otherwise, choose the post-collisional level l with rate
  $$\frac{\frac{g_l}{(E_2 + B_l)^2}}{\sum_l \frac{g_l}{(E_2 + B_l)^2}}.$$

  Step 3.3 Perform the recombination,
  $$(E_1, E_2) \to (l, E_0 = E_1 + E_2 + B_l).$$

6 Computational Results

This section presents computational results from the simulation method described above. 5 atomic levels are included, unless specified. All the results except Section 6.4 are obtained using the binary search method in recombination. However all the other methods described in Section 5.2 give the same results.

6.1 Equilibrium initial data

The first results are for a distribution of electrons, neutral atoms and ions that are in the equilibrium distribution given by (6), (9a) and (9b), with initial temperature of $T_e = 4.31$ eV and number density $n_{tot} = 10^{28} \text{m}^{-3}$ for all (free and bound) electrons. $100,000$ computational particles are used to represent the electron distribution function. The model for the neutral atoms consists of five levels.

The left of Figure 1 shows the time evolution of the atom density n_k, for different level k; the right shows the electron energy distribution function $f(E)$ at various times. The plot on the top is for a simulation that includes excitation/deexcitation alone with no ionization/recombination; while that on the bottom is for ionization/recombination with no excitation/deexcitation. In this simulation the time step is $\Delta t = 6.5^{-11}$ ps for the excitation/deexcitation, and $\Delta t = 4.5^{-10}$ ps for the ionization/recombination. The simulation is performed for about 10^8 time steps. These results show that the simulation method does preserve the equilibrium distribution as required. The fluctuations in the results are due to the statistical error from a finite number of computational particles.
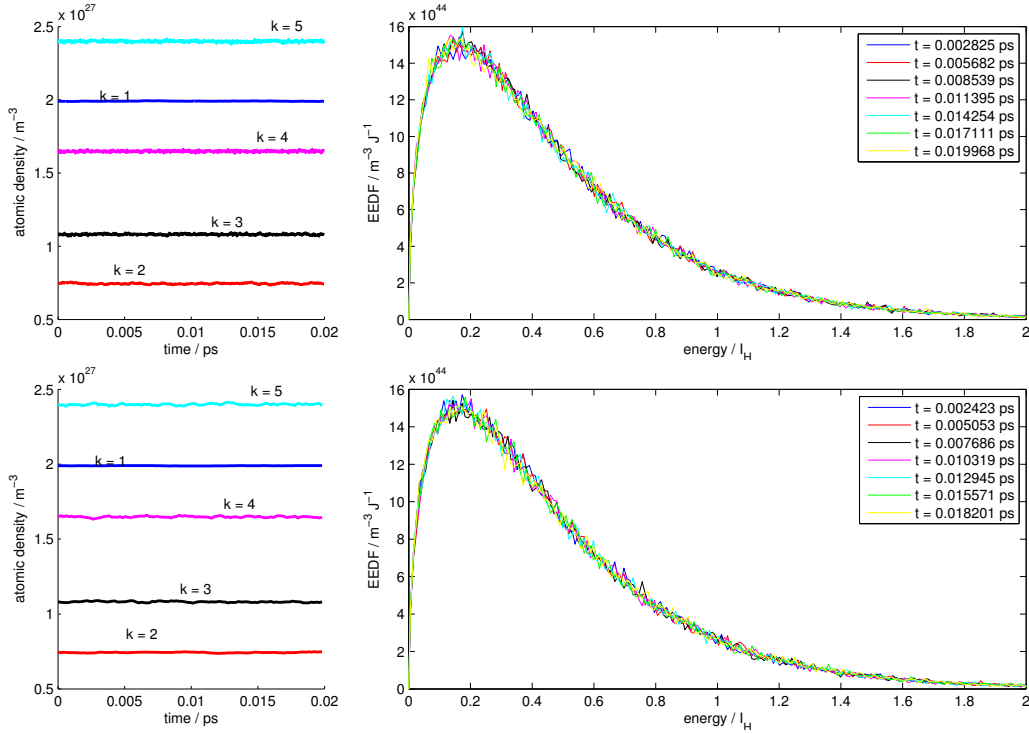
Figure 1: Atomic (left) and electron (right) density function at various times starting from equilibrium, with excitation/deexcitation only (top), and ionization/recombination only (bottom) 100000 samples for free electrons.

6.2 Non-equilibrium initial data

The second simulation results, shown in Figure 2 - 7, are for initial data for which all of the neutral atoms are distributed at the ground level, with total number density $n_a = 5 \times 10^{27} \text{m}^{-3}$. The electrons and ions are initially in an equilibrium distribution given by (6) and (9b), with initial temperature of $T_e = 50000\text{K} = 4.31$ eV and number density $n_e = 5 \times 10^{27} \text{m}^{-3}$. $1,000,000$ computational particles

are used to represent the electron distribution function. The model for the neutral atoms consists of five levels.

In Figures 2, 3, 4, only excitation/deexcitation processes are included. The plots in the left column of Figure 2 show the density of the five different atomic levels (blue bars) at various times, demonstrating convergence to equilibrium (white bars) given by (9a). The plots in the right column show the density distribution of free electrons (blue lines) at various times, demonstrating convergence to equilibrium (red dotted lines) given by (6). Note that the atomic level population inversion is expected, because the level degeneracy grows faster than the exponential drop off due to ΔE (except for between level 1 & 2) since the higher levels are close together.

Figure 3 shows the time evolution of the electron temperature (top)

$$T_e = \frac{\varepsilon_e}{(3/2)n_e} = \frac{2}{3}\frac{\int_0^\infty Ef(E)\,\mathrm{d}E}{\int_0^\infty f(E)\,\mathrm{d}E}$$

and the normalized relative entropy (bottom)

$$\overline{H} = \frac{H}{n_{tot}}$$

where H is defined by (44), with the equilibrium temperature $T_e^{eq} = 27959\mathrm{K}$ determined from the density and energy conservation. The electron temperature T_e decays to T_e^{eq} as time evolves, due to the fact that the excitations from ground level to excited levels dominate in the evolution. The normalized relative entropy function (negative entropy) is monotonically decreasing to 0, except for fluctuations due to the finite number of sampled particles which scales like $1/\sqrt{N}$.

Figure 4 shows the time evolution of various ratios. In the top we show $\frac{\tilde{r}^j}{\tilde{R}}$, the fraction of each type of virtual collision; in the middle $\frac{\bar{r}^j}{\tilde{R}}$, the ratio of each type of accepted collision over all virtual collisions; in the bottom $\frac{\bar{r}^j}{\tilde{r}^j}$, the acceptance rate of each type. Here $j \in \{exc, dex\}$. In the middle figure, the two ratios become equal as time evolves, meaning that the two processes get balanced. In the bottom figure, the acceptance rates of each virtual collision are above 50%, showing the high efficiency of our method. Each point in these figures is computed by taking average over 50000 consecutive collisions. Note that compared to the entropy decay in Figure 3, these ratios reach steady states in a much shorter time. This is because the collisions involving high levels (in this example, level 4 and 5) have much larger rates, and hence dominate in computing these ratios. The contribution from the low levels is very small. As the high levels can reach "equilibrium" in a very short time, these ratios reach steady states very fast. On the other hand, the contribution from the low levels in computing the entropy is not negligible, leading to the slow decay of the entropy in Figure 3.

Note that with only excitation/deexcitation, the stationary state of the electron distribution differs from the equilibrium by a periodic function η, according to (D.2). However with 5 excitation levels the period of η is

$$\Delta E = \frac{1}{3^2 4^2 5^2}I_H = \frac{I_H}{3600},$$

which is too small to be observed in this experiment. The relaxation towards this stationary state does not preclude the generation of physical entropy, as shown by Figure 3, since according to the discussion of Section 3.2, the evolution of the system can be described by either form of entropy, but it does imply that by allowing only transitions with finite energy gaps, the final value of $\overline{H}$ does not correspond to the absolute minimum (maximum of physical entropy). This effect was also observed in a non-stochastic solver [12], and is not an artifact of our numerical approach, but

rather a physical feature of the system, indicating breakdown of ergodicity for system with only excitation/deexcitation.

In Figure 5, 6, 7, similarly results are obtained with only ionization and recombination. In contrast to the previous case of excitation/deexcitation, there is a continuum of energy that can be exchanged with the free electrons. Therefore in this case the stationary state of the electron distribution is exactly the equilibrium state.

Figure 6 shows the time evolution of the degree of ionization (top), the electron temperature (middle) and the normalized relative entropy (bottom), with H defined by (44). More recombination collisions happen than the ionization, leading to the decay of the degree of ionization. In the early time, the electron temperature increases due to the fact that electron with lower energy is easied combined with an ion. This can also be observed in the second snapshot of EEDF in Figure 5. As the number of low energy electrons decreases, the high energy electrons start to dominate. More high energy electrons are combined with ions, leading to the decrease of the electron temperature. The relative entropy is monotonically decreasing to 0, except for the statistical fluctuations. Note that compared to the excitation/deexcitation collisions (see Figure 3), the ionization/recombination collisions take longer time to reach equilibrium. This is due to the fact that the collision rates for excitation/deexcitation are larger than those of ionization/recombination (see Figure 14 for an example).

Again Figure 7 shows the acceptance rate of each virtual ionization collision is above 50%. The acceptance rate of each virtual recombination collision is almost 100%, since in our algorithm (Step 3.2) the only rejected collisions are those with two identical incident electrons.

6.3   The stationary states without ionization/recombination

In this section we compute the stationary states with only excitation/deexcitation processes. The model includes only two atomic levels. The period of the stationary function $\eta(E)$ in (D.2) is

$$\Delta E = \Delta E_{12} = L_2 - L_1 = \frac{3}{4}I_H.$$

Initially the free electrons are placed near $E = \Delta E$ with distribution

$$f(E,0) = \frac{n_e}{\sqrt{2\pi T_0}}e^{-\frac{(E-\Delta E)^2}{2\sigma_0^2}},\tag{83}$$

with $\sigma_0 = \frac{I_H}{10}$ and $n_e = 0.9n_{tot}$, where the total density distribution is $n_{tot} = 10^{28}\mathrm{m}^{-3}$.

The time evolution is shown in Figure 8. The stationary electron distribution clearly shows the period of $\frac{3}{4}I_H$. Figure 9 shows the time evolution of the normalized entropy $\overline{H} = \frac{H}{n_{tot}}$, where H is the entropy defined by (51)(52) with the stationary solutions given by (48). This verifies the convergence to the theoretical result.

Furthermore, one can see from Figure 9 that the relaxation is much slower than the one in Figure 3. This is due to the fact that the collision between the electron and the higher atomic level has a larger rate. In Figure 3, five atomic levels are included; while in Figure 9 only two atomic levels included.

In the next we start with the same initial data, but with all the processes (excitation/deexcitation and ionization/recombination) included. The time evolutions of the atomic distribution, with only two levels, and the electron distribution are shown in Figure 10. With the ionization/recombination processes included, the EEDF f decays to the Maxwell-Boltzmann distribution. However the periodicity in electron distribution f can still be observed at the early time of evolution, due to the fact

Figure 2: Snapshots of time evolution of atom density (left) and electron distribution (right), compared to the equilibrium (white bars and red dotted lines), starting from all neutral atoms at the ground level. Only excitation/deexcitation processes are included.

Figure 3: Time evolution of the electron temperature (top) and the normalized relative entropy $\overline{H}$ (bottom), starting from all neutral atoms at the ground level. Only excitation/deexcitation processes are included.

Figure 4: Time evolution of the fraction of each type of virtual collision (top), the ratio of each type of accepted collision over all virtual collisions (middle) and acceptance rate (bottom), starting from all neutral atoms at the ground level. Only excitation/deexcitation processes are included.
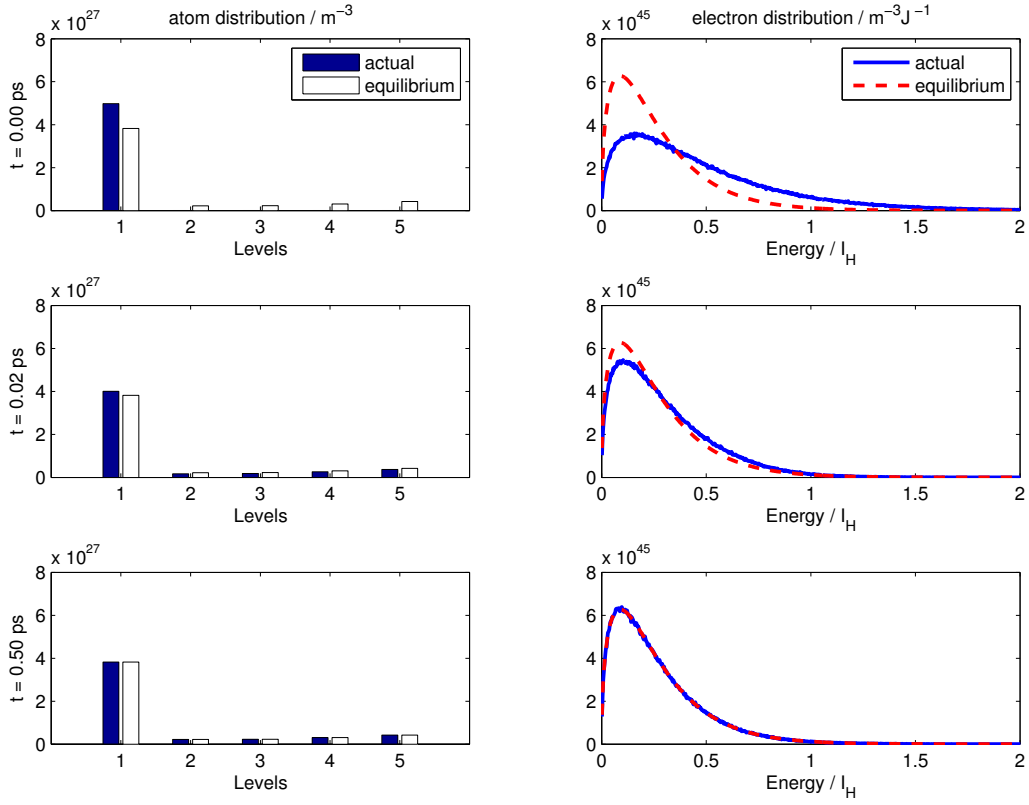
Figure 5: Snapshots of time evolution of atom density (left) and electron distribution (right), compared to the equilibrium (white bars and red dotted lines), starting from all neutral atoms at the ground level. Only ionization/recombination processes are included.
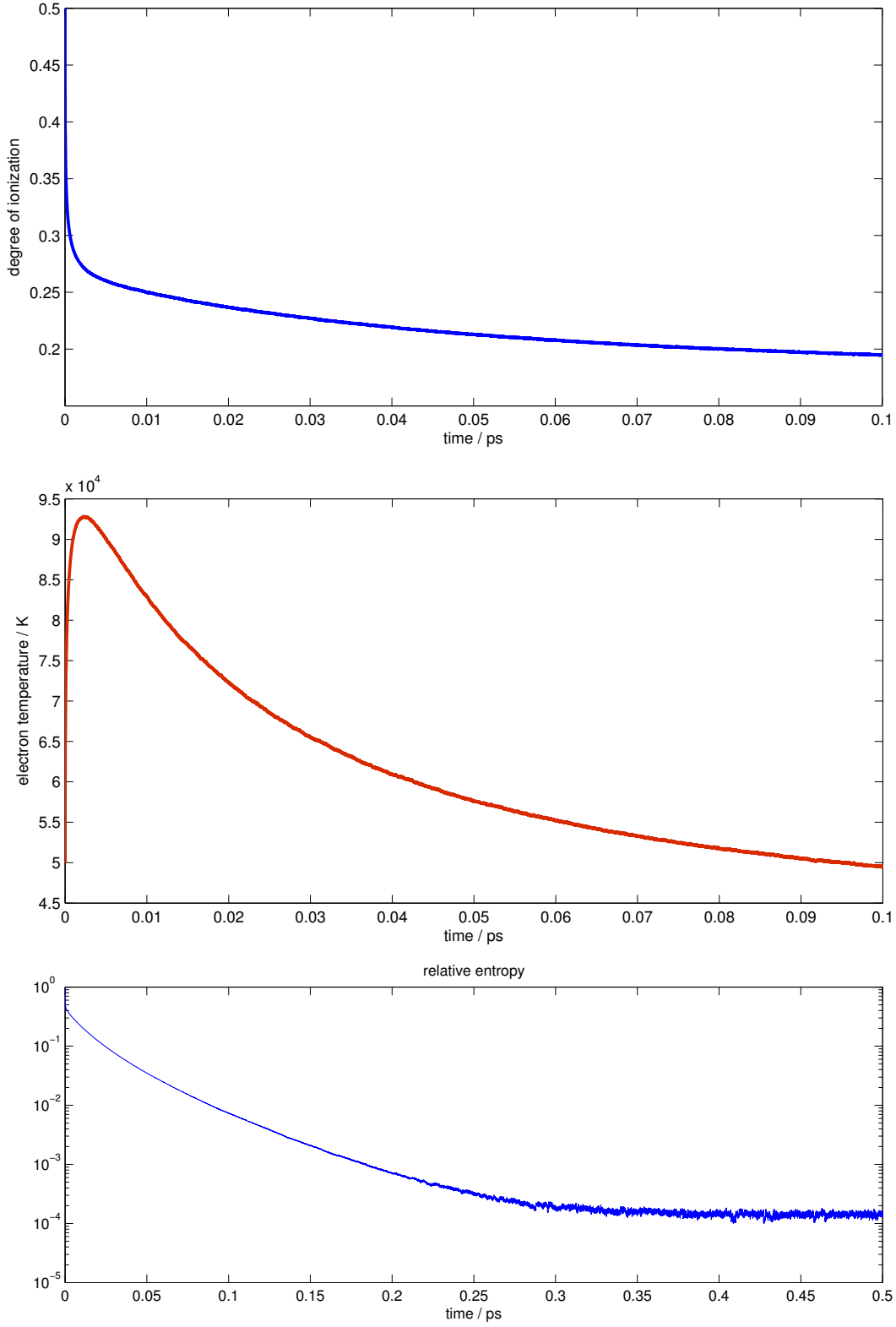
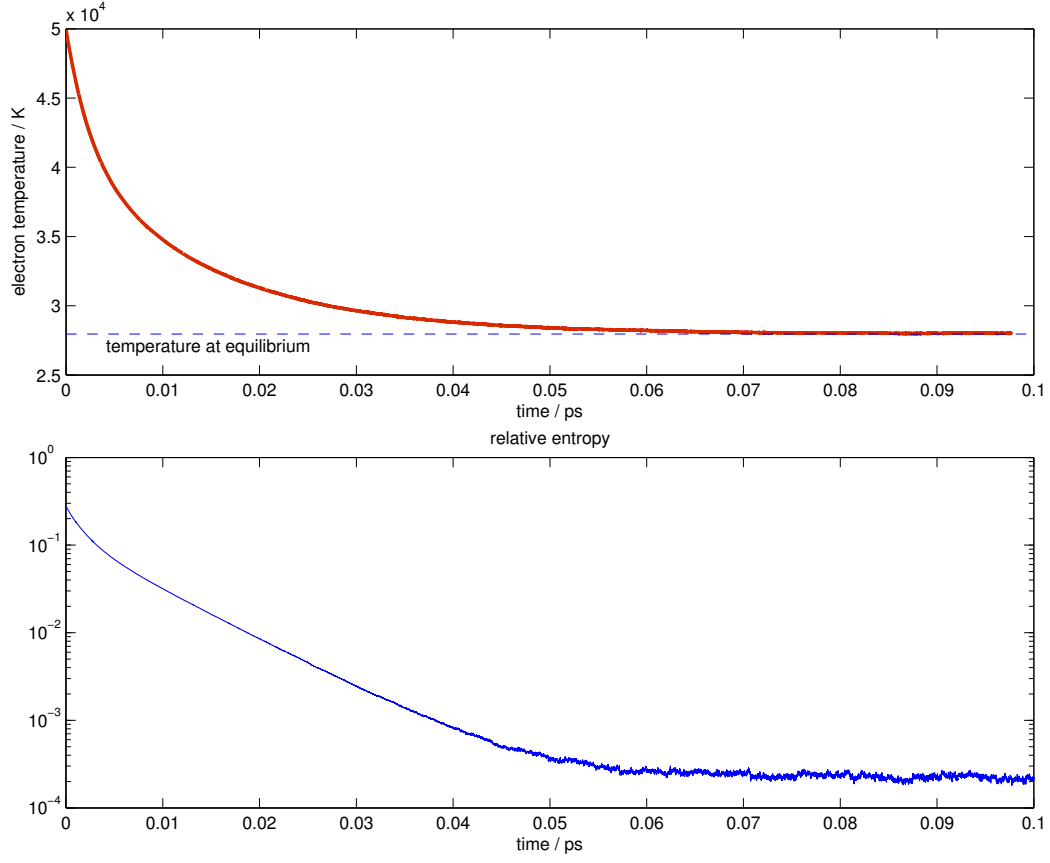Figure 6: Time evolution of the degree of ionization (top), the electron temperature (middle) and the normalized relative entropy $\overline{H}$ (bottom), starting from all neutral atoms at the ground level. Only ionization/recombination processes are included.
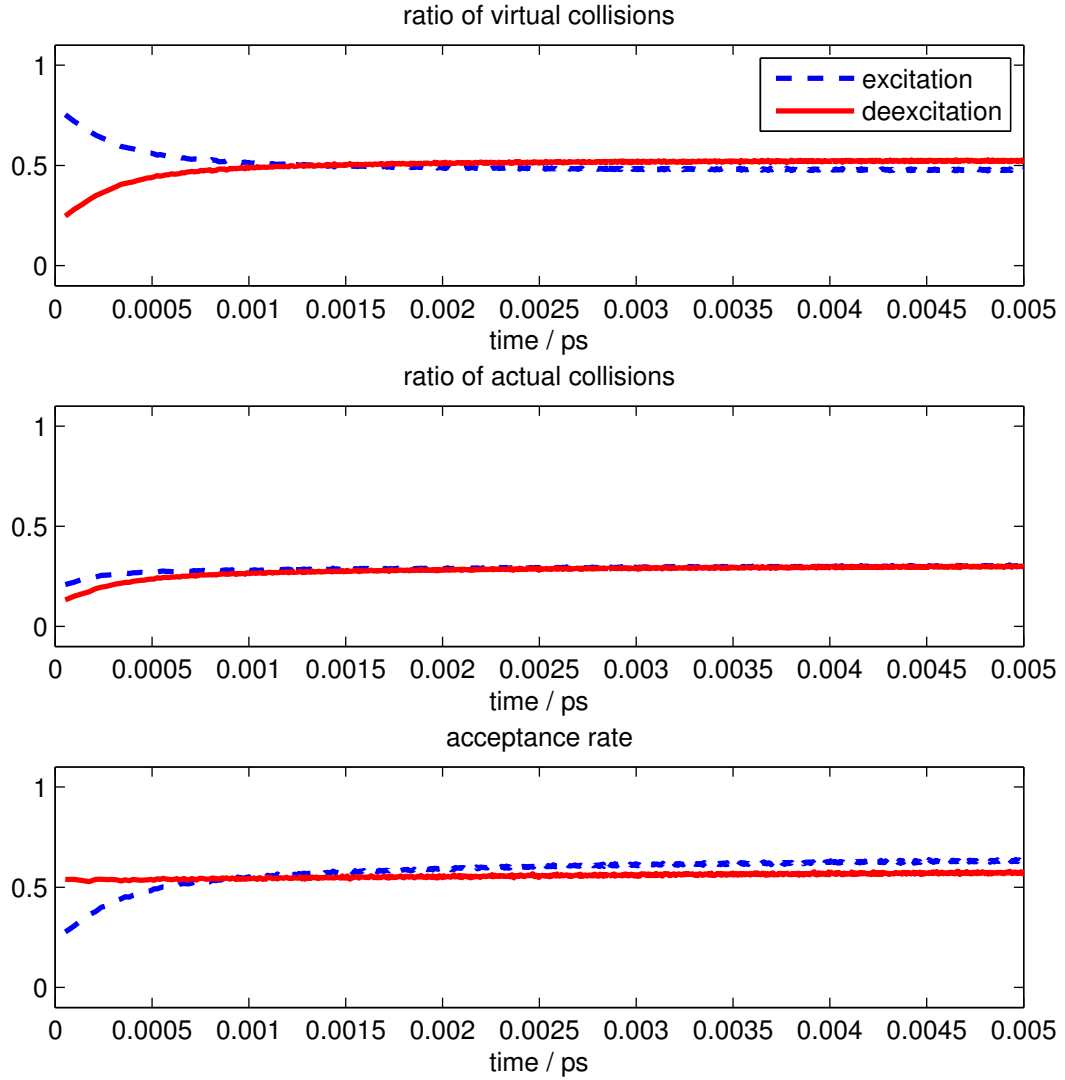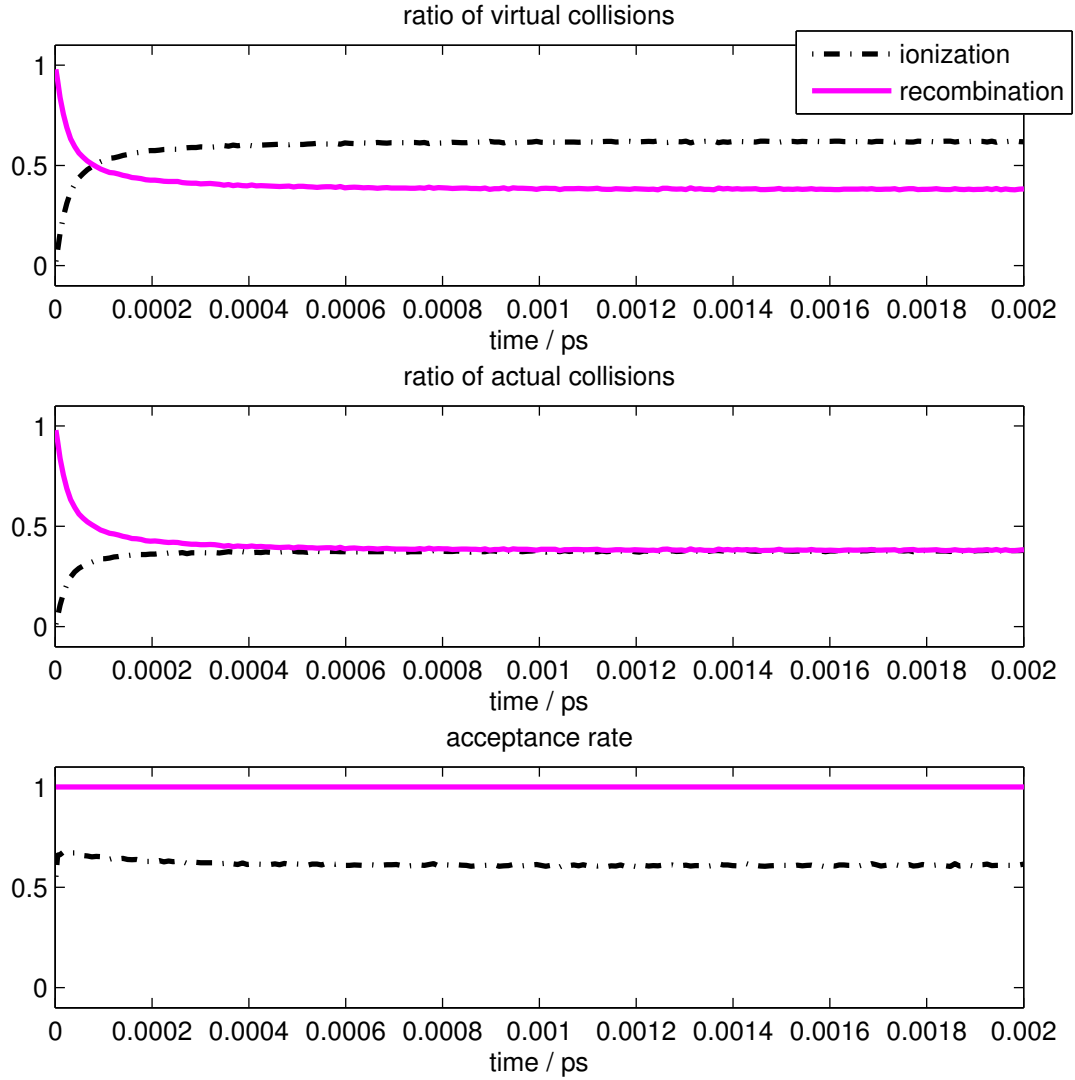
Figure 7: Time evolution of the fraction of each type of virtual collision (top), the ratio of each type of accepted collision over all virtual collisions (middle) and acceptance rate (bottom), starting from all neutral atoms at the ground level. Only ionization/recombination processes are included.

Figure 8: Snapshots of time evolution of atom density (left) and electron distribution (right), compared to the equilibrium (white bars and red dashed lines), starting from the initial data (83). Only excitation/deexcitation processes are included. 200000 samples are used for free electrons.
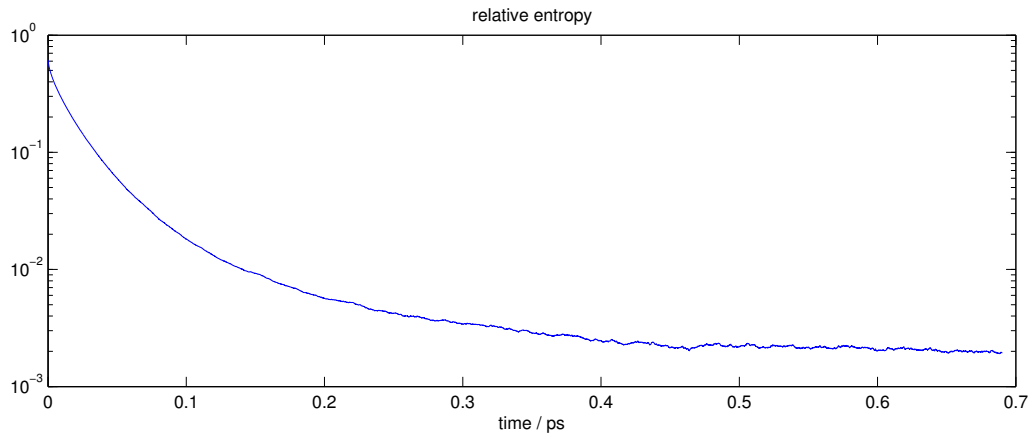
Figure 9: Time evolution of the normalized relative entropy $\overline{H}$ defined by (51)(52), with the initial data (83). Only excitation/deexcitation processes are included. 200000 samples are used for free electrons.

that the collision rates of excitation/deexcitation is higher than those of ionization/recombination (see Figure 14 for an example).

6.4 Comparison of different methods for sampling electrons in recombination

We apply the four methods described in Section 5.2 to the excitation/ionization problem and make a comparison.

The first test problem is the simulation of the equilibration process. Initially all atoms are ionized and free electrons are given by a Maxwellian. We take the total electron density $n_{tot} = 10^{28} \mathrm{m}^{-3}$ and the temperature of free electron $T_e = 4.31$ eV. In this case the degree of ionization at equilibrium is 38.04%. We simulate the decaying process until $t = 6 \times 10^{-2}$ ps, which requires around 10^8 time steps for $N_e = 100000$. At the end time, the degree of ionization is around 39.7%, indicating that the system is close to the equilibrium.

We solve this problem with numbers of simulation particles for electrons to be

$$N_e = 12500, 25000, 50000, 100000, 200000, 400000, 800000$$

respectively for the initial free electrons. We track the time spent on the processes related to the sampling of electrons for recombination collisions. For reduced rejection method this includes the rebuilding of the Marsaglia tables and the sampling process. For the binary search method, this includes the updating of the summation tables and the sampling process. For direct search method, only the sampling process are timed.

The results are shown in Figure 11. As expected the direct search method needs $O(N_e^2)$ computations. It is getting extremely slow when more than 10^6 samples are used. The acceptance/rejection method needs $O(N_e^{1.87})$ computation, which is worse than expected. The cost of reduced rejection method is $O(N_e^{1.1})$, which is slightly better than the theoretical result. The cost for binary search method is $O(N_e^{1.1})$, which is close to the theoretical result $O(N_e \log N_e)$. Note that the binary method is about 10 times faster than the reduced rejection method, although these two methods have almost the same convergence order.

A similar test is applied on the simulation of a system in equilibrium. Again we take the total electron density $n_{tot} = 10^{28} \mathrm{m}^{-3}$ and the temperature of free electron $T_e = 4.31$ eV. The degree of ionization stays around 38.04%. The simulation is performed until time $t = 10^{-3}$ ps, which requires around 10^7 time steps for $N_e = 100000$. The results are shown in Figure 12. We observe similar efficiencies as in the non-equilibrium test.

6.5 The large scale variation

This section numerically checks the large scale variation in the rates illustrated in Section 5.3.

Figure 13 shows the rates for excitation and deexcitation at equilibrium. Here 10 atomic levels are included. rate($k \rightarrow l$) gives the rate of excitation or deexcitation (for $k < l$ or $k > l$ respectively) from level k to level l. The rates with $k = l$ are not defined and left blank in the figure. For each level, the entries closest to the diagonal have the largest rates. These rates vary over a range of 10^6 for different levels. These rates are obtained by computing each terms in $\overline{r^{\mathrm{exc}}}$ and $\overline{r^{\mathrm{dex}}}$ in (82).

Figure 14 shows the total rates from/to each level. The blue circle shows the total rate of excitation/deexcitation from a given level. The red cross shows the total rate of excitation/deexcitation to a given level. The black square shows the total rate of ionization from a given level. The magenta plus shows the total rate of recombination to a given level. As predicted in Section 5.3, the rates of excitation/deexcitation vary over 10^6 while those of ionization/recombination vary over 10^4 for
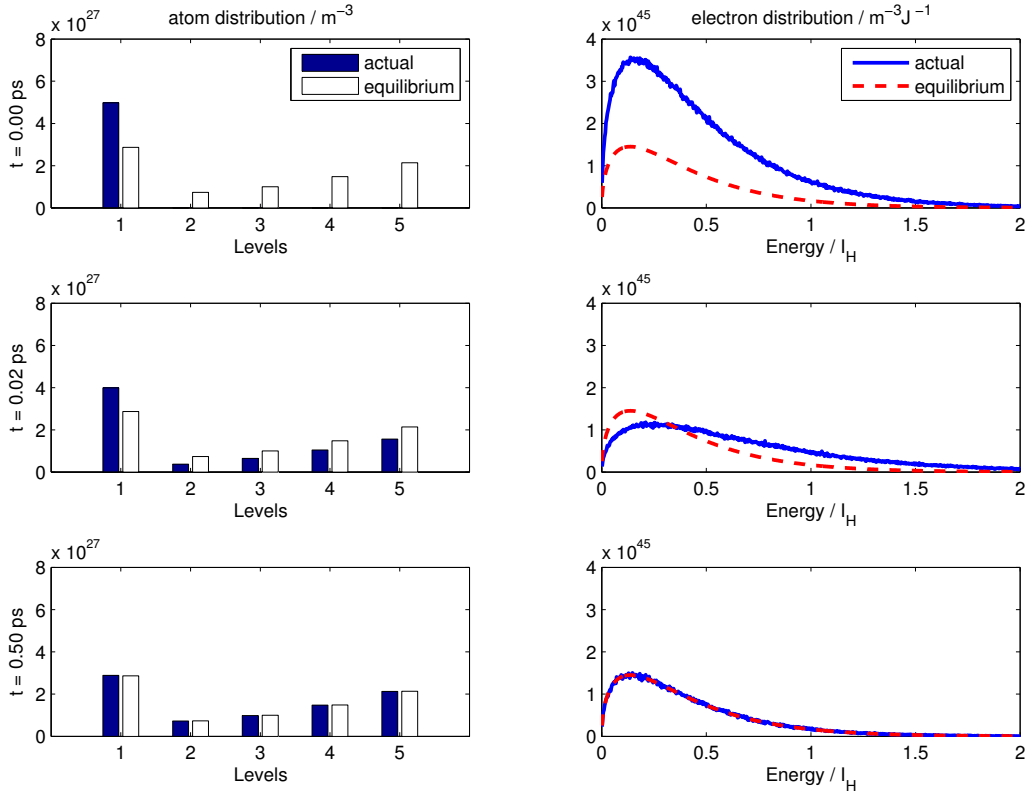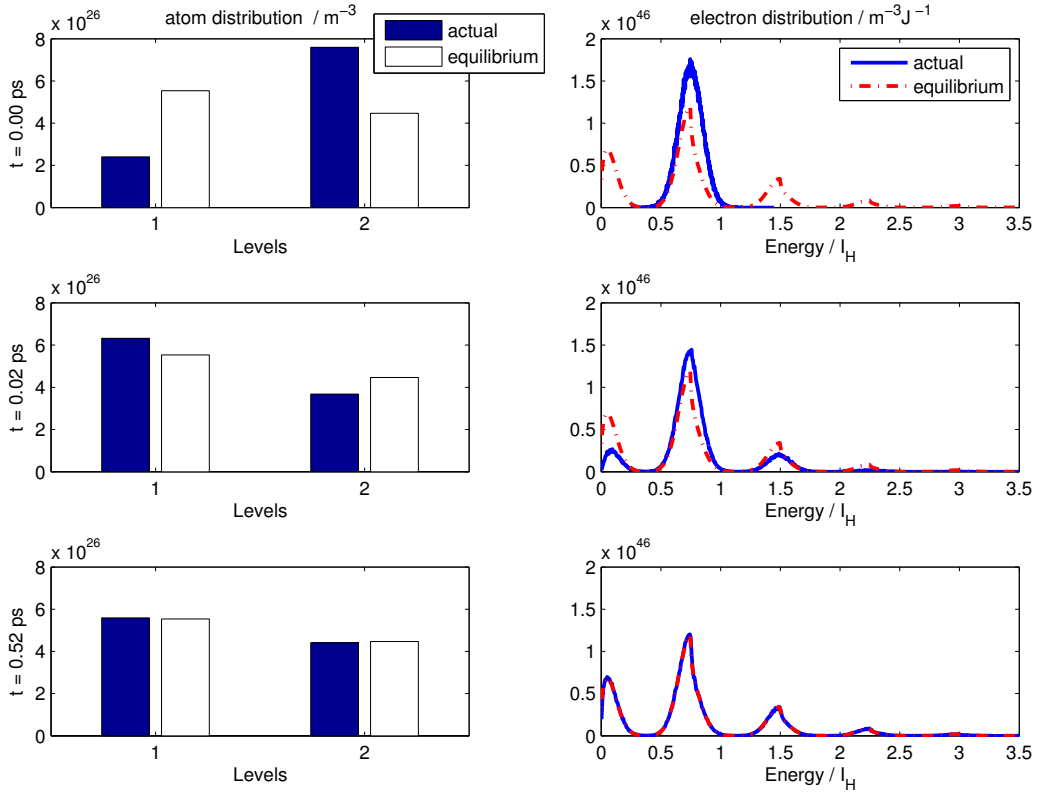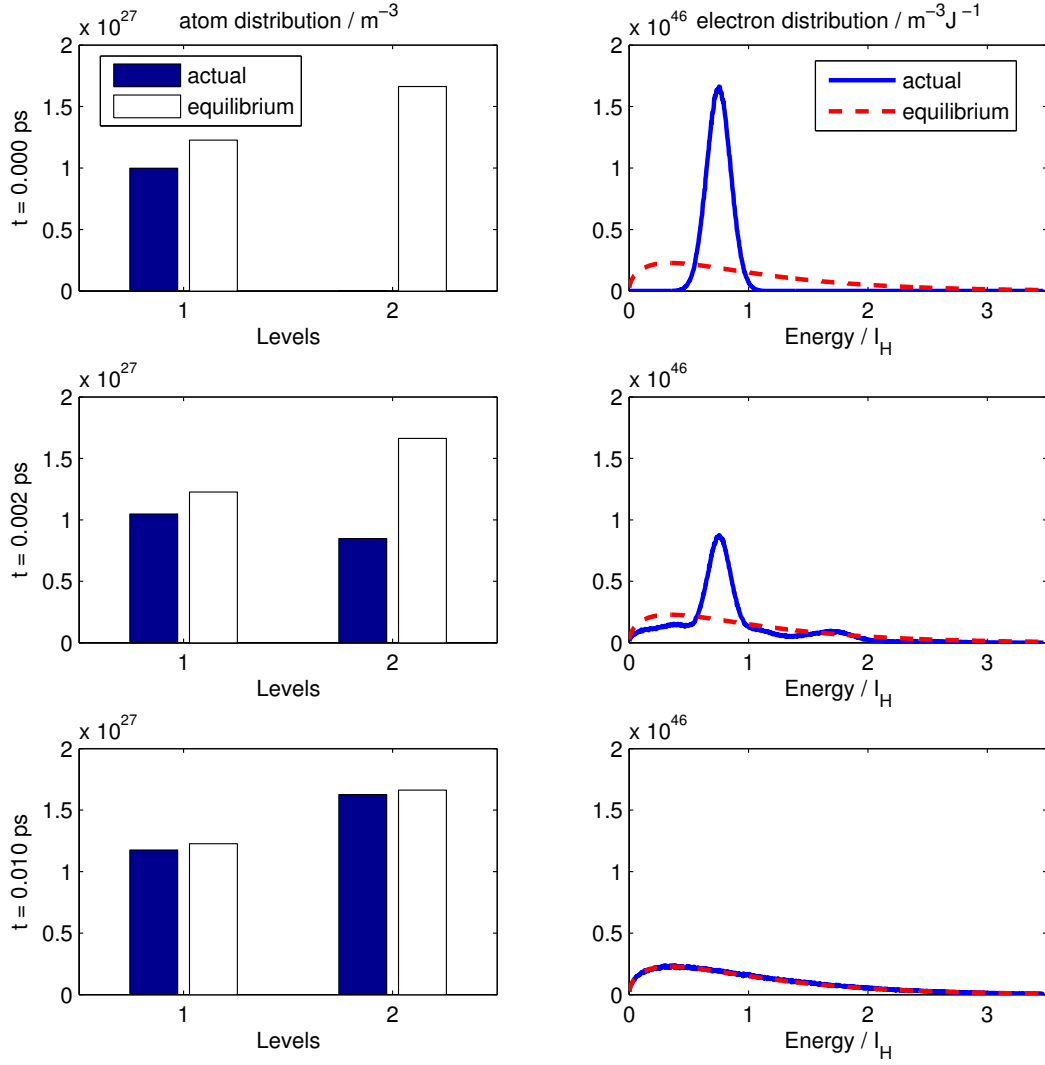
Figure 10: Snapshots of time evolution of atom density (left) and electron distribution (right), compared to the equilibrium (white bars and red dashed lines), starting from the initial data (83). All processes are included. 1000000 samples are used for free electrons.
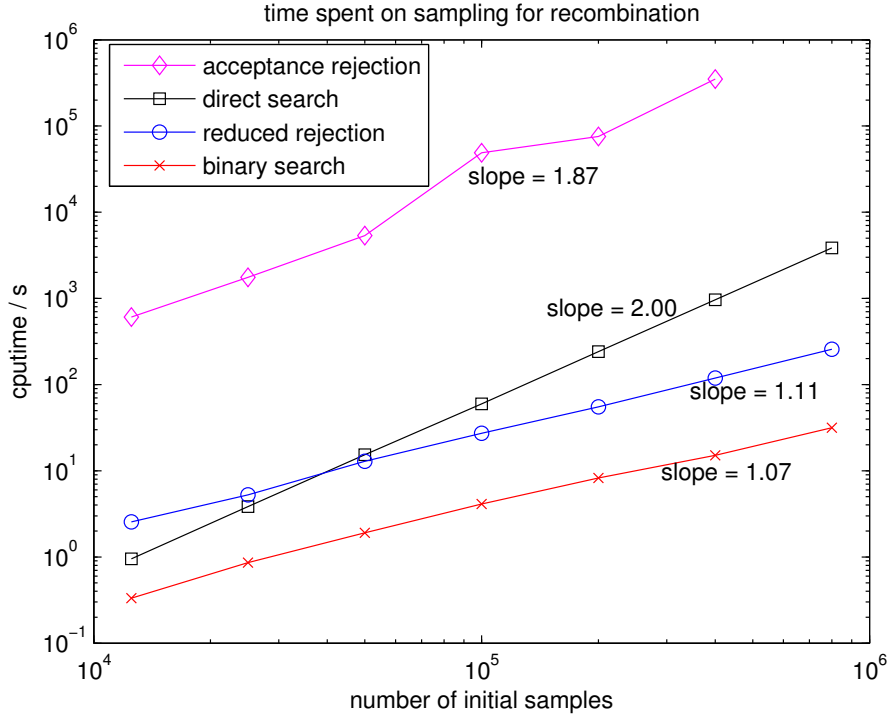
Figure 11: The time cost for recombination collisions when various numbers of samples are used for the initial free electron distribution. Initially all atoms are ionized.
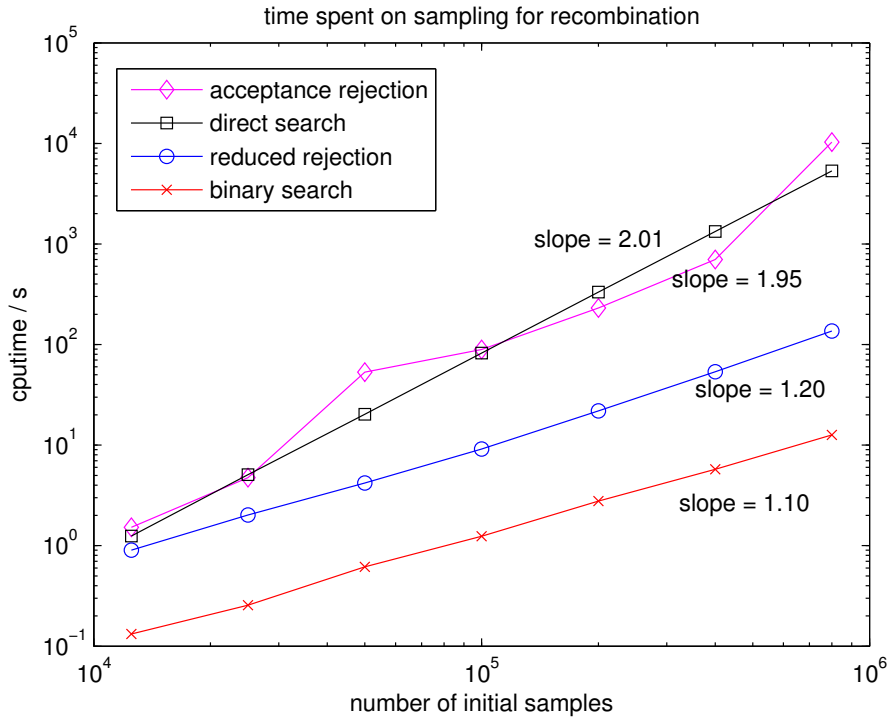
Figure 12: The time cost for recombination collisions when various numbers of samples are used for the initial free electron distribution. The system stays in equilibrium for all the time.
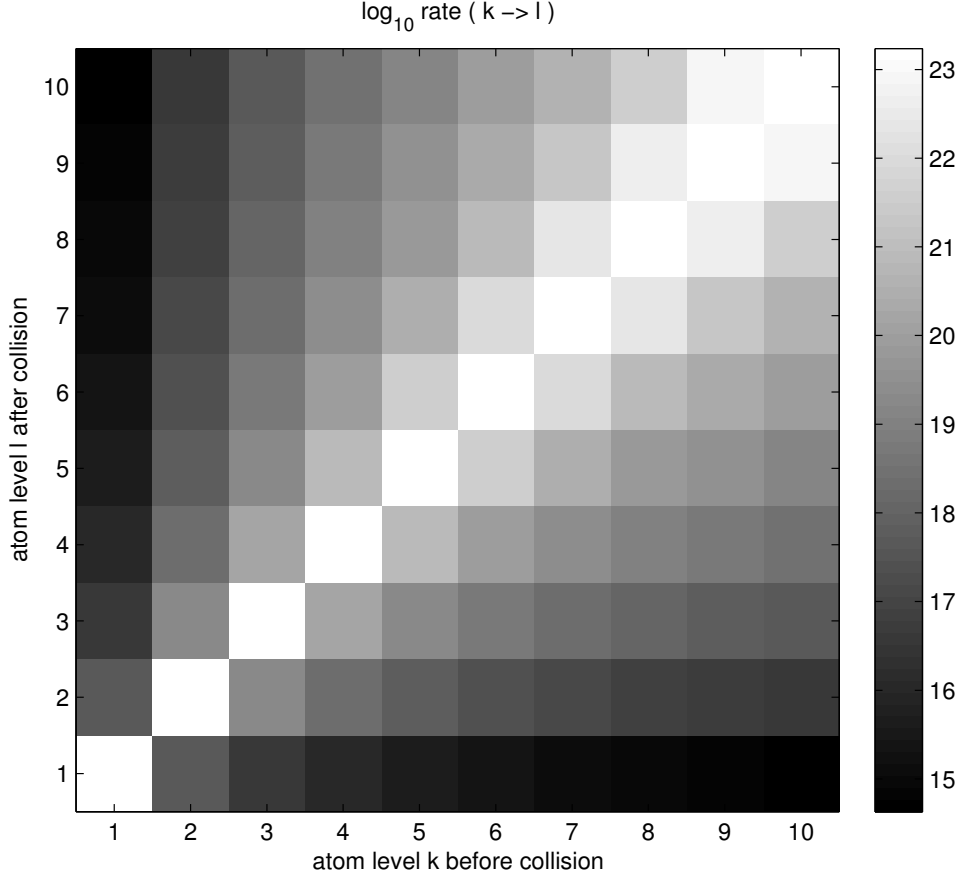
Figure 13: The total rates for excitation/deexcitation at equilibrium. The rates with $k = l$ are not defined and left blank in the figure.

different levels. For high levels like $k = 9, 10$, the rates of excitation/deexcitation are 100 times larger than those of ionization/recombination.

7   Conclusions and Future Work

This paper presents an idealized model for excitation/deexcitation and ionization/recombination by electron impact in plasma. The energetic cross sections for the model are all given by analytic formulas and they are consistent with detailed balance. A Boltzmann type equation for the energy distribution function is then formulated and an H-theorem is derived.

A conservative and equilibrium-preserving Direct Simulation Monte Carlo method is also developed for this system. The rates of recombination has a singularity as the energy of electron goes to 0. To overcome this difficulty, four different methods are proposed and compared, among which the binary search method and the reduced rejection method give the highest efficiency.

A simulation method suffers from two difficulties: First, there are a large number of kinetic processes (i.e., excitation and deexcitation between any two atomic levels) with widely varying rates. Fair representation of all of these processes can require very small time steps. Second, random fluctuations can exhaust the finite number of simulation particles in some state. In subsequent work, we
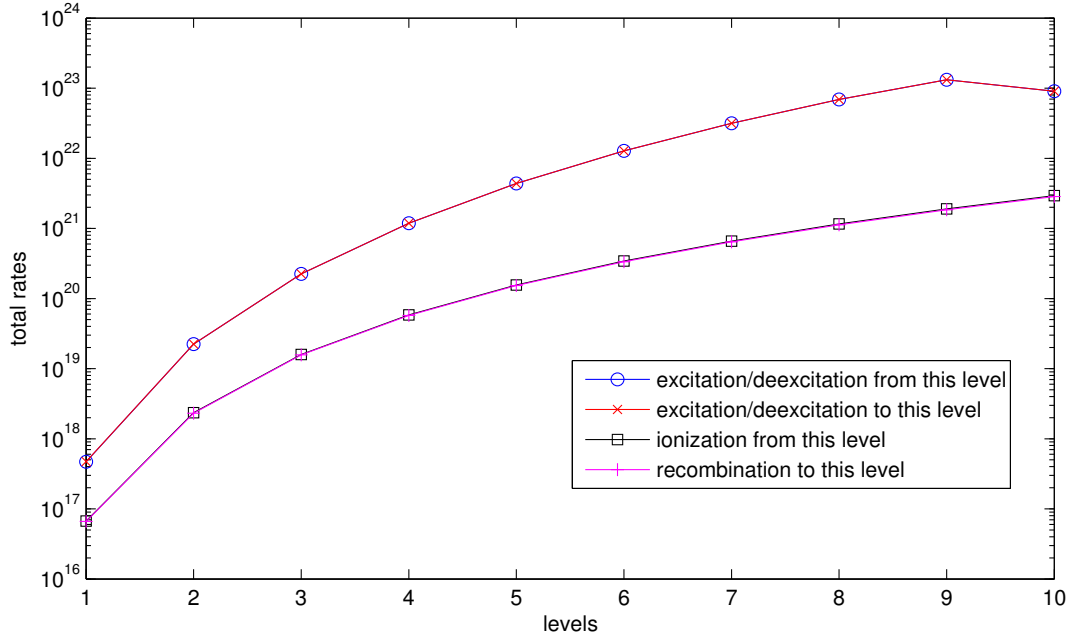
Figure 14: The total rates for all collisions at equilibrium.

plan to develop coarse-graining and a multi-scale simulation strategy to reduce the effect of these two computational bottlenecks.

The model and method here has been developed under a number of simplifying assumptions: The energy levels come from the Bohr model of hydrogen; only Hydrogen atoms and ions are included; Coulomb collisions have been neglected. Generalization to more realistic models can be easily performed.

References

[1] P. L. Bartlett and A. T. Stelbovics, "Ionization of atoms by electron impact," *Nuclear Instruments and Methods in Physics Research Section A: Accelerators, Spectrometers, Detectors and Associated Equipment*, vol. 619, pp. 1 – 6, 2010. Frontiers in radiation physics and applications:Proceedings of the 11th International Symposium on Radiation Physics.

[2] Y. B. Zel'dovich and Y. P. Raizer, *Physics of Shock Waves and High-Temperature Hydrodynamic Phenomena*. New York: Dover Publications, Inc., 2002.

[3] K. Steiner, "Weighted particle methods solving kinetic equations for dilute ionized gases," in *Flow Simulation with High-Performance Computers II* (E. Hirschel, ed.), vol. 48 of *Notes on Numerical Fluid Mechanics (NNFM)*, pp. 322–339, Vieweg+Teubner Verlag, 1996.

[4] T. Nedelea, B. Briehl, and H. M. Urbassek, "Simulation study of the effect of recombination processes in an expanding plasma," *Journal of Plasma Physics*, vol. 71, pp. 589–609, 10 2005.

[5] A. Barmin and A. Kozlov, "Structure of a steady-state ionization front in the plasma accelerator channel," *Fluid Dynamics*, vol. 48, no. 4, pp. 556–566, 2013.

[6] T. E. Glover, J. K. Crane, M. D. Perry, R. W. Lee, and R. W. Falcone, "Measurement of velocity distributions and recombination kinetics in tunnel-ionized helium plasmas," *Phys. Rev. Lett.*, vol. 75, pp. 445–448, Jul 1995.

[7] K. Nanbu, S. Yonemura, and A. Sasaki, "Particle modeling of ionization and three-body recombination in fully ionized plasmas," *Japan J. Appl. Phys.*, vol. 38, pp. 4460–4464, 1999.

[8] F. Barekat and R. Caflisch, "Simulation with fluctuating and singular rates," *Comm. Comp. Phys.*, vol. 16, pp. 287–306, 2014.

[9] D. R. Cox and H. D. Miller, *The theory of stochastic processes.* Boca Raton, FL : Chapman and Hall/CRC, 1965. "First CRC reprint 2001" – verso t.p.

[10] W. M. Young and E. W. Elcock, "Monte Carlo studies of vacancy migration in binary ordered alloys: I," *Proceedings of the Physical Society*, vol. 89, no. 3, p. 735, 1966.

[11] D. T. Gillespie, "A general method for numerically simulating the stochastic time evolution of coupled chemical reactions," *Journal of Computational Physics*, vol. 22, pp. 403–434, 1976.

[12] J.-L. Cambier and R. Caflisch, "A conservative scheme for the non-Maxwellian kinetics of collisional-radiative plasma with sub-cell resolution," *preprint*.

[13] J. T. Oxenius, *Kinetic Theory of Particles and Photons.* Berlin: Springer-Verlag, 1986.

[14] M. Baertschy, T. Rescigno, W. Isaacs, X. Li, and C. McCurdy, "Electron-impact ionization of atomic hydrogen," *Phys. Rev. A*, vol. 63, p. 022712, 2001.

[15] N. Mott and H. Massey, *The Theory of Atomic Collisions.* London: Oxford University Press, 1965.

[16] G. Bird, *Molecular Gas Dynamics.* London: Oxford University Press, 1976.

[17] G. Marsaglia, "Generating discrete random variables in a computer," *Commun. ACM*, vol. 6, pp. 37–38, Jan. 1963.

Appendix A Proof of Lemma 2.1

The proof of Lemma 2.1 is given in this appendix.

For ease of notation, the suffix eq is ignored, with the understanding that all quantities computed here are at thermodynamic equilibrium. For a given n_{tot}, the total energy at equilibrium with temperature T_e is

$$\varepsilon(T_e) = \frac{3}{2} n_e T_e + \sum_k n_k L_k + n_i L_i,$$

with n_k and n_i given by (9a)(9b). We only need to show ε is monotonic in T_e.

Charge neutrality gives

$$n_{tot} - n_a = n_e = n_i = n_a^{1/2} \gamma(T_e),$$

with

$$\gamma(T_e) = C T_e^{3/4} \mathbb{Z}_a^{-1/2} e^{-L_i/(2T_e)},$$

where $C = \left(2 g_i \left(\frac{2\pi m_e}{h^2} \right)^{3/2} \right)^{1/2}$ is a constant. The function γ can be shown to be monotonic in T_e:

$$\frac{\mathrm{d}\gamma}{\mathrm{d}T_e} = \frac{3}{4} \frac{\gamma}{T_e} + \frac{L_i}{T_e} \frac{\gamma}{2T_e} - \frac{\gamma}{2T_e^2} \frac{\sum_k g_k L_k e^{-L_k/T_e}}{\sum_k g_k e^{-L_k/T_e}}. \tag{A.1}$$

We define by $\langle \cdot \rangle$ the averaging over the atomic partition function $\mathbb{Z}_a$, i.e. for $\phi = (\phi_1, \ldots, \phi_{k_{\max}})$, define

$$\langle \phi \rangle = \frac{\sum_k \phi_k g_k e^{-L_k/T_e}}{\sum_k g_k e^{-L_k/T_e}} = \sum_k \frac{n_k}{n_a} \phi_k. \tag{A.2}$$

The last term in (A.1) can be recognized as $\langle L \rangle$. Since $L_i > L_k, \forall k$ and $\gamma \geqslant 0$, we can find a majorant for this expression

$$\frac{\mathrm{d}\gamma}{\mathrm{d}T_e} = \frac{\gamma}{2T_e} \left[\frac{3}{2} + \frac{L_i}{T_e} - \frac{\langle L \rangle}{T_e} \right] \geqslant \frac{3\gamma}{4T_e} > 0.$$

The solution for the neutral atom density is then

$$n_a^{1/2} = -\frac{\gamma}{2} + \frac{1}{2} \sqrt{\gamma^2 + 4 n_{tot}},$$

$$n_a = \frac{4 n_{tot}^2}{\left(\sqrt{\gamma^2 + 4 n_{tot}} + \gamma \right)^2},$$

with the following variation

$$\frac{\mathrm{d}n_a}{\mathrm{d}\gamma} = \frac{-2 n_a}{\sqrt{\gamma^2 + 4 n_{tot}} + \gamma} \left(1 + \frac{\gamma}{\sqrt{\gamma^2 + 4 n_{tot}}} \right) < 0.$$

Therefore, n_a monotonically decreases as T_e increases, and since $n_e = n_{tot} - n_a$, this implies that n_e monotonically increases with T_e, i.e. $\frac{\mathrm{d}n_e}{\mathrm{d}T_e} \geqslant 0$.

The variation of the energy can be computed as follows

$$\frac{\mathrm{d}\varepsilon}{\mathrm{d}T_e} = \frac{3}{2} n_e + \left(\frac{3}{2} T_e + L_i \right) \frac{\mathrm{d}n_e}{\mathrm{d}T_e} + \sum_k L_k \frac{\mathrm{d}n_k}{\mathrm{d}T_e}. \tag{A.3}$$

The last term is not a-priori trivial; we expect the population of excited states to increase with T_e (note that the ground state, being depleted, does not contribute to the sum since $L_1 \equiv 0$), but it is

entirely possible that the rate of changes of some levels increase while others decrease, especially as ionization proceeds preferentially from the upper states. Let us consider this variation,

$$\frac{\mathrm{d}n_k}{\mathrm{d}T_e} = \frac{\mathrm{d}n_a}{\mathrm{d}T_e}\mathbb{Z}_a^{-1}g_k e^{-L_k/T_e} - \frac{n_k}{T_e^2}\mathbb{Z}_a^{-1}\sum_k g_k L_k e^{-L_k/T_e} + \frac{n_k L_k}{T_e^2}.$$

Identifying again the averaging over the atomic partition function $\mathbb{Z}_a$, we obtain

$$\frac{\mathrm{d}n_k}{\mathrm{d}T_e} = \frac{n_k}{n_a}\frac{\mathrm{d}n_a}{\mathrm{d}T_e} + \frac{n_k}{T_e^2}\left(L_k - \langle L \rangle\right).$$

Inserting into (A.3),

$$\frac{\mathrm{d}\varepsilon}{\mathrm{d}T_e} = \frac{3}{2}n_e + \left(\frac{3}{2}T_e + L_i - \sum_k \frac{n_k L_k}{n_a}\right)\frac{\mathrm{d}n_e}{\mathrm{d}T_e} + \sum_k \frac{n_k}{T_e^2}\left(L_k^2 - L_k\langle L\rangle\right)$$

$$= \frac{3}{2}n_e + \left(\frac{3}{2}T_e + L_i - \langle L\rangle\right)\frac{\mathrm{d}n_e}{\mathrm{d}T_e} + \frac{n_a}{T_e^2}\left(\langle L^2\rangle - \langle L\rangle^2\right).$$

The second term is nonnegative since $L_i > L_k$ for any k and $\frac{\mathrm{d}n_e}{\mathrm{d}T_e} \geqslant 0$. The third term is nonnegative due to Cauchy-Schwarz inequality. Therefore at equilibrium, the total energy is also monotonically increasing as a function of T_e.

This completes the proof of Lemma 2.1.

Appendix B Proof of Lemma 3.5

This appendix gives the proof of Lemma 3.5. Denote

$$C_k = \frac{n_k}{n_k^{eq}}, \qquad C_i = \frac{n_i}{n_i^{eq}}, \qquad \tilde{f} = \frac{f}{f^{eq}}. \tag{B.1}$$

Then

$$C_k\tilde{f}(E_0) = C_i\tilde{f}(E_0 - E_t)\tilde{f}(E_t - B_k),$$

for any k, E_0 E_t satisfying $B_k \leqslant E_t \leqslant E_0$.

Take the derivative with respect to E_t on both sides to obtain

$$-\tilde{f}'(E_0 - E_t)\tilde{f}(E_t - B_k) + \tilde{f}(E_0 - E_t)\tilde{f}'(E_t - B_k) = 0,$$

$$\frac{\tilde{f}'(E_0 - E_t)}{\tilde{f}(E_0 - E_t)} = \frac{\tilde{f}'(E_t - B_k)}{\tilde{f}(E_t - B_k)}.$$

Denote $\phi = \log \tilde{f}$, then

$$\phi'(E_0 - E_t) = \phi'(E_t - B_k).$$

This formula is valid for any E_0, therefore ϕ' is a constant, so that $\tilde{f}$ has the form

$$\tilde{f} = e^{\alpha E + \beta},$$

where both α and β are constants. Then

$$C_k = C_i e^{-\alpha B_k + \beta} = C_i e^{-\alpha L_i + \beta}e^{\alpha L_k}.$$

Denote $c_0 = C_i e^{-\alpha L_i + \beta}$, then

$$C_k = c_0 e^{\alpha L_k}, \qquad C_i = c_0 e^{\alpha L_i - \beta}.$$

This means that f, n_k and n_i in (B.1) are at equilibrium with temperature

$$\left(\frac{1}{T_e} - \alpha\right)^{-1},$$

where T_e is the temperature of f^{eq}. From Lemma 2.1, the equilibrium temperature is unique, hence
$$\alpha = 0.$$

Then the conservation of number density gives $\beta = 0$ and $c_0 = 1$, so that
$$\tilde{f} \equiv 1, \qquad C_k = 1, \qquad C_i = 1,$$

which finishes the proof.

Appendix C   Proof of Proposition 3.1

For case (a), where only the ionization/recombinaiton processes are included, take $\phi = 1$ in (54) to obtain
$$\partial_t n_e = \sum_k \iint \left(\frac{n_k}{n_k^{eq}} \frac{f_0}{f_0^{eq}} - \frac{n_i}{n_i^{eq}} \frac{f_1}{f_1^{eq}} \frac{f_2}{f_2^{eq}} \right) n_k^{eq} f_0^{eq} v_0 \sigma^{ion} \, dE_0 \, dE_t.$$

Combining this with (55) leads to the conservation of total density of electrons
$$\frac{d}{dt} n_{tot} = \frac{d}{dt} n_e + \sum \frac{d}{dt} n_k = 0.$$

Now take $\phi = E$ in (54) to obtain
$$\partial_t \int E f(E) \, dE = \sum_k \iint (E_1 + E_2 - E_0) \left(\frac{n_k}{n_k^{eq}} \frac{f_0}{f_0^{eq}} - \frac{n_i}{n_i^{eq}} \frac{f_1}{f_1^{eq}} \frac{f_2}{f_2^{eq}} \right) n_k^{eq} f_0^{eq} v_0 \sigma^{ion} \, dE_0 \, dE_t.$$

Combining this with (55) and (56) leads to
$$\frac{d}{dt} \varepsilon_{tot} = \frac{d}{dt} \int E f(E) \, dE + \sum_k L_k \frac{d}{dt} n_k + L_{ion} \frac{d}{dt} n_i$$
$$= \sum_k \iint (E_1 + E_2 - E_0 - L_k + L_{ion}) \left(\frac{n_k}{n_k^{eq}} \frac{f_0}{f_0^{eq}} - \frac{n_i}{n_i^{eq}} \frac{f_1}{f_1^{eq}} \frac{f_2}{f_2^{eq}} \right) n_k^{eq} f_0^{eq} v_0 \sigma^{ion} \, dE_0 \, dE_t.$$

Noting that $E_1 + E_2 + B_k = E_0$ from energy conservation at the microscopic level, which yields $\frac{d}{dt} \varepsilon_{tot} = 0$.

For case (b), where only the excitation/deexcitataiton processes are included, take $\phi = 1$ in (58) and (60) to obtain
$$\frac{d}{dt} \int f(E) \, dE = \frac{d}{dt} \sum_k n_k = 0.$$

Now take $\phi = E$ in (58) to obtain
$$\partial_t \int E f(E) \, dE = \sum_{l<u} \int (E_1 - E_0) \left(\frac{n_l}{n_l^{eq}} \frac{f_0}{f_0^{eq}} - \frac{n_u}{n_u^{eq}} \frac{f_1}{f_1^{eq}} \right) n_l^{eq} f_0^{eq} v_0 \sigma^{exc} \, dE_0.$$

As for the energy of atoms, taking $\phi_k = L_k$ in (60) gives
$$\frac{d}{dt} \sum_k n_k L_k = \sum_{l<u} \int \left(\frac{n_l}{n_l^{eq}} \frac{f_0}{f_0^{eq}} - \frac{n_u}{n_u^{eq}} \frac{f_1}{f_1^{eq}} \right) (L_u - L_l) n_l^{eq} f_0^{eq} v_0 \sigma^{exc} \, dE_0.$$

Therefore,
$$\frac{d}{dt} \varepsilon_{tot} = \frac{d}{dt} \int E f(E) \, dE + \sum_k L_k \frac{d}{dt} n_k + L_{ion} \frac{d}{dt} n_i$$
$$= \sum_{l<u} \int (E_1 - E_0 + L_u - L_l) \left(\frac{n_l}{n_l^{eq}} \frac{f_0}{f_0^{eq}} - \frac{n_u}{n_u^{eq}} \frac{f_1}{f_1^{eq}} \right) n_l^{eq} f_0^{eq} v_0 \sigma^{exc} \, dE_0$$
$$= 0.$$

The last equal sign comes from microscopic energy conservation, $E_1 = E_0 - \Delta E_{lu}$.

For case (c), where all processes are included, the conservations of moments come from the fact that the "IR" operators and the "ED" operators conserve the moments separately.

Appendix D   Proof of Lemma 3.7 and Theorem 3.8

This appendix provides the proof of Lemma 3.7 and Theorem 3.8.

Proof of Lemma 3.7. (i). For any $\tilde{E} > 0$, take

$$\phi(E) = \sum_{j=0}^{\infty} \delta(E - \tilde{E} - j\Delta E) \tag{D.1}$$

in (58) to obtain (61), using the fact that

$$\phi(E_1) = \phi(E_0 - \Delta E_{lu}) = \phi(E_0),$$

since ϕ is a periodic function with period ΔE and ΔE_{lu} is an integer multiplication of ΔE.

(ii). If f is in the form of (63), multiply both sides of (63) by (D.1) and integrate over $\{E > 0\}$ to obtain

$$\int \sum_{j} \delta(E - \tilde{E} - j\Delta E) f(E) \, \mathrm{d}E = \int \sum_{j} \delta(E - \tilde{E} - j\Delta E) f^{eq}(E)\eta(E) \, \mathrm{d}E,$$

$$\sum_{j} f(\tilde{E} + j\Delta E) = \sum_{j} f^{eq}(\tilde{E} + j\Delta E)\eta(\tilde{E}).$$

Therefore,

$$\eta(\tilde{E}) = \frac{\sum_{j} f(\tilde{E} + j\Delta E)}{\sum_{j} f^{eq}(\tilde{E} + j\Delta E)} = \frac{\sum_{j} f(\tilde{E} + j\Delta E, t = 0)}{\sum_{j} f^{eq}(\tilde{E} + j\Delta E)}. \tag{D.2}$$

The last equality comes from (61).

(iii). With only excitation/deexcitation included, n_a and n_e are constant in time. The total energy for $f = f^{eq}(E; T_e)\eta(E; T_e)$ and $\{n_k^{eq}(T_e)\}$ at temperature T_e is

$$\varepsilon(T_e) = \int E f^{eq}(E; T_e)\eta(E; T_e) \, \mathrm{d}E + \sum_{k} n_k^{eq}(T_e)L_k + n_i L_i.$$

For a given total energy ε_{tot}, to prove $\varepsilon(T_e) = \varepsilon_{tot}$ has a unique solution T_e, we only need to show ε is monotonic in T_e.

First notice that $\frac{\mathrm{d}}{\mathrm{d}T_e}(n_i L_i) = 0$ and from the proof of Lemma 2.1,

$$\frac{\mathrm{d}}{\mathrm{d}T_e} \sum_{k} n_k^{eq} L_k = \sum_{k} L_k \frac{\mathrm{d}}{\mathrm{d}T_e} n_k^{eq} = \frac{n_a}{T_e^2} \left(\langle L^2 \rangle - \langle L \rangle^2 \right) \geqslant 0,$$

where $\langle \cdot \rangle$ is defined in (A.2).

Next one can check

$$\frac{\mathrm{d}}{\mathrm{d}T_e} f^{eq} = f^{eq} \frac{1}{T_e} \left(\frac{E}{T} - \frac{3}{2} \right),$$

and

$$\frac{\mathrm{d}}{\mathrm{d}T_e}\eta = \frac{-\eta}{\sum_j f^{eq}(E + j\Delta E)}\sum_j \frac{\mathrm{d}}{\mathrm{d}T_e}f^{eq}(E + j\Delta E)$$

$$= \frac{-\eta/T_e}{\sum_j f^{eq}(E + j\Delta E)}\sum_j f^{eq}(E + j\Delta E)\left(\frac{E + j\Delta E}{T_e} - \frac{3}{2}\right).$$

Hence, for $f = f^{eq}(E; T_e)\eta(E; T_e)$, after simplification,

$$\frac{\mathrm{d}}{\mathrm{d}T_e}f = \eta\frac{\mathrm{d}}{\mathrm{d}T_e}f^{eq} + f^{eq}\frac{\mathrm{d}}{\mathrm{d}T_e}\eta$$

$$= -\frac{f^{eq}\eta\Delta E}{T_e^2} \cdot \frac{\sum_j j f^{eq}(E + j\Delta E)}{\sum_j f^{eq}(E + j\Delta E)},$$

where the summation is over all integers $j = j(E)$ such that $E + j\Delta E \geqslant 0$, i.e. $j \geqslant -\left[\frac{E}{\Delta E}\right]$, with $[\cdot]$ representing the integer part.

Then for the electron energy

$$\varepsilon_e(T_e) = \int E f^{eq}(E; T_e)\eta(E; T_e)\,\mathrm{d}E,$$

one has

$$\frac{\mathrm{d}}{\mathrm{d}T_e}\varepsilon_e = -\frac{\Delta E}{T_e^2}\int E f^{eq}(E)\eta(E)\frac{\sum_j j f^{eq}(E + j\Delta E)}{\sum_j f^{eq}(E + j\Delta E)}\,\mathrm{d}E$$

$$= -\frac{\Delta E}{T_e^2}\sum_{j_0}\int_{j_0\Delta E}^{(j_0+1)\Delta E} E f^{eq}(E)\eta(E)\frac{\sum_j j f^{eq}(E + j\Delta E)}{\sum_j f^{eq}(E + j\Delta E)}\,\mathrm{d}E$$

$$= -\frac{\Delta E}{T_e^2}\int_0^{\Delta E}\sum_{j_0}(E + j_0\Delta E)f^{eq}(E + j_0\Delta E)\eta(E)\frac{\sum_j j f^{eq}(E + j_0\Delta E + j\Delta E)}{\sum_j f^{eq}(E + j\Delta E)}\,\mathrm{d}E.$$

Here the summation in the numerator is over all integers $j \geqslant -\left[\frac{E + j_0\Delta E}{\Delta E}\right] = -j_0 - \left[\frac{E}{\Delta E}\right]$.

For any $E \in [0, \Delta E)$, denote

$$A_{j_0}(E) = \sum_{j \geqslant -j_0 - [E/\Delta E]} j f^{eq}(E + j_0\Delta E + j\Delta E)$$

$$= \sum_{j' \geqslant -[E/\Delta E]}(j' - j_0)f^{eq}(E + j'\Delta E)$$

$$= \sum_{j' \geqslant -[E/\Delta E]} j' f^{eq}(E + j'\Delta E) - j_0\sum_{j' \geqslant -[E/\Delta E]} f^{eq}(E + j'\Delta E).$$

Let

$$j_0^* = j_0^*(E) = \left[\frac{\sum_{j' \geqslant -[E/\Delta E]} j' f^{eq}(E + j'\Delta E)}{\sum_{j' \geqslant -[E/\Delta E]} f^{eq}(E + j'\Delta E)}\right],$$

then $A_{j_0}(E) \leqslant 0$, for $j_0 \leqslant j_0^*$, and $A_{j_0}(E) > 0$, for $j_0 > j_0^*$.

Therefore

$$\frac{\mathrm{d}}{\mathrm{d}T_e}\varepsilon_e \geqslant -\frac{\Delta E}{T_e^2}\int_0^{\Delta E}\sum_{j_0}(E+j_0^*\Delta E)f^{eq}(E+j_0\Delta E)\eta(E)\frac{\sum_j j f^{eq}(E+j_0\Delta E+j\Delta E)}{\sum_j f^{eq}(E+j\Delta E)}\,\mathrm{d}E$$

$$=\int_0^{\Delta E}(E+j_0^*\Delta E)\sum_{j_0}\frac{\mathrm{d}}{\mathrm{d}T_e}f(E+j_0\Delta E)\,\mathrm{d}E$$

$$=\int_0^{\Delta E}(E+j_0^*\Delta E)\frac{\mathrm{d}}{\mathrm{d}T_e}\sum_{j_0}f(E+j_0\Delta E)\,\mathrm{d}E$$

$$=\int_0^{\Delta E}(E+j_0^*\Delta E)\frac{\mathrm{d}}{\mathrm{d}T_e}\sum_{j_0}f(E+j_0\Delta E,t=0)\,\mathrm{d}E.$$

We have used (61) in the last step. Note that $\frac{\mathrm{d}}{\mathrm{d}T_e}\sum_{j_0}f(E+j_0\Delta E,t=0)=0$, one has $\frac{\mathrm{d}}{\mathrm{d}T_e}\varepsilon_e=0$.
Therefore

$$\frac{\mathrm{d}}{\mathrm{d}T_e}\varepsilon = \frac{\mathrm{d}}{\mathrm{d}T_e}\varepsilon_e + \frac{\mathrm{d}}{\mathrm{d}T_e}\sum_k n_k^{eq}L_k + \frac{\mathrm{d}}{\mathrm{d}T_e}(n_iL_i) \geqslant 0.$$

This ends the proof. $\qquad\qquad\square$

Proof of Theorem 3.8. Denote

$$C_k = \frac{n_k}{n_k^{eq}}, \qquad \tilde{f} = \frac{f}{f^{eq}}.$$

Then

$$C_l\tilde{f}(E_0) = C_u\tilde{f}(E_0-\Delta E_{lu}),$$

for any l, u and E_0. Take the derivative with respect to E_0 on both sides to obtain

$$C_l\tilde{f}'(E_0) = C_u\tilde{f}'(E_0-\Delta E_{lu}),$$

$$\frac{\tilde{f}'(E_0)}{\tilde{f}(E_0)} = \frac{\tilde{f}'(E_0-\Delta E_{lu})}{\tilde{f}(E_0-\Delta E_{lu})}.$$

Denote $\psi = \log\tilde{f}$, then

$$\psi'(E_0) = \psi'(E_0-\Delta E_{lu}).$$

This formula is valid for any l, u and E_0. Therefore ψ' is a periodic function with period ΔE which is an integer multiplication of ΔE_{lu}.

Then $\psi(E_0) = \psi(E_0-\Delta E_{lu}) + C$, for some constant C. Let $\alpha = C/\Delta E_{lu}$, one has

$$\psi(E_0) - \alpha E_0 = \psi(E_0-\Delta E_{lu}) - \alpha(E_0-\Delta E_{lu}).$$

Denote

$$\eta(E) = \exp(\psi(E)-\alpha E),$$

then η is a periodic function with period ΔE and $f(E)$ is given by

$$f(E) = f^{eq}(E;T_e)\tilde{f}(E) = f^{eq}(E;T_e)\exp(\psi(E)) = e^{\alpha E}f^{eq}(E;T_e)\eta(E). \qquad (\text{D.3})$$

Moreover, from

$$C_l\tilde{f}(E_0) = C_u\tilde{f}(E_0-\Delta E_{lu})$$

one has

$$\frac{C_l}{C_u} = \frac{\tilde{f}(E_0-\Delta E_{lu})}{\tilde{f}(E_0)} = \frac{1}{e^{\alpha\Delta E_{lu}}} = \frac{e^{\alpha L_l}}{e^{\alpha L_u}}.$$

Choose a constant c_0 such that $C_1 = c_0 e^{\alpha L_1}$, then $C_u = c_0 e^{\alpha L_u}$ for any level u. Hence
$$n_k = C_k n_k^{eq}(T_e) = c_0 e^{\alpha L_k} n_k^{eq}(T_e).$$

Combined with (D.3), $f(E)$ and n_k are in the form of (63) with temperature $(1/T_e - \alpha)^{-1}$. From Lemma 3.7 (iii), the temperature is uniquely determined from the energy conservation, hence $\alpha = 0$. This completes the proof.

$\square$

Appendix E Algorithm for binary search method

This appendix provides the detailed algorithm for the application of binary search method in the recombination problem.

E.1 Padding by zeros

For a given set $\{v_k, k = 1, \ldots, N\}$, first enlarge its size to N_1 by padding zeros. Here N_1 is the minimum power of 2 satisfying $N_1 \geqslant N$. The method is easier to formulate for N_1, a power of two, and padding by zeros also reserves some slots for possible new electrons generated in the ionization collisions. In the following we assume N is a power of 2 and $N_1 = N$, without loss of generality.

E.2 Building a table

Let $L = \log_2 N$. Build a table to store the pre-computed summations,
$$s_{l,j} = \sum_{k=(j-1)2^{L-l}+1}^{j2^{L-l}} v_k, \quad \text{with } 0 \leqslant l \leqslant L, 1 \leqslant j \leqslant 2^l.$$

Note that $s_{L,j} = v_j$, there is no need to store $s_{L,j}$. The total memory used for storing this table is
$$1 + 2 + \cdots + 2^{L-1} = 2^L - 1 = N - 1.$$

Moreover, the table $\{s_{l,j}\}$ can be computed backwardly
$$s_{l,j} = s_{l+1,2j-1} + s_{l+1,2j}.$$

Hence we only need to carry out N summations.

E.3 Sampling a particle

Here we describe the algorithm for sampling.

Sample r uniformly from $(0, 1)$
Let $k = 1$, $q = s_{0,1} = \sum_j v_j$
for $l = 1, \ldots, L$ **do**
    $q_1 \leftarrow s_{l,2k-1}$
    $p \leftarrow \frac{q_1}{q}$
    if $r \leqslant p$ **then**
        $k \leftarrow 2k - 1$
        $q \leftarrow q_1$
        $r \leftarrow \frac{r}{p}$
    else
        $k \leftarrow 2k$
        $q \leftarrow q - q_1$
        $r \leftarrow \frac{r-p}{1-p}$

end if
   end for

The variable k gives the solution for (78). The computational cost is
$$\mathcal{O}(L) = \mathcal{O}(\log_2 N).$$

E.4   Update the table when some v_k changes

If v_k changes, there is exactly one entry in $\{s_{l,j}\}$ to be updated, for each l. Hence we need to update a total number of L entries in the table. More precisely, if we write the binary expansion of k,
$$k = \sum_{l=0}^{L} \beta_l 2^l,$$

one only needs to update
$$s_{l,\alpha_l} := s_{l,\alpha_l} + v_k^{new} - v_k^{old}, \quad l = 0, \dots, L,$$

where $\alpha_0 = 1$ and
$$\alpha_l = 2\alpha_{l-1} + \beta_{L+1-l} - 1.$$

This cost is also $\mathcal{O}(\log_2 N)$.

Appendix F   Non-Equilibrium Stationary States

Consider a single (l, u) transition, with no other collision processes, and let us use the simplifying notation:

$$E_n = n\Delta E_{lu} \tag{F.1a}$$
$$E_n^{\pm} = E_n \pm \varepsilon \quad \varepsilon \to 0 \tag{F.1b}$$
$$f_n^- = f(E_n^-) \tag{F.1c}$$
$$f_n^+ = f(E_n^+) \tag{F.1d}$$

Thus, $E_1^{\pm}$ is the particle energy just above (+) or below (-) the excitation threshold, and $E_0 \equiv 0$. We will allow for the possibility of a discontinuity in the distribution function f at multiple values of the threshold. Let us use another simplifying notation for the microscopic rates, $k^{\uparrow}(E) = \sigma^{\text{exc}}(E; E - \Delta E_{lu})v(E)$ and $k^{\downarrow}(E) = \sigma^{\text{dex}}(E; E + \Delta E_{lu})v(E)$, and consider now the evolution of the distribution function just below the first threshold:

$$\frac{df_1^-}{dt} = + k^{\uparrow}(E_2^-)n_l f_2^- + \cancel{k^{\downarrow}(E_0^-)n_u f_0^-} \\ - \cancel{k^{\uparrow}(E_1^-)n_l f_1^-} - k^{\downarrow}(E_1^-)n_u f_1^- \tag{F.2}$$

As shown, two terms are identically zero, because $f(E) \equiv 0$ for any $E \leqslant 0$ (thus, $f(E_0^- \equiv 0)$, and $k^{\uparrow}(E) \equiv 0$ for any $E < \Delta E_{lu}$ (thus, $k^{\uparrow}(E_1^-) \equiv 0$). For the *steady-state*, equation (F.2) leads to:

$$k \uparrow (E_2^-)n_l f_2^- = k^{\downarrow}(E_1^-)n_u f_1^- \tag{F.3}$$

Similarly, we can now consider the evolution of the distribution function near the next threshold:

$$\frac{df_2^-}{dt} = + k^{\uparrow}(E_3^-)n_l f_3^- + k^{\downarrow}(E_1^-)n_u f_1^- \\ - k^{\uparrow}(E_2^-)n_l f_2^- - k^{\downarrow}(E_2^-)n_u f_2^- \tag{F.4}$$

This time, all terms remain, since all variables are evaluated above their respective thresholds. Seeking the stationary solution, we have:

$$k \uparrow (E_3^-)n_l f_3^- = \left[k^{\uparrow}(E_2^-)n_l + k^{\downarrow}(E_2^-)n_u \right] f_2^- - k^{\downarrow}(E_1^-)n_u f_1^- \tag{F.5}$$

Using (F.3) to replace the last term on the right, we brain the following simplification:

$$\kappa\uparrow(E_3^-)n_l f_3^- = \left[\kappa^\uparrow(E_2^-)n_l + \kappa^\downarrow(E_2^-)n_u\right]f_2^- - \kappa^\uparrow(E_2^-)n_l f_2^- = \kappa^\downarrow(E_2^-)n_u f_2^- \qquad \text{(F.6)}$$

It is trivial to verify that the same procedure can be repeated for the next threshold, leading to the following sequence of stationary states:

$$\boxed{\kappa^\uparrow(E_n^-)n_l f_n^- = \kappa^\downarrow(E_{n-1}^-)n_u f_{n-1}^- \qquad n \geqslant 2} \qquad \text{(F.7)}$$

Consider now the evolution of f just above the threshold. The equivalent of (F.2), i.e. the first threshold, is found at E_0^+:

$$\frac{df_0^+}{dt} = +\kappa^\uparrow(E_1^+)n_l f_1^+ - \kappa^\downarrow(E_0^+)n_u f_0^+ \qquad \text{(F.8)}$$

with a stationary solution such that:

$$\kappa^\uparrow(E_1^+)n_l f_1^+ = \kappa^\downarrow(E_0^+)n_u f_0^+ \qquad \text{(F.9)}$$

For the next step, we have:

$$\begin{aligned}
\frac{df_1^+}{dt} = &+ \kappa^\uparrow(E_2^+)n_l f_3^- + \kappa^\downarrow(E_0^+)n_u f_0^+ \\
&- \kappa^\uparrow(E_1^+)n_l f_1^+ - \kappa^\downarrow(E_1^+)n_u f_1^+
\end{aligned} \qquad \text{(F.10)}$$

Looking for the stationary solution,

$$\kappa^\uparrow(E_2^+)n_l f_2^+ = \left[\kappa^\uparrow(E_1^+)n_l + \kappa^\downarrow(E_1^+)n_u\right]f_1^+ - \kappa^\downarrow(E_0^+)n_u f_0^+ \qquad \text{(F.11)}$$

Again, we can use the steady-state solution at the previous threshold (F.9) to simply this expression, and obtain:

$$\kappa^\uparrow(E_2^+)n_l f_2^+ = \kappa^\downarrow(E_1^+)n_u f_1^+ \qquad \text{(F.12)}$$

Therefore, we obtain a similar sequence of states, i.e.:

$$\boxed{\kappa^\uparrow(E_n^+)n_l f_n^+ = \kappa^\downarrow(E_{n-1}^+)n_u f_{n-1}^+ \qquad n \geqslant 1} \qquad \text{(F.13)}$$

At this point it is worth making a couple of important remarks:

- The sequences of states (F.7,F.13) are *independently* obtained, and nothing forces us to have a continuous solution across the thresholds, i.e. $f_n^- \neq f_n^+$ ($n \geqslant 1$).
- The stationary states are obtained *independently* of the evolution of the atomic states, i.e. the relations (F.7,F.13) are valid *irrespective* of whether the densities n_l, n_u are in Boltzmann equilibrium or not.

It is easy to see that the dynamics of eq. (F.8) remain the same for any value of energy $E \leqslant E_1^-$. Therefore, a generalization of (F.9) would be:

$$\kappa^\uparrow(E+\Delta E_{lu})n_l f(E+\Delta E_{lu}) = \kappa^\downarrow(E)n_u f(E) \qquad 0 \leqslant E \leqslant E_1^- \qquad \text{(F.14)}$$

Examining the dynamics in the next energy segment, $E_1^+ \leqslant E \leqslant E_2^-$, the generalization of (F.11) can again be simplified using (F.14), and we are led to the following relation:

$$\boxed{\kappa^\uparrow(E+\Delta E_{lu})n_l f(E+\Delta E_{lu}) = \kappa^\downarrow(E)n_u f(E) \qquad \text{for } E_{n-1}^+ \leqslant E \leqslant E_n^-, \ n \geqslant 1} \qquad \text{(F.15)}$$

Therefore, at steady state, the shape of the distribution function within each energy segment $\left[E_{n-1}^+, E_n^-\right]$ is duplicated onto the next segment according to (F.15), with possible discontinuous solutions across the boundaries of the energy segments.

Knowing that discontinuous stationary solutions are possible, it is worth examining how these can be generated. We consider now a case with initial conditions given by a hot, equilibrium electron

distribution and a cold atomic state distribution, i.e. the dynamics of the system are strongly biased towards excitation only. Since we consider only a single energy gap, we have $n_u \ll n_u^{eq}(T_e) \ll n_l$, and we can make the approximation $n_u \simeq 0$ (alternatively, we can simply choose $n_u = 0$ as the initial condition). This simplifies the initial dynamics, since near $t = 0$, we have:

$$\frac{df_1^-}{dt} \simeq \kappa^\uparrow(E_2^-)n_l f_2^- \tag{F.16a}$$

$$\frac{df_1^+}{dt} \simeq \kappa^\uparrow(E_2^+)n_l f_2^+ - \kappa^\uparrow(E_1^+)n_l f_1^+ \tag{F.16b}$$

The behavior of the cross-sections away from any physical threshold is smooth, and we can therefore use:

$$\kappa^\uparrow(E_n^+) \simeq \kappa^\uparrow(E_n^-) \equiv \kappa^\uparrow(E_n) \quad \text{for} \quad n \geqslant 2$$
$$\kappa^\downarrow(E_n^+) \simeq \kappa^\downarrow(E_n^-) \equiv \kappa^\downarrow(E_n) \quad \text{for} \quad n \geqslant 1$$

If we also assume that the initial distribution function is smooth, we have $f_2^+ \simeq f_2^-$. Therefore from (F.16), the dynamics for f on either side of the first energy threshold are the same, *except* for the second term on the right-hand-side of (F.16b), which corresponds to the excitation process *at the physical threshold*. If we denote the jump by $[f]_1 = f_1^- - f_1^+$, we have at $t \simeq 0$

$$\frac{d}{dt}[f]_1 \simeq +\kappa^\uparrow(E_1^+)n_l f_1^+ \tag{F.17}$$

and the value of the jump is increasing. To find out how much, we need to look at the strength of this rate. The behavior of the excitation cross-section near threshold is usually expressed by the first term of a Taylor series, i.e.:

$$\sigma_{lu}^\uparrow(\Delta E_{lu}+\varepsilon) \simeq \mathcal{C}\,\varepsilon \qquad \text{with } \mathcal{C} = \left.\frac{d\sigma^\uparrow}{dE}\right|_{E=\Delta E}$$

Therefore, $\kappa^\uparrow(E_1^+) \approx \mathcal{C}v_1\varepsilon$. Assuming the cross-section increases approximately linearly until a maximum value $\sigma_{\max}^\uparrow$, the discontinuity at $E = E_1$ is therefore contained within a boundary layer of approximate width $\delta E \leqslant \sigma_{\max}^\uparrow/\mathcal{C}$. If the average distance in energy of sampled particles, or the spacing of an energy grid is large enough, this layer will be under-resolved and an apparent discontinuity will appear in the solution and can remain, since stationary solutions with periodic discontinuities are allowed, according to the analysis above.

Modeling of inelastic collisions in a multifluid plasma: Ionization and recombination

Hai P. Le[1,a)] and Jean-Luc Cambier[2,b)]

[1]*Department of Mathematics, University of California, Los Angeles, California 90095, USA*
[2]*Air Force Research Laboratory, Edwards AFB, California 93524, USA*

A model for ionization and recombination collisions in a multifluid plasma is formulated using the framework introduced in previous work [H. P. Le and J.-L. Cambier, Phys. Plasmas **22**, 093512 (2015)]. The exchange source terms for density, momentum, and energy are detailed for the case of electron induced ionization and three body recombination collisions with isotropic scattering. The principle of detailed balance is enforced at the microscopic level. We describe how to incorporate the standard collisional-radiative model into the multifluid equations using the current formulation. Numerical solutions of the collisional-radiative rate equations for atomic hydrogen are presented to highlight the impact of the multifluid effect on the kinetics. *Published by AIP Publishing.*
[http://dx.doi.org/10.1063/1.4953050]

I. INTRODUCTION

The ability to accurately model plasmas in non-local thermodynamic equilibrium (non-LTE) is essential in understanding complex phenomena associated with atomic population kinetics, thermal equilibration, and radiation transport.[1] Collisional-radiative (CR) models are the most common numerical tool used in simulating non-LTE plasmas; these models are adapted to a wide range of applications ranging from low temperature plasmas to high energy density physics. There have been continuous improvements from theoretical calculations of atomic data and cross sections,[2–6] to computational models of time-accurate collisional-radiative kinetics for different plasma regimes.[7–10] Detailed CR models, however, are very computationally intensive due to the enormous amount of atomic data and elementary cross sections involved in the simulation. Therefore, these models are traditionally applicable to problems with low dimensionality or used as a post-processing tool for diagnostics. Recently, multi-dimensional hydrodynamic calculations with CR kinetics have become feasible for moderate size kinetic systems, thanks to the recent advances in high performance computing.[11,12] In addition, many coarse-graining techniques have been developed to further reduce the computational cost associated with modeling the CR kinetics.[13–15]

An important issue that must be addressed carefully in the CR modeling process is the treatment of non-thermal populations, e.g., hot electrons from laser produced plasmas or electrons emitted from cathode in a discharge system. A proper treatment of these systems requires solving the kinetic equation for the translational degree of freedom of the particles. The two most common approaches for these types of problem are the "two-term" approximation[16] and Monte

Carlo collision method.[17] These methods however are quite expensive for detailed CR modeling with many atomic states. In previous work,[18] we propose an alternative approach, which is to use the classical multifluid approximation,[19,20] in which non-thermal populations can be treated as separated fluids with their mean velocities and temperatures. The focus of this work is to extend the applicability of the CR models to the multifluid regime. Due to the assumption of individual Maxwellian velocity distribution functions (VDF), the relative drift velocity between two different fluids, if significant, can impact the kinetics of the collisions. Our previous work focuses on the modeling of excitation/deexcitation collisions using the multifluid description.[18] The significance of the relative drift velocity on the kinetics, hereby referred to as the multifluid effect, is characterized by a nondimensional parameter λ, which is defined as the ratio of the kinetic versus thermal energies computed using the reduced mass and relative (hydrodynamic) velocities of the two colliding particles. We note that this effect had also been examined by different authors.[18,20–25] In 1969, Burgers presented a framework for deriving exchange source terms for a system of moment equations.[20] Although most of his results are for a five-moment system, the framework is rather generic and can be readily applied to other moment systems. Horwitz and Banks derived the momentum and energy exchange rates for charge exchange collisions including the multifluid effect.[21] In their model, deviation from single-fluid results is characterized by a parameter δ, which is essentially the square root of the parameter λ defined in our work. Conde *et al.* studied the friction forces due to Coulomb collision for drifting ions in a partially ionized plasma.[25] Barakat and Schunk[22] derived momentum and energy exchange rates for elastic collisions using various forms of elastic cross sections, e.g., inverse-power interaction, hard sphere, and Maxwell molecules. Anisotropic effects are also considered in their work. We remark that all the work described above do not include inelastic and/or reactive collisions. These collisions are briefly considered in

a)Author to whom correspondence should be addressed. Electronic mail: hai.le@ucla.edu
b)Present address: Air Force Office of Scientific Research, Arlington, Virginia 22203, USA. Electronic mail: jean_luc.cambier@us.af.mil.

Burgers using a simple Bhatnagar-Gross-Krook (BGK) operator.[20] A more general model for a reactive collision can be found from the work of Benilov,[23,24] where the derivation is based on consideration of a general two-body collision of the form $\alpha + \beta \Longleftrightarrow \gamma + \delta$. Due to the general description of the collision, the exchange source terms are quite complicated making numerical implementation very challenging.

This paper presents a continuation of our previous work[18] to the case of ionization and three-body recombination collisions. The modeling of these collisions is more complicated than excitation/deexcitation collisions because they involve more than two particles. Using the multifluid approximation, each participating particle (electron, neutral, and ion) can be characterized as a fluid with its own set of conservation laws. In the most general case, one can have four different fluids associated with the scattered particle s, the target particle t, its ionized state i, and the free electron e. Fortunately, as will be shown, simplifications can be made for the special case of electron induced ionization and recombination, which is of particular interest for most applications. The derivation presented in this work follows naturally from our previous work. Some slight modifications are introduced to avoid complication in mathematical notations.

The rest of the paper is organized as follows. Sec. II describes the kinematics of the collision. The exchange rates for ionization and recombination collisions are considered in Secs. III and IV, respectively. For ionization collisions, we first formulate the exchange terms for the general case and then perform a systematic reduction to obtain a set of rate equations applicable for the case of electron induced collisions. For recombination collisions, we consider only the case of electron induced recombination using the same reduction technique. Utilizing these rates, we describe in Sec. V how to construct a CR model within the multifluid equations. In Sec. VI, we show the numerical evaluation of the rates and present zero dimensional calculations to demonstrate the impact of the multifluid effect. Finally, a summary is given in Sec. VII. Several appendixes are also provided to elaborate on the derivation of the exchange rates.

II. KINEMATICS

Let us consider an inelastic collision between two particles s (scattered) and t (target), the result of which leads to an ionization of t into its ionized stage i and creation of a new electron e. The reverse process is a three body recombination collision which involves three particles s, i, and e. Both of these processes can be represented by the following reaction:

$$s(\mathbf{v}_{s_0}) + t(\mathbf{v}_{t_0}) \Longleftrightarrow s(\mathbf{v}_{s_1}) + e(\mathbf{v}_{e_2}) + i(\mathbf{v}_{i_2}). \quad (1)$$

In the case of an ionization collision, the subscript 0 denotes pre-collision variables and both subscripts 1 and 2 denote post-collision variables. For recombination, we have the reverse order where the subscripts 1 and 2 denote pre-collision and 0 denotes post-collision. These notations are slightly different than the one used in excitation/deexcitation,[18] but they will prove convenient later in defining the

rate coefficients. The species names s, t, i, e also indicate the *fluid* to which the particles belong; hence in the general case, we have four different fluids. For $s \equiv e$, we have an electron induced ionization/recombination. Conservations of mass, momentum, and energy are expressed as

$$m_t = m_i + m_e, \quad (2a)$$

$$m_s\mathbf{v}_{s_0} + m_t\mathbf{v}_{t_0} = m_s\mathbf{v}_{s_1} + m_e\mathbf{v}_{e_2} + m_i\mathbf{v}_{i_2}, \quad (2b)$$

$$\frac{1}{2}m_s\mathbf{v}_{s_0}^2 + \frac{1}{2}m_t\mathbf{v}_{t_0}^2 = \frac{1}{2}m_s\mathbf{v}_{s_1}^2 + \frac{1}{2}m_e\mathbf{v}_{e_2}^2 + \frac{1}{2}m_i\mathbf{v}_{i_2}^2 + \varepsilon^*, \quad (2c)$$

where ε^* is the ionization energy of the target particle. Let us define the following center-of-mass (COM) and relative velocities for the particles both in the left and right hand side of (1)

$$\begin{bmatrix} \mathbf{V}_0 \\ \mathbf{g}_0 \end{bmatrix} = \begin{bmatrix} \dfrac{m_s}{M} & \dfrac{m_t}{M} \\ 1 & -1 \end{bmatrix} \cdot \begin{bmatrix} \mathbf{v}_{s_0} \\ \mathbf{v}_{t_0} \end{bmatrix};$$

$$\begin{bmatrix} \mathbf{V}_1 \\ \mathbf{g}_1 \\ \mathbf{g}_2 \end{bmatrix} = \begin{bmatrix} \dfrac{m_s}{M} & \dfrac{m_e}{M} & \dfrac{m_i}{M} \\ 1 & -\dfrac{m_e}{m_t} & -\dfrac{m_i}{m_t} \\ 0 & 1 & -1 \end{bmatrix} \cdot \begin{bmatrix} \mathbf{v}_{s_1} \\ \mathbf{v}_{e_2} \\ \mathbf{v}_{i_2} \end{bmatrix}, \quad (3)$$

where $M = m_s + m_t = m_s + m_e + m_i$. One can easily verify that both the transformations are unitary, i.e., $d\mathbf{V}_0 d\mathbf{g}_0 \equiv d\mathbf{v}_{s_0} d\mathbf{v}_{t_0}$ and $d\mathbf{V}_1 d\mathbf{g}_1 d\mathbf{g}_2 \equiv d\mathbf{v}_{s_1} d\mathbf{v}_{e_2} d\mathbf{v}_{i_2}$. The inverse transformation can be easily found from (3), leading to

$$\begin{bmatrix} \mathbf{v}_{s_0} \\ \mathbf{v}_{t_0} \end{bmatrix} = \begin{bmatrix} 1 & \dfrac{m_t}{M} \\ 1 & -\dfrac{m_s}{M} \end{bmatrix} \cdot \begin{bmatrix} \mathbf{V}_0 \\ \mathbf{g}_0 \end{bmatrix};$$

$$\begin{bmatrix} \mathbf{v}_{s_1} \\ \mathbf{v}_{e_2} \\ \mathbf{v}_{i_2} \end{bmatrix} = \begin{bmatrix} 1 & \dfrac{m_t}{M} & 0 \\ 1 & -\dfrac{m_s}{M} & \dfrac{m_i}{m_t} \\ 1 & -\dfrac{m_s}{M} & -\dfrac{m_e}{m_t} \end{bmatrix} \cdot \begin{bmatrix} \mathbf{V}_1 \\ \mathbf{g}_1 \\ \mathbf{g}_2 \end{bmatrix}. \quad (4)$$

We can apply the same transformation to the bulk hydrodynamic velocities

$$\begin{bmatrix} \mathbf{U}_0 \\ \mathbf{w}_0 \end{bmatrix} = \begin{bmatrix} \dfrac{m_s}{M} & \dfrac{m_t}{M} \\ 1 & -1 \end{bmatrix} \cdot \begin{bmatrix} \mathbf{u}_s \\ \mathbf{u}_t \end{bmatrix};$$

$$\begin{bmatrix} \mathbf{U}_1 \\ \mathbf{w}_1 \\ \mathbf{w}_2 \end{bmatrix} = \begin{bmatrix} \dfrac{m_s}{M} & \dfrac{m_e}{M} & \dfrac{m_i}{M} \\ 1 & -\dfrac{m_e}{m_t} & -\dfrac{m_i}{m_t} \\ 0 & 1 & -1 \end{bmatrix} \cdot \begin{bmatrix} \mathbf{u}_s \\ \mathbf{u}_e \\ \mathbf{u}_i \end{bmatrix}. \quad (5)$$

Using the COM and relative velocity variables defined in Eq. (3), conservations of momentum and energy can be expressed as

$$M\mathbf{V}_0 = M\mathbf{V}_1, \quad (6a)$$

$$\frac{1}{2}\mu\mathbf{g}_0^2 = \frac{1}{2}\mu\mathbf{g}_1^2 + \frac{1}{2}\mu_t\mathbf{g}_2^2 + \varepsilon^*, \quad (6b)$$

where $\mu = \frac{m_s m_t}{m_s + m_t}$ and $\mu_t = \frac{m_e m_i}{m_e + m_i}$. Note that conservation of momentum implies that the COM velocity is essentially unchanged after the collision; so for simplicity, we can take $\mathbf{V} \equiv \mathbf{V}_0 = \mathbf{V}_1$. Furthermore, let us define Υ to be the energy transferred during the collision

$$\Upsilon = \frac{1}{2}\mu \mathbf{g}_0^2 - \frac{1}{2}\mu \mathbf{g}_1^2 = \frac{1}{2}\mu_t \mathbf{g}_2^2 + \varepsilon^*. \qquad (7)$$

The last expression is obtained from energy conservation. For the case of ionization/recombination, $\Upsilon \in [\varepsilon^*, \varepsilon]$, where $\varepsilon = \frac{1}{2}\mu \mathbf{g}_0^2$ is the available kinetic energy in the COM reference frame.

III. IONIZATION

A. Transfer integral

Let us now look at an ionization collision which can be decomposed into a two-step process

$$s(\mathbf{v}_{s_0}) + t(\mathbf{v}_{t_0}) \Rightarrow s(\mathbf{v}_{s_1}) + t^*(\mathbf{v}_{t_1}), \qquad (8a)$$

$$t^*(\mathbf{v}_{t_1}) \Rightarrow e(\mathbf{v}_{e_2}) + i(\mathbf{v}_{i_2}), \qquad (8b)$$

where the first step is the formation of a *virtual* excited state t^* via scattering and the second step is a spontaneous ionization of t^*. The decomposition of (8) is used only for the convenience in expressing the exchange variables. We can write a transfer integral expressing the rate of change of any moment variable ψ as follows:

$$\Psi_{st}^{ion} = n_s n_t \int d^3\mathbf{v}_{s_0} d^3\mathbf{v}_{t_0} f_s f_t \, g_0 \int \psi$$
$$\times \, \omega_{st}^{ion}(\mathbf{v}_{s_0}, \mathbf{v}_{t_0}; \mathbf{v}_{s_1}, \mathbf{v}_{e_2}, \mathbf{v}_{i_2}) \, d^3\mathbf{v}_{s_1} d^3\mathbf{v}_{e_2} d^3\mathbf{v}_{i_2}, \qquad (9)$$

where $g_0 = |\mathbf{g}_0|$ and $\omega_{st}^{ion}(\mathbf{v}_{s_0}, \mathbf{v}_{t_0}; \mathbf{v}_{s_1}, \mathbf{v}_{e_2}, \mathbf{v}_{i_2})$ is the ionization differential cross section (DCS). Note that Ψ_{st}^{ion} includes a product of two Maxwellian VDF's f_s and f_t. Utilizing the same procedure described in Appendix B of Le and Cambier[18] for excitation/deexcitation, Ψ_{st}^{ion} can be written in the following form:

$$\Psi_{st}^{ion} = n_s n_t \underbrace{\frac{1}{\pi^{\frac{3}{2}}a^3} \int d^3\mathbf{V}^* e^{-\mathbf{V}^{*2}/a^2}}_{\int d^3\mathbf{V}^* f_{V^*}} \cdot \frac{1}{\pi^{\frac{3}{2}}\alpha^3} \int d^3\mathbf{g}_0 \, e^{-\tilde{\mathbf{g}}_0^2/\alpha^2} g_0$$
$$\times \int \psi \omega_{st}^{ion}(\mathbf{g}_0; \mathbf{g}_1, \mathbf{g}_2) \, d^3\mathbf{g}_1 d^3\mathbf{g}_2, \qquad (10)$$

where $\omega_{st}^{ion}(\mathbf{g}_0; \mathbf{g}_1, \mathbf{g}_2)$ is the DCS expressed in terms of relative velocities. The average quantities used in the transformation are summarized in Table I. Note that these variables are defined only for ionization. For recombination, we have a different set of average variables. Table I also shows the approximation of these average variables for the case of an electron induced ionization by making use of the small mass ratio $m_e/M \ll 1$, and further assuming that $\frac{m_e}{M} \ll \frac{T_e}{T_t}$. The latter assumption is almost always true for most of the practical cases, especially for electron induced collisions with heavy atoms. For brevity, the Boltzmann constant is omitted throughout the text.

TABLE I. Summary of variables used for ionization. The second column lists the general definition, and the third one is applicable for an electron induced ionization.

Variable	Definition	e-induced coll. ($s \equiv e$)
T^*	$\dfrac{M T_s T_t}{m_s T_t + m_t T_s}$	T_t
$\tilde{T}$	$\dfrac{m_s T_t + m_t T_s}{M}$	T_e
a	$\sqrt{\dfrac{2T^*}{M}}$	$\sqrt{\dfrac{2T_t}{m_t}}$
α	$\sqrt{\dfrac{2\tilde{T}}{\mu}}$	$\sqrt{\dfrac{2T_e}{m_e}}$
γ	$\dfrac{\mu}{M}\dfrac{T_t - T_s}{\tilde{T}}$	$\dfrac{m_e}{M}\dfrac{T_t - T_e}{T_e}$
$\tilde{\mathbf{g}}_0$	$\mathbf{g}_0 - \mathbf{w}_0$	
$\mathbf{V}^*$	$\mathbf{V} - \mathbf{U}_0 + \gamma\tilde{\mathbf{g}}_0$	

The DCS can be written as a triply differential cross section (TDCS)

$$\omega_{st}^{ion}(\mathbf{g}_0; \mathbf{g}_1, \mathbf{g}_2) \, d^3\mathbf{g}_1 \, d^3\mathbf{g}_2$$
$$= \frac{d^3\sigma_{st}^{ion}}{d\Upsilon d\Omega_1 d\Omega_2}(g_0, \Upsilon, \Omega_1, \Omega_2) \, d\Upsilon \, d\Omega_1 \, d\Omega_2, \qquad (11)$$

where Ω_1 and Ω_2 are the solid angles of $\mathbf{g}_1$ and $\mathbf{g}_2$. Also, we can define a singly differential cross section (SDCS) as

$$\frac{d\sigma_{st}^{ion}}{d\Upsilon}(g_0, \Upsilon) = \int \frac{d^3\sigma_{st}^{ion}}{d\Upsilon d\Omega_1 d\Omega_2} \, d\Omega_1 \, d\Omega_2. \qquad (12)$$

This can be used as a normalization factor to extract the strictly angular-dependent part of the TDCS, from $\mathcal{G}^{ion} = \frac{d^3\sigma_{st}^{ion}}{d\Upsilon d\Omega_1 d\Omega_2} / \frac{d\sigma_{st}^{ion}}{d\Upsilon}$ with the normalization $\int \mathcal{G}^{ion} d\Omega_1 d\Omega_2 = 1$. The total ionization cross section can be easily obtained from $\bar{\sigma}_{st}^{ion} = \int \frac{d\sigma_{st}^{ion}}{d\Upsilon}(g_0, \Upsilon) d\Upsilon$. It must be noted that all the cross sections have a threshold being the ionization energy of particle t.

Since we are concerned here with the exchanges of density, momentum, and energy, the moment variable ψ (scalar or vector) can always be expanded in terms of powers of $\mathbf{V}^*$

$$\psi = a + b\mathbf{V}^* + c\mathbf{V}^{*2} + \cdots \qquad (13)$$

and the expansion is at most quadratic in $\mathbf{V}^*$ since we are only considering the exchanges of mass, momentum, and energy. Using the fact that f_{V^*} is a Maxwellian, the integration over $\mathbf{V}^*$ can be easily performed

$$\int d^3\mathbf{V}^* f_{V^*} = 1; \quad \int d^3\mathbf{V}^* \, \mathbf{V}^* f_{V^*} = 0;$$
$$\int d^3\mathbf{V}^* \, \mathbf{V}^{*2} f_{V^*} = \frac{3}{M}T^*. \qquad (14)$$

Therefore, all the terms involving $\mathbf{V}^*$ can be easily evaluated (or eliminated), leaving us with the terms independent of $\mathbf{V}^*$. To evaluate those terms, we consider the following form of the transfer integral:

$$\Psi_{st}^{ion} = n_s n_t \frac{1}{\pi^{\frac{3}{2}}\alpha^3} e^{-w_0^2/\alpha^2} \int d^3\mathbf{g}_0 \, e^{-g_0^2/\alpha^2} e^{2\mathbf{g}_0 \cdot \mathbf{w}_0/\alpha^2} g_0$$

$$\times \int \psi \frac{d^3\sigma_{st}^{ion}}{d\Upsilon d\Omega_1 d\Omega_2} \, d\Upsilon \, d\Omega_1 \, d\Omega_2. \tag{15}$$

Without loss of generality, let us choose a coordinated system (x, y, z) such that $\mathbf{w}_0$ is aligned with the $\hat{\mathbf{z}}$ axis. The relative velocities $\mathbf{g}_0$, $\mathbf{g}_1$, and $\mathbf{g}_2$ can be obtained by the following rotations:

$$\hat{\mathbf{g}}_0 = R(\varphi, \theta) \cdot \hat{\mathbf{w}}_0; \quad \hat{\mathbf{g}}_1 = R(\phi_1, \chi_1) \cdot \hat{\mathbf{g}}_0;$$
$$\hat{\mathbf{g}}_2 = R(\phi_2, \chi_2) \cdot \hat{\mathbf{g}}_0, \tag{16}$$

where the rotation matrix is defined as follows:

$$R(\varphi, \theta) = \begin{pmatrix} c_\varphi c_\theta & -s_\varphi & c_\varphi s_\theta \\ s_\varphi c_\theta & c_\varphi & s_\varphi s_\theta \\ -s_\theta & 0 & c_\theta \end{pmatrix}. \tag{17}$$

Using $d^3\mathbf{g}_0 = g_0^2 dg_0 d\varphi dc_\theta$, where $c_\theta \equiv \cos\theta$, the transfer integral now becomes

$$\Psi_{st}^{ion} = n_s n_t \frac{1}{\pi^{\frac{3}{2}}\alpha^3} e^{-w_0^2/\alpha^2} \int dg_0 \, e^{-g_0^2/\alpha^2} g_0^3 \cdot \int d\varphi dc_\theta e^{2g_0 w_0 c_\theta/\alpha^2}$$

$$\times \int \psi \frac{d^3\sigma_{st}^{ion}}{d\Upsilon d\Omega_1 d\Omega_2} \, d\Upsilon \, d\Omega_1 \, d\Omega_2, \tag{18}$$

where $d\Omega_1 = d\phi_1 dc_{\chi_1}$ and $d\Omega_2 = d\phi_2 dc_{\chi_2}$. Let us define an averaging operator as follows:

$$\langle \psi \rangle_{\Omega_1, \Omega_2} = \int \psi \, \mathcal{G}^{ion} \, d\Omega_1 \, d\Omega_2. \tag{19}$$

Integration over φ yields

$$\Psi_{st}^{ion} = n_s n_t \frac{4\pi}{\pi^{\frac{3}{2}}\alpha^3} e^{-w_0^2/\alpha^2} \int dg_0 \, e^{-g_0^2/\alpha^2} g_0^3 \cdot \frac{1}{2}\int_{-1}^{1} dc_\theta \, e^{2g_0 w_0 c_\theta}$$

$$\times \int \langle\psi\rangle_{\Omega_1,\Omega_2} \frac{d\sigma_{st}^{ion}}{d\Upsilon}(g_0, \Upsilon) d\Upsilon. \tag{20}$$

We can now define the following normalized energy variables:

$$x_0 = \frac{\varepsilon_0}{\tilde{T}} = \frac{\frac{1}{2}\mu g_0^2}{\tilde{T}} \quad x_1 = \frac{\varepsilon_1}{\tilde{T}} = \frac{\frac{1}{2}\mu g_1^2}{\tilde{T}} \quad x_2 = \frac{\varepsilon_2}{\tilde{T}} = \frac{\frac{1}{2}\mu_t g_2^2}{\tilde{T}},$$

$$x^* = \frac{\varepsilon^*}{\tilde{T}} \quad \upsilon = \frac{\Upsilon}{\tilde{T}} \quad \lambda = \frac{\frac{1}{2}\mu w_0^2}{\tilde{T}}. \tag{21}$$

Using the variables above, we obtain

$$\Psi_{st}^{ion} = n_s n_t \bar{g}_{\tilde{T}} e^{-\lambda} \int_{x^*}^{\infty} dx_0 \, e^{-x_0} x_0 \cdot \frac{1}{2}\int_{-1}^{1} dc_\theta \, e^{2\sqrt{\lambda x_0}c_\theta}$$

$$\times \int_{x^*}^{x_0} \langle\psi\rangle_{\Omega_1,\Omega_2} \frac{d\sigma_{st}^{ion}}{d\upsilon}(x_0, \upsilon) d\upsilon, \tag{22}$$

where $\bar{g}_{\tilde{T}} = \sqrt{\frac{8\tilde{T}}{\pi\mu}}$. The exchange rates for moment variables can now be constructed starting from (20) or (22).

B. Zeroth-order moment: Number density

The rate of change of number density due to an ionization collision can be computed by substituting $\psi = 1$ in (22). We arrive at the following:

$$\Gamma^{ion} = n_s n_t \bar{g}_{\tilde{T}} e^{-\lambda} \int_{x^*}^{\infty} dx_0 \, x_0 \, e^{-x_0} \zeta^{(0)}(\sqrt{\lambda x_0})\bar{\sigma}_{st}^{ion}, \tag{23}$$

where $\zeta^{(0)}(\xi) = \frac{\sinh(2\xi)}{2\xi}$ as defined for the case of excitation/deexcitation.[18] Note that Γ^{ion} has a very similar form to the case of excitation/deexcitation. In the limit $\lambda \to 0$, using $\lim_{\xi \to 0}\zeta^{(0)}(\xi) = 1$, we recover the well-known expression for single-fluid kinetics

$$\Gamma^{ion} = n_s n_t \bar{g}_{\tilde{T}} \int_{x^*}^{\infty} dx_0 \, x_0 \, e^{-x_0} \, \bar{\sigma}_{st}^{ion}. \tag{24}$$

The rate equations for the number densities can be constructed as follows:

$$\frac{dn_s}{dt} = 0; \quad \frac{dn_t}{dt} = -\Gamma^{ion}; \quad \frac{dn_e}{dt} = +\Gamma^{ion}; \quad \frac{dn_i}{dt} = +\Gamma^{ion}. \tag{25}$$

C. First-order moment: Momentum density

We first note that for first-order moments, ψ can be represented by a linear combination of $\mathbf{V}^*$, $\mathbf{g}_p$ ($p = 0, 1, 2$) and other constant vectors. Since $\Psi_{st}^{ion}|_{\psi=\mathbf{V}^*} = 0$ as mentioned before, we can neglect all the terms involving $\mathbf{V}^*$; the remaining terms can be determined straight forward from the integration. For $\psi = \mathbf{g}_p$, the integration results in a vector parallel to the relative drift velocity $\mathbf{w}_0$. This is expected from the symmetry of the problem and can also be shown directly from the transfer integral. For convenience, let us define the following friction rate coefficients R^{ion} as follows:

$$\Psi_{st}^{ion}|_{\psi=\mu\mathbf{g}_p} = \mu R_p^{ion}\mathbf{w}_0; \quad p = 0, 1, 2. \tag{26}$$

The expressions for these friction coefficients are given in Appendix B. We now consider the rate of change of momentum for each particle.

1. Scattered particle s

The net rate of momentum exchange of the scattered particle s due to an ionization collision can be determined by substituting $\psi = -m_s(\mathbf{v}_{s_0} - \mathbf{v}_{s_1})$ into Eq. (20), which leads to

$$\mathbf{R}_s^{ion} = -\frac{4n_s n_t}{\pi^{\frac{1}{2}}\alpha^3} \cdot \int d^3\mathbf{V}^* f_{V^*} \cdot \int dg_0 \, g_0^3 \, e^{-g_0^2/\alpha^2}$$

$$\times \frac{1}{2}\int_{-1}^{1} dc_\theta \, e^{2g_0 w_0 c_\theta/\alpha^2} \int_{x^*}^{x_0} d\upsilon \frac{d\sigma_{st}^{ion}}{d\upsilon} \langle m_s(\mathbf{v}_{s_0} - \mathbf{v}_{s_1})\rangle_{\Omega_1,\Omega_2}. \tag{27}$$

Using $m_s(\mathbf{v}_{s_0} - \mathbf{v}_{s_1}) = \mu(\mathbf{g}_0 - \mathbf{g}_1)$ and the definitions of the friction coefficients, we can easily express the rate of change of the momentum of fluid s as follows:

$$\mathbf{R}_s^{ion} = -\mu(R_0^{ion} - R_1^{ion})\mathbf{w}_0. \tag{28}$$

The full expression can be obtained from the definitions of the coefficients in (B1)

$$\mathbf{R}_s^{ion} = -\frac{2}{3}\mu\mathbf{w}_0 n_s n_t \bar{g}_{\tilde{T}} e^{-\lambda} \int_{x^*}^{\infty} dx_0 \, x_0^{\frac{3}{2}} \, e^{-x_0} \, \zeta^{(1)}\left(\sqrt{\lambda x_0}\right)$$
$$\times \int_{x^*}^{x_0} dv \frac{d\sigma_{st}^{ion}}{dv}\left[\sqrt{x_0} - \sqrt{x_1}\langle c_{\chi_1}\rangle_{\Omega_1,\Omega_2}\right], \tag{29}$$

where $\zeta^{(1)}(\xi) = \frac{3}{4\xi^2}\left[\cosh(2\xi) - \frac{\sinh(2\xi)}{2\xi}\right]$ and $\lim_{\xi\to 0}\zeta^{(1)}(\xi)$ $= 1$. Note that the above expression is very similar to the ones for excitation/deexcitation collisions (Eq. (38) of Le and Cambier[18]).

2. Target particles t and t*

Let us now look at the rates of momentum loss and gain by t and t^*, respectively, in reaction (8a). Using (4), the pre-collision velocity and momentum of particle t can be expressed as

$$m_t\mathbf{v}_{t_0} = m_t\mathbf{V}^* + m_t\mathbf{U}_0 - \frac{m_t\gamma}{\mu}\mu(\mathbf{g}_0 - \mathbf{w}_0) - \mu\mathbf{g}_0. \tag{30}$$

Similarly, the post-collision momentum of t^* is

$$m_t\mathbf{v}_{t_1} = m_t\mathbf{V}^* + m_t\mathbf{U}_0 - \frac{m_t\gamma}{\mu}\mu(\mathbf{g}_0 - \mathbf{w}_0) - \mu\mathbf{g}_1. \tag{31}$$

Using the coefficients defined in (B1) and the identity $\gamma = \frac{\mu}{M}\frac{T_t - T_s}{T}$, we arrive at the following results:

$$\mathbf{R}_t^{ion} = -m_t\Gamma^{ion}\mathbf{U}_0 - \frac{m_t}{M}\frac{T_t - T_s}{\tilde{T}}\mu(\Gamma^{ion} - R_0^{ion})\mathbf{w}_0 + \mu R_0^{ion}\mathbf{w}_0, \tag{32a}$$

$$\mathbf{R}_{t^*}^{ion} = +m_t\Gamma^{ion}\mathbf{U}_0 + \frac{m_t}{M}\frac{T_t - T_s}{\tilde{T}}\mu(\Gamma^{ion} - R_0^{ion})\mathbf{w}_0 - \mu R_1^{ion}\mathbf{w}_0. \tag{32b}$$

Similar to the previous case, the full expressions can be obtained using the definitions of Γ^{ion} and R_p^{ion}. The first term on the right hand side of (32a) or (32b) represents the friction due to generation/removal of new particle from the ionization process. These terms also appear in the rate of change of momentum for s as $\pm m_s\Gamma^{ion}\mathbf{U}_0$, but the net effect is zero since we assume that particles s before and after the collision belong to the same fluid. The second term describes a thermal friction force since it is proportional to the temperature difference of the reactants. The last term represents the standard friction due to the relative drift of the two fluids s and t. One can easily check that

$$\mathbf{R}_t^{ion} + \mathbf{R}_{t^*}^{ion} + \mathbf{R}_s^{ion} = 0, \tag{33}$$

which is a statement of momentum conservation.

3. Electron and ion

From reaction (8b), the momentum gain of particle t^* is distributed to the ion and ejected electron. Using the following relations:

$$m_e\mathbf{v}_{e_2} = m_e\mathbf{v}_{t_1} + \mu_t\mathbf{g}_2, \tag{34a}$$

$$m_i\mathbf{v}_{i_2} = m_i\mathbf{v}_{t_1} - \mu_t\mathbf{g}_2, \tag{34b}$$

the rates of momentum exchange for the ion and ejected electron can be expressed as

$$\mathbf{R}_e^{ion} = m_e\Gamma^{ion}\mathbf{U}_0 + \frac{m_e}{M}\frac{T_t - T_s}{\tilde{T}}\mu(\Gamma^{ion} - R_0^{ion})\mathbf{w}_0$$
$$- \frac{m_e}{m_t}\mu R_1^{ion}\mathbf{w}_0 + \mu_t R_2^{ion}\mathbf{w}_0, \tag{35a}$$

$$\mathbf{R}_i^{ion} = m_i\Gamma^{ion}\mathbf{U}_0 + \frac{m_i}{M}\frac{T_t - T_s}{\tilde{T}}\mu(\Gamma^{ion} - R_0^{ion})\mathbf{w}_0$$
$$- \frac{m_i}{m_t}\mu R_1^{ion}\mathbf{w}_0 - \mu_t R_2^{ion}\mathbf{w}_0. \tag{35b}$$

The above equations have the same structure as Eq. (32) but with an additional term reflecting the three-body nature of the ionization/recombination processes. Again, one can easily check that momentum conservation is satisfied

$$\mathbf{R}_s^{ion} + \mathbf{R}_t^{ion} + \mathbf{R}_e^{ion} + \mathbf{R}_i^{ion} = 0. \tag{36}$$

D. Second-order moment: Total energy density

For the second-order moment (here we only consider scalar quantities), the exchange variables ψ can be expressed as scalar products of $\mathbf{V}^*$, $\mathbf{g}_p$ and other constant velocities. We note that since $\int d^3\mathbf{V}^*\,\mathbf{V}^* f_{V^*} = 0$, all the dot products linear in $\mathbf{V}^*$ vanish after the integration. For convenience, let us now define a set of energy transfer coefficients as follows:

$$\Psi_{st}^{ion}|_{\psi=\mathbf{g}_p\cdot\mathbf{g}_q} = J_{pq}^{ion}\alpha^2; \quad p,q = 0,1,2. \tag{37}$$

The explicit expressions for these coefficients are given in Appendix B. Note that we also have

$$\Psi_{st}^{ion}|_{\psi=\mathbf{g}_p\cdot\mathbf{U}_0} = R_p^{ion}\mathbf{w}_0\cdot\mathbf{U}_0, \tag{38a}$$

$$\Psi_{st}^{ion}|_{\psi=\mathbf{g}_p\cdot\mathbf{w}_0} = R_p^{ion}\mathbf{w}_0^2 = \lambda R_p^{ion}\alpha^2, \tag{38b}$$

$$\Psi_{st}^{ion}|_{\psi=\mathbf{w}_0\cdot\mathbf{U}_0} = \Gamma^{ion}\mathbf{w}_0\cdot\mathbf{U}_0. \tag{38c}$$

1. Scattered particle s

The rate of change of energy of particle s can be determined from the transfer integral (20) by substituting $\psi = \frac{1}{2}m_s(\mathbf{v}_{s_0}^2 - \mathbf{v}_{s_1}^2)$

$$Q_s^{ion} = -\frac{4n_s n_t}{\pi^{\frac{1}{2}}\alpha^3}\cdot\int d^3\mathbf{V}^* f_{V^*}\cdot\int dg_0\,g_0^3\,e^{-g_0^2/\alpha^2}$$
$$\times \frac{1}{2}\int_{-1}^{1} dc_\theta\,e^{2g_0w_0c_\theta/\alpha^2}\int dv\frac{d\sigma_{st}^{ion}}{dv}\left\langle\frac{1}{2}m_s\left(\mathbf{v}_{s_0}^2 - \mathbf{v}_{s_1}^2\right)\right\rangle_{\Omega_1,\Omega_2}. \tag{39}$$

The change in the kinetic energy of s can be re-expressed as follows:

$$\frac{1}{2}m_s\left(\mathbf{v}_{s_1}^2 - \mathbf{v}_{s_0}^2\right) = \mu(\mathbf{g}_1 - \mathbf{g}_0)\cdot\mathbf{V} + \frac{m_t}{M}\frac{\mu}{2}\left(\mathbf{g}_1^2 - \mathbf{g}_0^2\right),$$
$$= \mu(\mathbf{g}_1 - \mathbf{g}_0)\cdot\mathbf{V}^* + \mu(\mathbf{g}_1 - \mathbf{g}_0)\cdot\mathbf{U}_0$$
$$+ \gamma\mu(\mathbf{g}_0 - \mathbf{g}_1)\cdot\tilde{\mathbf{g}}_0 - \frac{m_t}{M}\Upsilon. \quad (40)$$

The integration of the first term is zero since it is linear in $\mathbf{V}^*$. The integration of the second term simply yields $\mathbf{R}_s^{ion}\cdot\mathbf{U}_0$. The product in third term can be easily expanded, and the energy transfer rates defined in Appendix B can be readily used. For the last term, the integration can be carried out using the relation $\Upsilon = \frac{1}{2}\mu\mathbf{g}_0^2 - \frac{1}{2}\mu\mathbf{g}_1^2$. The total rate of change becomes

$$Q_s^{ion} = \mathbf{R}_s^{ion}\cdot\mathbf{U}_0 + \frac{2\mu}{M}(T_t - T_s)\left[\left(J_{00}^{ion} - J_{01}^{ion}\right)\right.$$
$$\left. - \lambda\left(R_0^{ion} - R_1^{ion}\right)\right] - \frac{m_t}{M}\tilde{T}\left(J_{00}^{ion} - J_{11}^{ion}\right). \quad (41)$$

This expression is also similar to the one derived for the case of excitation/deexcitation albeit a less compact form (Eq. (55) of Le and Cambier[18]).

2. Target particles t and t*

The rate of change of the total energies of t and t^* can be determined in a similar fashion. Using (4), the kinetic energy of t can be written as

$$\frac{1}{2}m_t\mathbf{v}_{t_0}^2 = \frac{m_t}{M}\left(\frac{1}{2}M\mathbf{V}^{*2} + \frac{1}{2}M\mathbf{U}_0^2\right) + \frac{m_t\gamma^2}{\mu}\frac{1}{2}\mu\tilde{\mathbf{g}}_0^2 + \frac{m_s}{M}\frac{1}{2}\mu\mathbf{g}_0^2$$
$$- \frac{m_t}{\mu}\gamma\mu\tilde{\mathbf{g}}_0\cdot\mathbf{U}_0 - \mu\mathbf{g}_0\cdot\mathbf{U}_0 + \gamma\mu\tilde{\mathbf{g}}_0\cdot\mathbf{g}_0 + \mathbf{V}^*\cdot[\cdots], \quad (42)$$

where we did not explicitly write the terms linear in $\mathbf{V}^*$. Substituting the above expression into the transfer integral, we arrive at the following:

$$Q_t^{ion} = -\frac{m_t}{M}\Gamma^{ion}\mathcal{E}^* - \frac{m_t\mu}{M^2}\frac{(T_t - T_s)^2}{\tilde{T}}\left(J_{00}^{ion} - 2\lambda R_0^{ion} + \lambda\Gamma^{ion}\right)$$
$$- \frac{m_s}{M}\tilde{T}J_{00}^{ion} + \frac{m_t}{M}\frac{(T_t - T_s)}{\tilde{T}}\mu\left(R_0^{ion} - \Gamma^{ion}\right)\mathbf{w}_0\cdot\mathbf{U}_0$$
$$+ \mu R_0^{ion}\mathbf{w}_0\cdot\mathbf{U}_0 - \frac{2\mu}{M}(T_t - T_s)\left(J_{00}^{ion} - \lambda R_0^{ion}\right), \quad (43)$$

where $\mathcal{E}^* = \frac{1}{2}M\mathbf{U}_0^2 + \frac{3}{2}T^*$ is the total (kinetic + thermal) energies of the COM frame. Note that there are some terms proportional to $(T_t - T_s)^2$; these terms also appear in a general two-body reaction when considering reactants and products as separate fluids (see, for example, Benilov[23]). Similarly, for t^*, using

$$\frac{1}{2}m_t\mathbf{v}_{t_1}^2 = \frac{m_t}{M}\left(\frac{1}{2}M\mathbf{V}^{*2} + \frac{1}{2}M\mathbf{U}_0^2\right) + \frac{m_t\gamma^2}{\mu}\frac{1}{2}\mu\tilde{\mathbf{g}}_0^2 + \frac{m_s}{M}\frac{1}{2}\mu\mathbf{g}_1^2$$
$$- \frac{m_t}{\mu}\gamma\mu\tilde{\mathbf{g}}_0\cdot\mathbf{U}_0 - \mu\mathbf{g}_1\cdot\mathbf{U}_0 + \gamma\mu\tilde{\mathbf{g}}_0\cdot\mathbf{g}_1 + \mathbf{V}^*\cdot[\cdots] \quad (44)$$

we arrive at an equivalent expression for the rate of change of total energy of t^*

$$Q_{t^*}^{ion} = \frac{m_t}{M}\Gamma^{ion}\mathcal{E}^* + \frac{m_t\mu}{M^2}\frac{(T_t - T_s)^2}{\tilde{T}}\left(J_{00}^{ion} - 2\lambda R_0^{ion} + \lambda\Gamma^{ion}\right)$$
$$+ \frac{m_s}{M}\tilde{T}J_{11}^{ion} - \frac{m_t}{M}\frac{(T_t - T_s)}{\tilde{T}}\mu\left(R_0^{ion} - \Gamma^{ion}\right)\mathbf{w}_0\cdot\mathbf{U}_0$$
$$- \mu R_1^{ion}\mathbf{w}_0\cdot\mathbf{U}_0 + \frac{2\mu}{M}(T_t - T_s)\left(J_{01}^{ion} - \lambda R_1^{ion}\right). \quad (45)$$

In the second reaction, this energy is distributed between the ion and the ejected electron.

3. Electron and ion

Using the transformation in Appendix A, the kinetic energies of the ion and electron can be expressed as

$$\mathbf{v}_{e_2}^2 = \mathbf{v}_{t_1}^2 + 2\frac{m_i}{m_t}\mathbf{v}_{t_1}\cdot\mathbf{g}_2 + \frac{m_i^2}{m_t^2}\mathbf{g}_2^2,$$

$$\mathbf{v}_{i_2}^2 = \mathbf{v}_{t_1}^2 - 2\frac{m_e}{m_t}\mathbf{v}_{t_1}\cdot\mathbf{g}_2 + \frac{m_e^2}{m_t^2}\mathbf{g}_2^2.$$

Hence, the kinetic energies are

$$\frac{1}{2}m_e\mathbf{v}_{e_2}^2 = \frac{m_e}{m_t}\frac{1}{2}m_t\mathbf{v}_{t_1}^2 + \mu_t\mathbf{v}_{t_1}\cdot\mathbf{g}_2 + \frac{m_i}{m_t}\frac{1}{2}\mu_t\mathbf{g}_2^2, \quad (46a)$$

$$\frac{1}{2}m_i\mathbf{v}_{i_2}^2 = \frac{m_i}{m_t}\frac{1}{2}m_t\mathbf{v}_{t_1}^2 - \mu_t\mathbf{v}_{t_1}\cdot\mathbf{g}_2 + \frac{m_e}{m_t}\frac{1}{2}\mu_t\mathbf{g}_2^2. \quad (46b)$$

Using the rate coefficient defined in (37) and (38), we obtain

$$Q_e^{ion} = \frac{m_e}{M}\Gamma^{ion}\mathcal{E}^* + \frac{m_e\mu}{M^2}\frac{(T_t - T_s)^2}{\tilde{T}}\left(J_{00}^{ion} - 2\lambda R_0^{ion} + \lambda\Gamma^{ion}\right)$$
$$- \frac{m_e}{M}\frac{(T_t - T_s)}{\tilde{T}}\mu\left(R_0^{ion} - \Gamma^{ion}\right)\mathbf{w}_0\cdot\mathbf{U}_0 + \frac{m_sm_e}{Mm_t}\tilde{T}J_{11}^{ion}$$
$$- \frac{m_e}{m_t}\mu R_1^{ion}\mathbf{w}_0\cdot\mathbf{U}_0 + \frac{2\mu m_e}{Mm_t}(T_t - T_s)\left(J_{01}^{ion} - \lambda R_1^{ion}\right)$$
$$+ \mu_t R_2^{ion}\mathbf{w}_0\cdot\mathbf{U}_0 - \frac{2\mu_t}{M}(T_t - T_s)\left(J_{02}^{ion} - \lambda R_2^{ion}\right)$$
$$- \frac{2m_s\mu_t}{M\mu}\tilde{T}J_{12}^{ion} + \frac{m_i}{m_t}\tilde{T}J_{22}^{ion}, \quad (47a)$$

$$Q_i^{ion} = \frac{m_i}{M}\Gamma^{ion}\mathcal{E}^* + \frac{m_i\mu}{M^2}\frac{(T_t - T_s)^2}{\tilde{T}}\left(J_{00}^{ion} - 2\lambda R_0^{ion} + \lambda\Gamma^{ion}\right)$$
$$- \frac{m_i}{M}\frac{(T_t - T_s)}{\tilde{T}}\mu\left(R_0^{ion} - \Gamma^{ion}\right)\mathbf{w}_0\cdot\mathbf{U}_0 + \frac{m_sm_i}{Mm_t}\tilde{T}J_{11}^{ion}$$
$$- \frac{m_i}{m_t}\mu R_1^{ion}\mathbf{w}_0\cdot\mathbf{U}_0 + \frac{2\mu}{M}\frac{m_i}{m_t}(T_t - T_s)\left(J_{01}^{ion} - \lambda R_1^{ion}\right)$$
$$- \mu_t R_2^{ion}\mathbf{w}_0\cdot\mathbf{U}_0 + \frac{2\mu_t}{M}(T_t - T_s)\left(J_{02}^{ion} - \lambda R_2^{ion}\right)$$
$$+ \frac{2m_s\mu_t}{M\mu}\tilde{T}J_{12}^{ion} + \frac{m_e}{m_t}\tilde{T}J_{22}^{ion}. \quad (47b)$$

It is straight forward to verify that energy conservation is satisfied

$$Q_s^{ion} + Q_t^{ion} + Q_e^{ion} + Q_i^{ion} = \Gamma^{ion}\varepsilon^*. \quad (48)$$

E. Electron induced ionization

$t(\mathbf{v}_{t_0}) + e(\mathbf{v}_{e_0}) \Rightarrow e(\mathbf{v}_{e_1}) + e(\mathbf{v}_{e_2}) + i(\mathbf{v}_{i_2})$

In Sections III B–III D, we derive the exchange terms for a general ionization collision. The resultant equations are rather complicated for practical use. In this section, we perform a systematic reduction of the general system to obtain a set of equations for the special case of an electron induced ionization ($s \equiv e$); this type of collision is relevant for most applications of interest. Taking advantage of the small mass ratio $m_e/M \ll 1$, the following approximations can be used: $\mu \simeq \mu_t \simeq m_e$, $M \simeq m_t \simeq m_i$, and $g_{\bar{T}} \simeq \bar{v}_e = \sqrt{\frac{8T_e}{\pi m_e}}$. All the average variables are summarized in Table I (third column). To further simplify the problem, we also assume that the scattering is isotropic, i.e., $\mathcal{G}^{ion} = 1/16\pi^2$; hence, we have $R_p^{ion} = 0$ for $p > 0$ and $J_{pq}^{ion} = 0$ for $p \neq q$.

The reduction proceeds using the following general procedure. We first note that the rates of change of all the moment variables can always be expressed in terms of quantities in the COM frame. These quantities are then distributed to the particles according to some defined mass ratio. Therefore, we can reduce the system by taking the limit as $m_e/M \rightarrow 0$ and $m_t/M \rightarrow 1$ for each of the contributed term, that is, each particle (electron or heavy particle) will receive full contribution from terms proportional to m_t/M and none from terms proportional to m_e/M. For example, during an ionization collision, the momentum gain/lost from the COM momentum, i.e., $M\mathbf{V}$ is only distributed among the target (loss term) and the ion (gain term).

The rate of change of number densities can be expressed without any simplification

$$\frac{dn_e}{dt} = \Gamma^{ion} = -\frac{dn_t}{dt} = \frac{dn_i}{dt}. \tag{49}$$

For the rate of change of momentum densities, we can perform the reduction and arrive at the following:

$$\frac{d(\rho_t \mathbf{u}_t)}{dt} = -M\Gamma^{ion}\mathbf{U}_0 - \frac{T_t - T_e}{T_e}\mu\mathcal{K}^{ion}\mathbf{w}_0 + \mu\mathcal{R}^{ion}\mathbf{w}_0, \tag{50a}$$

$$\frac{d(\rho_i \mathbf{u}_i)}{dt} = +M\Gamma^{ion}\mathbf{U}_0 + \frac{T_t - T_e}{T_e}\mu\mathcal{K}^{ion}\mathbf{w}_0, \tag{50b}$$

$$\frac{d(\rho_e \mathbf{u}_e)}{dt} = -\mu\mathcal{R}^{ion}\mathbf{w}_0, \tag{50c}$$

where

$$\mathcal{R}^{ion} = R_0^{ion}; \quad \mathcal{K}^{ion} = \Gamma^{ion} - R_0^{ion}. \tag{51}$$

The system of equations above is formally equivalent to the following approximation at the particle level:

$$m_t \mathbf{v}_{t_0} \simeq M\mathbf{V} - \mu\mathbf{g}_0, \tag{52a}$$

$$m_i \mathbf{v}_{i_2} \simeq M\mathbf{V} - \mu(\mathbf{g}_1 + \mathbf{g}_2), \tag{52b}$$

$$m_e(\mathbf{v}_{e_0} - \mathbf{v}_{e_1} - \mathbf{v}_{e_2}) \simeq \mu(\mathbf{g}_0 - \mathbf{g}_1 - \mathbf{g}_2). \tag{52c}$$

It must be noted that all the error terms in (52) are $\mathcal{O}(m_e/M)$. For the rate of change of the total energies, we have

$$\frac{dE_t}{dt} = -\Gamma^{ion}\mathcal{E}^* - \frac{\mu}{M}\frac{(T_t - T_e)^2}{T_e}\mathcal{W}^{ion} + \frac{T_t - T_e}{T_e}\mu\mathcal{K}^{ion}\mathbf{w}_0 \cdot \mathbf{U}_0$$
$$+ \mu\mathcal{R}^{ion}\mathbf{w}_0 \cdot \mathbf{U}_0 - \frac{2\mu}{M}(T_t - T_e)\mathcal{J}^{ion}, \tag{53a}$$

$$\frac{dE_i}{dt} = +\Gamma^{ion}\mathcal{E}^* + \frac{\mu}{M}\frac{(T_t - T_e)^2}{T_e}\mathcal{W}^{ion} - \frac{T_t - T_e}{T_e}\mu\mathcal{K}^{ion}\mathbf{w}_0 \cdot \mathbf{U}_0, \tag{53b}$$

$$\frac{dE_e}{dt} = -\Gamma^{ion}\varepsilon^* - \mu\mathcal{R}^{ion}\mathbf{w}_0 \cdot \mathbf{U}_0 + \frac{2\mu}{M}(T_t - T_e)\mathcal{J}^{ion}, \tag{53c}$$

where

$$\mathcal{W}^{ion} = J_{00}^{ion} - 2\lambda R_0^{ion} + \lambda\Gamma^{ion}, \tag{54a}$$

$$\mathcal{J}^{ion} = J_{00}^{ion} - \lambda R_0^{ion}. \tag{54b}$$

The system above is equivalent to following approximation at the particle level:

$$\frac{1}{2}m_t\mathbf{v}_{t_0}^2 \simeq \frac{1}{2}M\mathbf{V}^2 - \mu\mathbf{V}\cdot\mathbf{g}_0, \tag{55a}$$

$$\frac{1}{2}m_i\mathbf{v}_{i_2}^2 \simeq \frac{1}{2}M\mathbf{V}^2 - \mu\mathbf{V}\cdot(\mathbf{g}_1 + \mathbf{g}_2), \tag{55b}$$

$$\frac{1}{2}m_e(\mathbf{v}_{e_0}^2 - \mathbf{v}_{e_1}^2 - \mathbf{v}_{e_2}^2) \simeq \frac{1}{2}\mu(\mathbf{g}_0^2 - \mathbf{g}_1^2 - \mathbf{g}_2^2) + \mu\mathbf{V}\cdot(\mathbf{g}_0 - \mathbf{g}_1 - \mathbf{g}_2)$$
$$= \varepsilon^* + \mu\mathbf{V}\cdot(\mathbf{g}_0 - \mathbf{g}_1 - \mathbf{g}_2). \tag{55c}$$

The system of equations consisting of (49), (50), and (53) describes the rates of change of number density, momentum, and energy for an electron induced ionization collision with isotropic scattering. For numerical calculation, one needs to pre-compute and store three basic rate coefficients Γ^{ion}, R_0^{ion}, and J_{00}^{ion} as functions of T_e and λ. All the other coefficients $\mathcal{K}^{ion}$, $\mathcal{R}^{ion}$, $\mathcal{J}^{ion}$, and $\mathcal{W}^{ion}$ can be constructed from these basic coefficients. Although not necessary, the isotropic scattering approximation has allowed us to greatly reduce the number of rate coefficients that need to be calculated.

IV. RECOMBINATION

A. Transfer integral

For recombination, we consider the reverse process of (8), which involves the following two-step process:

$$e(\mathbf{v}_{e_2}) + i(\mathbf{v}_{i_2}) \Rightarrow t^*(\mathbf{v}_{t_1}), \tag{56a}$$

$$s(\mathbf{v}_{s_1}) + t^*(\mathbf{v}_{t_1}) \Rightarrow s(\mathbf{v}_{s_0}) + t(\mathbf{v}_{t_0}). \tag{56b}$$

Similar to the case of an ionization collision, we can write a transfer integral as follows:

$$\Psi_{sei}^{rec} = n_s n_e n_i \int d^3\mathbf{v}_{s_1} d^3\mathbf{v}_{e_2} d^3\mathbf{v}_{i_2} f_s f_e f_i \, g_1 \, g_2 \psi$$
$$\times \omega_{sei}^{rec}(\mathbf{v}_{s_1}, \mathbf{v}_{e_2}, \mathbf{v}_{i_2}; \mathbf{v}_{s_0}, \mathbf{v}_{t_0}) \, d^3\mathbf{v}_{s_0} d^3\mathbf{v}_{t_0}, \tag{57}$$

where Ψ_{sei}^{rec} now contains a product of three Maxwellian distribution functions. In the general case, the three reactants belong to three different fluids. Using the procedure

described in Appendix A, the transfer integral can be expressed as

$$
\Psi_{sei}^{rec} = n_s n_e n_i \underbrace{\frac{1}{\pi^{\frac{3}{2}}a^3} \int d^3\mathbf{V}^{**} e^{-\mathbf{V}^{**2}/a^2}}_{\int d^3\mathbf{V}^{**} f_{V^{**}}} \cdot \frac{1}{\pi^{\frac{3}{2}}\alpha_t^3} \frac{1}{\pi^{\frac{3}{2}}\alpha^3} \int e^{-\tilde{\mathbf{g}}_2^2/\alpha_t^2}
$$
$$
\times \; e^{-(\tilde{\mathbf{g}}_1-\gamma_t\tilde{\mathbf{g}}_2)^2/\alpha^2} \times g_1 g_2 \, \psi \, \omega_{sei}^{rec}(\mathbf{g}_1,\mathbf{g}_2;\mathbf{g}_0)\, d^3\mathbf{g}_0 d^3\mathbf{g}_1 d^3\mathbf{g}_2,
\tag{58}
$$

where all the average quantities are listed in Table II. Similar to the case of an ionization collision, the integration over $\mathbf{V}^{**}$ can be easily eliminated since $f_{V^{**}}$ is a Maxwellian. Therefore, we need to consider only the case where ψ is independent of $\mathbf{V}^{**}$. The transfer integral can be arranged into

$$
\Psi_{sei}^{rec} = \frac{n_s n_e n_i}{\pi^3 \alpha_t^3 \alpha^3} \Lambda \int F_1 F_2 \cdot g_1 g_2 \, \psi \, \omega_{sei}^{rec}(\mathbf{g}_1,\mathbf{g}_2;\mathbf{g}_0)\, d^3\mathbf{g}_0 d^3\mathbf{g}_1 d^3\mathbf{g}_2,
\tag{59}
$$

where the product of all the exponential terms is separated into three parts

$$
\Lambda = e^{-w_2^2/\alpha_t^2} e^{-m^2/\alpha^2},
\tag{60a}
$$

$$
F_1 = e^{-g_2^2/\alpha_t^2} \cdot e^{-g_1^2/\alpha^2} \cdot e^{-\gamma_t^2 g_2^2/\alpha^2},
\tag{60b}
$$

$$
F_2 = e^{2\mathbf{g}_2\cdot\mathbf{w}_2/\alpha_t^2} \cdot e^{2\gamma_t\mathbf{g}_1\cdot\mathbf{g}_2/\alpha^2} \cdot e^{2\mathbf{g}_1\cdot\mathbf{m}/\alpha^2} \cdot e^{-2\gamma_t\mathbf{g}_2\cdot\mathbf{m}/\alpha^2}.
\tag{60c}
$$

For given values of mean velocities and temperatures, Λ is fixed, F_1 is angular-independent, and F_2 is angular-dependent.

TABLE II. Summary of variables used for recombination. The second column lists the general definition, and the third one is applicable for an electron-impact three-body recombination.

Variable	Definition	e-induced coll. ($s \equiv e$)
T^*	$\dfrac{MT_s T_e T_i}{m_s T_e T_i + m_e T_s T_i + m_i T_s T_e}$	T_i
$\tilde{T}_t$	$\dfrac{m_e T_i + m_i T_e}{m_e + m_i}$	T_e
$\tilde{T}$	$\dfrac{m_s T_e T_i + m_e T_s T_i + m_i T_s T_e}{M\tilde{T}_t}$	T_e
γ_t	$\dfrac{\mu(T_i - T_e)}{m_e T_i + m_i T_e}$	$\dfrac{\mu}{M}\dfrac{T_i - T_e}{T_e}$
$\tilde{\delta}$	$\dfrac{m_s T_e T_i}{m_s T_e T_i + m_e T_s T_i + m_i T_s T_e}$	$\dfrac{\mu}{M}\dfrac{T_i}{T_e}$
$\tilde{\gamma}$	$\dfrac{\mu_t T_s(T_i - T_e)}{m_s T_e T_i + m_e T_s T_i + m_i T_s T_e}$	$\dfrac{\mu}{M}\dfrac{T_i - T_e}{T_e}$
a	$\sqrt{\dfrac{2T^*}{M}}$	$\sqrt{\dfrac{2T_i}{m_i}}$
α_t	$\sqrt{\dfrac{2\tilde{T}_t}{\mu_t}}$	$\sqrt{\dfrac{2T_e}{m_e}}$
α	$\sqrt{\dfrac{2\tilde{T}}{\mu}}$	$\sqrt{\dfrac{2T_e}{m_e}}$
$\tilde{\mathbf{g}}_p$	$\mathbf{g}_p - \mathbf{w}_p, p = 0, 1, 2$	
$\mathbf{V}^{**}$	$\mathbf{V} - \mathbf{U}_1 - \dfrac{m_s}{M}\tilde{\mathbf{g}}_1 + \tilde{\gamma}\tilde{\mathbf{g}}_2 + \tilde{\delta}\tilde{\mathbf{g}}_1$	
$\mathbf{j}$	$\tilde{\mathbf{g}}_1 - \gamma_t\tilde{\mathbf{g}}_2$	
$\mathbf{m}$	$\mathbf{w}_1 - \gamma_t\mathbf{w}_2$	

It is more convenient to introduce the detailed balance (DB) relation aka Fowler relation[1] at this point

$$
g_1 g_2 \, \omega_{sei}^{rec}(\mathbf{g}_1,\mathbf{g}_2;\mathbf{g}_0) = \frac{g_t}{2g_i}\frac{h^3}{\mu_t^3} g_0 \, \omega_{st}^{ion}(\mathbf{g}_0;\mathbf{g}_1,\mathbf{g}_2),
\tag{61}
$$

where g is the degeneracy weight of the atomic state and h is the Planck constant. Substituting the DB relation back to the transfer integral, we obtain

$$
\Psi_{sie}^{rec} = \frac{g_t}{2g_i \mathbb{Z}_t}\frac{n_s n_i n_e}{\pi^{3/2}\alpha^3} \Lambda \int F_1 \cdot F_2
$$
$$
\times g_0 \, \psi \, \omega_{st}^{ion}(\mathbf{g}_0;\mathbf{g}_1,\mathbf{g}_2)\, d^3\mathbf{g}_0 d^3\mathbf{g}_1 d^3\mathbf{g}_2,
\tag{62}
$$

where $\mathbb{Z}_t \equiv \frac{(2\pi\mu_t\tilde{T}_t)^{3/2}}{h^3}$ is the translational partition function defined using the reduced mass and temperature of particle t. We can see that the integrand of Ψ_{sie}^{rec} is very similar to the one in (18) for ionization but with different exponential weighting functions. Note that F_1 and F_2 contain terms which are dependent on $\mathbf{g}_1$ and $\mathbf{g}_2$, so they must be integrated together with the differential cross section.

To proceed, let us define a reference frame (x, y, z) such that $\mathbf{m}$ is aligned with the $\hat{\mathbf{z}}$ axis. The remaining velocity vectors $\hat{\mathbf{w}}_2$, $\hat{\mathbf{g}}_0$, $\hat{\mathbf{g}}_1$, and $\hat{\mathbf{g}}_2$ can be defined according to the following rotation operations:

$$
\hat{\mathbf{w}}_2 = R(\varphi_w, \theta_w) \cdot \hat{\mathbf{m}}; \quad \hat{\mathbf{g}}_0 = R(\varphi, \theta) \cdot \hat{\mathbf{m}};
$$
$$
\hat{\mathbf{g}}_1 = R(\phi_1, \chi_1) \cdot \hat{\mathbf{g}}_0; \quad \hat{\mathbf{g}}_2 = R(\phi_2, \chi_2) \cdot \hat{\mathbf{g}}_0,
\tag{63}
$$

where φ_w and θ_w are fixed. Note that this choice of the coordinate system is not unique. In the rotated frame (ξ, η, ς) where $\hat{\mathbf{g}}_0$ is aligned with $\hat{\varsigma}$, the dot products in F_2 can be expanded as

$$
\hat{\mathbf{g}}_1 \cdot \hat{\mathbf{m}} = c_\theta c_{\chi_1} - s_\theta s_{\chi_1} c_{\phi_1},
\tag{64a}
$$

$$
\hat{\mathbf{g}}_2 \cdot \hat{\mathbf{m}} = c_\theta c_{\chi_2} - s_\theta s_{\chi_2} c_{\phi_2},
\tag{64b}
$$

$$
\hat{\mathbf{g}}_1 \cdot \hat{\mathbf{g}}_2 = c_{\chi_1} c_{\chi_2} + s_{\chi_1} s_{\chi_2} c_{\phi_1-\phi_2},
\tag{64c}
$$

$$
\hat{\mathbf{g}}_2 \cdot \hat{\mathbf{w}}_2 = f(\varphi_w, \theta_w, \varphi, \theta, \phi_2, \chi_2).
\tag{64d}
$$

For reason of brevity, we did not write the explicit expression for f. Using the same averaging operator defined in (19), the transfer integral can be rewritten as

$$
\Psi_{sie}^{rec} = \frac{g_t}{2g_i \mathbb{Z}_t}\frac{n_s n_i n_e}{\pi^{3/2}\alpha^3} \Lambda \int dg_0 \, g_0^3 \int d\varphi dc_\theta
$$
$$
\times \int F_1 \langle F_2 \psi \rangle_{\Omega_1,\Omega_2} \frac{d\sigma_{st}^{ion}}{d\Upsilon} d\Upsilon.
\tag{65}
$$

From conservation of energy, F_1 can be rewritten as

$$
F_1 = e^{-g_2^2/\alpha_t^2} \cdot e^{-g_1^2/\alpha^2} \cdot e^{-\gamma_t^2 g_2^2/\alpha^2},
$$
$$
= e^{\xi\varepsilon^*/\tilde{T}} e^{-\varepsilon_0/\tilde{T}} e^{(1-\xi)\Upsilon/\tilde{T}},
\tag{66}
$$

where $\xi = \frac{\tilde{T}}{\tilde{T}_t} + \gamma_t^2 \frac{\mu}{\mu_t}$. Using nondimensional energy variables, the transfer integral becomes

C-70

$$\Psi_{sie}^{rec} = \frac{g_t}{2 g_i \mathbb{Z}_t} n_s n_i n_e \frac{\bar{g} \bar{T}}{4\pi} \Lambda e^{\xi x^*} \int_{x^*}^{\infty} dx_0 \, e^{-x_0} \cdot x_0$$

$$\times \int d\varphi dc_\theta \int_{x^*}^{x_0} e^{(1-\xi)v} \langle F_2 \psi \rangle_{\Omega_1, \Omega_2} \frac{d\sigma_{st}^{ion}}{dv} dv. \quad (67)$$

Note that the above expression is the most general form of the transfer integral for a recombination collision, and various exchange source terms can be constructed in a similar manner. However, one can see that the rates need to be parametrized in terms of $\tilde{T}, \tilde{T}_t, \gamma_t, \lambda_1, \lambda_2, \varphi_w, \theta_w$, where $\lambda_1 = \frac{w_1^2}{\alpha^2}$ and $\lambda_2 = \frac{w_2^2}{\alpha_t^2}$. This is clearly not realistic for any numerical calculation due to excessive storage requirement. Therefore, in this work, we will consider only the special case of an electron induced recombination, which allows us to make further assumptions to simplify the description of the exchange coefficients.

B. Electron induced recombination

$e(v_{e_1}) + e(v_{e_2}) + i(v_{i_2}) \Rightarrow t(v_{t_0}) + e(v_{e_0})$

Let us now examine the case of an electron induced recombination with isotropic scattering, i.e., $\mathcal{G} = 1/16\pi^2$. Due to the small mass ratio $m_e/M \ll 1$, the average quantities can be approximated as listed in Table II (third column). In addition, we also have: $\mu \simeq \mu_t \simeq m_e$, $M \simeq m_t \simeq m_i$, $\mathbb{Z}_t \simeq \mathbb{Z}_e$, $\lambda = \lambda_1 \simeq \lambda_2$, $\varphi_w \simeq \theta_w \simeq 0$, and $\xi \simeq 1 + \gamma_t^2$. Here, we also assume that $\frac{m_e}{m_i} \ll \frac{T_e}{T_i}$ such that $\gamma_t \ll 1$. As mentioned before, this assumption holds for a wide range of physical domains of interest. Hereafter, the subscripts in the differential cross sections denoting colliding partners are omitted for brevity. The transfer integral (65) becomes

$$\Psi_{eie}^{rec} = \frac{g_t}{2 g_i \mathbb{Z}_e} \frac{n_e n_i n_e}{\pi^{3/2} \alpha^3} \Lambda \int dg_0 \, g_0^3 \int d\varphi dc_\theta$$

$$\times \int F_1 \langle F_2 \psi \rangle_{\Omega_1, \Omega_2} \frac{d\sigma^{ion}}{d\Upsilon} d\Upsilon. \quad (68)$$

Using the definitions of $\tilde{\delta}$ and $\tilde{\gamma}$ in (B12), we also have

$$\tilde{\delta} \simeq \frac{\mu}{M} \frac{T_i}{T_e}; \quad \tilde{\gamma} \simeq \gamma_t \simeq \frac{\mu}{M} \frac{T_i - T_e}{T_e} \simeq \tilde{\delta} - \frac{\mu}{M}. \quad (69)$$

The product of the exponential terms can be approximated as

$$\Lambda \simeq e^{-2w_1^2/\alpha^2}, \quad (70a)$$

$$F_1 \simeq e^{\varepsilon^*/\bar{T}} e^{-\varepsilon_0/\bar{T}}, \quad (70b)$$

$$F_2 \simeq e^{2\mathbf{g}_1 \cdot \mathbf{w}_1/\alpha^2} e^{2\mathbf{g}_2 \cdot \mathbf{w}_1/\alpha^2}. \quad (70c)$$

Note that we have neglected terms of $\mathcal{O}(\gamma_t)$ and higher in (70); these terms correspond to thermal nonequilibrium effect between the ion and electrons. However, this effect is weaker than the multifluid effect (note the multiplication of the mass ratio of m_e/m_i in the definition of γ_t and $\tilde{\delta}$). Hence, the assumptions in (70) are reasonable for a wide range of conditions. These approximations are equivalent to neglecting terms of $\mathcal{O}(\gamma_t)$ directly from Eq. (58), i.e., $\mathbf{j} \simeq \tilde{\mathbf{g}}_1$ and $\mathbf{m} \simeq \mathbf{w}_1$. We have also performed the integration of the full transfer integral (68), and the results indicate that the rates

are very weakly dependent on γ_t. The errors due to the approximations in (70) are negligible, with some discrepancies observed only for the case of $\psi = \mathbf{g}_1 \cdot \mathbf{g}_2$. However, the errors are not very significant and only limited to the region of large γ_t ($T_i \gg T_e$), which again falls outside of our physical domain of interest. Nevertheless, these approximations allow us to reduce the parameter space to characterize the exchange rates and obtain a more compact form of the transfer integral.

For the case of isotropic scattering, it is more convenient to define a reference frame such that $\mathbf{w}_1$ is aligned with the $\hat{\mathbf{z}}$ axis and rotated frames such that $\hat{\mathbf{g}}_0 = R(\varphi, \theta) \cdot \hat{\mathbf{w}}_1$, $\hat{\mathbf{g}}_1 = R(\phi_1, \chi_1) \cdot \hat{\mathbf{w}}_1$ and $\hat{\mathbf{g}}_2 = R(\phi_2, \chi_2) \cdot \hat{\mathbf{w}}_1$. F_2 then becomes

$$F_2 = e^{2g_1 w_1 c_{\chi_1}/\alpha^2} e^{2g_2 w_1 c_{\chi_2}/\alpha^2} = e^{2\sqrt{\lambda x_1} c_{\chi_1}} e^{2\sqrt{\lambda x_2} c_{\chi_2}}. \quad (71)$$

Using non-dimensional energy variables and after a trivial integration over φ and c_θ, the transfer integral is

$$\Psi_{eie}^{rec} = \frac{g_t}{2 g_i \mathbb{Z}_e} n_e n_i n_e \bar{g}_{\bar{T}} e^{-2\lambda} e^{x^*} \int_{x^*}^{\infty} dx_0 \, e^{-x_0} \cdot x_0$$

$$\times \int_{x^*}^{x_0} \langle F_2 \psi \rangle_{\Omega_1, \Omega_2} \frac{d\sigma^{ion}}{dv} dv. \quad (72)$$

C. Zeroth-order moment: Number density

For zeroth order exchange rate, substituting $\psi = 1$ into (72) leads to

$$\Gamma^{rec} = \frac{g_t}{2 g_i \mathbb{Z}_e} n_i n_e^2 \bar{g}_{\bar{T}} e^{-2\lambda} e^{x^*} \int_{x^*}^{\infty} dx_0 \, e^{-x_0}$$

$$\times x_0 \int_{x^*}^{x_0} \zeta^{(0)} \left(\sqrt{\lambda x_1} \right) \zeta^{(0)} \left(\sqrt{\lambda x_2} \right) \frac{d\sigma^{ion}}{dv} dv, \quad (73)$$

where $\zeta^{(0)}(\xi)$ is defined the same as before. One can easily check that in the limit of $\lambda \to 0$, we recover the Saha equation

$$\lim_{\lambda \to 0} \frac{\varpi^{rec}}{\varpi^{ion}} = \frac{g_t}{2 g_i \mathbb{Z}_e} e^{x^*}, \quad (74)$$

where $\varpi^{ion} \equiv \Gamma^{ion}/n_t n_e$ and $\varpi^{rec} \equiv \Gamma^{rec}/n_i n_e^2$ are the ionization and recombination rates. Note that the parameter λ is defined differently for ionization and recombination.

The rate equations for the number densities due to recombination can be constructed as follows:

$$\frac{dn_t}{dt} = +\Gamma^{rec}; \quad \frac{dn_e}{dt} = -\Gamma^{rec}; \quad \frac{dn_i}{dt} = -\Gamma^{rec}. \quad (75)$$

D. First-order moment: Momentum density

Similar to the case of ionization, the integral with $\psi = \mathbf{g}_p$ results in a vector proportional to the relative drift velocity $\mathbf{w}_1$. Let us define the following friction coefficients for recombination

$$\Psi_{eie}^{rec}|_{\psi = \mu \mathbf{g}_p} = \mu R_p^{rec} \mathbf{w}_1; \quad p = 0, 1, 2. \quad (76)$$

The explicit forms of these coefficients are given in (C1). In order to compute the exchange rates for momentum densities, we can start from the approximation in (52) and arrive at

$$m_t \mathbf{v}_{t_0} \simeq M\mathbf{V}^{**} + M\mathbf{U}_1 - \tilde{\gamma}M(\tilde{\mathbf{g}}_1 + \tilde{\mathbf{g}}_2) - \mu\mathbf{g}_0, \qquad (77a)$$

$$m_i \mathbf{v}_{i_2} \simeq M\mathbf{V}^{**} + M\mathbf{U}_1 - \tilde{\gamma}M(\tilde{\mathbf{g}}_1 + \tilde{\mathbf{g}}_2) - \mu(\mathbf{g}_1 + \mathbf{g}_2), \quad (77b)$$

$$m_e(\mathbf{v}_{e_0} - \mathbf{v}_{e_1} - \mathbf{v}_{e_2}) \simeq \mu(\mathbf{g}_0 - \mathbf{g}_1 - \mathbf{g}_2). \qquad (77c)$$

Substituting these expressions for the exchange variables, we obtain

$$\mathbf{R}_t^{rec} = +M\Gamma^{rec}\mathbf{U}_1 + \frac{T_i - T_e}{T_e}\mu(2\Gamma^{rec} - R_1^{rec} - R_2^{rec})\mathbf{w}_1$$
$$- \mu R_0^{rec}\mathbf{w}_1, \qquad (78a)$$

$$\mathbf{R}_i^{rec} = -M\Gamma^{rec}\mathbf{U}_1 - \frac{T_i - T_e}{T_e}\mu(2\Gamma^{rec} - R_1^{rec} - R_2^{rec})\mathbf{w}_1$$
$$+ \mu(R_1^{rec} + R_2^{rec})\mathbf{w}_1, \qquad (78b)$$

$$\mathbf{R}_e^{rec} = \mu(R_0^{rec} - R_1^{rec} - R_2^{rec})\mathbf{w}_1. \qquad (78c)$$

For isotropic scattering, it is easy to see that $R_0^{rec} = 0$ so we can re-write the above equations into the same form as (50)

$$\mathbf{R}_t^{rec} = +M\Gamma^{rec}\mathbf{U}_1 + \frac{T_i - T_e}{T_e}\mu\mathcal{K}^{rec}\mathbf{w}_1, \qquad (79a)$$

$$\mathbf{R}_i^{rec} = -M\Gamma^{rec}\mathbf{U}_1 - \frac{T_i - T_e}{T_e}\mu\mathcal{K}^{rec}\mathbf{w}_1 + \mu\mathcal{R}^{rec}\mathbf{w}_1, \quad (79b)$$

$$\mathbf{R}_e^{rec} = -\mu\mathcal{R}^{rec}\mathbf{w}_1, \qquad (79c)$$

where

$$\mathcal{R}^{rec} = R_1^{rec} + R_2^{rec}, \qquad (80a)$$

$$\mathcal{K}^{rec} = 2\Gamma^{rec} - R_1^{rec} - R_2^{rec}. \qquad (80b)$$

E. Second-order moment: Energy density

For second order moment, we can define a set of energy exchange coefficients for recombination

$$\Psi_{eie}^{rec}|_{\psi=\mathbf{g}_p \cdot \mathbf{g}_q} = J_{pq}^{rec}\alpha^2; \quad p, q = 0, 1, 2. \qquad (81)$$

The explicit forms of these coefficients are given in (C2). We can use the same approximation in (55) to express the kinetic energy of each particle in terms of variables in the COM frame. The total kinetic energy of the COM motion $\frac{1}{2}M\mathbf{V}^2$ can be expressed as

$$\frac{1}{2}M\mathbf{V}^2 = \frac{1}{2}M\mathbf{V}^{**2} + \frac{1}{2}M\mathbf{U}_1^2 + \tilde{\gamma}^2\frac{1}{2}M(\tilde{\mathbf{g}}_1 + \tilde{\mathbf{g}}_2)^2$$
$$- \tilde{\gamma}M\mathbf{U}_1 \cdot (\tilde{\mathbf{g}}_1 + \tilde{\mathbf{g}}_2) + \mathbf{V}^{**} \cdot [\cdots]. \qquad (82)$$

Therefore, the rate equations for energy densities can be written as

$$Q_t = +\Gamma^{rec}\mathcal{E}^* + \frac{\mu}{M}\frac{(T_i - T_e)^2}{T_e}\mathcal{W}^{rec} + \frac{T_i - T_e}{T_e}\mu\mathcal{K}^{rec}\mathbf{w}_1 \cdot \mathbf{U}_1, \tag{83a}$$

$$Q_i = -\Gamma^{rec}\mathcal{E}^* - \frac{\mu}{M}\frac{(T_i - T_e)^2}{T_e}\mathcal{W}^{rec} - \frac{T_i - T_e}{T_e}\mu\mathcal{K}^{rec}\mathbf{w}_1 \cdot \mathbf{U}_1$$
$$+ \mu\mathcal{R}^{rec}\mathbf{w}_1 \cdot \mathbf{U}_1 - \frac{2\mu}{M}(T_i - T_e)\mathcal{J}^{rec}, \tag{83b}$$

$$Q_e = \Gamma^{rec}\varepsilon^* - \mu\mathcal{R}^{rec}\mathbf{w}_1 \cdot \mathbf{U}_1 + \frac{2\mu}{M}(T_i - T_e)\mathcal{J}^{rec}, \tag{83c}$$

where $\mathcal{E}^* = \frac{3}{2}T^* + \frac{1}{2}M\mathbf{U}_1^2$ and

$$\mathcal{W}^{rec} = J_{11}^{rec} + J_{22}^{rec} + 2J_{12}^{rec} + 4\lambda\Gamma^{rec} - 4\lambda R_1^{rec} - 4\lambda R_2^{rec}, \tag{84a}$$

$$\mathcal{J}^{rec} = J_{11}^{rec} + J_{22}^{rec} + 2J_{12}^{rec} - 2\lambda R_1^{rec} - 2\lambda R_2^{rec}. \tag{84b}$$

Note that the system of Equations (83) has a similar form to (53).

V. COLLISIONAL-RADIATIVE MODELING USING THE MULTIFLUID EQUATIONS

Before presenting the numerical results, we briefly describe how to apply the previous formulation of the rates to construct CR models in the context of the multifluid equations. We first note that the same set of atomic data and cross sections is required as in standard CR model. The only difference is that the rates now include corrections due to the multifluid effect. Hence for a given set of data, the results obtained using the multifluid model will approach the standard (single-fluid) results in the limit of $\lambda \to 0$. This can be seen easily from the fact that all the expressions of the multifluid rates converge to single-fluid results in same limit. We will also demonstrate this convergence in Sec. VI by numerical calculations.

Let us now consider an example of an atomic hydrogen plasma, which consists of H, H$^+$, and the free electron e. The neutral atom H can have many bound states, the interactions between which can occur via a number of processes. In addition, ionization can proceed from those atomic levels by collisions with the free electrons. Consider now a three-fluid model (neutral-ion-electron) where the all atomic states of H belong to the same fluid (neutral). We also assume that the VDF of each fluid is a perfect Maxwellian so transport fluxes can be omitted. In this case, we end up with three sets of fluid equations (Euler), one for each fluid.[20] For neutral H, the fluid equations must be extended to the multi-species Euler equations to accommodate the different atomic states of H. The excitation/deexcitation rates between these atomic states can be constructed following our previous work.[18] The ionization/recombination rate for each atomic level can be computed using the formulas in Sections III and IV. For example, with 10 atomic levels, one would need to compute the rates for 90 excitation/deexcitation transitions and 20 ionization/recombination transitions. All these rates are tabulated as functions of λ and T_e. During the calculation, the rates for a specific condition can be obtained by interpolation. In addition, one can also compute momentum and

energy exchange rate coefficients in a similar fashion. Although we have only discussed electron induced excitation and ionization processes, other processes can also be incorporated in a consistent manner.

Generalization to multiply charged ions is also straightforward. Let us consider an example of helium where the plasma contains He, He$^+$, He^{++}, and e. In the simplest three-fluid formulation, we can treat He as a neutral fluid, He$^+$ and He^{++} together as an ion fluid, and the free electrons as an electron fluid. Since He and He$^+$ also include multiple excited states, the neutral and the ion fluid equations are extended to multi-species Euler equations. The exchange rates (number densities, momentum, and energy) for excitation and ionization (and their reverses) can be constructed similarly. In all cases, we also need to consider elastic collisions between different fluids: electron-ion, electron-neutral, and ion-neutral. These will appear through the momentum and energy equations of all the fluids. Note that here the collision between He$^+$ and He^{++} are omitted because they belong to the same fluid. In the case where each charge state is considered as an individual fluid, we end up with a four-fluid model, and He$^+$-He^{++} collision now must be taken into account. In the presence of hot electrons, we can treat the bulk and the hot electrons as two separate fluids in a straightforward manner.

VI. NUMERICAL RESULTS

A. Exchange rates

In this section, the numerical results of the reaction rates are presented. We consider a partially ionized hydrogen plasma with neutrals, ions, and free electrons. The neutral atomic states are defined according to the principle quantum number n and the energy levels are given from the Bohr model, e.g., $E_n = I_H(1 - 1/n^2)$, where $I_H = 13.6$ eV is the ionization energy of the ground state. The differential ionization cross section of state n is defined according to the semi-classical model[26]

$$\frac{d\sigma_n^{ion}}{d\Upsilon} = \frac{4\pi a_0^2 I_H^2}{\Upsilon^2} \frac{1}{\varepsilon} \quad \text{s.t.} \quad \bar{\sigma}_n^{ion} = \left(4\pi a_0^2\right) \frac{I_H^2(\varepsilon - I_n)}{I_n \varepsilon^2}, \quad (85)$$

where $I_n = I_H - E_n$ and $a_0 = 0.529$ Å is the Bohr radius.

The numerical integrations of all the exchange rate coefficients are carried out using the adaptive algorithm from the cubature package.[27] These results are also compared with the Monte Carlo integrations of the full transfer integral with excellent agreement. For brevity, we only show the results for zeroth-order reaction rates. Figures 1 and 2 show the ionization and recombination rates of ground state hydrogen for an electron induced collision with different values of λ. It must be noted that λ refers to the relative drift between H and e for ionization, and H$^+$ and e for recombination. For simplicity, H and H$^+$ are treated as the same fluid in our next calculations, so λ is the same for both processes. The results from Figures 1 and 2 confirm that both thermal (single-fluid) and beam asymptotic limits of the rates are recovered from the derived expressions. Figure 1 also indicates that the relative drift between two fluids (measured by λ) can increase the ionization rates at low temperature; this observation is similar to the case of excitation/deexcitation. On the contrary, Figure 2 suggests that the recombination rates get weaker as λ increases. It must be noted that the standard Saha relation (macroscopic) is only satisfied in the thermal limit. For $\lambda \neq 0$, detailed balance is enforced through the Fowler relation (microscopic).

B. Collisional-radiative rate equations

The multifluid reaction rates from Sections III and IV are used to solve the collisional-radiative (CR) rate equations. In the first test, we consider an isothermal system of atomic hydrogen plasma with constant electron number density. A total number of 10 atomic states of H is used in the calculation in addition to H$^+$. The parameter λ is introduced as a constant to examine the multifluid effect. This relative drift can be realized in a system where there is a steady state current. For example, in the magnetohydrodynamic (MHD) limit,[28] the plasma current $\mathbf{J}$ can be approximated by $\mathbf{J} \simeq \frac{1}{\eta}(\mathbf{E} + \mathbf{u} \times \mathbf{B})$, where η is the plasma resistivity. To make the problem more realistic, we also include line radiation between bound states and further assume that the plasma is optically thin.

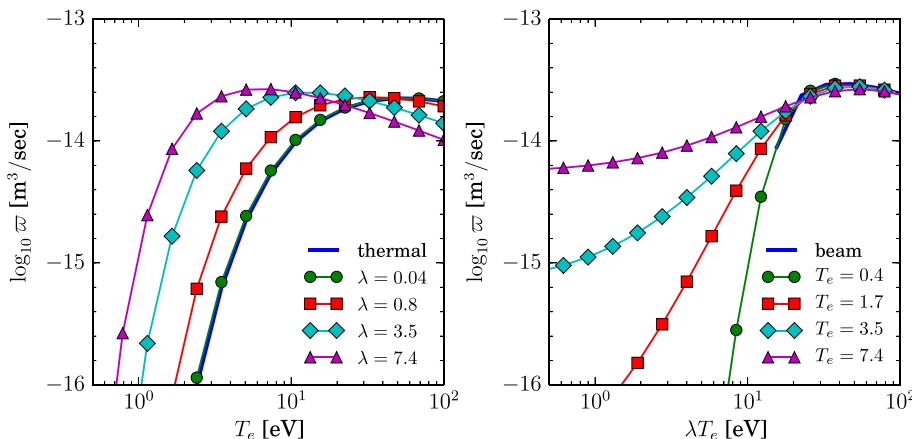The resultant system of rate equations can be put into the following form:

FIG. 1. Multifluid reaction rates for electron induced ionization collision. The solid lines correspond to the two asymptotic limits: thermal $(\lambda \to 0)$ and beam $(T_e \to 0)$.
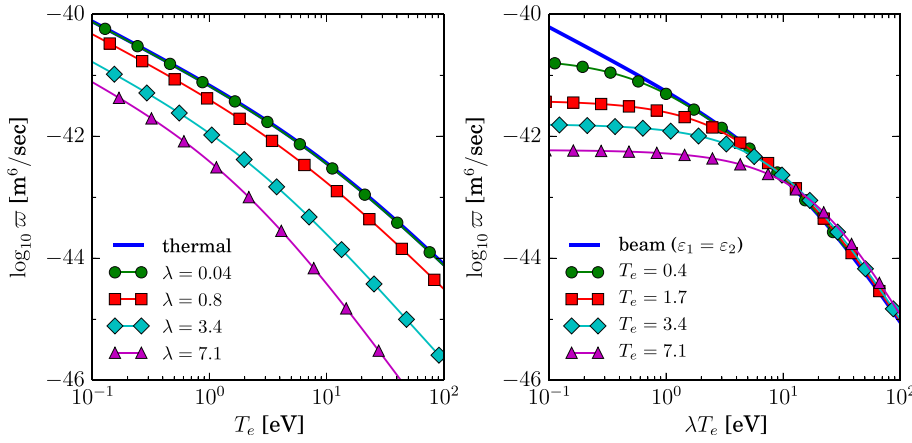
FIG. 2. Multifluid reaction rates for electron induced recombination collision. The solid lines correspond to the two asymptotic limits: thermal ($\lambda \to 0$) and beam ($T_e \to 0$). The beam limit is computed for $\varepsilon_1 = \varepsilon_2$, i.e., the scattered and ejected electrons share equal amount of energy.

$$\frac{d\tilde{\mathbf{n}}}{dt} = \bar{\mathbf{R}} \cdot \tilde{\mathbf{n}}, \qquad (86)$$

where $\tilde{\mathbf{n}}$ is the state population vector and $\bar{\mathbf{R}}$ is the rate matrix. For constant n_e, T_e, and λ, $\bar{\mathbf{R}}$ is also constant. The steady-state solutions of (86) can be obtained by setting $\frac{d\tilde{\mathbf{n}}}{dt} = 0$ and solving $\bar{\mathbf{R}} \cdot \tilde{\mathbf{n}} = 0$. In order to avoid the trivial solution of $\tilde{\mathbf{n}} = 0$, charge neutrality is used as a constraint. Equation (86) is solved for a range of (n_e, T_e, λ). Figure 3 shows the resultant ion fraction for the case of $n_e = 10^{20}$ m^{-3}. It can be seen that the ion fraction deviates from the single-fluid result when $\lambda \neq 0$. We note that the solutions plotted in Figure 3 are different from the LTE solutions since line radiation is included in the system. Furthermore, when $\lambda \neq 0$, the ratio of the forward and the backward rates of the inelastic processes also deviate from the standard Boltzmann/Saha relation.

In the next test, we consider an isochoric system of a two-fluid hydrogen plasma (electrons and heavy particles). Since the system is closed, the momentum densities and temperatures of the two fluids are coupled to the rate equations for number densities and evolved self-consistently. We assume that the all the heavy particles (neutrals and ions) belong to the same fluid, so that the momentum and energy exchange processes between these particles are infinitely
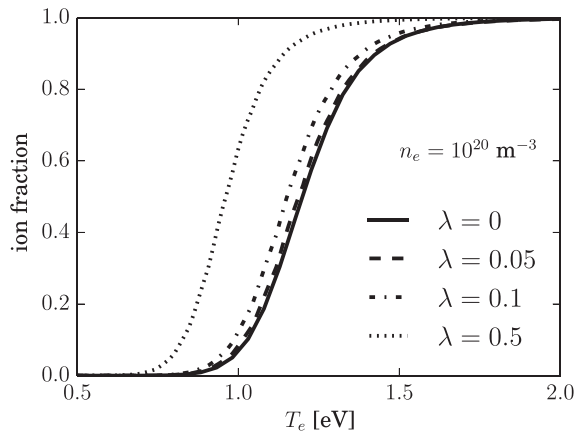
fast. The governing equations for this system are the same as the ones described in our previous paper[18] (see Appendix D) but with additional terms due to ionization/recombination. The initial conditions of these simulations are listed in Table III. Initially, all the atoms are at rest, and the atomic states are in Boltzmann equilibrium at 0.3 eV. A fraction of hot electrons at $T_e = 3$ eV is added, and their mean velocities are varied to demonstrate the multifluid effect. The ion density follows from charge neutrality.

Figure 4 shows the time evolution of the atomic state density (top) and the temperatures (bottom) of two different cases. Case I, shown in solid lines, corresponds to an initial zero relative drift velocity ($\lambda = 0$) and case II, shown in dashed lines, to a large initial relative drift velocity ($\lambda = 3.3$). Similar to the observation made when considering excitation/deexcitation only, the kinetics of inelastic collisions is enhanced when the relative drift between the two fluids is significant. This is indicated by an early increase in the population of the excitation states from Figure 4. Moreover, the temperature relaxation between two cases is also different as can be seen from the bottom plot of Figure 4. We remark that in this test case, the enhancement to the kinetics due to the relative drift only persists on the momentum relaxation time scale.

To further examine the relaxation process in the presence of the multifluid effect, Figure 5 shows the time evolution of the Boltzmann temperatures of the excited states and the energy exchange rates due to different types of collision for case II. The Boltzmann temperatures, defined between two adjacent states ℓ and u ($\ell < u$), are as follows:

$$T_{\ell u} = \frac{E_u - E_\ell}{\ln\left(\frac{n_\ell/g_\ell}{n_u/g_u}\right)}, \qquad (87)$$

FIG. 3. Ion fraction vs T_e for the case of atomic hydrogen plasma with $n_e = 10^{20}$ m^{-3} and different values of the multifluid λ parameters. The solutions are obtained by solving the steady-state rate equations for fixed values of n_e, T_e, and λ. Line radiation is included, and the plasma is assumed to be optically thin.

TABLE III. Initial conditions of 0D test cases. The total atomic density n_t is 10^{20} m^{-3}. The atomic states are initialized according to a Boltzmann distribution at T_h, i.e., $\mathcal{B}_k = \frac{g_k e^{-E_k/T_h}}{\mathbb{Z}_n}$, where $\mathbb{Z}_n$ is the electronic partition function.

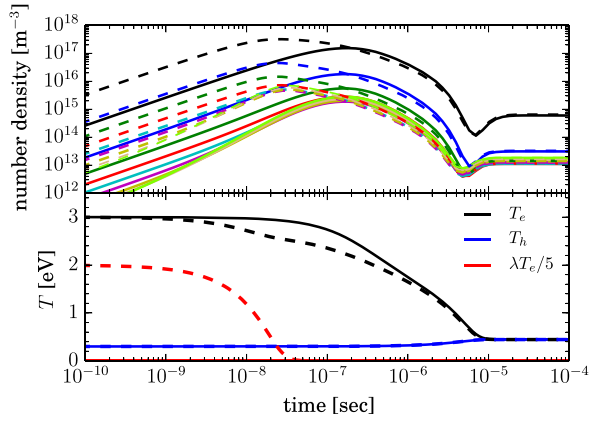|	Number density	Temperature
Atomic states	$n_k = 0.9\mathcal{B}_k n_t$ for $k = 1 - 10$	0.3 eV
Ion	$n_i = 0.1 n_t$	0.3 eV
Electron	$n_e = 0.1 n_t$	3 eV

FIG. 4. Time evolution of number densities of the atomic states $(2-10)$ and temperatures for the two test cases with initial conditions from Table III. Solid lines denote case I with $\lambda = 0.01$ initially, and dashed lines denote case II with $\lambda = 3.3$ initially. The evolution of the equivalent drift temperature λT_e (red) is shown for case II. For case I, $\lambda T_e \simeq 0$, which corresponds to a single-fluid calculation.

where n_ℓ, n_u are the number densities of levels ℓ, u. These temperatures are used to measure deviation from the Boltzmann equilibrium of the atomic states. It can be seen from the top of Figure 5 that at approximately 4×10^{-6} s, all the higher states $(n > 3)$ have reached equilibrium with the free electrons. Due to the large energy gaps between the first 3 atomic states, these states take a longer time to equilibrate,
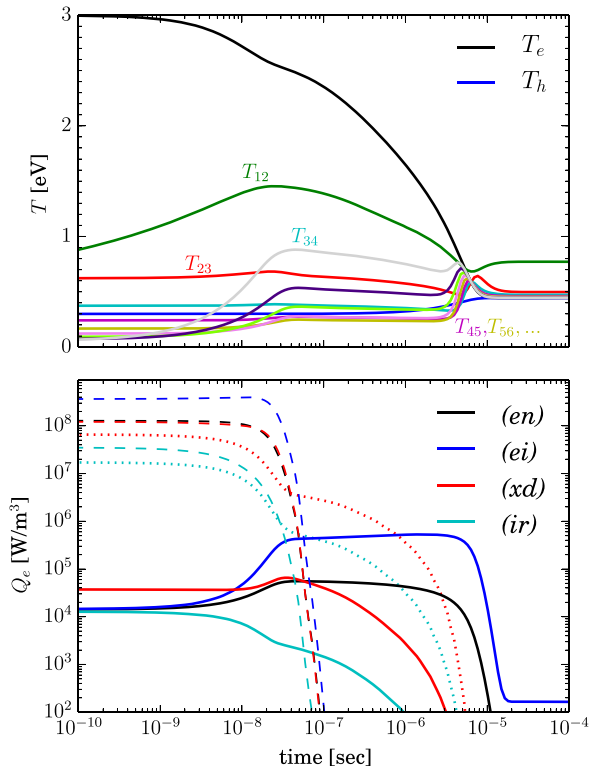

FIG. 5. Boltzmann temperatures of the excited states and energy exchange rates of the electrons. The Boltzmann temperatures are defined according to Eq. (87). In the bottom plot, different colors indicate different processes: (en) refers to electron-neutral, (ie) to Coulomb, (xd) to excitation/deexcitation, and (ir) to ionization/recombination collisions. The line types (solid, dashed, and dotted) are used to distinguish between different terms in the energy exchange.

e.g., $T_{23} \simeq T_e$ at approximately 2×10^{-5} s. This condition is known as partial local thermodynamic equilibrium.[29] Although not shown in here, the system eventually achieves complete thermodynamic equilibrium at a much later time.

The energy exchange rates of the electrons are shown in the bottom plot of Figure 5. The solid lines denote thermal relaxation (terms proportional to $\mathcal{J}$), the dashed lines denote frictional work (terms proportional to $\mathcal{R}$), and the dotted lines denote heat of formation due to inelastic collisions (terms proportional to Γ). In general, these terms can have different signs where positive and negative mean heating and cooling, respectively. For this particular case, the electrons are losing energy due excitation/ionization and thermal relaxation with the heavy particles; therefore, the solid and the dotted lines indicate cooling rates. On the other hand, the friction between the electrons and heavy particles can do work to heat the electrons, so the dashed lines here refer to heating rates. One can see from the bottom plot of Figure 5 that up to 10^{-7} s, frictional heating and heat of formation are the two main energy transfer mechanisms. This also corresponds to the momentum relaxation time scale, after which the momentum of the electrons has been completely absorbed by the heavy particles, signalling a change to single-fluid kinetics. One can also note that during $10^{-8} < t < 10^{-7}$, there are competing effects between all the processes, and inelastic collisions in general can also contribute to the total energy exchange and should not be neglected. Although this test case suggests that the multifluid effect only persists on the momentum relaxation time scale, we expect that this effect becomes more significant for system where there exists a steady state current (since the drift is always maintained due to the current). This will be examined in a future publication where spatial inhomogeneity will also be included.

VII. CONCLUSION

We have presented a model for ionization and recombination collisions in a multifluid plasma. The model is rigorously derived from kinetic theory and follows directly from our previous work on the modeling of excitation and deexcitation collisions.[18] The derived exchange coefficients are shown to have proper asymptotic limits and satisfy the principle of detailed balance. Using the new set of rate coefficients, we have developed and tested a new multifluid collisional-radiative model for atomic hydrogen with semi-classical cross sections for all the elementary processes. This model has two important features: (a) multifluid effect is captured in the definitions of the rate, and (b) the momentum and energy exchanges due to inelastic collisions are included.

Numerical calculations of the exchange rates are carried out, and the accuracy is confirmed with direct Monte Carlo integration. The results indicate that in the presence of a relative drift between two reactant fluids, the rates can be significantly different than the single-fluid limit. Two numerical tests are conducted to demonstrate the capability of the new model. In the first test, we compare the steady-state solutions of the collisional-radiative rate equations with constant n_e, T_e, and λ. The results converge to the single-fluid solution as

$\lambda \to 0$ and can deviate from that when $\lambda \neq 0$. In the second test, an isochoric heating of a partially ionized hydrogen plasma is performed in a virtual test cell to demonstrate the coupling between various collision processes. We observe that in general inelastic collisions can participate in the overall energy exchange process and should be included in the model. The present work can be extended to other types of collision, e.g., charge exchange and molecular collisions, with slight modifications. Future work focuses on examining the nonlinear coupling of transport with collisional-radiative kinetics by means of the multifluid transport equations.[19]

ACKNOWLEDGMENTS

APPENDIX A: SEPARATION OF VARIABLES

Similarly to excitation, the ionization process has two particles in the initial i state, but the final state includes a third particle, since an electron extracted from the target to yield an ion state ($t \to i + e$). The process is therefore

$$s(\mathbf{v}_{s_0}) + t(\mathbf{v}_{t_0}) \Longleftrightarrow s(\mathbf{v}_{s_1}) + i(\mathbf{v}_{i_2}) + e(\mathbf{v}_{e_2}). \quad \text{(A1)}$$

In the case of ionization, one must integrate over the distribution functions of the initial variables, which remain s, t, and the procedure used in an excitation collision remains valid. However, for recombination, we have a triple product of VDFs

$$f_s(\mathbf{v}_{s_1})f_i(\mathbf{v}_{i_2})f_e(\mathbf{v}_{e_2}) = \left(\frac{m_s}{2\pi T_s}\right)^{\frac{3}{2}}\left(\frac{m_i}{2\pi T_i}\right)^{\frac{3}{2}}\left(\frac{m_e}{2\pi T_e}\right)^{\frac{3}{2}} \exp[\mathcal{A}]. \quad \text{(A2)}$$

The argument of the exponential function is

$$\mathcal{A} = \beta_s(\mathbf{v}_{s_1} - \mathbf{u}_s)^2 + \underbrace{\beta_e(\mathbf{v}_{e_2} - \mathbf{u}_e)^2 + \beta_i(\mathbf{v}_{i_2} - \mathbf{u}_i)^2}_{\mathcal{A}_{ei}}, \quad \text{(A3)}$$

where $\beta_s = \frac{m_s}{2T_s}$. In order to perform the separation of variables, it is necessary to proceed in two steps. Thus, we can consider the ionization process as follows:

(a) the formation of an excited state t^* via scattering: $s(\mathbf{v}_{s_0}) + t(\mathbf{v}_{t_0}) \Rightarrow s(\mathbf{v}_{s_1}) + t^*(\mathbf{v}_{t_1})$
(b) the spontaneous ionization of the t^* state into ion and electron: $t^*(\mathbf{v}_{t_1}) \Rightarrow e(\mathbf{v}_{e_2}) + i(\mathbf{v}_{i_2})$

The reverse process, recombination, would similarly follow two steps:

(a) the formation of an excited state t^* via recombination: $e(\mathbf{v}_{e_2}) + i(\mathbf{v}_{i_2}) \Rightarrow t^*(\mathbf{v}_{t_1})$
(b) the spontaneous deexcitation of the t^* state via scattering: $s(\mathbf{v}_{s_1}) + t^*(\mathbf{v}_{t_1}) \Rightarrow s(\mathbf{v}_s) + t(\mathbf{v}_t)$

Consider now the first part of this two-step recombination process, which involves the product of the two VDFs for electron and ion: $f_e(\mathbf{v}_{e_2}) \cdot f_i(\mathbf{v}_{i_2})$. The argument of the

exponential function resulting from this product is $\mathcal{A}_{ei}$ as defined in (A3). Let us first perform the separation of variables for the product $f_e \cdot f_i$ (see Appendix B of Le and Cambier[18]), such that the argument becomes

$$\mathcal{A}_{ei} = (\beta_e + \beta_i)\mathbf{C}_t^2 + \frac{\beta_e\beta_i}{\beta_e + \beta_i}\tilde{\mathbf{g}}_2^2, \quad \text{(A4)}$$

where

$$\mathbf{C}_t = \mathbf{v}_{t_1} - \mathbf{u}_{t_1} + \gamma_t\tilde{\mathbf{g}}_2, \quad \text{(A5a)}$$

$$\tilde{\mathbf{g}}_2 = \mathbf{g}_2 - \mathbf{w}_2, \quad \text{(A5b)}$$

$$\mathbf{v}_{t_1} = \frac{m_e\mathbf{v}_{e_2} + m_i\mathbf{v}_{i_2}}{m_t}, \quad \text{(A5c)}$$

$$\mathbf{u}_{t_1} = \frac{m_e\mathbf{u}_e + m_i\mathbf{u}_i}{m_t}, \quad \text{(A5d)}$$

$$\gamma_t = \frac{1}{\beta_e + \beta_i}\left(\beta_e\frac{m_i}{m_t} - \beta_i\frac{m_e}{m_t}\right), \quad \text{(A5e)}$$

and the relative velocity $\mathbf{g}_2$ is defined according to (3).

We can now multiply by the VDF for the scattering particle for the second step of the recombination process. This leads to the total argument

$$\mathcal{A} = (\beta_e + \beta_i)\mathbf{C}_t^2 + \frac{\beta_e\beta_i}{\beta_e + \beta_i}\tilde{\mathbf{g}}_2^2 + \beta_s(\mathbf{v}_{s_1} - \mathbf{u}_s)^2. \quad \text{(A6)}$$

Let us also define

$$\mathbf{V}^* = \mathbf{v}_{t_1} - \mathbf{u}_{t_1} = \mathbf{V} - \mathbf{U}_1 - \frac{m_s}{M}\tilde{\mathbf{g}}_1, \quad \text{(A7)}$$

with $\tilde{\mathbf{g}}_1 = \mathbf{g}_1 - \mathbf{w}_1$. This yields

$$\mathbf{v}_{s_1} - \mathbf{u}_s = \mathbf{V} - \mathbf{U}_1 + \frac{m_t}{M}\tilde{\mathbf{g}}_1 = \mathbf{V}^* + \tilde{\mathbf{g}}_1 \quad \text{(A8)}$$

and from (A5a),

$$\mathbf{C}_t = \mathbf{V}^* + \gamma_t\tilde{\mathbf{g}}_2. \quad \text{(A9)}$$

Inserting into (A6)

$$\mathcal{A} = (\beta_s + \beta_e + \beta_i)\mathbf{V}^{*2} + \beta_s\tilde{\mathbf{g}}_1^2 + \left[(\beta_e + \beta_i)\gamma_t^2 + \frac{\beta_e\beta_i}{\beta_e + \beta_i}\right]\tilde{\mathbf{g}}_2^2$$
$$+ 2\gamma_t(\beta_e + \beta_i)\mathbf{V}^* \cdot \tilde{\mathbf{g}}_2 + 2\beta_s\mathbf{V}^* \cdot \tilde{\mathbf{g}}_1. \quad \text{(A10)}$$

Let us now try the following variable substitution:

$$\mathbf{V}^{**} = \mathbf{V}^* + \tilde{\gamma}\tilde{\mathbf{g}}_2 + \tilde{\delta}\tilde{\mathbf{g}}_1. \quad \text{(A11)}$$

Thus,

$$\mathbf{V}^{**2} = \mathbf{V}^{*2} + \tilde{\gamma}^2\tilde{\mathbf{g}}_2^2 + \tilde{\delta}^2\tilde{\mathbf{g}}_1^2 + 2\tilde{\gamma}\mathbf{V}^* \cdot \tilde{\mathbf{g}}_2 + 2\tilde{\delta}\mathbf{V}^* \cdot \tilde{\mathbf{g}}_1 + 2\tilde{\gamma}\tilde{\delta}\tilde{\mathbf{g}}_1 \cdot \tilde{\mathbf{g}}_2.$$

Defining $\Sigma_\beta = \beta_s + \beta_s + \beta_i$ and choosing

$$\tilde{\delta} = \frac{\beta_s}{\Sigma_\beta}, \quad \tilde{\gamma} = \frac{\beta_e + \beta_i}{\Sigma_\beta}\gamma_t, \quad \text{(A12)}$$

we obtain

$$\Sigma_\beta \mathbf{V}^{**2} = \Sigma_\beta \mathbf{V}^{*2} + \frac{\beta_s^2}{\Sigma_\beta}\tilde{\mathbf{g}}_1^2 + \frac{(\beta_e + \beta_i)^2}{\Sigma_\beta}\gamma_t^2 \tilde{\mathbf{g}}_2^2$$
$$+ 2\gamma_t(\beta_e + \beta_i)\mathbf{V}^* \cdot \tilde{\mathbf{g}}_2 + 2\beta_s \mathbf{V}^* \cdot \tilde{\mathbf{g}}_1$$
$$+ 2\gamma_t \frac{\beta_s(\beta_e + \beta_i)}{\Sigma_\beta}\tilde{\mathbf{g}}_1 \cdot \tilde{\mathbf{g}}_2.$$

Comparing with (A10), we can simplify the argument as

$$\mathcal{A} = \Sigma_\beta \mathbf{V}^{**2} + \left[\frac{\beta_s(\beta_e + \beta_i)}{\Sigma_\beta}\gamma_t^2 + \frac{\beta_e\beta_i}{\beta_e + \beta_i}\right]\tilde{\mathbf{g}}_2^2$$
$$+ \left[\frac{\beta_s(\beta_e + \beta_i)}{\Sigma_\beta}\right]\left[\tilde{\mathbf{g}}_1^2 - 2\gamma_t\tilde{\mathbf{g}}_1 \cdot \tilde{\mathbf{g}}_2\right]. \quad (A13)$$

Define now

$$\mathbf{j} = \tilde{\mathbf{g}}_1 - \gamma_t\tilde{\mathbf{g}}_2. \quad (A14)$$

We can now eliminate the last dot product, since $\tilde{\mathbf{g}}_1^2 - 2\gamma_t\tilde{\mathbf{g}}_1 \cdot \tilde{\mathbf{g}}_2 = \mathbf{j}^2 - \gamma_t^2\tilde{\mathbf{g}}_2^2$. Inserting into (A13), we finally obtain

$$\mathcal{A} = (\beta_s + \beta_e + \beta_i)\mathbf{V}^{**2} + \frac{\beta_e\beta_i}{\beta_e + \beta_i}\tilde{\mathbf{g}}_2^2 + \frac{\beta_s(\beta_e + \beta_i)}{\beta_s + \beta_e + \beta_i}\mathbf{j}^2. \quad (A15)$$

Here, all dot products have been removed with the proper change of variables. One can also show that

$$\beta_s + \beta_e + \beta_i = \frac{M}{2}\frac{m_s T_e T_i + m_e T_s T_i + m_i T_s T_e}{M T_s T_e T_i} \equiv \frac{M}{2T^*}, \quad (A16)$$

$$\frac{\beta_e\beta_i}{\beta_e + \beta_i} = \frac{m_e m_i}{2(m_e + m_i)}\frac{m_e + m_i}{m_e T_i + m_i T_e} \equiv \frac{\mu_t}{2\tilde{T}_t}, \quad (A17)$$

$$\frac{\beta_s(\beta_e + \beta_i)}{\beta_s + \beta_e + \beta_i} = \frac{m_s(m_e + m_i)}{2M}\frac{M\tilde{T}_t}{m_s T_e T_i + m_e T_s T_i + m_i T_s T_e} \equiv \frac{\mu}{2\tilde{T}}, \quad (A18)$$

where

$$T^* = \frac{M T_s T_e T_i}{m_s T_e T_i + m_e T_s T_i + m_i T_s T_e}, \quad (A19)$$

$$\tilde{T}_t = \frac{m_e T_i + m_i T_e}{m_e + m_i}, \quad (A20)$$

$$\tilde{T} = \frac{m_s T_e T_i + m_e T_s T_i + m_i T_s T_e}{M\tilde{T}_t}, \quad (A21)$$

$$\mu_t = \frac{m_e m_i}{m_e + m_i}, \quad (A22)$$

$$\mu = \frac{m_s(m_e + m_i)}{M}. \quad (A23)$$

The product of the three Maxwellian VDF becomes

$$f_s(\mathbf{v}_{s_1}) \cdot f_e(\mathbf{v}_{e_2}) \cdot f_i(\mathbf{v}_{i_2})$$
$$= \left(\frac{M}{2\pi T^*}\right)^{\frac{3}{2}}\exp\left[-\frac{M\mathbf{V}^{**2}}{2T^*}\right] \cdot \left(\frac{\mu_t}{2\pi\tilde{T}_t}\right)^{\frac{3}{2}}\exp\left[-\frac{\mu_t\tilde{\mathbf{g}}_2^2}{2\tilde{T}_t}\right]$$
$$\times \left(\frac{\mu}{2\pi\tilde{T}}\right)^{\frac{3}{2}}\exp\left[-\frac{\mu\mathbf{j}^2}{2\tilde{T}}\right] \equiv f^{**}(\mathbf{V}^{**}) \cdot \tilde{f}_t(\tilde{\mathbf{g}}_2) \cdot \tilde{f}(\mathbf{j}).$$
$$(A24)$$

All subsequent expressions can now be simplified with this separation of variables. For example, any operator $\mathcal{O}$ that depends only on variables expressed using the relative velocities $(\mathbf{g}_0, \mathbf{g}_1, \mathbf{g}_2)$, we have

$$\int d^3\mathbf{v}_{s_1} d^3\mathbf{v}_{e_2} d^3\mathbf{v}_{i_2} f_s f_e f_i \mathcal{O}(\mathbf{g}_0, \mathbf{g}_1, \mathbf{g}_2)$$
$$= \underbrace{\int d^3\mathbf{V}^{**} f^{**}(\mathbf{V}^{**})}_{\equiv 1} \cdot \int d^3\tilde{\mathbf{g}}_1 d^3\tilde{\mathbf{g}}_2 \tilde{f}_t(\tilde{\mathbf{g}}_2)\tilde{f}(\mathbf{j})\mathcal{O}(\mathbf{g}_0, \mathbf{g}_1, \mathbf{g}_2).$$
$$(A25)$$

APPENDIX B: EXCHANGE COEFFICIENTS FOR IONIZATION

We describe in this Appendix various exchange terms computed from the transfer integral for an ionization collision, starting from the transfer integral given in Eq. (10). The exchange variables during the collision can be expressed in terms of $\mathbf{V}^*$, $\mathbf{g}_0$, $\mathbf{g}_1$, and $\mathbf{g}_2$. Since f_{V^*} represents a Maxwellian VDF centered at zero, we have $\int d^3\mathbf{V}^* f_{V^*} = 1$, $\int d^3\mathbf{V}^* \mathbf{V}^* f_{V^*} = 0$ and $\int d^3\mathbf{V}^* \frac{1}{2}M\mathbf{V}^{*2} f_{V^*} = \frac{3}{2}T^*$. Thus, if ψ is independent of $\mathbf{V}^*$, we can eliminate the integral over $\mathbf{V}^*$. For the case where ψ is linear in $\mathbf{V}^*$, the transfer integral goes to zero. Here, the subscripts st in the differential cross sections are omitted for brevity.

Let us now consider the case where $\psi = \mathbf{g}_p$ ($p = 0, 1, 2$). As shown in Le and Cambier,[18] the only non-zero velocity component survived after the integration is the one parallel to the relative drift velocity $\mathbf{w}_0$. Using the definition from (26), the friction coefficients can be written as follows:

$$R_0^{ion} = \frac{2}{3}n_s n_t \bar{g}_{\tilde{T}} e^{-\lambda}\int_{x^*}^\infty dx_0 x_0^2 e^{-x_0}\zeta^{(1)}\left(\sqrt{\lambda x_0}\right)\bar{\sigma}^{ion}, \quad (B1a)$$

$$R_1^{ion} = \frac{2}{3}n_s n_t \bar{g}_{\tilde{T}} e^{-\lambda}\int_{x^*}^\infty dx_0 x_0^{\frac{3}{2}} e^{-x_0}\zeta^{(1)}\left(\sqrt{\lambda x_0}\right)$$
$$\times \int_{x^*}^{x_0}\sqrt{x_1}\langle c_{\chi_1}\rangle_{\Omega_1,\Omega_2}\frac{d\sigma^{ion}}{d\upsilon}d\upsilon, \quad (B1b)$$

$$R_2^{ion} = \frac{2}{3}n_s n_t \bar{g}_{\tilde{T}} e^{-\lambda}\int_{x^*}^\infty dx_0 x_0^{\frac{3}{2}} e^{-x_0}$$
$$\times \zeta^{(1)}\left(\sqrt{\lambda x_0}\right)\int_{x^*}^{x_0}\sqrt{x_2}\langle c_{\chi_2}\rangle_{\Omega_1,\Omega_2}\frac{d\sigma^{ion}}{d\upsilon}d\upsilon, \quad (B1c)$$

where $\zeta^{(1)}(\xi) = \frac{3}{4\xi^2}\left[\cosh(2\xi) - \frac{\sinh(2\xi)}{2\xi}\right]$ and $\lim_{\xi\to 0}\zeta^{(1)}(\xi) = 1$. For isotropic scattering, i.e., $\mathcal{G}^{ion} = $ constant, $R_1^{ion} = R_2^{ion} = 0$.

For the case of $\psi = \mathbf{g}_p \cdot \mathbf{g}_q$ ($p, q = 0, 1, 2$), we arrive at the following thermal relaxation coefficients using the definitions in (37):

$$J_{00}^{ion} = n_s n_t \bar{g}_{\tilde{T}} e^{-\lambda}\int_{x^*}^\infty dx_0 x_0^2 e^{-x_0}\zeta^{(0)}\left(\sqrt{\lambda x_0}\right)\bar{\sigma}^{ion}, \quad (B2a)$$

$$J_{11}^{ion} = n_s n_t \bar{g}_{\tilde{T}} e^{-\lambda}\int_{x^*}^\infty dx_0 x_0 e^{-x_0}\zeta^{(0)}\left(\sqrt{\lambda x_0}\right)\int_{x^*}^{x_0}x_1\frac{d\sigma^{ion}}{d\upsilon}d\upsilon, \quad (B2b)$$

$$J_{22}^{ion} = n_s n_t \bar{g}_{\bar{T}} e^{-\lambda} \int_{x^*}^{\infty} dx_0 \, x_0 \, e^{-x_0} \, \zeta^{(0)}\left(\sqrt{\lambda x_0}\right) \int_{x^*}^{x_0} x_2 \frac{d\sigma^{ion}}{dv} dv,$$
$$\text{(B2c)}$$

$$J_{01}^{ion} = n_s n_t \bar{g}_{\bar{T}} e^{-\lambda} \int_{x^*}^{\infty} dx_0 \, x_0 \, e^{-x_0} \, \zeta^{(0)}\left(\sqrt{\lambda x_0}\right)$$
$$\times \int_{x^*}^{x_0} \sqrt{x_0 x_1} \langle c_{\chi_1} \rangle_{\Omega_1, \Omega_2} \frac{d\sigma^{ion}}{dv} dv, \quad \text{(B2d)}$$

$$J_{02}^{ion} = n_s n_t \bar{g}_{\bar{T}} e^{-\lambda} \int_{x^*}^{\infty} dx_0 \, x_0 \, e^{-x_0} \, \zeta^{(0)}\left(\sqrt{\lambda x_0}\right)$$
$$\times \int_{x^*}^{x_0} \sqrt{x_0 x_2} \langle c_{\chi_2} \rangle_{\Omega_1, \Omega_2} \frac{d\sigma^{ion}}{dv} dv, \quad \text{(B2e)}$$

$$J_{12}^{ion} = n_s n_t \bar{g}_{\bar{T}} e^{-\lambda} \int_{x^*}^{\infty} dx_0 \, x_0 \, e^{-x_0} \, \zeta^{(0)}\left(\sqrt{\lambda x_0}\right)$$
$$\times \int_{x^*}^{x_0} \sqrt{x_1 x_2} \langle c_{\chi_1} c_{\chi_2} \rangle_{\Omega_1, \Omega_2} \frac{d\sigma^{ion}}{dv} dv, \quad \text{(B2f)}$$

where we have used the result $\langle s_{\chi_1} s_{\chi_2} c_{\phi_1 - \phi_2} \rangle_{\Omega_1, \Omega_2} = 0$, since the scattering is isotropic in ϕ_1 and ϕ_2. Note that energy conservation implies that $x_1 = x_0 - v$ and $x_2 = v - x^*$.

APPENDIX C: EXCHANGE COEFFICIENTS FOR RECOMBINATION

We describe in this Appendix various exchange terms computed from the transfer integral for recombination processes. Here, we only consider electron induced recombination with isotropic scattering. For the case of zeroth order moment ($\psi = 1$), we arrive at Eq. (73).

Let us now consider the case where $\psi = \mathbf{g}_p$ ($p = 0, 1, 2$). It can be shown that the only non-zero velocity component survived after the integration is the one parallel to the relative drift velocity $\mathbf{w}_1$. This is due to the fact that $\langle F_2 c_{\phi_1} \rangle_{\Omega_1, \Omega_2} = \langle F_2 c_{\phi_2} \rangle_{\Omega_1, \Omega_2} = 0$. Using the definition from (76), the friction coefficients can be written as follows:

$$R_0^{rec} = 0, \quad \text{(C1a)}$$

$$R_1^{rec} = \frac{2}{3} \frac{g_t}{2 g_i \mathbb{Z}_e} n_i n_e^2 \bar{g}_{\bar{T}} e^{-2\lambda} e^{x^*} \int_{x^*}^{\infty} dx_0 \, e^{-x_0}$$
$$\times x_0 \int_{x^*}^{x_0} x_1 \, \zeta^{(1)}\left(\sqrt{\lambda x_1}\right) \zeta^{(0)}\left(\sqrt{\lambda x_2}\right) \frac{d\sigma^{ion}}{dv} dv, \quad \text{(C1b)}$$

$$R_2^{rec} = \frac{2}{3} \frac{g_t}{2 g_i \mathbb{Z}_e} n_i n_e^2 \bar{g}_{\bar{T}} e^{-2\lambda} e^{x^*} \int_{x^*}^{\infty} dx_0 \, e^{-x_0}$$
$$\times x_0 \int_{x^*}^{x_0} x_2 \, \zeta^{(0)}\left(\sqrt{\lambda x_1}\right) \zeta^{(1)}\left(\sqrt{\lambda x_2}\right) \frac{d\sigma^{ion}}{dv} dv. \quad \text{(C1c)}$$

For the case of $\psi = \mathbf{g}_p \cdot \mathbf{g}_q$ ($p, q = 0, 1, 2$), we arrive at the following thermal relaxation coefficients using the definition in (81):

$$J_{00}^{rec} = \frac{g_t}{2 g_i \mathbb{Z}_e} n_i n_e^2 \bar{g}_{\bar{T}} e^{-2\lambda} e^{x^*} \int_{x^*}^{\infty} dx_0 \, e^{-x_0}$$
$$\times x_0^2 \int_{x^*}^{x_0} \zeta^{(0)}\left(\sqrt{\lambda x_1}\right) \zeta^{(0)}\left(\sqrt{\lambda x_2}\right) \frac{d\sigma^{ion}}{dv} dv, \quad \text{(C2a)}$$

$$J_{11}^{rec} = \frac{g_t}{2 g_i \mathbb{Z}_e} n_i n_e^2 \bar{g}_{\bar{T}} e^{-2\lambda} e^{x^*} \int_{x^*}^{\infty} dx_0 \, e^{-x_0}$$
$$\times x_0 \int_{x^*}^{x_0} x_1 \zeta^{(0)}\left(\sqrt{\lambda x_1}\right) \zeta^{(0)}\left(\sqrt{\lambda x_2}\right) \frac{d\sigma^{ion}}{dv} dv, \quad \text{(C2b)}$$

$$J_{22}^{rec} = \frac{g_t}{2 g_i \mathbb{Z}_e} n_i n_e^2 \bar{g}_{\bar{T}} e^{-2\lambda} e^{x^*} \int_{x^*}^{\infty} dx_0 \, e^{-x_0}$$
$$\times x_0 \int_{x^*}^{x_0} x_2 \zeta^{(0)}\left(\sqrt{\lambda x_1}\right) \zeta^{(0)}\left(\sqrt{\lambda x_2}\right) \frac{d\sigma^{ion}}{dv} dv, \quad \text{(C2c)}$$

$$J_{01}^{rec} = 0, \quad \text{(C2d)}$$

$$J_{02}^{rec} = 0, \quad \text{(C2e)}$$

$$J_{12}^{rec} = \frac{4}{9} \frac{g_t}{2 g_i \mathbb{Z}_e} n_i n_e^2 \bar{g}_{\bar{T}} e^{-2\lambda} e^{x^*} \int_{x^*}^{\infty} dx_0 \, e^{-x_0}$$
$$\times x_0 \int_{x^*}^{x_0} \lambda x_1 x_2 \zeta^{(1)}\left(\sqrt{\lambda x_1}\right) \zeta^{(1)}\left(\sqrt{\lambda x_2}\right) \frac{d\sigma^{ion}}{dv} dv. \quad \text{(C2f)}$$

[1] J. Oxenius, *Kinetic Theory of Particles and Photons* (Springer, 1986).
[2] A. Bar-Shalom, M. Klapisch, and J. Oreg, J. Quant. Spectrosc. Radiat. Transfer **71**, 169 (2001).
[3] M. Gu, Can. J. Phys. **86**, 675 (2008).
[4] O. Zatsarinny, Comput. Phys. Commun. **174**, 273 (2006).
[5] P. Jonsson, G. Gaigalas, J. Biero, C. F. Fischer, and I. Grant, Comput. Phys. Commun. **184**, 2197 (2013).
[6] T. R. Kallman and P. Palmeri, Rev. Mod. Phys. **79**, 79 (2007).
[7] J. Annaloro and A. Bultel, Phys. Plasmas **21**, 123512 (2014).
[8] H. A. Scott, J. Quant. Spectrosc. Radiat. Transfer **71**, 689 (2001).
[9] H.-K. Chung, M. Chen, W. Morgan, Y. Ralchenko, and R. Lee, High Energy Density Phys. **1**, 3 (2005).
[10] S. Hansen, J. Bauche, C. Bauche-Arnoult, and M. Gu, High Energy Density Phys. **3**, 109 (2007).
[11] M. G. Kapper and J.-L. Cambier, J. Appl. Phys. **109**, 113309 (2011).
[12] M. Panesi and A. Lani, Phys. Fluids **25**, 057101 (2013).
[13] H. P. Le, A. R. Karagozian, and J.-L. Cambier, Phys. Plasmas **20**, 123304 (2013).
[14] A. Munafo, M. Panesi, and T. E. Magin, Phys. Rev. E **89**, 023001 (2014).
[15] A. Guy, A. Bourdon, and M.-Y. Perrin, Phys. Plasmas **22**, 043507 (2015).
[16] G. J. M. Hagelaar and L. C. Pitchford, Plasma Sources Sci. Technol. **14**, 722 (2005).
[17] S. Longo, Plasma Sources Sci. Technol. **9**, 468 (2000).
[18] H. P. Le and J.-L. Cambier, Phys. Plasmas **22**, 093512 (2015).
[19] S. I. Braginskii, "Transport processes in a plasma," in *Review of Plasma Physics* (Consultants Bureau, New York, 1965), Vol. 1, pp. 205–311.
[20] J. M. Burgers, *Flow Equations for Composite Gases* (Academic Press, 1969).
[21] J. Horwitz and P. Banks, Planet. Space Sci. **21**, 1975 (1973).
[22] A. R. Barakat and R. W. Schunk, J. Phys. D: Appl. Phys. **14**, 421 (1981).
[23] M. S. Benilov, Phys. Plasmas **3**, 2805 (1996).
[24] M. S. Benilov, Phys. Plasmas **4**, 521 (1997).
[25] L. Conde, L. F. Ibez, and J. Lambs, Phys. Rev. E **78**, 026407 (2008).
[26] Y. B. Zeldovich and Y. B. Raizer, *Physics of Shock Waves and High-Temperature Hydrodynamic Phenomena* (Dover Publications, 2002).
[27] S. G. Johnson, Cubature package, 2014.
[28] R. J. Rosa, *Magnetohydrodynamic Energy Conversion* (McGraw-Hill, 1968).
[29] J. van der Mullen, Phys. Rep. **191**, 109 (1990).

Resource Summary

	FY14	FY15	FY16
Funding Expended ($K)			
Non-Military Govt. Personnel Costs	0*	0*	0*
In-House Contractor Costs	345	373	360
External Contractor Costs	27	0	12
Travel (AFOSR)	0	0	3
Supplies, Computers	3	2	0
Total Resource Requirements	375	375	375

Table 1: Funding Table. *Cost of non-military government personnel is offset by leveraged 6.2 funding contributed by AFRL/RQR and is not included; per guidance of AFRL/FM Comptroller (10 Nov 2010), AFRL civilian pay cannot be-reimbursed from other AF organizations; furthermore, listing of actual salary cost of various government employees would violate privacy act unless proposal was prepared by an official supervisor.

This Page Intentionally Left Blank

AFRL-RQ-ED-TR-2017-0002
Primary Distribution of this Report:

RQR
AFRL R&D Case Files
Completed Interim and Final Tech Reports Repository

AFRL/RQ Technical Library (2 CD + 1 HC)
6 Draco Drive
Edwards AFB, CA 93524-7130

Johns Hopkins University
Whiting School of Engineering
ATTN: Mary T. Gannaway/FSO
10630 Little Patuxent Pkwy, Suite 202
Columbia, MD 21044-3286

Defense Technical Information Center
(1 Electronic Submission via STINT)
Attn: DTIC-ACQS
8725 John J. Kingman Road, Suite 94
Ft. Belvoir, VA 22060-6218